# MORPHOLOGY OF SURFACE DAMAGE RESULTING FROM STATIC AND DYNAMIC CONTACTS

A thesis submitted for the degree of Doctor of Philosophy

By

Pratip Vongbandit
BSc, ME

Department of Mechanical Engineering, Brunel University

July 2008

# Abstract

Contact fatigue damages resulting either from static or dynamic contact are of interest for understanding the failure modes and mechanisms leading to improvement of the components' performances in tribological applications. The objective of this research was to ascertain how and to what extent the counterface materials, loading conditions, contact configuration, lubrication, and the environment affect the failure behaviours of material under static and dynamic contact fatigue loading.

An experimental ball-on-flat test configuration was employed for both static and dynamic contact fatigue testing. In house designed test rig was used to study static cyclic loading contact fatigue behaviours of brittle polymethylmethacrylate (PMMA) in contact with balls made of different materials, i.e. $Si_3N_4$, steel, aluminium, bronze and PMMA in dry and oil-lubricated conditions. A modified four ball test machine was used to study dynamic rolling contact fatigue behaviours of thermally sprayed molybdenum and titanium coatings in contact with steel balls in dry and seawater conditions.

The static contact fatigue and the dynamic contact fatigue test results revealed that counterface material, loading magnitude, lubricant and the environment play a vital role in controlling failure modes and the extent of damage.

In static contact fatigue, adhesive strength of the interface was the key factor controlling damage of the PMMA plate in both dry and oil-lubricated conditions. In dry conditions, three failure modes, i.e. adhesive wear, ring cracks, and radial cracks controlled the damage of PMMA to a different degree for each combination of materials. Whereas, the damage of each combination in oil-lubricated conditions was affected by the extent of three failure modes, i.e. adhesive wear, radial cracks and abrasive wear.

In dynamic contact fatigue tests, adhesive wear and inter-lamellar cracking were the major failure modes controlling damage of molybdenum coating and titanium coating in dry contact conditions while abrasive wear, corrosion and lubrication controlled damage processes in seawater conditions.

# LIST OF PUBLICATIONS

(1) Vongbandit, P. and Stolarski, T. A. (2008)
Surface damage of brittle polymer resulting from static contact loading, *J. Mater. Sci.*, vol. 43, pp. 1180-1190.

(2) Vongbandit, P. and Stolarski, T. A. (2008)
Wear behaviour of molybdenum and titanium thermal spray coatings under dry and seawater conditions, Proceedings Friction, Wear and Wear Protection, 9-11 April 2008, Aachen, Germany.

# ACKNOLEDGEMENTS

I owe a debt of gratitude to my thesis advisors, Professor T. A. Stolarski, for his guidance, assistance, encouragement and patience to make the completion of this thesis possible.

Special thanks to The Ministry of Scientific and Technology, Thai government for financial support throughout my research.

I would like to thank Dr. Nongluck Pankurddee, the governor of Thailand Institute of Scientific and Technological Research (TISTR) for inspiring me to become a better person.

I thank to Keith Withers for his assistance in the laboratory works, and for being a great friend. The work of the technicians those involved in the modification of the test facility, in particular, Len Soans and Clive Barrett.

I would also like to extend my gratitude the Experimental Techniques Centre for the use of the equipments and the time of their technical staff, especially Nita.

My acknowledgements also extend to some fellow students at Mechanical Engineering Department and friends outside, for helping hand, discussions, motivations and supporting. To name a few: Somchoke Sontikeaw, Masaaki Yamane, Duc Nhim Ha and Yusuke Ida.

Finally, I would like to thank my mother and my wife Kratin and Jutamas for all their love and support.

# TABLE OF CONTENTS

# LIST OF FIGURES

# LIST OF TABLES

# Nomenclature

## Chapter 1

| | |
|---|---|
| $\lambda$ | Elastohydrodynamic film parameter |
| $\Delta$ | Non-dimension coating thickness parameter |
| $P_o$ | Contact pressure |

## Chapter 2

| | |
|---|---|
| $A$ | Constant depending on the material and test conditions |
| A | Area of contact |
| $c$ | Crack length |
| D | Diameter of sphere |
| $dc/dN$ | The fatigue crack growth rate per cycle |
| $E^*$ | Relative Modulus |
| F | Lateral force |
| $F_A$ | Adhesive or shearing force of friction |
| $F_D$ | Deformation or ploughing force of friction |
| $F_{total}$ | Total force of friction |
| $K_c$ | Critical stress intensity factor |
| $K_{max}$ | Maximum stress intensity factor |
| $K_{min}$ | Minimum stress intensity factor |
| $K_{th}$ | Threshold value of stress intensity factor |
| $m$ | Constant depending on the material and test conditions |
| $N$ | Number of cycles |
| n | Constant |
| P | Normal force |
| R | Radius of sphere |
| r | Asperities radius |
| $R_1$, $R_2$ | Radius of body 1 and body 2, respectively |
| $T_m$ | Melting point of crystallites |
| $T_g$ | Glass temperature |
| $\mu_s$ | Coefficient of static friction |
| $\mu_k$ | Coefficient of dynamic friction |
| $\Delta K$ | Range of the stress intensity factor |
| $\Delta K_{th}$ | Range of threshold of stress intensity factor |
| $\mu$ | Coefficient of friction |
| $\tau$ | Shear force |

## Chapter 3

| | |
|---|---|
| $a$ | Radius of contact circle |
| $a_{max}$ | Maximum radius of contact circle in case adhesion superimpose |
| $G$ | Shear modulus or strain energy release rate |
| $G_d$ | Work of adhesion during receding of contact |
| $K_I$ | Mode I stress intensity factor at the contact perimeter, $a_{max}$ |
| $L$ | Stress cycles factor on the sample |
| $M$ | Mass |
| $max\ G$ | Strain energy release rate at maximum contact load, $P_{max}$ |
| max $T_{rr}$ | Maximum radial of the non-singular stresses owing to contact at maximum load |
| max $T_{\varphi\varphi}$ | Maximum circumferential of the non-singular stresses owing to contact at maximum load |
| max $\sigma_r$ | Maximum tensile stress |
| $P$ | Applied load |
| $P_1$ | Load |
| $p_0$ | Maximum contact pressure |
| $P_s$ | Pressure on the plate |
| $P_c$ | Pressure on the wall of the cup |
| $p_m$ | Mean contact pressure |
| $P_{min}$ | Minimum cycling normal contact load is applied the in the range |
| $P_{max}$ | Maximum cycling normal contact load is applied the in the range |
| $P^*_{max}$ | Apparent load |
| $R$ | Load ratio, $R = (min\ K_I/max\ K_I) = (P_{min}/P_{max})$ |
| $R_{ball}$ | Radius of ball |
| $R_{cup}$ | Radius of cup |
| $R^*$ | Relative radius |
| $T_{rr}$ and $T_{\varphi\varphi}$ | Non-singular circumferential stress terms in radial and circumferential directions |
| $\sigma_0$ | Tensile stress |
| $\xi$ | Elasticity parameter |
| $\mu$ | Coefficient of friction |
| $q$ | Tangential traction, $q = \pm\mu P$ |
| $v$ | Poisson ratio |
| $w$ | Work of adhesion |
| $\gamma_1$ and $\gamma_2$ | Surface energy of body 1 and body 2 respectively |
| $\gamma_{12}$ | Interface surface energy |
| $\rho$ and $\theta$ | Local polar coordinates at the contact perimeter, |
| $\varphi$ | Angular circumferential coordinate, |
| $\rho_k$ | Size of K-dominance around the contact perimeter |
| $\Delta K_{th}$ | Mode I threshold stress intensity range for long crack initiation |
| $\Delta K_I$ | Mode I stress intensity factor range at the contact perimeter, $a_{max}$ |
| $\theta$ and $\beta$ | Angles |
| $\omega_A$ | Angular velocity of the upper ball |
| $\omega_P$ | Angular velocity of the lower ball |
| z | Number of the driven balls |

| | |
|---|---|
| $\mu$ | Coefficient of internal friction |
| $\sigma_{rr}^{nor}$ , $\sigma_{zz}^{nor}$ , $\sigma_{rz}^{nor}$ , $\sigma_{\theta\theta}^{nor}$ | Tensile stress field in different direction |

**Chapter 4**

| | |
|---|---|
| $K_{15}$ | Conductivity ratio |
| $R_q$ | Root mean square surface roughness |
| λ | Elastohydrodynamic film parameter |
| α | Pressure-viscosity coefficient |

# Abbreviations

| | |
|---|---|
| Al | Aluminium |
| $Al_2O_3$ | Aluminium oxide |
| Ar | Argon |
| APS | Air plasma spraying |
| BR | polybutadiene |
| CVD | Chemical vapour deposition |
| D-Gun | Detonation gun spraying |
| $Cr_2O_3$ | Chromium oxide |
| EB | Electron beam |
| EDX | Energy dispersive X-ray |
| EHL | Elastohydrodynamic lubrication |
| EP | Epoxy resins |
| FCP | Fatigue crack propagation |
| HDPE | High density polyethylene |
| HIP | Hot isostatic pressing |
| HVOF | High velocity oxy-fuel spraying |
| IBAD | Ion beam assisted deposition |
| IAPSO | International Association for the Physical Sciences of the Oceans |
| LPPS | Low-pressure plasma spraying |
| MIC | Microbiologically influenced corrosion |
| Mo | Molybdenum |
| $MoS_2$ | Molybdenum disulfide |
| NR | natural rubber |
| PAPVD | Plasma assisted physical vapour deposition |
| PC | Polycarbonate |
| PCTFE | Polychlorotrifluoroethylene |
| PE | Polyethylene |
| PMMA | Polymethylmethacrylate |
| PS | Polystrylene |
| PTFE | Polytetrafluoroethylene |
| PUR | polyurethane |
| PVC | Polyvinylchloride |
| PVD | Physical vapour deposition |
| PVDF | Polyvinylidene fluoride |
| RCF | Rolling contact fatigue |
| RPS | Reactive plasma spray |
| SEM | Scanning electron microscope |
| SiC | Silicon carbide |
| $Si_3N_4$ | Silicon nitride |
| $SiO_2$ | Silica |
| SPS | Shrouded plasma spraying |
| Ti | Titanium |
| TiC | Titanium carbide |

| | |
|---|---|
| TiN | Titanium nitride |
| $TiO_2$ | Titanium dioxide |
| UF, UW | amino plastics |
| VPS | Vacuum plasma spraying |
| WC-Co | Tungsten cobalt coating |
| XRD | X-ray diffraction |

# Chapter 1 INTRODUCTION

## 1.1 Preliminary

Tribology deals with friction, wear and lubrication. Those phenomena occur in contact of the components. The performance of the components involves many variables such as tribological conditions, materials and surface conditions, and environment. Many efforts have been made in order to understand the influence of these variables and interaction between them. The aim of tribology research is to understand the friction and wear processes and their mechanisms. It is also aiming to improve the life span of such components and to fulfil the need of working under conditions of harsh environments such as higher load, speed and temperature. Previous attempts produced a considerable knowledge about failure modes and mechanisms. However, it is well known in general that wear of materials is a complicated phenomenon. Therefore, the need for knowledge to fill the understanding gap in this field is still remaining.

This thesis is divided into two major parts. The first part presents investigation into the surface damage of brittle polymer under static conditions when in contact with different counterface materials in both dry and lubricated conditions. The second part presents study on rolling contact fatigue of metallic coatings under dry and seawater conditions.

The objective of the first investigation is to study and to establish damage mechanisms of brittle materials which typical representative is polymethylmethacrylate (PMMA) when in static contact with silicon nitride ($Si_3N_4$), steel, aluminium, bronze and PMMA as counterface materials. The test configuration was ball-on-flat. The rationale behind this investigation is to increase the understanding of surface damage morphology of brittle materials under static contact conditions.

The objective of the second investigation is to study and establish the damage mechanisms of molybdenum (Mo) and titanium (Ti) plasma sprayed coatings on the carbon steel substrate under rolling contact fatigue (RCF) conditions in dry and seawater environment. In this investigation ball-on-flat test configuration was also used. Rolling contact fatigue of

metallic coatings such as molybdenum and titanium is still rather limited and rolling contact fatigue tests in seawater has never been reported.

The objectives were accomplished by using contact mechanics theory, fracture mechanics, elastrohydrodynamic lubrication theory, surface and sub-surface observations with the aid of an optical and scanning electron microscopy, hardness measurements by micro hardness tester, chemical analysis by energy dispersive X-ray (EDX), surface roughness and profile measurements using Talysurf.

## 1.2 General Background

Tribology has been developed more than 30 years ago. Since then, the knowledge in this field has steadily accumulated. However, increasing demands on improving the performance and integrity of components force the conduct of more research in this field. Contact fatigue is a major factor affecting the life span of the machine components under static repeating contact or dynamic rolling contact loading conditions. Until now, contact fatigue mechanisms are not fully understood because the failures depend on many variables such as load conditions, contact geometry, materials in contact, environments and lubricants. Furthermore, those factors are found to have mutual interdependence. Therefore, static contact and dynamic contact fatigue behaviours and performance of each material are very important information for engineers to understand for design and operation. This thesis concerns about the static contact fatigue of PMMA polymer and rolling contact fatigue of plasma spray molybdenum and titanium coatings.

Many reports on contact fatigue of polymers have been presented. They focused mainly on static fretting contact fatigue and dynamic rolling contact fatigue. Linear fretting contact fatigue (fretting mode I) of polymer is well established. Polymer static or normal oscillating (fretting mode II) contact fatigue, however, has not been widely published recently.

The first purpose of this research was to experimentally investigate the performance and the failure modes of polymers in repeating contact. Five different ball types were used to

study the effect of mating material on fretting performance and failures mechanisms. This was achieved by using a test apparatus based on ball-on-flat contact configuration.
PMMA material was selected for this investigation for various reasons. Firstly, the material is almost behaving as brittle material and nearly obeys Hooke's law under compression. Secondly, the material has high light transmitivity. Thirdly, due to its low stiffness large areas of contact can be attained at moderate loads. Finally, crack formation in material, especially subsurface cracks, can be easily observed (Al-Sabti, 2000).

The purpose of coatings is to improve tribological properties such as friction, wear, RCF in application pertinent to severe service conditions. Thermal spray coatings have been developed and used to improve the performance of components in respect of wear and corrosion resistance.

Recently, many efforts have been made to understand the performance, failure modes and failure mechanisms of thermal sprayed coatings operating under rolling contact fatigue conditions. Thermally sprayed cermets and alumina coatings have been well established. Nevertheless, the amount of published literature on performance of thermally sprayed coating of other materials in RCF is still limited. Furthermore, the data on rolling contact fatigue of metallic coatings operating in seawater is not available.

The second purpose of this research was to experimentally observe failure modes and generalised failure mechanisms of thermal sprayed metallic coatings under rolling contact fatigue. This study was a comparison investigation of RCF performance of molybdenum and titanium coatings in both dry contact and seawater lubricated contact.

The practical relevance of results generated by this study is twofold.

(i) improvement of understanding of surface damage mechanism of a brittle material when it is on static contact.
(ii) surface damage of both molybdenum and titanium coatings in the presence of seawater has a potential for informing engineers about the conditions required to use both coatings in a corrosive environment.

## 1.3 Objectives and Scope of Research

The overall objective of this study was to experimentally investigate the performance, the failure modes and their mechanisms of different materials under static repeating contact and dynamic rolling contact conditions. Qualitative and quantitative approaches were used in this study. The scope of this research includes the following:

(I) For static repeating contact of PMMA:

a. Damage modes and mechanisms of PMMA under static contact fatigue.
b. The effect of spherical counterface material types i.e. aluminium, bronze, steel, silicon nitride and polymethylmethacrylate on the performance, failure modes and mechanisms of PMMA.
c. The role of lubricants on the performance and failure modes of PMMA.

(II) For rolling contact fatigue of metallic coatings:

a. The effect of contact stress on rolling contact fatigue performance, failure modes and mechanisms of molybdenum coating.
b. Comparison of rolling contact fatigue performance and failure modes of molybdenum and titanium coatings in dry conditions.
c. The rolling contact fatigue performance and failure modes and mechanisms of molybdenum and titanium coatings in seawater conditions.

## 1.4 Thesis Outline

This thesis is presented in 7 chapters. Chapter 1 provides background and literature survey.

Chapter 2 reviews theoretical and experimental work related to the fatigue performance of polymers in repeating contact and thermal sprayed coating in rolling contact fatigue. This chapter is composed of three main sections. The first section is introduction. The second section deals with general knowledge on polymers, their physical and mechanical properties, fatigue and cyclic contact fatigue performance. The third section presents the metallic coatings, their wear and rolling contact fatigue.

Chapter 3 explains the modification introduced to testing equipment. The contact stresses were analysed for cyclical static fatigue test and rolling contact fatigue test. Also, the design of experiment for the investigation of the lubrication effect on the repeating contact fatigue of PMMA and a seawater influence on molybdenum and titanium coating are presented.

Chapter 4 gives details on specimen's preparation, testing apparatus, experimental procedures and damage analysis.

Chapter 5 presents test conditions and test results of static contact fatigue test of PMMA and rolling contact fatigue test of molybdenum and titanium coatings. The results of static contact fatigue of PMMA concern micro-hardness measurements, friction test results, surface observations, surface profile measurements, and fatigue life. The results of rolling contact fatigue of molybdenum and titanium coatings consist of surface damage observations, micro-hardness measurement, section examinations, fatigue progression, and wear track measurements.

Chapter 6 discusses the test results. This chapter consists of five sections. The first section is introduction. The second section elaborates the effect of ball's material types on damage of PMMA by static contact fatigue test. The third section shows the effect of lubrication on the damage of PMMA generated in static contact fatigue test. The fourth section discusses the damage mechanisms of molybdenum and titanium thermal sprayed coatings produced during rolling contact fatigue testing in dry conditions. The last section deals with failures mechanisms of molybdenum and titanium thermal sprayed coatings obtained under rolling contact fatigue in seawater.

Chapter 7 states the main conclusions of the study. The outline of summarized results and the contribution of the work, further research and development areas are also given.

Appendices A to D contain details of repeating contact test machine design, modified four ball machine for rolling contact fatigue test, and elastohydrodynamic lubrication analysis, and preliminary and auxiliary experiments.

## 1.5 **Literature Survey**

### *1.5.1 Static repeating contact*

Static contact fatigue is named differently i.e. fretting fatigue, repeating sinusoidal contact fatigue, standing contact fatigue and Mode II fretting contact fatigue. The following is the survey of the static contact fatigue in different materials.

#### *1.5.1.1 Steel*

Burton and Ku (1963) reported the repeating sinusoidal contact between sphere and flat where their surfaces were always in touch (sited in Waterhouse, 1972). The shape of contact appeared as two rings. It was pointed out that there was some sliding between surfaces at the asperities level though the surfaces in the outer ring were in normal contact with each other. This was demonstrated by the staining appearance of the surface in this area. It was argued that the tangential movement and the normal movement would be in phase.

Higham *et al.* (1978) studied wear of steel during fretting fatigue contact with various types of polymers. The results showed that under the same test conditions metal could be worn by the plastics to different severity levels. The severity of metal wear by plastics was in the following order polytetrafluoroethylene (PTFE), polyethylene (PE), polyvinylidene fluoride (PVDF), polychlorotrifluoroethylene (PCTFE), polysulphone, polyvinylchloride (PVC), polymethylmethacrylate (PMMA), polycarbonate (PC), nylon 66. The authors demonstrated that there was a close relation between amount of metal wear and the adhesive properties of the polymers determined by the difference in their surface energies, the critical surface tension and coefficient of friction.

Wear of metal has three stage i.e. (1) incubation period (no wear), (2) running-in period (wear rate decrease with the increase in test time), (3) steady-state (rate of wear constant). The length of incubation period depended on the polymer counterface and decreased in the order PTFE, PE, PVDF, PCTFE, PVC, PMMA, PC, nylon 66. The material was removed from metal surface by adhesive transfer of $\alpha$-$Fe_2O_3$ particles to the polymer surface. Wear of the polymer during fretting was in the form of fibre formation for polysulphone, PVC, polycarbonate, nylon 66 and, to a small extent, PE, while it took the form of a transfer of a

polymer film to the metal for PTFE and PVDF. No polymer wear occurred for PCTFE or PMMA.

Zhu and Zhou (2001[a]) have studied static fatigue of three contact pairs between 52100 steel ball against 52100, 1045, 1045 steel with TiN coating. The test program was to investigate the relations between normal load and indentation depth as a function of loading cycles and the degradation mechanisms. Two degradation mechanisms were observed i.e. deformation and detachment of particles. The authors found that the indentation depth was highly changed at the first cycle. The depth was proportional to the level of load. As the test proceeded, the change of the depth decreased until steady state was attained at whichever contact condition. They argued that this was because of strain-hardening of the materials. The indentation depth at the first cycle was sensitive to test speed. Examinations by Talysurf and SEM revealed that there was adhesion between the counterfaces. Detachment of particles was attributed to adhesion for similar contact pairs (52100/52100) and to delamination for TiN coating. Contact with different materials promoted micro-slip in the radial direction as confirmed by red powder – a clear indication of a fretting damage. They argued that fretting was not expected at the interface between the same metals.

Alfredsson and Olsson (2000) have conducted static contact fatigue test of case-hardened material loaded by hard sphere in dry conditions. Four types of cracks were observed including two surface cracks, i.e. ring/cone and radial cracks, and subsurface cracks, i.e. lateral and median cracks, see Figure 1.1. Among cracks, the ring/cone cracks firstly developed. The authors argued that the ductility of the material was the most important factor for crack initiation. By numerical simulation, it was demonstrated that all cracks were opened by tensile stress during alternating load.

Alfredsson and Olsson (2001) have also investigated multiaxial fatigue criteria to predict the initiation of static contact fatigue in flat case-hardened steel from the indenter. They evaluated various criteria i.e. Sines, Haigh principal stress, Finley, Mc Diarmid and Dang Van multiaxial fatigue criteria. They found that a single criterion was not enough to describe all aspects of the experimental results. The best criterion was that proposed by Finley followed by Haigh principal stress. They pointed out that the Sines, McDiaramid and Dang Van criteria were unsuitable to apply for contact fatigue of case hardened steel.

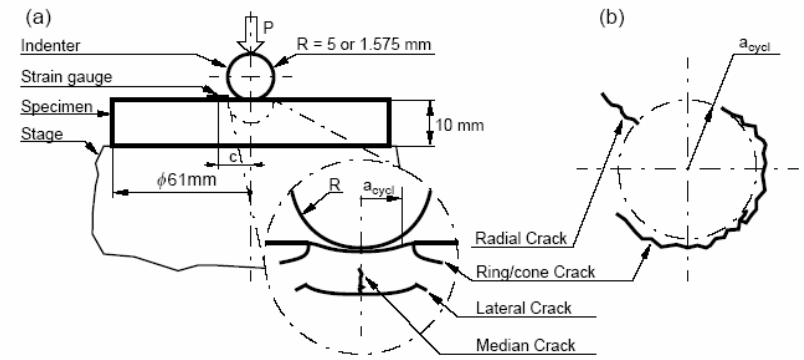


Figure 1.1 Damage modes of case hardened steel by static contact fatigue (Alfredsson and Olsson, 2000).

Subsequent study by Alfredsson and Olsson (2003) concerned the effect of tangential load induced by incline of the specimen at the angle below the angle of friction on the static contact fatigue performance of the material. The results showed that the endurance limit of the material was decreased comparing to normal static fatigue load conditions. The authors argued that tangential load changed both surface and subsurface stresses.

#### *1.5.1.2 Ceramics*

Guiberteau *et al.* (1993) investigated repeating contact fatigue of coarse grain alumina. The results showed that alumina was damaged by deformation-induced intergranular micro-fracture, leading ultimately at large numbers of cycles and high contact pressures to severe grain dislodgement. The damage developed in a zone of high shear stress and hydrostatic compression beneath the contact circle. The authors pointed out that the damage was a mechanical process because the fatigue damage also existed in inert environments. However, they reported that the test in a humid environment accelerated the damage.

Chen *et al.* (1996) studied damage mechanisms of $Si_3N_4$ material against WC ball under static repeating contact load in the presence of turbo oil. They discovered that wear process consisted of three stages that is roughening of the contact surface (stage I), cone crack initiation and propagation (stage II) and large volume material removal from outside the contact area (stage III). Stage I wear was fatigue damage in the form of cracks formation along grain boundaries due to tensile stress resulting from heterogeneous mechanical

behaviour between grain and grain boundaries during loading cycle. Wear process was further developed by shear stress pulling out the grain from the surface. Stage II was cone crack initiation in the maximum tensile stress region outside contact circumference under cyclic contact fatigue. The cracks initiated at the grain boundary and propagated along this weaker path. In stage III a large volume of material was removed from outside the contact area. The generation of secondary cone cracks was due to the shift of tensile stress distribution along the lateral direction. The authors pointed out that wear debris were generated from the joint of the cracks.

Ezop and Karlsson (1999) have conducted static contact fatigue or repeating contact fatigue tests on two commercial silicon nitride materials in different environments including air, water and ethylene glycol. The tungsten carbide ball was used as an indenter. They claimed that wear damage in air and in water began with a small indentation in the flat and develop into a cavity. Thereafter, layer of wear debris was formed in the contact zone. The damage mechanism in ethylene glycol was impossible to be established. The specimen tested in air at 5 GPa for 2 million cycles was not damaged, but at 15 GPa intergranular cracks occurred with grain pulled out; similar to that reported by Chen *et al*. (1996). The specimen tested in water suffered severe damage. The indentation was deep and large with cracks smaller than those in the air. However, no grain pulled out was observed. The results obtained in ethylene glycol showed the indentation as deep as that in water, but without cracks.

Another static fatigue tests by Ezop and Karlsson (2001) were an investigation to determine the influence of microstructure and the environments on the static fatigue of four types of silicon nitride. Fatigue test conditions were close to those described in their previous paper (Ezop and Karlsson, 1999). As their previous observation, wear process started with an accumulation of wear debris and formation of a layer in the dry contact zone. By contrast, wear debris was continuously removed when tests were in water and glycol. The authors found the differences of the time required to initiate cracks and the rate of crack propagation in each type of specimen.

The specimen with coarse microstructure produced a deep indentation. In air and ethylene glycol the material containing higher amount of glass phase suffered the least damage because of glass phase softening at a higher temperature, smoothing asperities and,

therefore, inhibiting micro-fracture. However, this material was sensitive to stress corrosion in water. The resistance to water decreased especially for specimens with inhomogeneous glass phase distribution. The most homogeneous microstructure exhibited the best overall cyclic performance in the air and glycol. Crack appeared on specimens tested in water at stress level lower than that in air.

Kim *et al.* (1999) have investigated static contact fatigue of relatively brittle ceramics under contact load created by a spherical indenter in humid environments (water and air). Two damage modes i.e. macro cone fracture, and radial and secondary cone crack formation were identified. Figure 1.2 shows damage modes of soda-lime glass and porcelain in water under static contact fatigue. Macro cone fracture was in a brittle region and radial and secondary cone cracks were in a quasi-plastic region. The brittle region was driven by tensile stress and was a fast process involving chemical process. Power law could be used to describe cone crack formation for defining the critical number of cycles to initiate cone crack for a fixed maximum cyclic contact load in region where applied load was lower than the critical load for initiating cone crack. It could also predict the number of cycles required for cone crack initiation when applied load and stress are lower than the critical load and stress for initiating cone crack. Quasi-plastic mode was driven by shear stress to cause micro-damage. This mode was a mechanical process and was claimed to occur in the subsurface region. Radial cracks and secondary cone cracks were also generated in this mode. Microstructure plays an important role in the damage behaviours. Increase heterogeneities increases brittle-plastics transition.

Huq and Celis (2002) have investigated static fatigue of an alumina ball on flat WC-Co. Two forms of damage, wear and fretting fatigue, appeared in this couple of materials. Wear and cracking were caused by alternating shear traction in the slip region. Wear took place in the slip region on alumina balls and on WC-Co flats. Fatigue cracks along grain boundary did occur only on the alumina ball. Crack formed was not a cone crack. No crack formation was observed on the WC-Co flats surface.

Elements transfer between contacting surfaces was not observed in the stick region. However, materials exchange in the slip region was observed. EDX results showed transferring of WC-Co onto the alumina surface.

Fine debris present in the slip region indicates the action of a frictional degradation mechanism. Contact area increased with prolonging test cycles. The authors argued that it was resulted from the accumulation and extrusion of debris. Static load tested at the same contact time as the cyclic load cycles did not cause cracking of the materials.

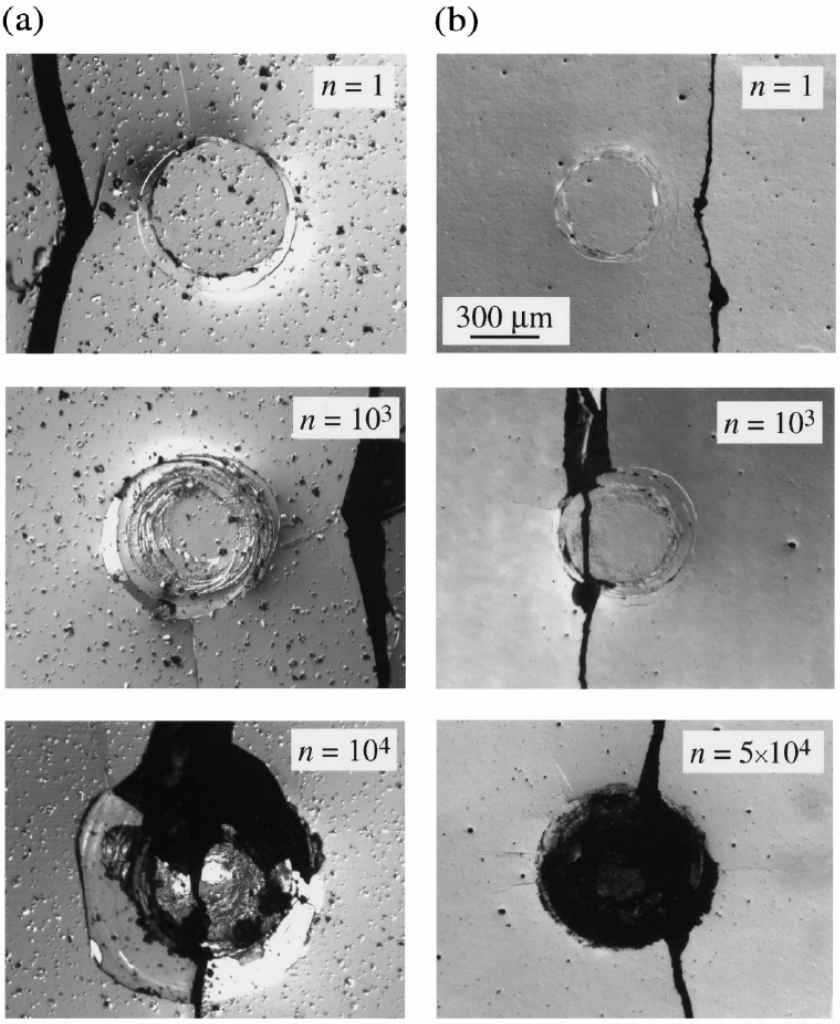


Fig. 6. Optical micrographs of Hertzian indentation failure sites in broken inert strength specimens, after indentation at $P = 500$ N, $r = 3.18$ mm, for $n$ values indicated: (a) soda-lime glass/water; (b) porcelain/water. Flexural tension axis horizontal. Surface views, reflected light (Nomarski contrast, after gold coating). Note how fracture origins begin outside the contact circle at low $n$, and move inside as damage intensifies at large $n$.

Figure 1.2 Damage modes of brittle ceramics by static contact fatigue (Kim *et al.*, 1999).

Zhu *et al.* (2005) have conducted static contact fatigue of the dental feldspathic ceramics flats against two types of ball specimens (52100 steel and $Si_3N_4$ ceramics). The results showed that the damage mechanisms were the combination of adhesion and delamination for normal load below the critical value. No macro-crack formation was detected. When

normal load was above the critical level, four damage zones from the centre of contact to the edge of contact, i.e. contact centre, slight wear zone, severe wear zone and cracking zone, were identified. Schematic diagram of the failure zones is shown in Figure 1.3. The main damage modes were the delamination in the wear zone and combination of cracking and delamination in the cracking zone. The damages significantly decreased in oil lubricated conditions. This result was attributed to the reduction of friction at the interface.

A subsequent investigation by Zhu et al. (2006) was on a static contact fatigue of two dental ceramics flats against $Si_3N_4$ ceramics ball in air. They identified damage modes of dental ceramics in static contact fatigue as delamination under low normal load and the combination of cracking and delamination under high normal load the same as previously reported (Zhu et al., 2005).

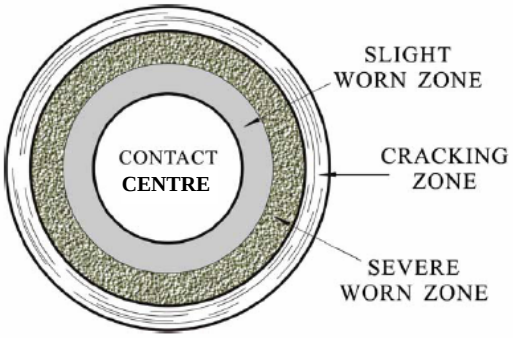


Figure 1.3 Schematic diagram of damage zones of ceramics under static contact fatigue load (Zhu et al., 2005).

The four damage zones, similar to those previously reported, in the contact area were explained. The centre zone was undamaged because the surfaces of both bodies were in contact continuously. The slight wear zone and the severe wear zone were attributed to the micro-slip, which was more pronounced at a far distance from the centre of contact. In the cracking zone, the density of cracks decreased from the boundary to the centre conversely to the increasing of the interspaces of cracks. The authors proposed that cracking and wear behaviours may be influenced by a combination of cyclic strain–stress and relative micro-slip at the interface. The key materials parameters for crack initiation and propagation were the plasticity and toughness. They argued that the wear was possibly a consequence of the

formation of the cracks, and the detachment of particles was accelerated by the cracks. The mechanism for wear was the octahedral shear stress.

*1.5.1.3 Coatings*

Zhu *et al*. (2001[b]) have conducted static fatigue tests using 52100 steel ball on TiN, $MoS_2$ and TiN+$MoS_2$ coatings created on a 1045 steel flat under different normal loads in dry conditions. They found that by increasing the number of cycles, superposition the loading and unloading curves tended to take place and the dissipated energy reached zero. This occurrence was due to increasing of contact stiffness that was induced by strain-hardening process of the materials under cyclic load. The depth of indentation and the shakedown limit increased with increase of the normal load. TiN coating had the best loading capacity among three studied materials. The indentation depth of TiN/$MoS_2$ was in the middle of the three coatings. The indentation depth of all materials increased with decreasing in loading frequency.

The detachment of particles in case of TiN coating seemed to be caused by the delamination mechanism. $MoS_2$ coating and TiN + $MoS_2$ coating showed the same characteristic and have little damage. $MoS_2$ coating had the best fatigue resistance. TiN + $MoS_2$ coating occurred micro-cracks formed by fatigue failure of the adhesive without propagation of cracks.

Additionally, varieties of investigations have been conducted on the static contact fatigue in various materials, materials combinations, and contact conditions. The following is summary of previous investigations.

For steel: Some sliding between surfaces at the asperities contact occurred in ball on flat test configuration under static contact fatigue load as reported by Burton and Ku (1963) and quoted in Waterhouse (1972). However, Zhu and Zhou (2001[a]) claimed that fretting was not expected at the interface between the same metal. They pointed out that contact with different materials promoted micro-slip in the radial direction.

Degradation mechanism of static contact fatigue between steel balls on flat steels was deformation according to Zhu and Zhou (2001[a]). However, various kinds of cracks were observed by Alfredsson and Olsson (2000).

The indentation depth was highly changed at the first cycle and gradually decreased reaching steady state because of strain hardening of the materials (Zhu and Zhou, 2001[a]). The level of load and test speed affected the indentation depth.

Four types of cracks were observed including two surface cracks, i.e. ring/cone, radial cracks, and subsurface cracks, i.e. lateral and median cracks in case hardening steel (Alfredsson and Olsson, 2000). By numerical simulation, all cracks were opened by tensile stress during alternating load. A single multi-axial criterion was not enough to describe all aspect of the experimental results (Alfredsson and Olsson, 2001). The endurance limit of the material was decreased by superposing a static tangential load on a normal static fatigue load (Alfredsson and Olsson, 2003).

Steel was worn out by polymers during static contact fatigue in different severity in laboratory air (Higham *et al.*, 1978). Wear of metal was attributed to the adhesive properties. The material was loosed from metal surface by adhesive transfer of $\alpha$-$Fe_2O_3$ particles to the polymer surface.

For ceramics: Coarse alumina was damaged by deformation-induced inter-granular microfracture (Guiberteau *et al.,* 1993). The damage developed beneath the contact circle in a zone of high shear stress and hydrostatic compression. The damage process was a mechanical and enhanced by a moist environment. Another study on static fatigue test of alumina ball on flat WC-Co was reported by Huq and Celis (2002). Two forms of damage, wear and fretting fatigue, caused by alternating shear traction in the slip region were observed. Element transfer in the slip region from WC-Co onto the alumina surface was observed.

Wear process composed of three stages in static contact fatigue of $Si_3N_4$ material against WC ball was reported by Chen *et al.* (1996). These stage included: stage I - roughening of the contact surface, stage II - cone crack initiation and propagation and stage III - large

volume material removal from outside the contact area. Static contact fatigue of silicon nitride materials in air, water and ethylene glycol was studied by Ezop and Karlsson (1999, 2001) who found that environments and microstructure of silicon nitride have the effect on fatigue performance and characteristics. At high contact pressure intergranular cracks occurred with grains pulled out.

The test of relative brittle ceramics in moist environments showed two damage modes i.e. macro cone fracture, and radial and secondary cone crack (Kim *et al.*, 1999). Macro cone fracture was of brittle nature, driven by tensile stress and was fast process involving chemical process. Radial and secondary cone cracks were of quasi-plastic nature, driven by shear stress. It was purely mechanically process occurring at subsurface. Brittle-plastics transition was increased by increasing heterogeneities microstructure.

The level of normal load affected damage mechanisms of the dental feldspathic ceramics flats against balls (Zhu *et al.*, 2005). The combination of adhesion and delamination exhibited for normal load below the critical value. Above the critical level, four damage zones i.e. contact centre, slight wear zone, severe wear zone and cracking zone were identified (Zhu *et al.*, 2005, 2006). The main damage modes were the delamination in the wear zone and combination of cracking and delamination in the cracking zone.

The static contact fatigue was rarely conducted for coatings. Investigations were carried out for TiN, $MoS_2$ and TiN+$MoS_2$ coatings on steel in dry conditions (Zhu *et al.*, 2001[b]). Increasing of number of cycles induced increase in contact stiffness due to strain-hardening process. The increasing of indentation depth is proportional to normal load but inversely proportional to the loading speed. The fatigue resistance ranking from the best to the worst was: $MoS_2$, TiN + $MoS_2$, TiN. The delamination of TiN coating generated the detachment of particles (Zhu *et al.*, 2001[a, b]).

However, there are no reports explaining this kind of damage for polymeric materials. Therefore, in the research reported here experiments will be conducted on static contact fatigue of PMMA.

### *1.5.2 Rolling contact fatigue of thermal sprayed coatings*

Thermal sprayed coatings have been developed many years ago to serve the engineering needs. Spray materials could be ceramics, metals, cermets, or plastics whichever suits the application. Thermal sprayed coatings have been applied in many fields such as corrosion control, thermal barrier, and wear resistance etc. For the wear resistance purpose, the coating has to improve the base materials properties such as lower the coefficient of friction or secure high sliding wear resistance or RCF. Many efforts have been made, both theoretical and experimental, in order to understand the damage modes and mechanisms of thermal sprayed coatings operating under sliding and/or rolling contact conditions. The pioneer works reported parameters influencing the performance of coatings in RCF, which include surface finish, coating thickness, residual stress, lubrication, interfacial bonding.

The following presents previous research on rolling contact fatigue of various thermal spray coatings.

Tobe *et al.* (1988) have firstly studied plasma sprayed ceramic and metallic coatings on steel substrate using twin disc test configuration. It was found that surface roughness of the roller was importance for fatigue performance. They argued that cracks initiation was in mode I as a result of tensile stresses at the edge of contact area. Delamination was found as a main failure mode. Failure depth was not corresponding to the depth of maximum shear stress, therefore it might be attributed to maximum compressive Hertz stress. Weak adhesive strength was supported by the occurrence of delamination between the coating/substrate interfaces. Ceramic coatings may have mismatch properties between coating/substrate leading to a low adhesion. Poor adhesion between coating/substrate of the alumina coating may be caused by unmelted particles.

A subsequent study by Tobe et al. (1990), in which the same type of fatigue test apparatus was used to test an aluminium alloy substrate, showed that RCF performance of coatings depended on compressive strength of coatings and shear stress between the coating/substrate. The RCF life of coatings was superior to substrate materials. Failure mode was also delamination due to blisters generation at the interface in case of metallic coatings and at the interface between the bond coat and substrate in case of ceramic

coatings. These results revealed that altering tribological conditions changes the failure mechanisms of thermal sprayed coatings. The authors pointed out that residual stress could be created within the coatings during the rolling contact fatigue tests, so it implied plastics deformation of the coatings. They have also reported the rolling contact fatigue behaviour of plasma sprayed coating using two-roller fatigue test machine (Tobe *et al.*, 1991). The three coatings, $Al_2O_3$-$TiO_2$, $Cr_2O_3$-$SiO_2$-$TiO_2$ and Mo, were coated onto high strength aluminium alloy substrates. The results showed that the highest rolling fatigue strength was for the Mo coating while the rolling fatigue strength of two ceramics coatings was at the similar level. They argued that the most important factors for the rolling fatigue behaviour were the compressive strength of the coatings and the shear strength between the coated layer and the substrate.

Sahoo (1993) investigated rolling contact fatigue resistance of WC-Co coatings under high load. The author observed crack initiation from the surface and its propagation through the coating thickness. It was found that coating delaminated just above the coating/substrate interface. The author argued that initiation of surface crack might have resulted from the tribological conditions at the contact such as high friction and sliding action leading to crack initiation in shear mode (mode II). The delamination behaviour change might relate to a strong mechanical interlock and advance nature of residual stress at coating/substrate interface.

Makela *et al.* (1994) studied rolling contact fatigue of thermally sprayed WC-12%Co coating on steel rollers using HVOF and D-Gun process using three roller type RCF test machine in unlubricated conditions. It was concluded that the rolling contact behaviours of coatings depended on Hertz contact stress, tribological conditions, and vibration during the test. The coating was damaged at the coating/substrate interface the as same location as reported by *Tobe et al.* (1988, 1990 and 1991). The authors argued that plastics deformation at cracks and micropits contributed to the performance of cermet coatings, such as WC-12%Co coating, and led to a high stress concentration. For this reason, crack propagation and ultimate delamination took place.

Yoshida *et al.* (1995) has conducted rolling contact fatigue performance of WC-Cr-Ni coatings under pure rolling and rolling/sliding conditions. It was reported that the coating failure at the initial stage of the test at the coating/substrate interface in case the substrate

was not blasted before coating. By contrast, the coating fatigue performance increased and the failure occurred within the coatings when the substrate was blasted before coating. The authors reported that the thick coating resisted fatigue better than thin coating under the test conditions, however, the results have high scatter possibly due to complex microstructure of thermal sprayed coating resulting in poor reproducibility. The authors reported that the coatings performance in rolling/sliding condition were not only dependence on the magnitude of tangential force or another words slip ratio but also the sliding direction. It was observed that the friction value in the initial stage was high and gradually decreased to steady level. Furthermore, flaking occurred at the early stage of the test when subsurface hardness was low indicating plastics deformation of the substrate. Therefore, hardness of the substrate should be sufficient to support the coatings.

Nieminen *et al.* (1995) have conducted RCF tests on WC-12% Co coatings produced by APS and HVOF using a roller type test rig under dry and non-sliding conditions. It was observed that the APS coating RCF performance was lower than that of HVOF coating due to its high porosity and subsurface cracks initiation at the depth of maximum shear stress. This was, nevertheless, a non-consistent tendency. The depth of crack was much shallower in HVOF coating.

Hadfield *et al.* (1995) have presented delamination failure mode in some thermal sprayed coatings in rolling contact loading. By observation, dalamination of WC-Co occurred in the coating layer while for alumina it took place at the coating/substrate interface.

Ahmed and Hadfield (1996) have studied RCF of WC-15%Co coated produced by a superdetonation gun using modified four balls machine in oil lubricated conditions. The results showed that the coating was failing within itself and in a shear plain at the edge of the contact area. The edge cracks starting from the surface implied the relationships with the tensile stress induced fracture. The mode of failure was delamination.

Rolling contact fatigue of tungsten carbide (WC-5%Co) and aluminium oxide ($Al_2O_3$), thermally sprayed with D-Gun, has been investigated using a modified four balls testing machine (Ahmed and Hadfield, 1997). The test was performed with conventional steel bearing balls and hybrid ceramic bearing balls configuration in lubricated conditions. The results showed that WC-5%Co fatigue performance was superior to that of $Al_2O_3$. Both

coatings when in contact with steel balls generally showed a better performance than when in contact with ceramic balls. The suggested reason for that was the higher elastic modulus of ceramic material.

Failure mode of a tungsten carbide coating was delamination without a significant wear track i.e. specimen failed prior to the wear track creation. This indicates that the failure of the coating was more dependent on subsurface effects rather than on surface effects. Edge crack was produced on the edge of the wear track, which was subjected to higher contact stress. This type of crack might be an initiation of a fatigue failure. Edge depth of the delamination cliff less than the coating thickness implied that the failure was not due to de-bonding from substrate. The delamination was proposed to result from the porosities/microcracks occurring during coating and secondary phases i.e. voids due to plastic flow of matrix around hard particles while subjected to contact fatigue load.
Failure mode of $Al_2O_3$ coating was also delamination occurring at the coating/substrate interface. The authors proposed that it was due to a poor adhesive strength of the coating resulting from thermal and mechanical mismatch between coating and substrate.

Ahmed and Hadfield (1998) have studied RCF failure mechanisms of plasma sprayed tungsten carbide cobalt (WC-15%Co) coatings using modified four ball machine at different tribological conditions, i.e. contact stress and balls' materials, in lubricated conditions. The balls were made of bearing steel and ceramic. The results showed that RCF performance of thick coating was superior to that of thin coating. Damage occurred within the coating for thick coating and at the coating/substrate interface for thin coating. The authors pointed out that the bond strength of the coating itself and between coating/substrate were the key of fatigue performance. Two types of damage were observed, i.e. delamination and coating wear. The authors argued that the type of damage and tribological test conditions have no relationships. In general, better RCF performance was obtained when the test was performed in the presence of high viscosity lubricant (higher value of $\lambda$). Test against steel balls produced higher load cycle duration than the test against ceramic balls. They claimed that at similar contact load, the coating in contact with ceramic balls was subjected to more severe tribological conditions i.e. contact stress and abrasion higher than that for steel balls.

Ahmed and Hadfield (1999) have investigated failure modes of WC-15%Co plasma sprayed coating in rolling contact fatigue. The coating was done on a surface of bearing steel (440-C). The coating thickness was varied and was categorized into thick and thin coating. The thick coating was defined by the position of maximum shear stress, calculated by Hertz's formula, within the coating. This stress was located at or close to the coating/substrate boundary for the thin coating. The tests were conducted using modified four ball test machine in two different viscosity oils. An elastohydrodynamic lubrication and mixed regime lubrication were selected. Two modes of failure were observed i.e. surface wear and coating delamination. Figure 1.4 shows failure features of these coatings. The coatings failed in either individual or mixed mode. Wear occurred in the form of micropitting due to microslip/sliding of asperities contact in the contact region. The later stage wear was accelerated by debris or third body abrasion. The occurrence of delamination was found at the early stage of the test. Resistance to delamination of the thin coating was lower than that of the thick coating. The authors argued that it was due to the mismatched properties of coating and substrate. The results indicate that the delamination of coating is rarely related to the entrapment of lubricant.

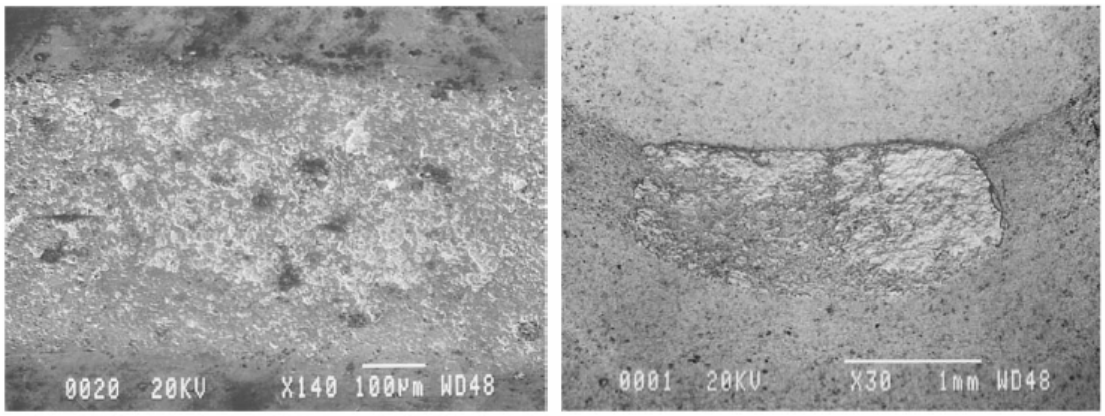


(a) (b)

Figure 1.4 Damage modes of WC-15%Co plasma sprayed coating under rolling contact fatigue (a) wear (b) delamination (Ahmed and Hadfield, 1999).

Nakajima *et al.* (2000) have studied the effects of coating thickness and slip ratio on the rolling/sliding contact fatigue life of HVOF sprayed WC-Cr-Ni cermet coating in oil lubricated conditions. The life of the coating was defined as life-to-flaking. The coating was deposited on two types of substrates that is the induction hardened steel substrate (harder) and the thermally refined steel substrate (softer). The results showed that fatigue

life of the coating tended to increase with increasing of coating thickness. The flaking characteristics depended on substrate type. The induction hardened steel substrate showed flaking in the coating whereas the thermally refined steel substrate failed at the coating/substrate. The authors claimed that the position and nature of failure on the thermally refined steel substrate is attributed to different residual stress near the coating layer as confirmed by analytical results.

Sarma and Mayuram (2000) have conducted rolling contact fatigue (RCF) of nickel base alloy (Ni-B-Si-Cr-Fe-C) thermal sprayed coating against bearing steel using twin disk test configuration. The experiment program was varied in contact stress, coating thickness, and lubrication conditions. Two analytical methods, i.e. Lundberg-Palmgren and Tallian life prediction models, were used to predict spalling life of coatings. The first method used shear stress criterion for prediction of life. The results showed that the nickel base coating performance was satisfied under moderate stress levels (500-700 MPa). The spalling life of the coatings, based on the octahedral shear stress, lied between the Lundberg-Palmgren and Tallian life prediction models. They argued that the calculation criteria of these models were safe for prediction RCF life of thermal sprayed coating. Failure of coating was delamination in ductile mode in most case.

Ahmed (2002[a]) has investigated the effects of coating thickness and contact stress on the performance and failure modes of WC–12%Co HVOF coating under rolling contact fatigue load. The test was conducted using a modified four ball machine. Three failure modes were identified under tested conditions including wear, delamination and spalling. It was found that resistance to delamination of HVOF coating was superior to that of air plasma sprayed coating (APS) as previous reported by Ahmed and Hadfield (1999). Spalling happened to HVOF coating because the coating was highly dense and homogeneous; almost comparable to that of steel.

The investigation results demonstrated that a non-dimension coating thickness parameter ($\Delta$), which is the ratio between coating thickness and the depth of maximum shear stress, was useful for optimizing resistance of the coating to delamination. The optimized value of this parameter should be $\Delta \geq 1.5$. The coating could withstand more than $70 \times 10^6$ load cycles for WC–12%Co HVOF coating when the following was met: $\Delta \geq 1.5$, contact stress ($P_o < 2.7$GPa) and lubrication regime ($\lambda > 3$).

Stewart and Ahmed (2002) have reviewed rolling contact fatigue (RCF) performance of coatings for different design parameters including type of deposition process, coating materials, thickness, hardness, tribological test condition and configuration, contact stress, and lubrication.

Thermal sprayed deposition process affected discontinuities such as pores, thermal stress induced cracks, oxide lamellas or incompletely molten particles. Coating thickness was responsible for surface stress distribution and caused the change of delamination behaviour from interfacial (adhesive) delamination to cohesive delamination within coating.

Rolling fatigue strength of metal coating was better than ceramics coating. It resulted from the coating microstructure and quenching, and micro-stress and macro-stress induced by differences in thermal expansion coefficients between the substrate and the coating. The anisotropy of thermally spray coating has affected the magnitude and orientation of residual stresses within the coating. The residual stress magnitude depended on the measurement direction, type of coating process, coating thickness and deformation, and micro-crack formation in the coating.

Residual stress level also influences the RCF performance. Residual stress in the coating of metallic and ceramic plasma sprayed on aluminium substrate was measured before and after the RCF test. Residual stresses of both coatings before the test was low. It was due to micro cracking relieving the stress during cooling. The residual stress of both metal and ceramic coatings increased after RCF test. However, the increase of compressive residual stress in metal coating was higher than that in ceramic coating. For metal coating, the higher compressive residual stress after the RCF test led to higher RCF resistance. Higher residual stress after RCF test implied plastic deformation under Hertzian loading and can be superimposed by shakedown effect. Comparing with brittle material coating, the rising of compressive stress level was attributed to micro cracking in the coating layer. Lubricant is an important parameter because it helps to share the asperity load.

Ahmed (2002[b]) has summarized RCF performance and failure modes of thermal sprayed coatings, especially WC-Co and $Al_2O_3$ under rolling contact load. Failure modes of thermal sprayed WC-Co and $Al_2O_3$ coatings were categorized into four modes as follows.

(I) Abrasive Failure:

This failure type is affected by a combination of micropitting and surface wear occurring on the wear track. The failure mechanism attributes to asperities contact in the presence of microslip and sliding within the contact region. It occurs when partial elastohydrodynamic lubrication (EHL) is in the mixed regime. Asperity contacts produce high stresses very close to surface but unchange the Hertzian stress pattern. Hard coating reduces high shear stress in the presence of microslip by microcracking and eventual micropitting.

Another mechanism is linked to maximum tensile stress at the edge of contact area induced by Hertzian stress and equal to fracture stress of coating for brittle materials.

(II) Delamination Failure:

Delamination mechanism in RCF is similar to that of sliding contact fatigue. Crack propagates parallel to the surface at a depth governed by material properties and friction coefficient. Cracks grow from defects in coating such as microvoids, microcracks or secondary phases during cyclic loading. A crack extends at the maximum shear stress or orthogonal shear stress region. For thermal sprayed coating, delamination is classified into two types i.e. cohesive and adhesive delamination. The first type failure occurs within the coating and normally takes place in thick coating. The second type failure occurs at coating/substrate interface and normally takes place for thin coating.

The delamination processes are as follows:

- Crack initiation: Cracks starts at different depths under contact region. However, they propagate at the depths of maximum shear stress and orthogonal shear stress. Position of delamination in WC-Co depends on thickness of coating. Cracks initiate in the coating when the depth of maximum shear stress is less than coating thickness and at coating/substrate when the depth is greater than coating thickness. For $Al_2O_3$ coatings, cracks are usually initiated at the coating/substrate interface.

- Crack propagation: If the thickness of WC-Co coating is greater than the depth at which the maximum shear stress is located, cracks propagates slowly in the coatings. For the WC-Co and $Al_2O_3$ coatings thinner than the depth of maximum shear stress, cracks at the coating/substrate interface propagate quicker than cracks at the depths of orthogonal shear stress. This thin coating results in a poor RCF resistance.

- Crack extension: For WC-Co coatings thicker than the depth of maximum shear stress, the crack at the maximum shear stress extends and joins the cracks at the depth of orthogonal shear stress. For the coatings thinner than the depth of maximum shear stress or for $Al_2O_3$ coatings, the cracks at the interface have the tendency, in some cases, to combine with the cracks at the depth of orthogonal shear stress and eventually reach the surface.

- Delamination: For WC-Co coatings thicker than the depth of maximum shear stress, delamination, resulting from the cracks at the depth of orthogonal shear stress, occurs faster than from other cracks. Thin WC-Co coating and $Al_2O_3$ are delaminated at the coating/substrate interface.

(III) Coating failure due to bulk deformation:

Bulk deformation could happen when the substrate experiences plastic flow and results in contact region conformity and a hump at the edge of the track. This situation leads to bending or cracking at the middle of the track because substrate is unable to support the load on the coatings. On further cyclic loading, the substrate will deform continuously and extrude to the edge of the contact leading to more conformity of contact. Consequently, edge cracks within the wear track result. The cracks propagate by tensile stress as the cyclic load is applied. The contact deformation proceeds until contact stress no longer exceeds the flow stress of the substrate material; the substrate migration terminates and a steady state is obtained. The features of surface failure in this mode are shown in Figure 1.5.

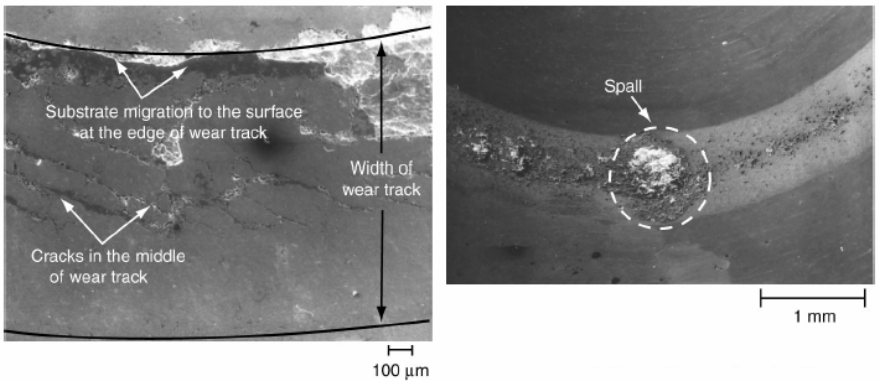


(a) (b)

Figure 1.5 Damage modes of WC-Co thermal spray coating (a) Coating failure due to bulk deformation (b) spalling (Ahmed, 2002[b])

(IV) Spalling:

This mode of failure is rarely seen in thermal sprayed coatings subjected to RCF (see Figure 1.5b). Unlike delamination, spalling has smaller surface area (width-to-depth ratio). The damage occurs within the wear track initiated, probably, from micropits, furrows, grinding marks or dents on the surface with the wear track, subsurface inclusions and defects. The occurrence of micropits before spalling indicates that spalling originates from micropits and propagates under cyclic loading. Once the spalling initiation occurs, hydrostatic pressure may assist cracks propagation. However, the exact mechanism of spalling in RCF is not completely understood especially if its initiation and propagation is surface or subsurface process.

Akdogan *et al.* (2002) have investigated surface fatigue of Mo and Al-coating on steel disc substrates. The test was conducted in rolling line contact type (two discs configuration) under pure rolling and rolling/sliding (5%) contact. The load applied was below the yielding stress.

Under the test conditions, the performance of Al-bronze coating was poorer than that of the Mo coating. The life to flaking of Al-bronze was decreased with an increase of applied load and slip ratio. However, Mo coating demonstrated non-significant life dependency on load and had high performance in both pure rolling and rolling/sliding contacts.

For pure rolling, the formation of edge cracks at the contact edge occurred first in both case. For molybdenum coating, surface suffered in consequence of grain detachment, micro-spall craters formation, and micro-crack and spalling fatigue. For Al-bronze the damage took the form of asperities smoothening, high rate of weight loss, detachment and debris entrapment promoting abrasive wear and flaking. The rolling/sliding condition reduced wear rate for Mo coating, but resulted reversely in Al-bronze coating.

Stewart and Ahmed (2003) have studied failure modes of thermal sprayed WC-12%Co coatings under rolling contact fatigue load in oil lubricated conditions. The effects of the hot isostatic pressing (HIP) on fatigue performance, using two different HIP temperatures (850 ºC and 1200 ºC) and "as sprayed condition" were investigated. It was found that the HIP coating created at 1200 ºC performed much better in terms of damage resistance than the coating produced under "as sprayed condition". The HIP process altered microstructure of the coated layer. At high HIP temperature recrystalization associated with diffusion occurred. The bonding between coating/substrate interfaces was improved. The delamination caused by shear stress at the coating/substrate interfaces in the thin coating was diminished. The failure for both "as sprayed" coating and 850 ºC HIP coating was delamination. For 1200 ºC HIP coating, surface distress and denting were observed.

The previous research on the RCF of thermal sprayed coatings has identified factors affecting their performance, fatigue strength and behaviour. Also, failure modes and mechanisms have been elaborated.

Various factors affect to the performance of thermal spray coatings in RCF test. They included type of coating materials (Akdogan *et al.*, 2002), surface roughness of the roller (Tobe *et al.*, 1988), compressive strength of coatings, and shear stress between the coating/substrate (Tobe *et al.,* 1990, 1991). The coatings performance in rolling/sliding condition was not only depending on the magnitude of tangential force or the slip/roll ratio but also on the direction of the sliding and coating materials (Yoshida *et al.,* 1995; Akdogan *et al.*, 2002). Deposition process controlled discontinuities such as pores, thermal stress induced cracks, oxide lamellas or incompletely molten particles (Stewart and Ahmed, 2002). Performance in terms of RCF of APS coating is lower than that of HVOF coating due to a high porosity in the coating (Nieminen *et al.*, 1995; Ahmed and Hadfield, 1999 and Ahmed, 2002[a]). Type of counterface material was another important factor for

RCF performance (Ahmed and Hadfield, 1997, 1998). Residual stress was also found to affect the fatigue performance of coatings. The magnitude of residual stress depended on the measurement direction, type of coating process, coating thickness, and deformation and microcrack formation in the coating during deposition or RCF test (Tobe *et al.*, 1990; Stewart and Ahmed, 2002). Lubricant was another important parameter because it shared some of the asperity load (Stewart and Ahmed, 2002). Better RCF performance was obtained when test was conducted in the presence of high viscosity lubricant (Ahmed and Hadfield, 1998). Post heat treatment such as hot isostatic pressing (HIP) may improve performance of the coating (Stewart and Ahmed, 2003).

Rolling fatigue strength depended on type of coating materials e.g. the Mo coating higher than ceramics coatings (Tobe *et al.*, 1991; Akdogan *et al.*, 2002; Stewart and Ahmed, 2002). Plastics deformation at cracks and micropits did not occur in cermet coatings led to high stress concentration (Mekela *et al.,* 1994).

Rolling contact behaviour of coatings was affected by Hertz's contact stress, tribological conditions (friction and sliding), and vibration during the test (Mekela *et al.*, 1994). Crack could initiate from surface and propagate through the coating thickness (Sahoo, 1993). Surface treatment before coating application was another factor influencing the RCF behaviour of thermal sprayed coatings. Failure occurred at the coating/substrate interface in the case when substrate was not blasted before coating application but it occurred within the coating when the substrate was blasted before coating (Yoshida *et al.*, 1995). Coating thickness was responsible for surface stress distribution and caused the change of delamination behaviour between adhesive delamination and cohesive delamination (Stewart and Ahmed, 2002). Thick coatings performed better in RCF than thin coatings. Damage occurred within the coating for thick coatings and at the coating/substrate interface for thin coating (Ahmed and Hadfield, 1998). Resistance to delamination of thin coatings was worse than that of thick coating due to properties mismatch of coating and substrate (Ahmed and Hadfield, 1999). Fatigue life of the coating tended to increase with the increase of coating thickness (Nakajima *et al.*, 2000). Non-dimension coating thickness parameter ($\Delta$), the ratio between coating thickness and the depth of maximum shear stress, were used for optimizing delamination resistance of the coating (Ahmed, 2002[a]). The optimized value of this parameter should be greater than 1.5. The damage behaviour of the coatings could be changed by post heat treatment process (Stewart and Ahmed, 2003).

Failure modes of thermal sprayed coating under rolling contact fatigue can be categorized as abrasive wear, delamination, bulk deformation, and spalling. The mechanisms of each mode can be summarised as follows.

Abrasive wear is affected by a combination of micropitting and surface wear (Ahmed, 2002[a]) occurring within the wear track. The failure mechanism was attributed to asperity contact in the presence of microslip and sliding within the contact region when elastodynamic lubrication (EHL) was in a mixed regime during the first stage (Ahmed and Hadfield, 1998). The latter stage wear was accelerated by debris or third body abrasion. Another contributory factor was a maximum tensile stress at the edge of contact area induced by Hertzian stress and equal to fracture stress of coating for brittle materials.

Delamination mechanism started with the initiation of cracks by mode I as a result of tensile stresses at the edge of contact area (Tobe *et al.*, 1988). These cracks extended from defects in the coating such as microvoids, microcracks or secondary phases during cyclic loading. The crack propagated in the maximum shear stress or orthogonal shear stress region. For thermal sprayed coating delamination was classified into two types i.e. cohesive and adhesive delamination (Tobe *et al.*, 1988, 1990; Saho, 1993; Keshavan *et al.*, 1993; Mekela *et al.*, 1994; Ahmed and Hadfield, 1999 and Ahmed, 2002[a]). The first type takes place in thick coating while the second type failure occurs at coating/substrate interface of thin coating.

The cohesive delamination originated from the porosities/microcracks and secondary phases created during coating. Failure started from the edge cracks originating at the surface with relationships to tensile stress fracture. Adhesive delamination occurred at the coating/substrate interface because of poor adhesive strength of the coating, such as $Al_2O_3$, due to thermal and mechanical mismatch between coating and substrate (Ahmed and Hadfield, 1996, 1997).

Delamination behaviour change might be related to mechanical interlock and the nature of residual stress at coating/substrate (Sahoo, 1993). The position of delamination depends on type of coatings; for example in the case of WC-Co it occurs in the coatings layer while in the case of alumina it takes place at the coating/substrate interface (Hadfield *et al.*, 1995).

The coating/substrate failure position is attributed to the difference in residual stress near the coating layer (Nakajima *et al.,* 2000). Delamination, in some case such as tungsten carbide, much depends on subsurface effects rather than surface effects (Ahmed and Hadfield, 1997). The flaking characteristics were affected by substrate type. Hardness of the substrate should be high enough to support the load on a coating in order to increase the time to flaking (Yoshida *et al.*, 1995). The life of the coatings located between the octahedral shear stress follows the Lundberg-Palmgren and Tallian life prediction models (Sarma and Mayuram, 2000). Delamination of coating was rarely related to entrapment of lubrication (Ahmed and Hadfield, 1998). The failure can be brittle or ductile; ductile mode was found for nickel alloys' coating and brittle mode for alumna coating (Sarma and Mayuram, 2000 and Tobe *et al.*,1988).

Bulk deformation could happen when the substrate was experiencing plastic deformation leding to bending or cracking of coating at the middle of the contact track. The substrate deforms continuously and extrudes to the edge of contact for a number of cyclic loading. This can result in edge crack formation which are propagated by tensile stress as the cyclic load is applied (Ahmed, 2002[b]).

Spalling occurs within the wear track and is initiated, probably, from micropits, furrows, grinding marks and dents on the surface of the wear track, and subsurface inclusions and defects (Ahmed, 2002[a,b]).

**Referrences:**

Ahmed, R. and Hadfield, M. (1996) "Rolling contact fatigue behaviour of thermally sprayed rolling elements" *Surface and Coatings Technology*, vol. 82, pp. 176-186.

Ahmed, R. and Hadfield, M. (1997) "Rolling contact fatigue performance of detonation gun coated elements" *Tribology International*, vol. 30, no. 2, pp. 129-137.

Ahmed, R. and Hadfield, M. (1998) "Rolling contact fatigue performance of plasma sprayed coatings" *Wear*, vol. 220, pp. 80-91.

Ahmed, R. and Hadfield, M. (1999) "Failure modes of plasma sprayed WC–15%Co coated rolling elements" *Wear*, vol. 230, pp. 39–55.

Ahmed, R. (2002[a]) "Contact fatigue failure modes of HVOF coatings" *Wear,* vol. 253, pp. 473–487.

Ahmed, R. (2002[b]) "Rolling contact fatigue" in *ASM Handbook vol. 11: Failure analysis and prevention*, OHIO: ASM International. pp. 941-956.

Akdogan, G., Stolarski, T. A. and Tobe, S. (2002) "Surface fatigue of molybdenum and Al-bronze Coatings in unlubricated rolling/sliding contact" *Wear*, vol. 253, pp. 319-330.

Alfredsson, B., and Olsson, M. (2000) "Standing contact fatigue testing of a ductile material: surface and subsurface cracks" *Fatigue Frac Engng Mater Struct*, vol. 23, pp. 229-240.

Alfredsson, B., and Olsson, M. (2001) "Applying multiaxial fatigue criteria to standing contact fatigue" *International Journal of Fatigue*, vol. 23, pp. 533–548.

Alfredsson, B., and Olsson, M. (2003) "Incline standing contact fatigue" *Fatigue Frac Engng Mater Struct*, vol. 23, pp. 229-240.

Al-Sabti, S. L. (2000) "Thesis failure modes of polymethymethacrylate resulting from rolling line contact" *Brunel University*, London.

Chen, Z., Cuneo, J. C., Mecholsky, J. J. Jr., and Hub, S. (1996) "Damage processes in $Si_3N_4$ bearing material under contact loading" *Wear*, vol. 198, pp. 197-207.

Eyzop, B.L. and Karlsson, S. (1999) "Cyclic contact fatigue of silicon nitride" *Wear*, vol. 225-229, pp. 1303-1308.

Eyzop, B.L. and Karlsson, S. (2001) "Contact fatigue of silicon nitride" *Wear*, vol. 249, pp. 208-213.

Guiberteau, F., Padture, N. P., Cai, H., and Lawn, B. R. (1993) "Indentation fatigue: a simple cyclic Hertzian test for measuring damage accumulation in polycrystalline ceramics" *Philosophical Magazine A (USA).*, vol. 68, pp. 1003-1016.

Hadfield, M., Ahmed, R. and Tobe, S. (1995) "Rolling contact fatigue of thermally spray coated cones" *Proc. Int. Thermal Spray Conf., Kobe, May 1995*, High Temperature Society of Japan, Kobe, pp. 1097-1102.

Higham, P. A., Stott, F. H., and Bethune, B. (1978) "The influence of polymer composition on the wear of metal surface during fretting of steel on polymer" *wear*, vol. 47, pp. 71-80.

Huq, Z. M. and Celis, J-P. (2002) "Fretting Fatigue in Alumina Tested under Oscillating Normal Load" *J. Am. Ceram. Soc.*, vol. 85, pp. 986–88.

Kim, D. K., Jung, Y.-G., Peterson, I. M. and Lawn, B. R. (1999) "Cyclic fatigue of intrinsically brittle ceramics in contact with spheres" *Acta mater.,* vol. 47, pp. 4711-4725.

Makela, A., Vuoristo, P., Lahdensuo, M., Niemi, K. and Mantyla, T. (1994) "Rolling contact fatigue testing of thermal sprayed coatings" *Conference proceedings, Thremal spray industrial applications*, pp. 759-764.

Nakajima, A., Mawatari, T., Yoshida, M., Tani, K., and Nakahira, A. (2000) "Effects of coating thickness and slip ratio on durability of thermally sprayed WC cermet coating in rolling/sliding contact" *Wear*, vol. 241, pp. 166–173.

Nieminen, R., Vuoristo, K., Niemi, K., and Mantyla, T. (1995) "Rolling contact fatigue characteristics of thermal spray coatings" *National thermal spray conference*, Houston, USA, pp. 651-657.

Sahoo, P. (1993) "Performance wear coatings – the quest continues" *Powder metallurgy International*, vol. 25, pp. 73 - 78.

Sarma, B.Y., and Mayuram, M.M. (2000) "Some studies on life prediction of thermal sprayed coatings under rolling contact conditions" *Journal of Tribology*, 122 (3), pp. 503-510.

Stewart, S. and Ahmed, R. (2002) "Rolling contact fatigue of surface coatings – a Review" *Wear*, vol. 253, pp. 1132-1144.

Stewart, S. and Ahmed, R. (2003) "Contact fatigue failure modes in hot isostatically pressed WC-12%Co coatings" *Surface and Coatings Technology*, vol. 721, pp. 172 204–216.

Tobe, S., Kodama, S. and K. Sekiguchi (1988) "Rolling Fatigue behaviour of plasma coat steel" *Surface Engineering International Conference,* Tokyo, Japan, pp. 35-44.

Tobe, S., Kodama, S., and Misawa, H. (1990) "Rolling fatigue behaviours of plasma coated steel" Tokyo, Japan, pp. 35-44.

Tobe, S., Kodama, S., Misawa, H. and Ishikawa, K. (1991) "Rolling Fatigue Behavior of Plasma Sprayed Coatings on Aluminum Alloy" *Thermal Spray Research and Applications*, Long Beach, California, USA 20-25 May 1990, pp. 171-177.

Waterhouse, R. B. (1972) "*Fretting corrosion*" Hungary: Pergamon press.

Yoshida, M., Tani, K., Nakahira, A., Nakajima, A. and Mawatari, T. (1995) "Durability and tribological properties of thermally sprayed WC cermet coating in rolling/sliding contact" *Thermal Spraying--Current Status and Future Trends.* Vol. 2; Kobe; Japan; 22-26 May 1995. pp. 663-668. 1995.

Zhu, M.H. and Zhou, Z.R. (2001[a]) "An experimental study on radial fretting behaviour" *Tribology International*, vol. 34, pp. 321–326.

Zhu, M.H., Zhou, Z.R., Kapsa, Ph. and Vincent, L. (2001[b]) "Radial fretting fatigue damage of surface coatings" *Wear*, vol. 250, pp. 650–657.

Zhu, M.H., Yu, H.Y., Cai, Z.B. and Zhou, Z.R., (2005) "Radial fretting behaviours of dental feldspathic ceramics against different counterbodies" *Wear*, vol. 259, pp. 996–1004.

Zhu, M.H., Yu, H.Y., and Zhou, Z.R. (2006) "Radial fretting behaviours of dental ceramics" *Tribology International*, vol. 39, pp. 1255–1261.

# Chapter 2 FAILURE MECHANISMS OF POLYMERS UNDER CYCLING CONTACT LOAD AND ROLLING CONTACT FATIGUE OF METALLIC COATING

## 2.1 Introduction

Contact fatigue is complex processes. The damage behaviours and mechanisms depend on many factors such as counterfaces materials, mode and magnitude of loading, coatings, lubrication etc. The mechanisms of damage can be explained when a specific contact system is defined. However, the general knowledge from the previous findings can be used to support the other system.

The objectives for this chapter are to review knowledge of surface fatigue of polymers and metallic coatings. For polymers, the deformation properties, friction, fatigue and contact properties are discussed with special reference to a brittle polymer such as PMMA. For metallic coatings, the coating process, especially thermal spray coating, coating properties and wear of coatings are reviewed and focus is on molybdenum and titanium thermal spray coatings.

## 2.2 Polymers

### *2.2.1 Introduction to Polymers*

Polymer is the macromolecular organic compound produced by monomers synthesis or high molecular weight organic natural products conversions (Engel et al., 1981). Production of polymers from the reaction of monomers can be selected by various methods such as polymerization, poly-addition or poly-condensation. Polymer types are identified by their molecules that could be cross-linked, linear or branched. The cross-linked polymers are bonded together between the chains by chemical covalent bond, which is strong and form one single molecule. The linear or branched macromolecules are secondary bonds physically held together by intermolecular forces i.e. van der Waals'

forces and hydrogen bond which are weak and can be easily broken by chemical or physical means e.g. solvents, water or heat.

### *2.2.2 Types of Polymers*

Polymers are divided into three groups i.e. thermoplastics, thermosets, and elastomers. Thermoplastic polymers are normally of amorphous structure with linear or branched molecules (Engel *et al.*, 1981). The materials can be reprocessed by heat and their properties are a function of temperature. They are hard at low temperature, soften and become plastic upon heating. These states are reversible. Polyethylene (PE), polyvinyl chloride (PVC) and polystyrene (PS) are such materials in this group. Thermosetting polymers are frequently three dimensional cross linked macromolecules. They are hard at room temperature and may decompose before softening by heating. Epoxy resins (EP), and amino plastics (UF, UW) are examples of the materials in this group. Elastomer molecules are similar to thermosets but with less frequent cross-linking. They cannot be made plastic by heating, but exhibit a rubber-like properties. The materials in this group include cross-linked polyisoprene as natural rubber (NR), polybutadiene (BR), polyurethane (PUR).

All thermosets and most of elastomers as well as irregular chain structure thermoplastics are amorphous (Engel *et al.,* 1981). However, sometime they exhibit crystallization. The polymers that comprise of crystalline and amorphous regions are named semi-crystalline polymer (Al-Sabti, 2000). The ratio between these regions depends on chemical compositions, molecular arrangement and its processing method. The tendency to crystallisation is the regularity or smoothness dependence of the chain for example, strong for PE, but impossible for PMMA (Engel *et al.,* 1981). The group with irregularity is difficult to pack in a regular way. Fast cooling rate in solidification reduces crystallinity. Increasing crystallinity leads to increasing in softening temperature, the specific gravity and the elastic modulus (Engel *et al.,* 1981). Predominant crystalline polymers are fairly strong and rigid (Al-Sabti, 2000).

The most widely used plastic is thermoplastics accounting for approximately 90% of the total plastic utilisation (Al-Sabti, 2000). These materials are utilized in many industries such as mechanical engineering, transportation and electrical engineering.

### *2.2.3 Physical Properties and Deformation of Polymers*

This section will discuss the physical and deformation properties of polymers. The discussion will focus on thermoplastic polymers.

#### *2.2.3.1 Physical property of polymer*

Each type of plastic has an identical softening process, which influence on physical and mechanical properties of polymers (Engel *et al.*, 1981), see Figure 2.1. Molecules of polymer move increasingly as temperature is rising and gradually overcome the intermolecular bonds. Eventually, the characteristic of amorphous thermoplastics is different from partially crystallised thermoplastics. In case of amorphous thermoplastics, the softening phase occurs first and is followed by a relatively stable phase or rubber-like state. In this state temperature has little effect on material properties. When temperature passes the softening range the plastics begin to flow. In case of partially crystalline thermoplastics, the flow starts only above the melting point of crystallites ($T_m$) and thermoplastics are readily deformed in this state. This is a reversible process as long as polymer does not experience thermal degradation. The significant changes in shear modulus can be noticed when softening process occurs.

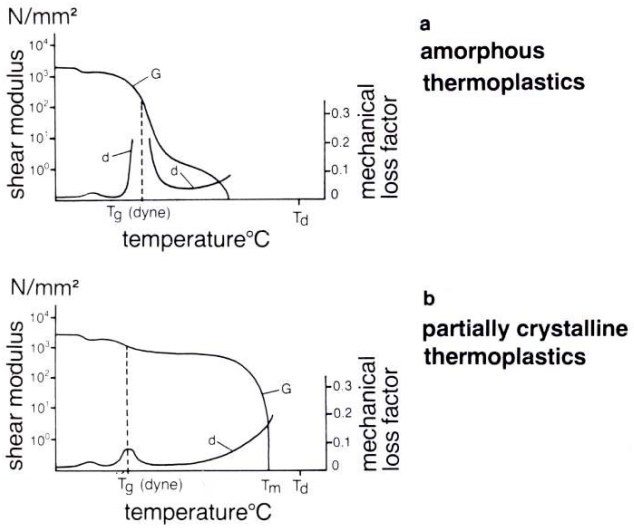


Figure 2.1 Variation of shear modulus and mechanical loss factor as a function of temperature (Engel *et al*., 1981).

*2.2.3.2 Deformation of polymer*

Mechanical behaviour of polymers is often a time-dependent namely, viscoelastic, even at low stress level (McClintock and Argon, 1969; Engel *et al.*, 1981). Viscoelastic properties are found in thermoplastics polymers. In general, the deformation behaviours of plastics attribute to the reaction of macromolecules in both spontaneous and individual rearrangement of molecules until the balance is reached, that is "relaxation". Furthermore, the arrangement in each chain is different. The speed of the arrangement is influenced by stress level and rate of stress, polymer structure and temperature. Physical and chemical bonds as well as bulky side groups affect the chain mobility of the polymers. Vibration of the molecules is increased as the material is heated resulting in the increase of the size of the empty space.

The same polymeric material can exhibit brittle or tough deformation behaviour depending on temperature and loading speed (Engel *et al.*, 1981). Comparing the loading period with the time taken for molecular rearrangement to establish equilibrium the deformation behaviours of polymers can be predicted. If the first is shorter than the second the polymer will be brittle. If, however, the first is longer than the second the material will be tough and flexible.

### *2.2.4 Friction of polymer*

In general, friction of polymers composes of an adhesion mechanism and a deformation mechanism (Steijn, 1986 and Hutchings, 1992). It may be written in the equation as

$$F_{total} = F_A + F_D$$

where $F_{total}$ is the total force of friction, $F_A$ is the adhesive or shearing force of friction and $F_D$ is the deformation or ploughing force of friction.

The adhesion term originates from the contact interface and the second term involves ploughing in sliding and the dissipation of energy or dynamic mechanical losses of polymer around the area of contact in rolling (Bowden, 1964; Hutchings, 1992 and Steijn, 1986). The adhesion term normally dominates in polymeric materials.

When two surfaces are in contact, the junction between asperities occurs and these asperities may experience elastic deformation or both elastic and plastic deformation depending on load magnitude (Steijn, 1986). Junction welding could be formed and sheared during sliding. Frictional force depends on the load magnitude. From the analysis and experimental results, the coefficient of friction for polymers decreases with increasing load. The adhesion in polar polymers is stronger than in non-polar polymers.

Ploughing of hard asperities depends on sliding speed and temperature. Rolling friction is directly associated with dynamic mechanical losses of polymer and strongly depend on rolling speed and temperature.

For dry friction it can be divided into 2 categories including coefficient of static friction ($\mu_s$) and coefficient of dynamic friction ($\mu_k$) (Yamaguchi, 1990).

The kinetic coefficient of friction is affected by many parameters. Therefore, it is mandatory to include a precise definition of sliding conditions when reporting on the coefficient of kinetic friction during dry conditions. The important factors are: internal structure of the polymers, surface contact pressure, sliding speed, temperature and humidity, surface roughness, and counterface material.

Internal structure of polymers including arrangement of atoms, molecular weight, crystal structure and molecular orientation, affects the kinetic coefficient of friction. Shearing resistance between two molecules is influenced by arrangement of atoms. The shearing resistance between symmetrical molecules would be expected to be much lower than that for asymmetric molecules. When molecular weight of the same plastic increases the coefficient of friction is increased. For the same plastic, semi-crystalline structure exhibits the value of $\mu_k$ lower than the amorphous structure and the value of $\mu_k$ decline with increasing degree of crystallization. Stretching can increase molecular orientation. The $\mu_k$ decreases with increasing of stretch when sliding is along stretching direction, but increase slightly for right-angle direction.

The surface contact pressure is dependent on the geometry of the surface, the scale of surface roughness and the load (Bowden, 1964; Steijn, 1986 and Yamaguchi, 1990). This also can be demonstrated by the theoretical equations below (Yamaguchi, 1990).

According to Hertz's elastic law for contact between two spheres,

$$\mu = F/P = A\tau/P = 3/4\pi \{R_1 \cdot R_2/E^*(R_1+R_2)\}^{2/3} \cdot P^{-1/3}\cdot\tau$$

where P is contact pressure, A is contact area, $R_1$ and $R_2$ are radii of contact body 1 and 2 respectively, $\tau$ is shear stress and $E^* = (1-\nu_1^2/E_1 + 1-\nu_2^2/E_2)$.

In case of a sphere of radius R with small asperities radius of r contacting a plain flat surface,

$$\mu = A\tau/P = K_5\cdot r^{2/3} \cdot n^{1/3} \cdot R^{2/9} P^{-1/9}\cdot\tau$$

where $K_5$ is constant.

According Mayer's law contact between sphere and a flat,

$$\mu = A\tau/P = \pi/4 \cdot\tau(1/K)^{2/n} \cdot D^{2(n-2)/n} \cdot P^{(2/n-1)}$$

where K is constant, D is diameter of sphere, n = 3 for a perfectly elastic material and n = 2 for a perfectly plastic material. In all cases, μ is proportional to $P^0 \sim P^{-1/3}$.

The sliding speed and $\mu_k$ have complicate relationship due to the rising of temperature resulting from frictional heating as sliding speed increases. Each material responds differently to sliding speed (Bowden, 1964 and Yamaguchi, 1990). In general, at slow sliding speed friction of polymers can be simply explained by the adhesion, but it is more complicated at higher sliding speed because of the dependency on both sliding speed and temperature. At very high speeds, friction value depends on the properties of molten surface film resulting from frictional heating.

Temperature and humidity are another main factors affecting $\mu_k$. However, it is impossible to predict the relative direction between temperature and the $\mu_k$ because the friction resistance force depend on both Young's modulus (effect to area of contact) and shear strength of the polymer, which have a complex relationships with temperature. The flexibility of the polymer chain is the main factor for rigid plastics. The greater chain-

flexibility results in the greater effect. The effect of humidity on the coefficient of friction is also still unclear. Increasing humidity can increase the value of $\mu_k$ for some polymers absorbing water, such as nylon, whereas decrease the value of $\mu_k$ in polymers, which do not absorb water, i.e. PTFE.

The surface roughness is normally related to ploughing term and different counterface materials give different values of $\mu_k$ .

### *2.2.5 Fatigue of polymers*

Fatigue of material occurs when cyclic stress is applied below that required to cause yield of bulk material (Ward and Hadley, 1996). The fatigue lifetime composes of two stages including crack initiation and crack propagation (Moet, 1986). Depending on the severity of defects the initiation stage may take 20% to 80% of the total lifetime. The microscopic cracks initiate at centres of stress concentration on the surface or within the material and consequently propagate until the final rupture is attained.

#### *2.2.5.1 Mechanisms of fatigue*

Fatigue failure of polymers can occur in one of two general mechanisms depending on the stress amplitude and the frequency of applied load (Moet, 1986). The first involves thermal softening (yielding or thermal failure) at a localized region under certain loading conditions before crack propagation. The second is a conventional form of fatigue crack propagation (FCP) mechanism, which occurs at low stress amplitude or at high stress amplitude and low frequency.

During cyclic loading mechanical work done is used for two interdependent processes including the irreversible molecular process causing microscopic deformations such as crazes, shear bands, voids, etc. and the other process generates heat. These processes can explain fatigue mechanisms of polymers.

*2.2.5.2 Fatigue crack initiation*

The initiation of macroscopic fatigue cracks, normally in the order of $10^{-3}$ m, is studied through two approaches (Moet, 1986). The first involves fracture mechanics approach achieved by characterization of a threshold value of stress intensity factor $K_{th}$ or its range $\Delta K_{th}$. The other is attained by the energy release rate $\Delta G_{th}$. However, the quantitative analysis of polymers is not completed and techniques are still being developed. The following explains briefly on the previous studies.

The role of crazing in fatigue crack initiation in glassy and semi-crystalline polymers has been intensely investigated. It is known that the formation of microcrazes ends with shear bands before crack initiation. The main crack initiates when the crazing density reaches a critical level. Consequently, a subcritical crack propagates through a craze surrounded by a pair of shear bands forming. Prior to crack initiation, the stress level and the test frequency affects the magnitude of crazing. Crack will initiate when a critical level of damage is reached. This critical level of damage is apparently corresponding to the abrupt crack jump characterized by $\Delta K_{th}$. Under certain conditions in glassy polymers, crack initiation and propagation takes place through a single craze.

*2.2.5.3 Fatigue crack propagation (FCP).*

FCP experiment can be examined by measurements of the average change in crack length from a sharp notch of a known depth in a specimen with a defined geometry as a function of the total load cycles (Hertzberg and Manson, 1980). The fatigue crack growth rate per cycle, $dc/dN$, generally increases with increasing stress level.

For glassy polymers, fracture mechanics dealing with the rate of FCP can be explained by an empirical relationship

$$dc/dN = A(\Delta K)^m$$

where $c$ is the crack length, $N$ the number of cycles, $\Delta K$ the range of the stress intensity factor (i.e. $K_{max}$-$K_{min}$, where $K_{min}$ is generally zero), and $A$ and $m$ are constants depending

on the material and test conditions (Ward and Hadley, 1996). This equation is the general form proposed by Paris-Erdogan for predicting crack growth rates in metals, but can apply to other materials too.

From the above equation, the rate of FCP is suggested to be logarithmically linear function $\Delta K$ (Moet, 1986). In fact, three distinctive regions, as illustrates in Fig. 2.2(a), are expected for a typical FCP behaviours. Region I begins with a threshold value of the stress intensity factor range $\Delta K_{th}$, below which crack is not propagated. Generally, the initial slope of region I is very steep. As the crack extends longer, i.e. $\Delta K$ become larger, crack propagation rate reduces leading to region II. The effectively linear FCP in region II is obtained in the most cases. The transition of the FCP rate from stable to unstable crack propagation occurs when $K = K_c$ is approach.

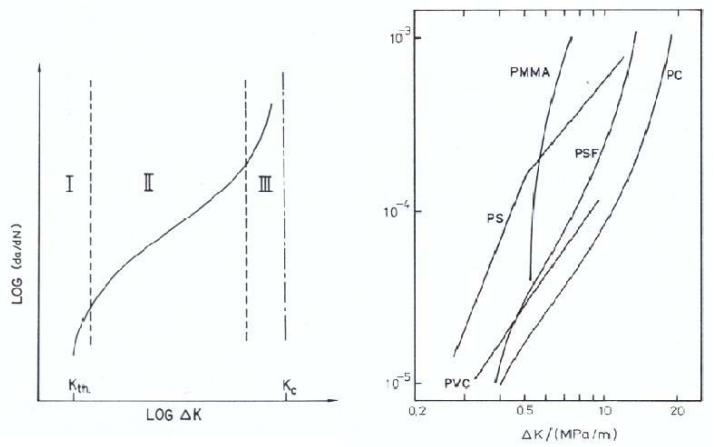


(a) (b)

Figure 2.2 (a) Three regions of FCP and (b) FCP behaviours of various polymers (Moet, 1986).

The Paris-Erdogan equation is generally accepted from the common observation on the effective linearity of region II (Moet, 1986). However, the equation can not demonstrate the influence of the mean stress which usually has an important influence on the crack growth rate. Furthermore, the FCP rate characteristics of polymers are normally not linear for the full range of $\Delta K$, see Figure 2.2(b). Therefore, the entire FCP should be assessed to ascertain conclusion concerning the FCP resistance of polymers.

*2.2.5.4 The factors effecting fatigue crack propagation*

Many attempts try to approach the FCP rate to cover more factors. However, supplementary developments in this area are required (Ward and Hadley, 1996). The major factors include test frequency, test temperature, environments, mean stress and load history, molecular weight and molecular weight distribution (Hertzberg and Manson, 1980).

The effect of test frequency on the FCP for the pre-notched samples showed different influence on FCP rates. In case of PMMA, PVC, PS FCP rates decreased with increasing frequency, but other polymers, such as PC, nylon 66, PVDF, FCP rates were apparently insensitive to frequency of load application. Many efforts have been done to rationalize these data. The initial conclusion is that the strong FCP frequency sensitivity polymers (e.g. PMMA, PS, PVC) tend to exhibit heterogeneous deformation by crazing while negligible frequency sensitivity materials (e.g. nylon 66, PVDF) are craze resistant with some exception, such as PC, that experiences craze deformation. The frequency-sensitive polymers exhibit glassy character at the test temperature with insignificant change of modulus E over several decades of test frequency except in case of PMMA. High frequencies fatigue testing could produce a temperature rise at the crack tip, for example up to 20 K at 11 Hz in fatigue tests of PVC, PMMA and PC. Significant temperature rise leads to yielding processes adjacent to the crack tip and results in larger crack tip radius. Accordingly, this lowers effective $\Delta K$ and thus decreases the fatigue crack growth rate.

The effect of temperature on the FCP is unclear because the experimental results obtained under different test conditions are contradictory. For example, macroscopic FCP rates in PMMA increase with decreasing temperature over a testing range of 50 to -10 ºC under fix displacement test condition. Under fix load test conditions, FCP rate in PMMA increases as the temperature decreases from 40 to 10 ºC, but decreases with further lowering of the temperature.

The effect of environments on $K_c$ and the stress for crazing, thus FCP, depends on the specifics of material-environment system.

It is known in general that the resistance to FCP depends on mean stress. Many researchers propose relationship formulations between the mean stress and *da/dN* at different $\Delta K$ levels. Unfortunately, these formulations have been found incapable to explain all aspects. The *da/dN* increases with increasing of stress range, *R*, in some polymers, but in some decreases. It is of interest that application of a single over load or short cluster of over load cycles decreases the subsequent crack extension rate in short-term in some polymer such as PMMA and PC.

The FCP resistance improves when molecular weight (M) increase in many polymers, e.g. PC, PVC and PMMA.

### *2.2.6 Contact Damage of PMMA*

This section deals with previous research on the contact damage of polymer including fretting, stationary rolling and torsional repeating contact, sliding wear and rolling contact fatigue of PMMA.

#### *2.2.6.1 Fretting*

A number of publications have reported on linear fretting of PMMA. Fretting mechanisms has been established (Krichen *et al.*, 1998, 1999) and many factors have been investigated including slip amplitude, load frequency and load magnitude (Geringer *et al.*, 2007; Krichen *et al.*, 1998, 1999 and Teng and Sato, 2004).

Krichen *et al.* (1998, 1999) have intensively studied fretting mechanisms and the effect of fretting conditions in a glass/PMMA contact using a cylinder on flat contact configuration, i.e. borosilicate glass rod and PMMA flat specimens. The initial damage in the form of micro-crack nucleated at the contact edge on the PMMA's surface related to the combination of high tensile stress and positive hydrostatic pressure, which are known to enhance crazing.

The distribution of the detached particles within the contact was attributed to the spatial distribution of the cumulative interfacial energy dissipated by friction at the interface during the early stages. The detached particles migrated toward the middle of contact as

the number of cycles increase. The analysis in term of the contact zone kinematics explained the existence of differential micro-displacements owing to the dissimilar elastic constants of the glass counterface and the PMMA during the fretting cycle. The presence of the third body layer reduced the degradation rate of substrates.

Three different wear domains were identified by increasing the displacement amplitude due to the change of the shape of the energy profile along the contact area, see Figure 2.3. The first domain, namely partial slip condition, is about localisation of the detached particles in two narrow strips character in the partial slip areas location induced by the two sharp maxima in the spatial distribution of dissipated energy. The final two domains corresponded to gross slip conditions. They were separated by the transition from two maxima of dissipated energy to a single one as increasing of the tangential displacement.

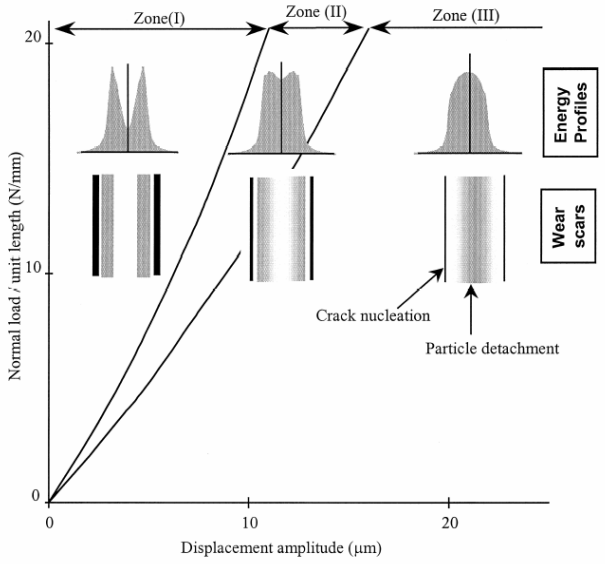


Figure 2.3 Schematic diagram illustrates three domains for particles detachment (Krichen *et al.*, 1999).

Geringer *et al.*, (2007) have reported the effect of load magnitude on wear behaviour in the line contact between PMMA round face and 316L stainless steel flat in dry conditions. Wear debris were easily expelled from the contact zone at lower normal load, but accumulated inside the contact and adhered the metal surface at higher loads. The debris generation could be explained in term of plastic or viscoelastic deformation. The driving force of the debris adhesion was accounted for the acid–base interaction on the metal

surface. The third body is claimed to be the bulk PMMA protection especially at high load. The PMMA wear volume associated with the dissipated energy. This energy is spent for transformation third body structure and for expelling from the contact counterparts during fretting.

The tangential loading frequency was highly effective on the wear process of PMMA flat contacted with a steel sphere (Teng and Sato, 2004). Under the constant normal applied load, the higher frequency results in increased damage severity and the fretting life time to initiate crack was proportional to the fretting amplitude.

*2.2.6.2 Stationary rolling and torsional repeating contact*

The wear of the PMMA plate contacted against the steel ball has been studied under stationary rolling and torsional repeating contact conditions (Briscoe *et al.*, 1998: 2000[a]). The effect of contact zone kinematics was considered a very pronounce on the wear resistance of the PMMA which related to particles detachment and third body elimination. The wear volume resulting from testing in stationary rolling contact condition was much lower than that in torsional contact condition. Stationary rolling gives ripple oriented perpendicular to the displacement at the middle of the wear scar resulting from progressive accumulation and compaction of wear debris into rolls. The third body consolidation created from debris with mechanical properties similar to the original PMMA substrate enhanced the load carrying capacity of the contact. Hardness measurements by nano-indentation in layer of third body in the central part of the wear scars showed a heterogeneous microstructure (Briscoe *et al.*, 2000[b]). By contrast, debris were expelled from the periphery of contact in the torsional contact condition leading deeper wear scar comparing to stationary contact condition.

*2.2.6.3 Sliding wear*

The sliding wear of PMMA rod in contact with the periphery of lubricated rotating steel disc was affected by the mode of loading and contact configuration (Stolarski and Williams, 1996). The wear of PMMA under cyclic loading was found to be appreciably lower compared to static loading of a magnitude equal to the mean load of the cycle. A cyclic loading, it was proposed, interfered with the wear process possibly by a periodic

reduction in interfacial shear stresses. Therefore, overall heat generation is affected, or the severity of the contact conditions is regularly eased resulting in deceleration the material removal rate. The wear of PMMA was slightly affected by the angle between the axis of the PMMA rod and the axis of the steel disc. The lowest wear rate was observed for smaller angles for both static and cyclic loading.

#### *2.2.6.4 RCF Damage*

Crazing was the main form of PMMA failure against metal in both pure rolling contact and rolling/sliding contact using two disc test configuration (Al-Sabati and Stolarski, 1998). However, failure was diverse between both contacts in the appearance of crazes, their amounts and the time of initiation and failure size and time. Crack initiated somewhere on the surface of PMMA under rolling contact fatigue in ball on flat configurations in lubricants (Stolarski *et al.,* 1998). The lubricating oil types are found to be sensitive to number of load cycles to failure. The cycles to failure life decreases with increasing the contact load.

## 2.3 Metallic coating

### *2.3.1 Introduction to Metallic Coatings*

Coatings are increasing important specially to control friction, wear, thermal loads and corrosion (Holmberg and Matthews, 1994). There are various kinds of coating methods available nowadays. Each method has its own advantages and limitations. Considerations of what needs to serve the requirements of applications are the criteria of selection coating methods.

Metallic thermal sprayed coatings are used for many purposes such as wear resistance, thermal barrier, and corrosion resistance. For example, NiCrMoW for corrosion and wear resistance, austenitic stainless steel for corrosion resistance, zirconia alloys for thermal barrier and resistance to molten metal, and NiCrAl for high temperature resistance (Rickerby and Matthews 1991). Molybdenum and titanium coatings are of interest for rolling contact fatigue in this research since these materials have many desired properties.

*2.3.1.1 Molybdenum*

Molybdenum has been known long as a refractory metal. In tribological applications, molybdenum is used as a hard coating for heat resistance or wear resistance against abrasion and possesses excellent sliding properties when applied in plasma spraying (Matejka and Benko, 1989; Rickerby and Matthews, 1991). The coating is applied for rotating journals, hydraulic elements, and piston rings in automotive and aircraft industries (Matejka and Benko, 1989; Rickerby and Matthews, 1991 and Herman *et al.*, 2000). Molybdenum adheres very well to most metals and alloys because of self-bonded property. The properties of molybdenum are as follows; HV 169, Melting point 2617 ˚C, density 10.22 g/cm$^3$.

*2.3.1.2 Titanium*

Titanium is well known as excellent corrosion resistance material in wide range of environments such as pro-oxidizing solutions, water, seawater and event in polluted seawater (Matejka and Benko, 1989 and Mountford, 2002). Titanium offers complete resistance to general corrosion up to 260˚C and crevice corrosion up to 80˚C. It is not affected by microbiologically influenced corrosion (MIC) even in stagnant conditions. It is highly resistant to erosion; 27 ms$^{-1}$ by water in the absence of suspended solid and in the range 4.6-5.5 ms$^{-1}$ in sand-laden conditions. Furthermore, it exhibits corrosion resistance superior to superaustenitic stainless steel, Hastelloy C-276, and 316L and 430 stainless steels testing in laboratory using anodic electrochemical technique in salt water under static and flow conditions (Khalid *et al.*, 2003). Therefore, it is increasingly utilised for a components in marine services because it provides a reliability and long-term proven life cycle, cost economies, and reduction of maintenance. Pure commercial titanium, Grade 2, is approximately 99.6 % with tensile strength 345 MPa, yield 275 MPa, HV 157, mp 1665 ˚C, density 4.5 g/cm$^3$ (Matejka and Benko, 1989 and Mountford, 2002).

### *2.3.2 Coating methods*

There are plenty of coating technologies available nowadays. Coating processes can be categorized by coating state into 4 groups consisting of gaseous state process, solution state process, molten or semi-molten process and solid state process (Holmberg and Matthews, 1994).

The major coating processes in each coating state include the chemical vapour deposition (CVD), physical vapour deposition (PVD), and ion beam assisted deposition (IBAD) for gaseous state processes; chemical solution deposition, electrochemical deposition, sol-gel processing for solution state process; laser, thermal spraying and welding for molten or semi-molten process.

#### *2.3.2.1 Gaseous state process*

CVD process uses volatile compound to condense onto substrate. The coating materials can be borides, carbides, nitrides, oxides, carbo-nitrides and oxy-nitrides of almost all the transition metals e.g. for TiN or TiC and diamond. Coating layers by this method can be adjusted to well adherent, uniform and dense surface.

PVD is achieved by atomization or vaporization of solid material and deposition on the substrate. This process can deposit alloy compounds, multi-layer compositions and structures. The process employs an excellent adhesion and structure control of coatings. The advance method namely, plasma assisted physical vapour deposition (PAPVD) is of a major application in tribology.

IBAD is an embedding process of elemental species i.e. nitrogen, titanium, or carbon into the surface of the substrate, which can be metals, ceramics, cermets, plastics. Different mechanisms could be used to explain for this coating process such as interstitial additive in case of nitrogen or formation of stable compound in case of metal nitride.

*2.3.2.2 Solution state processes*

The major coating techniques in this process are electroless plating and electroplating. These processes are normally conducted in aqueous solution. While an electrochemical deposition uses an electrical current assisted metallic coating such as hard chrome, Cu/Ni/Cr, or others alloys, an electroless plating involves chemical reduction reaction of metallic ion with or without reducing agent such as nickel.

*2.3.2.3 Molten and semi-molten state processes*

Laser surface treatments may involve different purpose i.e. wear, transformation hardening, alloying for corrosion improvement or plating.

Thermal spraying applies to a wide range of techniques. This coating technique was used for samples preparation for the rolling contact fatigue in this research and will be discussed in details in the next section.

Welding process also has variety techniques. They are particularly suitable for improving abrasive wear e.g. carbide of chromium, tungsten or boron, and impact wear i.e. austenitic manganese steel.

### *2.3.3 Thermal Sprayed Coatings*

Thermal spray coating is the common name for the thick coating processes group that can be processed for the wide range of both coating materials and substrates (Rickerby and Matthews, 1991). Applications involve various fields such as automotive industry (cylinder bores, piston rings, valve lifters, transmissions, and oxygen sensors), gas turbine industry (blades, vanes, shrouds, etc.), corrosion protection (infrastructure and marine), biomedical implants (orthopaedic and dental parts), petrochemical industry (valves and pump) etc. (Herman *et al*., 2000).

In the coating process, a material is generally melted, atomised, accelerated to high velocity, project onto the prepared substrate surface and solidify to form a thin splat. Continuous process repeats to build up lamella overlay layers with inter-bonding among

the splats. The composition of the feedstock determines chemistry of the coatings.

*2.3.3.1 Types of Thermal-Spray Processes*

Various processes are applied to thermal spraying including combustion flame spraying, high velocity oxy-fuel (HVOF) spraying, two-wire electric-arc spraying, plasma spraying, detonation gun spraying (D-Gun) and etc (Herman *et al.*, 2000). The followings will briefly outline thermal spray processes. However, plasma spray coating is explained in more details because the samples used in this study were prepared by this process.

2.3.3.1.1 Combustion flame spraying of powder or thermo spraying

This technique uses a simple oxyacetylene gas torch, into which the spray powder is aspirated. The mixtures of compressed air or oxygen and a fuel (e.g., acetylene, propylene, propane, or hydrogen) are used as a heating source (Department of Trade and Industry, 1986; Herman *et al.*, 2000). Flame velocity and temperature are low resulting in high coating porosity, approximately 20%, and weak bonding to the substrate. Combustion flame spraying technique, however, is a low cost and easy to operate.

2.3.3.1.2 Detonation or D-gun process

The detonation gun process uses combustion gas to heat the particles that are molten or partially molten and deposits them with high particle velocity about 800 $ms^{-1}$ (Department of Trade and Industry, 1986). This process is more costly and with lower deposition rate as compared to plasma spray.

2.3.3.1.3 High-velocity oxy-fuel (HVOF) spraying

High-velocity oxy-fuel (HVOF) spraying is a relatively new process and variety of HVOF spray torches is available on the market (Herman *et al.,* 2000). The combusting fuel is a combination of oxygen and kerosene to provide a very high-velocity, low-thermal-input torch. The powder is fed into the barrel, heated, accelerated to a very high velocity and impinged on to the surface of the substrate. The particle spreads out very thinly and bonds instantly to the substrate.

2.3.3.1.4 Wire spraying

The wire is melted continuously by feeding into an oxyacetylene flame and is atomised by auxiliary blast of compress air (Department of Trade and Industry, 1986). This process results in a high coating porosity.

2.3.3.1.5 Arc wire spraying or two-wire electric-arc spraying

Arc wire spraying is achieved by melting two wires, which are continuously fed into the gun and atomized by compressed air, forming a molten spray (Department of Trade and Industry, 1986 and Herman *et al.*, 2000). The process yields high deposition rate so that it is suitable for thick coating. This process, however, produces loud noise and copious fumes. The electric arc guns can spray reactive metals such as titanium and zirconium when operating in inert atomizing atmospheres i.e. argon or nitrogen.

2.3.3.1.6 Plasma spraying

Plasma spray can be applied to a wide range of industrial materials, including most metals, both ferrous and non-ferrous, oxide and carbide such as nickel and ferrous alloys, aluminium oxide, and zirconia-based ceramics (Department of Trade and Industry, 1986 and Herman *et al.*, 2000). It lies between thermo-spraying and D-gun coating process (Department of Trade and Industry, 1986). Density and bonding of coatings to the substrate are superior to the thermo-spraying and the coating process is of low cost and more available comparing to the D-gun process.

The torch comprises of cathode and anode where the anode also serves as nozzle. The current densities and temperature are very high e.g. 1,000 A at 80 VDC and 15,000 -20,000 K (Rickerby and Matthews, 1991) (see Figure 2.4). Passing through the gases between anode and cathode where the arc is taking place generates plasma. The gases are dissociated and/or ionized resulting in a plasma jet, which is ejected from the nozzle at velocities of several hundred $ms^{-1}$. The major plasma gas can be argon, nitrogen or helium plus small amount of hydrogen in order to increase the power of enthalpy of the flame. Particles are fed into the plasma stream with a very efficient energy transfer to particles prior to impingement on the substrate. Parameters affecting density and adhesion of the

coatings comprise of nozzle type, gas pressure and flow rate, power level, powder feed rate, and spray distance (Department of Trade and Industry, 1986).

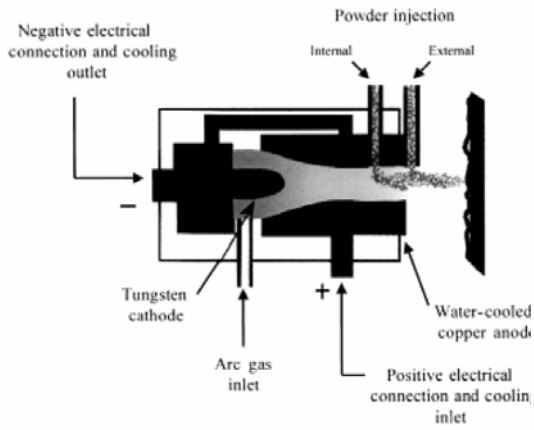


Figure 2.4 Schematic diagram of a generic plasma torch (Herman *et al.*, 2000).

Particles are normally melted without significant dissociation or evaporation. The turbulent trap air causes the essential inert plasmas to become active resulting in oxide (Rickerby and Matthews, 1991). This will deteriorates the density and adhesion strength of coatings. To achieve theoretical bulk density and extremely high adhesion strength an advance technique i.e. vacuum plasma spraying (VPS) or low-pressure plasma spraying (LPPS) is used (Rickerby and Matthews, 1991; Herman *et al.*, 2000). The process is conducted in a chamber held at low pressure inert-gas chamber or through a shrouded flame. Decreasing of the ambient spray pressure raises the flame velocity and particle velocity that can be higher than 800 $ms^{-1}$. The higher velocity of molten particles impact onto the substrate results the higher flattening of the splats leading to a denser and lower porosity deposit.

Radio-frequency-induction plasma spray is a non-traditional thermal spray processes in this field which has recently been introduced to the market (Herman *et al.*, 2000). High purity plasma is generated by radio frequency induction due to the absence of electrodes employing highest efficiency of all thermal-spray techniques.

### *2.3.4 Properties of Coatings*

The measures for integrity and quality of a coating deposition include bond strength and microstructure, imperfections, of which oxides and porosity are the critical concerns. Properties of thermal spray coatings to be discussed in this section concern microstructure, imperfections, bond strength factors, and their effect on the coating properties.

#### *2.3.4.1 Factors effecting coating properties*

The physical characteristics and the properties of the coatings are primarily influenced by the stability of the particles within the flame, the particle-impact conditions (velocity and temperature), and the temperature of substrate ((Rickerby and Matthews 1991 and Herman *et al.*, 2000). In the case of metals, substrate roughness, wettability, and oxidation play additionally vital roles.

#### *2.3.4.2 Microstructure and imperfections*

Thermal spray coating microstructure is consisted of cohesively bonded splats. Thermal spray microstructures contain various kinds of imperfections depending on the spray process and materials used (Herman *et al.*, 2000). These imperfections can be oxide, porosity, microcracks, morphologies, different particle sizes, volume densities, and sometimes orientations. They can significantly affect a broad number of properties such as elastic moduli, fracture strength and thermal conductivity. Oxide and porosity are always observed in coatings and generally present in metals, whereas pores and microcracks are the major defects in brittle materials e.g. ceramic.

When metal spraying processes takes place in air oxides might contaminate coatings (Rickerby and Matthews 1991). The form and character of the oxide depend strongly on spray environment, especially in the metals (Herman *et al.*, 2000). Pores or voids arise from out gassing, shrinkage or topographical effects (e.g. shadowing) during spraying. They are nominally disc-like shaped and accommodate between splat layers (Herman *et al.*, 2000). Open porosity is a problem when adherence, corrosion or oxidation resistance of coating is required (Department of Trade and Industry, 1986). The major factors effecting porosity are the ambient spray environment, powder characteristics (i.e. particle

size and size distribution), and spray parameters (e.g. power level, gas flow features, and spray distance) (Herman *et al.*, 2000). Normally, spraying in an inert atmosphere decreases the porosity level in most metal coatings. Increasing the particle velocity decreases the porosity, while greater the feedstock particle size, the larger the average porosity is attained.

#### *2.3.4.3 The bond strength*

The bond strength may be defined as adherence to the substrate - the most property concerning coating quality (Matejka and Benko, 1989). The adherence is a measure of the tear off force per unit area of coating from the substrate. In general, chemical interactions at the interfacial layer are minimal during the deposition process (Herman *et al.*, 2000). A well prepared substrate surface ensures good bonding of coating with the substrate (Rickerby and Matthews, 1991). The most critical factor is the cleanliness of the surface. Also, roughening surface of the substrate should be conducted to increase the mechanical interlocking between coating and substrate. This is practically done by cutting and grit blasting (Department of Trade and Industry, 1986). Surface roughening may not be necessary for self-bonding materials, i.e. molybdenum and nickel-aluminium, due to strong adherence even to substrate surface smooth or poorly prepared (Rickerby and Matthews, 1991). In some cases, a bond coat may be necessary. Spraying operation must be conducted as soon as possible after surface preparation owing to a very reactive environment.

Bond strength is generally proportional to particle velocity, but opposite relationship holds for coating thickness (Department of Trade and Industry, 1986). Pre-heating is required to maximize bond strength in some coating and for some systems.

### *2.3.5 Wear of Metallic Coating*

This section deals with current knowledge on wear of molybdenum and titanium thermal sprayed coatings, which were studied in this research.

*2.3.5.1 Molybdenum coating*

In general, sliding wear rate of molybdenum coating increases with increasing normal load (Hwang *et al.*, 2004 and 2005; Liu and Hua, 1999 and Prchlik *et al*., 2001). However, Uyulgan *et al.*, (2003) reported that wear loss was insignificantly affected by the normal load.

2.3.5.1.1 Friction and wear mechanisms

Friction characteristics of atmospheric plasma-sprayed molybdenum coatings are time-dependent and are similar to those observed in monolithic iron-base materials (Usmani and Sampath 1999). The friction behaviour could be categorized into six stages. The initial coefficient of friction resulted mainly from ploughing. After the formation of wear debris and their removal from the sliding surface the coefficient of friction decreased. Uyulgan *et al.*, (2003) reported that friction coefficient initially rapidly increased and approached a steady state in both dry and acidic conditions. The coefficient of friction tested in acid condition was slightly lower than in dry condition due to acidic corrosion. An average coefficient of friction in oil lubricated conditions was slightly lower than in dry conditions because of high hardness of coating (Laribi *et al.*, 2006 and 2007).

Examination of Mo thermal spray coatings subjected to wear beneath worn region using microstructural technique revealed that fracture of splats and their de-cohesion constitutes the main mode of failure (Wayne *et al.*, 1994). The investigation of molybdenum coating by Usmani and Sampath (1999) revealed that friction and wear behaviour was attributed to lamellar fracture and delamination, ploughing of the surfaces by hard asperities or particles, and adhesion at the interfaces. Hwang et al. (2004, 2005) confirmed that wear of Mo coating was due to delamination resulting from fracture either between splats in low load range or within splats themselves in high load range.

Wear transitions and mechanisms of molybdenum coating contact performance, studied under boundary lubricated conditions against bearing steel using twin discs machine, could be divided into three regimes. In every regime, wear rate of molybdenum coating obeyed simple power law with different constant (Liu and Hua, 1999). Regime I: the harder phase assists to support load and oxide from the counterface is transferred to Mo coating. The

latter increases wear resistance of the Mo coating. The local stress beneath the coating was lower than fracture strength of the phases. Regime II: fragmentation of the harder phase occurs. Delamination and third body abrasion are the mechanisms of wear in this regime. Regime III: harder phase fractures and the softer phase is subjected to shear stress. Severe wear and surface damage results. The wear mechanisms in this regime are deformation and damage accumulation process. Wear rate increases with increasing sliding speed.

Different test configuration of thermal sprayed molybdenum coating resulted in different wear mechanisms (Stolarski and Tobe, 2001). Test configurations including block-on disc, ball-on-disc and ball-on-plate produced adhesive and abrasive wear, surface fatigue and fretting wear and abrasive wear respectively.

Impact wear test of thermal sprayed molybdenum coating under dried and oil lubricated conditions showed that the diameter of worn zone increases with increasing test cycles in both conditions (Laribi *et al.*, 2007). However, the worn diameter in oil lubricated contact condition was lager than that under dry contact condition after the same number of test cycles due to the presence of oil at the contact interface. They explained that oil evacuated debris from the contact area and facilitated the coating deformation.

2.3.5.1.2 Spray techniques and spray conditions

The reports on the effect of spray technique and spray distance are very limit. Flame sprayed molybdenum coating with Ni-Al bond coat on 35 CrMo 4 steel gives very high compressive residual stress (Laribi *et al.,* 2003), which reaches zero at the interface of both sides of bond coat. The substrate has compressive residual stress the same as that when direct spray is used. Spray distance influenced wear resistance of thermal sprayed molybdenum coating because it affected the coating hardness resulting from enhanced oxide content in the coatings (Stolarski and Tobe, 2001).

2.3.5.1.3 Alloying of molybdenum coating

The first study on alloyed molybdenum coating, using the pin-on-disk and single-point scratch test methods, was reported by Wayne *et al.* (1994). Pre-alloying Mo with NiCrBSi prior to thermal spraying improved wear resistance and the stability of low coefficient of

friction.

Later, Prchlik *et al.* (2001) investigated wear characteristics of Mo-$Mo_2C$ plasma sprayed coating using pin-on-disc wear test. Delamination occurred due to brittleness of the phase and interlayer. Adding stainless steel to the coating increases toughness and wear resistance, but limit is reached at a certain amount because the hard phase should also be at an optimum level otherwise the wear rate increases again.
Wear resistance of plasma sprayed molybdenum coatings blended with various alloys e.g. brass, bronze, aluminium-silicon was intensively studied (Hwang *et al.* 2004, 2005 and Ahn *et al.*, 2005). The blend coating gave a better wear resistant than the pure Mo coating because of appropriate microstructure and good bonding between the splats even though the hardness was lower than that of pure molybdenum coating. Microstructure showed mixed phases of blend coating and new phases formed in same blends. The mixed coating exhibited better resistant to delamination due to fracture or cracking between the splats especially at high load. In addition, the formation of new hard phases contributed to abrasive wear resistance.

2.3.5.1.4 Environmental effects

Friction and wear properties in dry and acid (0.1% $H_2SO_4$) conditions of thermal sprayed Mo coating on cast iron were assessed against AISI 303 steel using pin-on-disc type (Uyulgan *et al.*, 2003). In general, surface damage morphology appeared as smooth areas, cracks and pits. The amount of cracks and pits varied with applied load and acidic condition. At low load, weight loss in acid condition was higher than in dry condition. At higher load more wear debris was stuck on the surface and some cracks were observed. In acidic condition cracks were not found but scratches. The absence of debris due to acid dissolution and the scratches indicated abrasive wear.

2.3.5.1.5 Post treatment

The effect of post heat treatment on the residual stress, adhesion, coefficient of friction and impact wear resistance was studied (Laribi *et al.*, 2003; 2006; 2007). Annealing decreased the residual stress in both coating and substrate for two thermal sprayed molybdenum coatings including direct coating and Ni-Al bond coat (Laribi *et al.*, 2003). Immediately

after spraying both coating systems already showed good adherence to the substrate. Annealing further improved the adherence in Ni-Al bond coating, but had adverse effect for direct coating. An adverse effect on pure molybdenum coating occurred because of the formation of brittle intermediate phase, $\varepsilon(Fe_xMo_y)$, between coating and substrate (Laribi *et al.*, 2003; 2006). Annealing has not affected the coefficient of friction due to its high hardness although the hardness has reduced from about 1700 – 1800 HV to 1300 HV (Laribi *et al*., 2006). The impact wear of annealed thermal sprayed molybdenum coating showed larger contact diameter in both dry and oil lubricated contact conditions at the same test time compare to the as sprayed coating (Laribi *et al*., 2007).

*2.3.5.2 Titanium coating*

There are not many publications on titanium thermal sprayed coating. The following presents research summaries on thermal sprayed titanium coating categorized by spray techniques and spray conditions, alloying, corrosion resistance and post treatment which influences the coating structure, wear and corrosion properties.

2.3.5.2.1 Spray techniques and spray conditions

Titanium is a very active metal. Its surface can readily react with the atmosphere to form an oxide layer. Spray techniques and coating atmosphere are the major factors for controlling the titanium coating properties produced by thermal spray method.

The advance shrouded plasma spraying (SPS) reported by Kinos *et al.* (1996) produces coating layer denser than air plasma spraying (APS). In addition, SPS coating technique reduces oxide formation. The best results could be achieved by optimization of important parameters, i.e. flow gas rate and spray distance. Cold spray technique can retain the coating structure similar to a feed stock powder as confirmed by the XRD results (Wang *et al.*, 2007).

Gas atomization and spraying distance affect the chemistry and microstructure of the titanium coating through the formation phase of titanium and titanium nitrides ($Ti_2N$, $TiN_{0.3}$ or TiN) which are the hardness enhancers of the coating layer (Bacci *et al.*, 2000 and Sakoda *et al.*, 2003). The volume fraction of nitrides was proportional to nitrogen

contents in Ar:$N_2$ plasma gas and spraying distance (Bacci *et al.*, 2000). The coating tends to increase porosity and coating adhesion strength decreases when nitride phase exceeds a certain amount. For, Ar atomization the alloyed layer is formed between coating and substrate (Sakoda *et al.*, 2003). The α-Ti phase in Ar atomized coating functioned as a binder between lamellas resulting in a good cohesion. The $N_2$ atomization induces the formation of TiN, which in turn reduces α-Ti. As a result, coating layer becomes more brittle and wear resistance decreases.

2.3.5.2.2 Alloying of titanium coating

Published research on alloying of titanium coating is very rare. Sliding wear resistance of Ti plasma sprayed coatings mixed with TiN depended on test conditions (Borgioli *et al.*, 2006). The highest volume of wear resulted at high applied test load and slow sliding speed due to adhesion to the tool steel counterface and de-cohesion of coating particles. The wear volume was proportion to the sliding speed due to surface oxidation because of surface temperature rise. The oxide film prevented adhesion between contacting surfaces leading to decreasing coefficient of friction.

2.3.5.2.3 Corrosion resistance of titanium coating

Corrosion resistance of the as sprayed titanium coatings by shrouded plasma spraying (SPS), wire flame spray, reactive plasma spray (RPS) and cold spraying exhibited the same characteristics as uncoated substrates or only little improvement as measured by electrochemical technique (Galvanetto *et al.*, 2006; Ishikawa *et al.*, 1999; Kinos *et al.*, 1996 and Wang *et al.*, 2007). This is because the solution can penetrate through the porosity of coating and react with the base metal. Therefore, the pores in coating must be diminished or filled by inert phases to enhance corrosion resistance. Various post treatment methods have been reported to improve the corrosion resistance, i.e. coating densification by electron beam (EB) fusion, hot isostatic pressing (HIP), post heat treatment in oxidising atmosphere, surface polishing, sealing the coating with organic polymers (silicon or epoxy resin or mixture of both resin).

2.3.5.2.4 Effect of post treatment

The post treatment of titanium thermal sprayed coating has been reported to improve corrosion resistance and wear resistance. The effect of post treatment on wear resistance of titanium coating is limited. Wear volume loss of reactive plasma sprayed (RPS) Ti-TiN coating in dry sliding conditions was improved by the post heat treatment in oxidizing atmosphere (Galvanetto *et al.*, 2006). Post heat treatment was claimed to exhibit interdiffusion processes between coating layers and coating/substrate interface. This process enhanced internal cohesion of the coating.

**References:**

Ahn, J., Hwang, B., and Lee, S. (2005) "Improvement of Wear Resistance of Plasma-Sprayed Molybdenum Blend Coatings" *Journal of Thermal Spray Technology*, vol. 14, pp. 251-257.

Al-Sabati, S. L., and Stolarski, T. A. (1998) "Surface fatigue of brittle polymers in rolling line contact" *Tribology International* vol. 31, pp. 695-699.

Al-Sabti, S. L. (2000) "Thesis failure modes of polymethymethacrylate resulting from rolling line contact" *Brunel University*, London.

Bacci, T., Bertamini, L., Ferrari, F., Galliano, F.P., and Galvanetto, E. (2000) "Reactive plasma spraying of titanium in nitrogen containing plasma gas" *Materials Science and Engineering,* vol. A283, pp. 189–195.

Bowden, F. P., (1964) "*The friction and lubrication of solids / Part 2*" London: Clarendon Press.

Borgioli, F., Galvanetto, E., Galliano, F.P., and Bacci, T. (2006) "Sliding wear resistance of reactive plasma sprayed Ti–TiN coatings" *Wear*, vol. 260, pp. 832–837.

Briscoe, B. J., Chateaumenois, T. C., Linley, T. C., and Parsonate, D. (1998) "Fretting wear behaviour of polymethylmethacrylate under linear motions and torsional contact conditions" *Tribology International*, vol.13, pp. 701-711.

Briscoe, B.J., Chateauminois, A., Lindley, T.C., and Parsonage, D. (2000[a]) "Contact damage of poly methylmethacrylate during complex microdisplacements" *Wear*, vol.240, pp. 27–39.

Briscoe, B.J., Chateauminois, A., and Parsonage, D. (200[b]) "Indentation behaviour of the polymer third body generated in a PMMA/steel fretting contact" *American Chemical Society, Polymer Preprints, Division of Polymer Chemistry*, vol. 41, pp. 1467-1466.

Department of trade and industry (1986) "*Wear resistant surfaces in engineering: a guide to their production, properties and selection*" London: Her Majesty's stationery office, pp. 123-141.

Engel, L., Klingele, H., Ehrenstein, G.W., and Schaper, H. (1981) "*An atlas of polymer damage*" London: Wolfe Publishing Ltd, assoc. with Carl Hanser Verlag.

Galvanetto, E., Borgioli, F., Galliano, F.P., and Bacci, T. (2006) "Improvement of wear and corrosion resistance of RPS Ti–TiN coatings by means of thermal oxidation" *Surface & Coatings Technology*, vol.200, pp. 3650– 3655.

Geringer, J., Forest, B., and Combrade, P. (2007) "Wear of poly (methyl methacrylate) against a metallic surface in dry conditions" *Polymer Engineering and Science*, vol. 47, pp. 633-648.

Herman, H., Sampath, S., and McCune, R. (2000) "Thermal Spray: Current Status and Future Trends" *MRS Bulletin*, vol. 23, pp. 17-25.

Hertzberg, R. W. and Manson, J. A. (1980) "*Fatigue of engineering plastics*" New York: Academic Press, Inc.

Holmberg, K. and Matthews, A. (1994) "Coatings tribology: properties, techniques and applications in surface engineering" *Tribology series 28*, Dowson, D., Ed., Amsterdam: Elsevier.

Hutchings, I.M. (1992) "*Tribology Friction and Wear of Engineering Materials*" London: Edwards Arnold.

Hwang, B., Lee, S., andAhn, J. (2004) "Correlation of microstructure and wear resistance of molybdenum blend coatings fabricated by atmospheric plasma spraying" *Materials Science and Engineering,* vol. A 366, pp. 152–163.

Hwang, B., Ahn, J., and Lee, S. (2005) "Effects of blending elements on wear resistance of plasma-sprayed molybdenum blend coatings used for automotive synchronizer rings"

*Surface & Coatings Technology*, vol.194, pp. 256– 264.

Ishikawa, K., Suzuki, T., Kitamura, Y., and Tobe, S. (1999) "Corrosion resistance of thermal sprayed titanium coatings in chloride solution" *Journal of Thermal Spray Technology*, vol. 8, pp. 273-278.

Khalid, S. E., Al-Malahy and Hodgkiess, T. (2003) "Comparative studies of the seawater corrosion behaviour of a range of materials" *Desalination,* vol. 158, pp. 35-42.

Kinos, T., Chen, S.L., Siitonen, P., and Kettunen, P. (1996) "Densification of plasma-sprayed titanium and tantalum coatings" *Journal of Thermal Spray Technology*, vol. 5, pp. 439-444.

Krichen, A., Kharrat, M., and Chateauminois, A. (1998) "Effects of frequency on the fretting conditions in a contact between PMMA and a rigid counterface" *Journal of Tribology*, vol. 120, pp. 736-729.

Krichen, A., Bradia, C., Chateaminois, A., and Kharrat, M. (1999) "Surface damage of poly(methymethacrylate) under fretting loading" *Wear*, vol. 230, pp.146-155.

Laribi, M., Mesrati, N., Vannes, A.B., and Treheux, D. (2003) "Adhesion and residual stresses determination of thermally sprayed molybdenum on steel" *Surface and Coatings Technology*, vol.166, pp. 206–212.

Laribi, M., Vannes, A.B., and Treheux, D. (2006) "On a determination of wear resistance and adhesion of molybdenum, Cr–Ni and Cr–Mn steel coatings thermally sprayed on a 35CrMo4 steel" *Surface & Coatings Technology*, vol. 200, pp. 2704– 2710.

Laribi, M., Vannes, A.B., and Treheux, D. (2007) "Study of mechanical behaviour of molybdenum coating using sliding wear and impact tests" *Wear,* vol. 262, pp. 1330–1336.

Liu, Z. and Hua, M. (1999) "Wear transitions and mechanisms in lubricated sliding of a molybdenum coating" *Tribology International*, vol. 32, pp. 499–506.

Matejka, D. and Benko, B. (1989) "*Plasma spraying of metallic and ceramic materials*" Czechoslovakia: John Wiley & Sons ltd., pp. 157-159.

McClintock, F.A. and Argon, A.S. (1966) "*Mechanical behaviour of materials"* Massachusetts: Addison-Wesley Publishing, Inc.

Mountford, Jr. J. A. (2002) "Titanium-Properties, Advantages and applications solving the corrosion problems in marine service" Paper 02170, *NACE International*, Houston.

Moet A. (1986) "fatigue failure" Chapter 18 in Brostow, W. and R.D. Corneliussen (ed.) *Failure of plastics*, Wuerzburg: Carl Hanser Verlag.

Prchlik, L., Sampath, S., Gutleber, J., Bancke, G., and Ruff, A.W. (2001) "Friction and wear properties of WC-Co and Mo-$Mo_2C$ based functionally graded materials" *Wear,* vol. 249, pp.1103–1115.

Rickerby, D. S., and Matthews, A. (1991) "*Advanced surface coatings: A handbook of surface engineering*" New York: Chapman and Hall, pp. 216-243.

Sakoda, N., Hida, M., Takemoto, Y., Sakakibara, A., and T. Tajiri (2003) "Influence of atomization gas on coating properties under Ti arc spraying" *Materials Science and Engineering,* vol.A342, pp.264-269.

Steijn, R. P. (1986) "Friction and wear" in *Failure of plastics*, ed. by Brostow, W. and Corneliussen R. D., Wuerzburg: Carl Hanser Verlag.

Stolarski, T. A., and Williams, H. (1996) "Mode of Loading and Contact Configuration Effects in the Wear of Polymers" *Journal of Applied Polymer Science* vol. 61, pp.1217-1222.

Stolarski, T. A., Hosseini, S. M., and Tobe, S. (1998) "Surface fatigue of polymers in rolling contact" *Wear*, vol. 214, pp. 271-278.

Stolarski, T.A. and Tobe, S. (2001) "The Effect of Spraying Distance on Wear Resistance

of Molybdenum Coatings" *Wear*, vol. 249, pp. 1096-1102.

Teng, J., and Sato, K. (2004) "In situ observation of fretting wear behaviour in PMMA/steel model" *material and design,* vol. 25, pp. 471-478.

Usmani, S. and Sampath, S. (1999) "Time-dependent friction response of plasma-sprayed molybdenum" *Wear*, vol. 225–229, pp. 1131–1140.

Uyulgan, B., Cetinel, H., Ozdemir, I., Tekmen , C., Okumus, S.C., and Celik, E. (2003) "Friction and wear properties of Mo coatings on cast-iron substrates" *Surface and Coatings Technology*, vol.174 –175, pp. 1082–1088.

Wang, H-R., Li, W-Y., Ma, L., Wang J., and Wang, Q. (2007) "Corrosion behavior of cold sprayed titanium protective coating on1Cr13 substrate in seawater" *Surface & Coatings Technology*, vol.201, pp. 5203–5206.

Ward, I.M. and Hadley, D.W. (1996) "*An introduction to mechanical properties of solid polymers*" Guildfords and King Lynn: John Wiley & Sons Ltd.

Wayne, S. F., Sampath, S., and V. Anand (1994) "Wear mechanisms in thermally sprayed Mo-based coatings" *Tribology Transactions* Vol. 37, no. 3, pp. 636-40.
Yamaguchi, Y., Tribology of plastic materials, Elsilvier science publishers B.V., 1990.

# Chapter 3 DESIGN AND MODIFICATIONS OF TEST FACILITIES

## 3.1 Introduction

Contact fatigue testing conducted in this research used ball-on-flat configuration in both static and dynamic contact fatigue tests, hence this chapter deals with the modifications and developments of the test rigs used and analyses of the contact stresses created in both fatigue tests. In addition, the effects of environment will be discussed as in static contact fatigue of PMMA a lubricant was employed and seawater was used in RCF of molybdenum and titanium plasma spray coatings.

## 3.2 Static Contact Fatigue Tests

### *3.2.1 Development of the Static Contact Fatigue Test Apparatus*

The static contact fatigue test apparatus was specially designed for this test. The schematic diagram of the test rig is shown in Figure 3.1. From the diagram, an eccentric shaft, connected to and driven by an electric motor, generates oscillatory movement of the upper slider via the loading arm. This results in cyclic compression of the spring, which, in turn, imposes cyclic loading on the ball and the test plate via lower slider. The apparatus is capable of generating a constant sinusoidal load pattern, whose frequency, amplitude and mean values can be adjusted.

The photograph of the test apparatus is shown in Figure 3.2 and detailed drawings are in Appendix A.

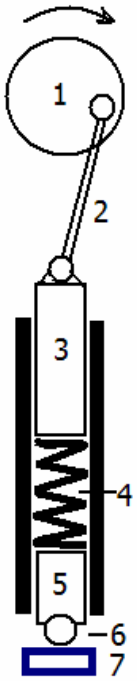


Figure 3.1 Schematic diagram of test apparatus; (1) eccentric shaft, (2) loading arm, (3) upper slider, (4) spring, (5) lower slider, (6) ball, (7) PMMA plate.

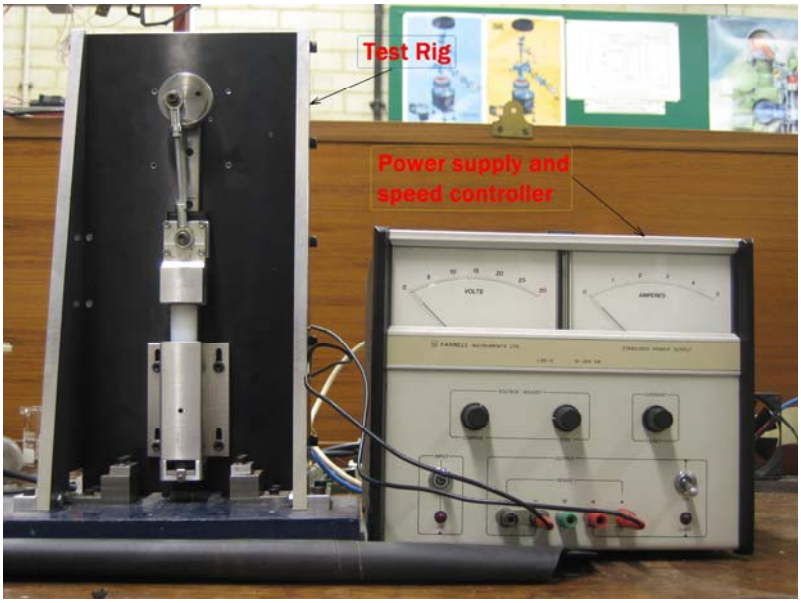


Figure 3.2 Static contact fatigue test apparatus.

### *3.2.2 Analysis of Contact Load*

The contact between spheres was firstly analysed by Hertz in 1881. In case of the contact of the spherical indenter and the half space, as seen in Figure 3.3 (a), with load *P* applied in the elastic range, the followings parameter can be calculated (Johnson, 1985 and Williams, 1994).

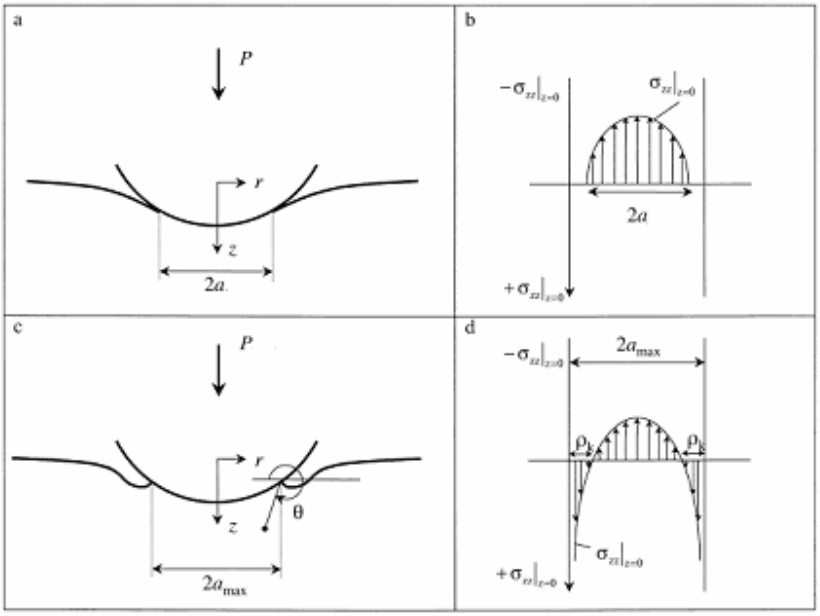


Figure 3.3 Schematic illustrating; (a) non-adhesive contacts and (b) the corresponding non-singular contact stress field; (c) adhesive contacts and (d) the corresponding stress field exhibiting tensile square-root singularity (Giannakopoulos *et al.*, 1999)

Radius of contact circle, $$a = \{\frac{3PR^*}{4E^*}\}^{1/3} \quad (3.1)$$

Maximum contact pressure, $$p_0 = \{\frac{6PE^{*2}}{\pi^3 R^{*2}}\}^{1/3} \quad (3.2)$$

Mean contact pressure, $$p_m = \frac{2}{3} \times p_0 \quad (3.3)$$

Maximum shear stress, $\tau_0 = 0.31 p_0$ at x = 0, z = 0.48$a$ (3.4)

Tensile stress $$\sigma_r = \frac{2E^* a}{\pi R^*}\left(1-(\frac{r}{a})^2\right)^{\frac{1}{2}} \quad (3.5)$$

Maximum tensile stress; $$\max \sigma_r = \frac{1}{3}(1-2\nu)p_0 \quad \text{at } r = a, \text{ and } z = 0 \quad (3.6)$$

where $$\frac{1}{E^*} = \frac{1-\nu_1^2}{E_1} + \frac{1-\nu_2^2}{E_2} \quad (3.7)$$

$$\frac{1}{R^*} = \frac{1}{R_1} + \frac{1}{R_2}. \quad (3.8)$$

The surface and subsurface stresses in graphical profiles can be presented as in Figure 3.4.

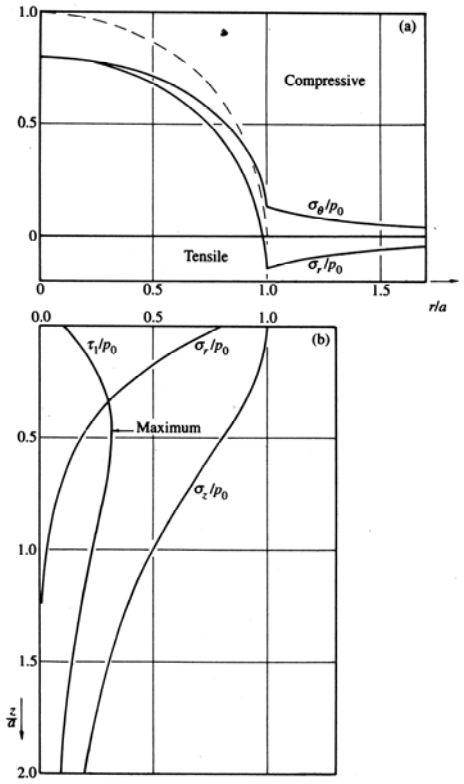


Figure 3.4 Elastic contact of spheres; (a) surface stresses Hertz pressure show in dotted line And (b) variation of the subsurface stresses along the axis of symmetry with depth (Williams, 1994).

It should be noted that the above formulae are subject to the assumptions as in (Mangipudi and Tirrell, 1998 and Stolarski and Tobe, 2000);

1. the contacted bodies are homogeneous and isotropic,
2. the surfaces of the counterfaces are topographically smooth at both macro and micro scale,
3. the contact is perfectly elastic,
4. the contact between counterfaces is frictionless and
5. the surface traction from the adhesive forces is ignored in the calculation.

However, in reality the contact often comprises of both friction and adhesion. Therefore, the Hertz's theory must be revised. The following presents the correction resulting from friction and adhesion between contacting bodies.

*3.2.2.1 The friction effect*

Herztian theory assumes that the contact shear stress is absence. However, the friction at the contact interface apparently occurs when the dissimilar materials, i.e. different elastic constant, are in contact under normal load (Stolarski and Tobe, 2000). The surfaces of the spheres with similar material under normal mutual contact pressure experience radially inward tangential displacements by the magnitude proportional to the respective values of the parameter *(1-2v)/G,* where $G$ is shear modulus. However, the case of dissimilar materials induces different displacement between their surfaces. Thus the slip could occur. The interfacial friction will resist this slip. Theoretically, the interfacial slip is prevented if the friction coefficient at the interface is sufficiently high and involves full stick of the counterfaces. However, the slip will occur all over the contact area when the coefficient of friction is extremely small. The tangential traction, $q = \pm\mu P$, will be radial. The contact generally consists of both stick and slip area which the stick is in the central area of contact surrounded by the annulus of slip area and this situation is called partial slip condition.

Two non-dimensional parameters controlled the contact behaviour including,

$$\xi = \frac{[(1-2\nu_1/G_1)]-[(1-2\nu_2/G_2)]}{[(1+\nu_1)/G_1]+[(1+\nu_2/G_2]} \tag{3.9}$$

and $\mu$.

Where $\xi$ is elasticity parameter and $\mu$ is coefficient of friction.

In practice, the influence of the frictional traction upon the compliance and the load bearing capacity of most contacting bodies is small when the value of $\xi$ (<0.4) and $\mu$ (<0.5) are reached. Under these conditions the Hertz theory can be used with a small error.

Recently, a semi-analytical approach has been used to investigate stress distribution in the contact region created by a normal load for dissimilar materials with friction between spherical indenter and flat surface (Li and Berger, 2003). The contour plot of the tangential interface traction is shown in Figure 3.5. It is indicating that the friction load is the highest at the boundary of the stick-slip region and gradually decreasing to zero at the edge of the contact. The drop of the friction load in the stick area is very fast and reaches to zero at the center of the stick area.

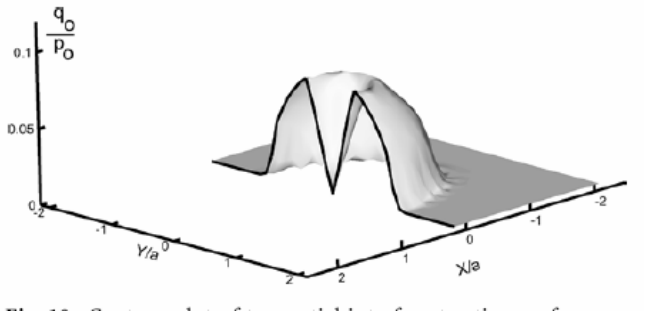


Figure 3.5 Contour plot of the tangential traction

Under the same contact load, friction brings higher contact pressure but lower contact area than the results from the Hertzian contact. However, the difference is only a few percent. The calculation results show small sensitivity of contact pressure and area to the changes in friction coefficient. They claim that the grid sizes they used are too large to resolve the small changes. The ratio between the stick radius, c and the contact radius, a increases with increasing of friction.

*3.2.2.2 The adhesion effect*

The adhesion part of contact was proposed in two important theories i.e. JKR theory (Johnson *et al*., 1971) and DMT theory (Derjaguin *et al.*, 1975). These theories were firstly in contradiction and were debated at the beginning. However, the succeeding corrected and

adjusted proposal for both theories found that they are valid in different region. Subsequently, Johnson and Greenwood (1997) have constructed the adhesion map for contact mechanics by normal load in which the regions of application are filled up with Hertz theory, Bradley, DMT theory, M-D (Maugis-Dugdale) theory, and JKR theory. Later, Giannakopoulos *et al.*, (1999) have proposed the quantitative analytical approach using contact mechanics and fracture mechanics theories for static contact and static contact fatigue conditions incorporating the adhesion. The following analysis is based on their works.

The presence of the adhesive force in contact interface should account for the work of adhesion ($w$). This work of adhesion is calculated from surface and interface surface energy as

$$w = \gamma_1 + \gamma_2 - \gamma_{12} \geq 0 \tag{3.10}$$

where $\gamma_1$ and $\gamma_2$ are surface energy of body 1 and body 2 respectively

$\gamma_{12}$ is interface surface energy.

The surface and interface surface energies are macroscopic intrinsic material properties (Mangipudi and Tirrell, 1998). The surface energy of the material is defined as the energy required to create an unit new area on the surface of a material.

The work of adhesion is a short-range force of attraction. It superimposes the external applied load across the interface of contact resulting in increased contact radius from $a$ to $a_{max}$ (see Figure 3.3).

$$a_{\max} = \left[ \frac{3R^*}{4E^*} \left( P + 3\pi R^* w + \sqrt{6\pi R^* wP + \left(3\pi R^* w\right)^2} \right) \right]^{1/3} \tag{3.11}$$

According to Hertz contact given by equation (3.1), the apparent load, $P^*_{max}$, that is necessary to achieve this contact radius, $a_{max}$, without adhesion is

$$P_{\max}^{*} = \frac{4E^{*}a_{\max}^{3}}{3R^{*}}. \tag{3.12}$$

The adhesive contact gives tensile square root singular stress field which is asymptotically equal to the mode I crack field at the contact perimeter, see Figure 3.3 (d), and is given by

$$\sigma_{rr}^{nor} = \frac{K_I}{\sqrt{2\pi\rho}}\cos\frac{\theta}{2}\left(1-\sin\frac{\theta}{2}\times\sin\frac{3\theta}{2}\right)+T_{rr}$$

$$\sigma_{zz}^{nor} = \frac{K_I}{\sqrt{2\pi\rho}}\cos\frac{\theta}{2}\left(1+\sin\frac{\theta}{2}\times\sin\frac{3\theta}{2}\right)$$

$$\sigma_{rz}^{nor} = \frac{K_I}{\sqrt{2\pi\rho}}\cos\frac{\theta}{2}\left(\sin\frac{\theta}{2}\times\cos\frac{3\theta}{2}\right)$$

$$\sigma_{\varphi\varphi}^{nor} = \nu(\sigma_{rr}^{nor} - T_{rr} + \sigma_{zz}^{nor}) + T_{\varphi\varphi} \tag{3.13}$$

$$K_I = \frac{P_{\max}^{*} - P}{2a_{\max}\sqrt{\pi a_{\max}}} \tag{3.14}$$

where $\rho$ and $\theta$ are the local polar coordinates at the contact perimeter,

$\varphi$ is the angular circumferential coordinate,

$T_{rr}$ and $T_{\varphi\varphi}$ are non-singular circumferential stress terms in radial and circumferential directions.

The size of K-dominance around the contact perimeter, $\rho_k$, as seen in Figure 3.3(d) is identified by nodal positions in the stress field and calculated by

$$\rho_k = \frac{R^{*}}{2}\sqrt{\frac{\pi w}{E^{*}a_{\max}}} \tag{3.15}$$

The maximum radial and circumferential of the non-singular stresses owing to contact at maximum load are given by

$$\max T_{rr} = -\max T_{\varphi\varphi} = \max T = \frac{(1-2\nu)P^*_{\max}}{2\pi a^2_{\max}} \qquad (3.16)$$

Consider the cycling normal contact load is applied the in the range $P_{max} > P_{min} \geq 0$. The strain energy release rate, $G$, at the contact perimeter increases accordingly as the load decreases from $P_{max}$ to $P_{min}$. It is defined that *max G* is the strain energy release rate at maximum contact load, $P_{max}$, and $G_d$ is the work of adhesion for receding contact which is generally greater than the work of adhesion for advancing contact, $w$. The stress intensity, $\Delta K_I$, is dependent on the strength of adhesion whether strong or weak.

Strong adhesion is attained when $max\ G < G_d$ or $P_{max} - P_{min} \leq 3\pi G_d R^*/2$. The $a_{max}$ in this condition is the same for the load range. The mode I cyclic stress intensity factor at the contact perimeter is computed as

$$\Delta K_I = K_{\max} - K_{\min} = \frac{P_{\max} - P_{\min}}{2a_{\max}\sqrt{\pi a_{\max}}} \qquad (3.17)$$

with the corresponding load ratio, $R = (min\ K_I/max\ K_I) = (P_{min}/P_{max})$.

Weak adhesion is obtained when $max\ G > G_d$ or $P_{max} - P_{min} \geq 3\pi G_d R^*/2$. In this condition, the work of adhesion is unsustainable for the singularity at the maximum contact radius, $a_{max}$. Accordingly, the contact perimeter is debonded and the contact radius is decreased. The mode I stress intensity factor at the contact perimeter, $a_{max}$, is computed as

$$\Delta K_I = \frac{3\pi G_d R^*}{4a_{\max}\sqrt{\pi a_{\max}}} \qquad (3.18)$$

with the correspond loading ratio, $R$, being

$$R = \frac{P_{\max} - (3\pi G_d R^* / 2)}{P_{\max}} \tag{3.19}$$

where $G_d = 14.3651\sqrt{0.3 + \mu^2}$ (N/m) which is an estimated empirical relationship.

The analysis on the contact conditions implies a ring crack front coincident with the contact perimeter, $a_{max}$, and a fatigue crack is predicted to initiate at this position when $\Delta K_I \geq \Delta K_{th}$ for both strong and weak adhesion and to propagate from this pre-existing crack. The $\Delta K_{th}$ is the mode I threshold stress intensity range for long crack initiation the corresponding values of *R* and *max T*.

## *3.3* Rolling Contact Fatigue (RCF) Tests

### *3.3.1* ***Modification of the Four-Ball Tester***

Dynamic contact fatigue test used the modified four-ball test machine. The four-ball test machine and its schematic diagram are shown in Figure 3.6 and Figure 3.7. The modified four-ball test machine consists of eleven major components. The specimen is fitted in the cup assembly wherein the driven balls, the lower balls, will roll on the specimen. The dead weight applied at the end of the loading arm is used to generate the required Hertz stress on the specimen via the loading piston. The driving ball, the upper ball, sits in the collet and is fixed to the spindle, which is rotated by the driving motor via the drive belt. The cup type ball on flat configuration is modified. The schematic diagram of the cup is shown in Figure 3.8. The drawing of the cup is shown in Appendix B.

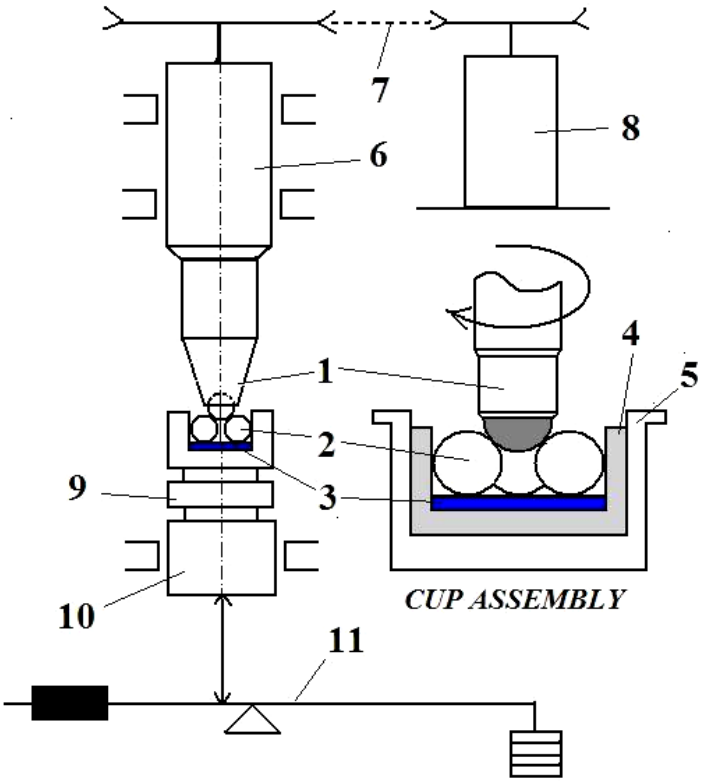


Figure 3.6 Schematic diagram of modified four ball test machine; (1) upper ball and collet, (2) lower balls, (3) coated specimen, (4) cup, (5) housing, (6) spindle, (7) belt drive, (8) motor, (9) heater plate, (10) loading piston, (11) loading lever.

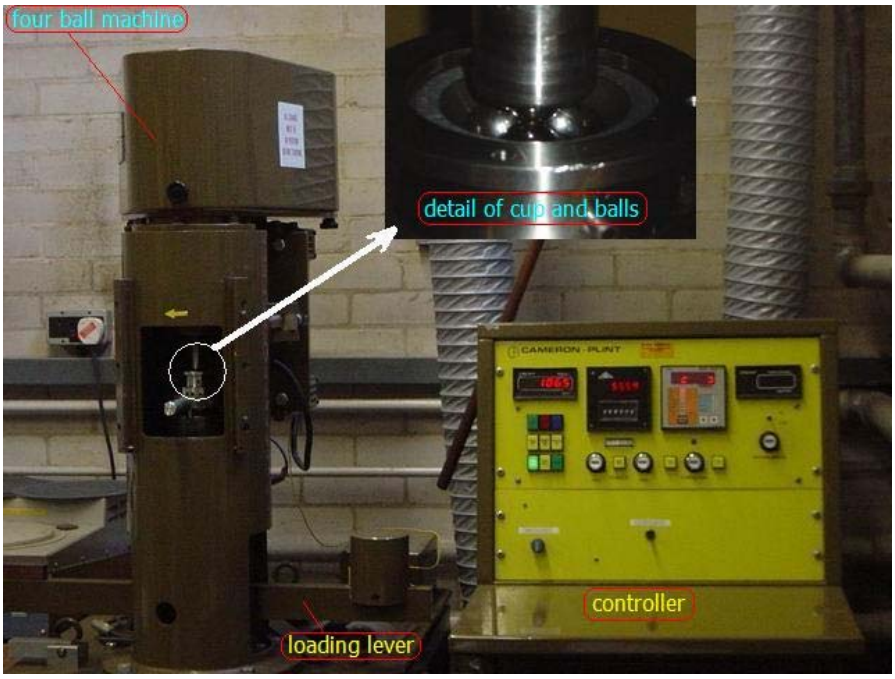


Figure 3.7 Four ball machine picture.

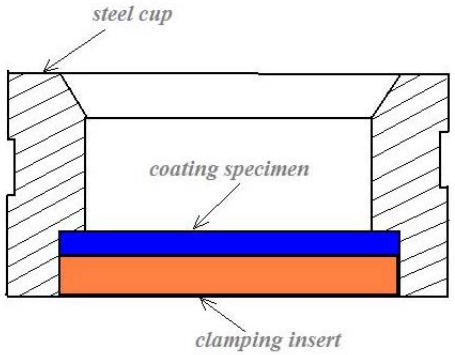


Figure 3.8 Schematic diagram of the cup.

### *3.3.2 Analytical Contact Load and Kinematics of the Balls*

The stress on the specimen can be calculated from the load applied by the upper ball using a simple trigonometric analysis. Also, the kinematics of the balls and velocity relationships of the ball have been well demonstrated by Krüger and Bartz (1977). Using the schematic illustration in Figure 3.9 together with the cup and the balls geometries in Figure 3.10, the angles, θ and β can be calculated by

$$\theta = \sin^{-1}\left(\frac{R_{cup} - R_{ball}}{2R_{ball}}\right) \tag{3.20a}$$

$$\beta = \tan^{-1}\left(\frac{R_{cup} - R_{ball}}{R_{cup}}\right) \tag{3.20b}$$

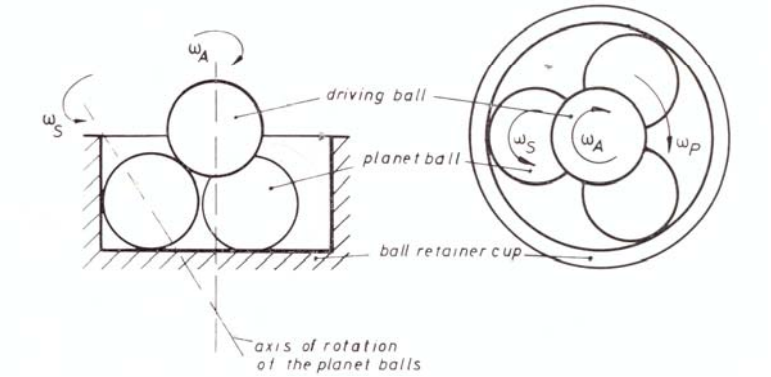


Figure 3.9 Schematic illustration of the cup and angular velocities of the balls (Krüger and Bartz, 1977).

When a mass $M$ in [kg] is applied to the loading arm, there will be the load $P_1$ on the driving ball. Therefore, the applied load $P$ on each driven ball is given as

$$P = \frac{P_1}{3\cos\theta}. \tag{3.21}$$

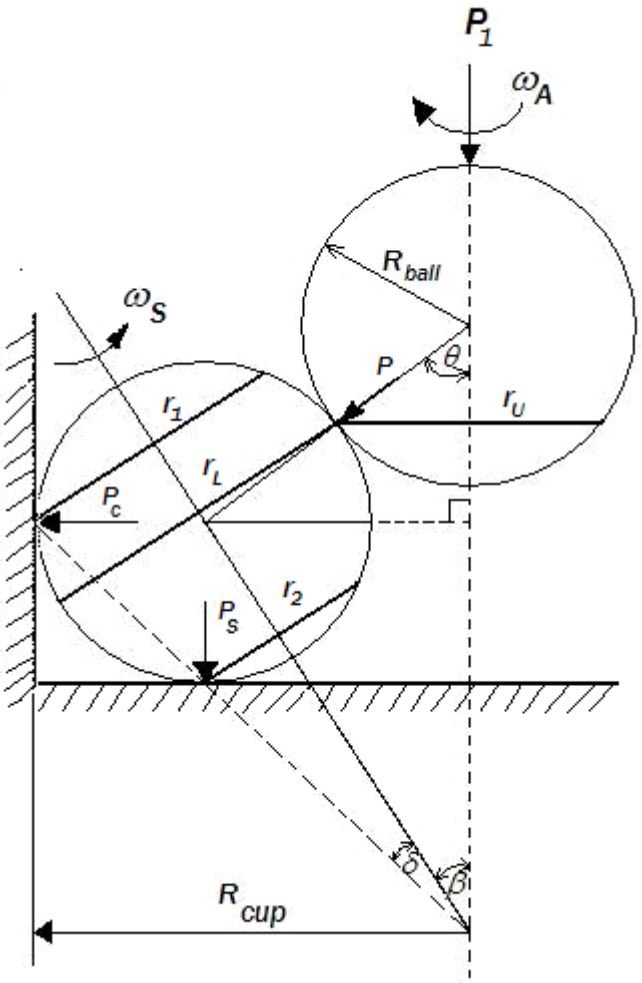


Figure 3.10 Geometric relationships of the rolling four-ball machine.

It should be not that the magnitude of the load $P_1$ is equal to $20\times9.81\times M$ because the lever arm ratio is equal to 1:20. As seen in Figure 3.10, the force acting on the plate can be calculated using simple trigonometric sine law

$$\frac{P}{\sin 90^{\circ}} = \frac{P_s}{\sin(90^{\circ} - \theta)} = \frac{P_c}{\sin\theta} \tag{3.22}$$

where $P_s$ is the pressure on the plate

$P_c$ is the pressure on the wall of the cup.

Substitute $P$ from equation (3.21) into equation (3.22) gives

$$P_s = \frac{P_1 \sin(90^{\circ} - \theta)}{3\cos\theta} = \frac{P_1}{3}. \tag{3.23}$$

It should be noted that $P_s$ is independence of cup diameter.

From equation (3.23) it can be calculated the contact stress, the area of contact and others parameters by using the equations (3.1) to (3.8).

The kinetic of the balls and the velocity relationships are predetermined by the radii of the driving, the driven balls and the cup. The ratio of the angular velocity of the upper ball, $\omega_A$, and $\omega_P$ of the lower ball may be expressed by

$$\frac{\omega_A}{\omega_P} = 1 + \frac{R_{cup}}{R_{ball}}\left(1 + \frac{\tan\beta}{\tan\theta}\right) \tag{3.24}$$

If z is the number of the driven balls, then the stress cycles factor $L$ on the sample equal to

$$L = z \times \left[1 + \frac{R_{cup}}{R_{ball}}\left(1 + \frac{\tan\beta}{\tan\theta}\right)\right]^{-1} \tag{3.25}$$

Therefore, the load cycle on the plate in each revolution of the driving ball equal to $\omega_A L$.

### *3.3.3 Friction in rolling contact*

Friction in rolling contact is greatly lower than that in sliding contact, but it has a finite value. Rolling friction is a complicate physical phenomena and difficult to present in analytical term (Stolarski and Tobe, 2000 and Williams, 1994). Many factors contribute to the friction in rolling contact including plastic work of deformation, micro-slip, Heatcote slip, adhesion, hysteresis loss and the energy loss within viscous lubricant film in lubricated condition.

The plastic work of deformation is a major part of rolling friction in soft material such as lead, but it is insignificant in bearing steel.

Microslip arises from different elastic deformation in contact region. When local tangential stress which develops at the interface between the ball and the substrate exceeds some value local slip will occur. The external energy of motion is converted into heat. It may contribute to a major part of total rolling resistance.

Heatcote slip proposed by Heatcote in 1921 is another mechanism contributed to the rolling resistance of a sphere rolling in a groove or conformal geometry of the rolling components. Within the contact zone will have two lines along which there is zero surface slip. However, on the either side of them exist regions in which the relative sliding between sphere and the track is in opposite directions. Accordingly, the rolling friction can be significant.

Adhesion can be taking place during rolling. However, the interfacial adhesion at the trailing edge is peeled apart which is easier than shearing in sliding. Only small part of the total energy is spent to overcome interfacial adhesion during rolling. Therefore, lubrication has insignificant influence on the total rolling friction although adhesion is reduced.

Hysteresis loss, alternating name as internal friction, occurs during rolling when alternating stress is stored as elastic store energy and then releases. This phenomenon is not in adiabatic such that the internal friction has some part convert to heat. However, rolling resistance due to internal friction is very small in case steel ball rolling on steel because the coefficient of internal friction is in the range of $\mu < 10^{-5}$.

Finally, an energy loss within the viscous lubricant film is taken a part under elasto-hydrodynamic lubrication.

## 3.6 Effect of Environment on Surface Damage

Effect of environment on damage of the specimen surface under static and dynamic fatigue was tested using mineral oil and seawater respectively. The environment may either enhance or degrade the resistant to contact fatigue of the materials.

### *3.6.1 Effect of Lubricant on PMMA Static Contact Fatigue*

PMMA is resistant to petroleum, fats, and oils (Engel *et al.*, 1981). However, it was reported that oil affects the fracture toughness of PMMA and the onset of cracking under monotonically increasing displacement in tension test at 23 to 25 ºC (Mai, 1975). The fracture toughness values increase from 0.38 $kJm^{-2}$ in air to 0.54 $kJm^{-2}$ in lubricating oil. Presoaking PMMA in lubrication oil for 2 weeks before testing showed no significant effect on the material fracture toughness.

The effect of oil lubrication on RCF has not been much published. Stolarski *et al.*, (1998) reported that type of lubrication affected on the RCF life of PMMA. The mineral base oil resulted caused longer fatigue life than that caused by a brake fluid, which induced network of cracks on the PMMA surface.

### *3.6.2 Effect of Seawater on Molybdenum and Titanium Rolling Contact Fatigue*

There are no reports on the effect of seawater on RCF of molybdenum and titanium either bulk or coatings in seawater although titanium was found to be used for a journal bearing operating in seawater. The effect of seawater on static contact fatigue such as fretting is also limited.

Titanium is used in journal bearing with HDPE in seawater (Lagally, 1973). The HDPE is claimed to be acting as a lubricant together with seawater.

Fretting of 0.64% C high tensile steel against an austenitic stainless steel in artificial seawater showed that an additional electrochemical corrosion process contributed in addition to mechanical and oxidation processes (Pearson, 1985). Seawater induced corrosion process resulted in high wear rates although it performed as a lubricant in the early stages of fretting. As the test was prolonged the coefficient of friction increased due to the corrosion debris accumulation in the contact area. This seems to contrast with the fretting test results of bearing steel (SUJ-2) conducted in natural seawater by Sato *et al.*, (1986). They reported that corrosion products behaved as lubricant especially at large amplitudes resulting in decreasing the fretting damage.

Only ceramic materials were reported for application as rolling elements in the seawater. The silicon carbide (SiC) rolling element bearings were used in the centrifugal injection seawater pump with relatively short life time (Katz, 1994). However, full ceramic bearings have been successfully applied in tidal seawater flow meter.

### 3.7 Discussion

The static fatigue test rig, developed in this research, is suitable for testing the plastic materials as it can produce a low load range. The rig can vary frequency, load amplitude and mean stress. The dynamic fatigue testing was carried out in the modified four-ball machine. The cup to accommodate coated test specimens was modified in order to make it suitable for testing the flat specimen.

The stresses analysis for both static and dynamic conditions and the ball on flat configuration is present. In static contact conditions, friction and adhesion affects on the stresses in the contact area have been considered and proposed formulas may be used for predicting the damage. In dynamic contact conditions, the magnitude of the load acting on the test plate is found in relation to the cup diameter. The friction in the rolling contact is discussed. The friction mechanisms are generally complex, but friction force small in magnitude.

Review of the effect of a lubricant on the static contact fatigue of PMMA and the seawater on the dynamic contact fatigue of molybdenum and titanium has been carried out, however, no substantial publications had been found. Therefore, RCF tests in seawater were

conducted. It was anticipated that an elastohydrodynamic lubrication would be a dominant factor so its mechanism is presented in Appendix C.

## 4 References

Derjaguin, B. V., Muller, V. M. and Toporov, Y. P. (1975) "Effect of contact deformations on the adhesion of particles" *J. Colloid Interface Sci.*, vol. 67, pp. 378-326.

Engel, L., Klingele, H., Ehrenstein, G.W., and Schaper, H. (1981) "*An atlas of polymer damage*" London: Wolfe Publishing Ltd, assoc. with Carl Hanser Verlag, pp. 250.

Giannakopoulos, A. E., Venkatesh, T. A. Lindley, T. C. and Suresh, S. (1999) "The role of adhesion in contact fatigue" *Acta mater.*, vol. 47, pp. 4653-4664.

Johnson, KL. (1985) "*Contact Mechanics*" Cambridge: Cambridge University Press, pp. 84- 93.

Johnson, K. L., Kendall, K., and Roberts, A. D. (1971) "Surface energy and the contact of elastic solids" *Proc. R. Soc. Lond.*, vol. A. 324, pp. 301-313.

Johnson K.L., and Greenwood, J. A. (1997) "An adhesion map for the contact of elastic spheres" *J. colloid Interface Sci.*, vol. 192, pp. 326-333.

Katz, R. N. (1994) "Ceramic materials for rolling element bearing applications" in *Friction and wear of ceramics* ed. by Jahanmir, S., New York: Marcel Dekker, Inc., pp. 326.

Krüger, V and Bartz, W. J. (1977) " Comparison of different ball fatigue test machines and significance of test results to gear lubrication" in *Rolling contact fatigue performance testing of lubricants* ed. by Tourret, R. and E. P. Wright, London: Hyden & Son Ltd., pp. 137-159.

Lagally, P (1973) "Low friction bearing- journal arrangement" *United States Patent no. 3,724,919*.

Li, J. and Berger, E. J. (2003) "A semi-analytical approach to three-dimensional normal contact problems with friction" *Computational Mechanics*, vol. 30, pp. 310-322.

Mangipudi, V. S. and Tirrell, M. (1998) "Contact-mechanics-based studies of adhesion between polymers" *Rubber Chemistry and Technology*, vol. 71, pp. 1998.

Mai, Y. W. (1975) "On the environmental fracture of polymethyl methacrylate" *J. Mater. Sci.*, vol.10, pp.943-954.

Pearson, B. R., Brook, P. A., and Waterhouse, R. B. (1985) "Fretting in aqueous media, particularly of roping steels in seawater" *Wear*, vol. 106, pp. 225-260.

Sato, J., Shima, M. and Takeuchi, M. (1986) "Fretting wear in seawater" *Wear*, vol. 110, pp. 227-238.

Stolarski, T.A., Hosseini, S.M., and Tobe, S. (1998) "Surface fatigue of polymers in rolling contact" *Wear*, vol. 214, pp. 271-278.

Stolarski, T.A. and Tobe, S. (2000) "*Rolling contact*" London: Professional Engineering Publishing Limited.

Williams, J. A. (1994) "*Engineering tribology*" Avon: Oxford University Press.

# Chapter 4 EXPERIMENTAL TECHNIQUES

## 4.1 Introduction

This chapter deals with a brief discussion of experimental techniques used for investigating damage processes of brittle plastic under static contact fatigue and metallic plasma spray coatings under dynamic rolling contact fatigue. The techniques include hardness measurements, surface profile and roughness measurements, friction tests, optical microscope examinations, scanning electron microscope investigations, and energy dispersive X-ray studies.

## 4.2 Materials under Investigations

### *4.2.1 Material for static contact fatigue*

The PMMA sheet with thickness of 5 mm was used for studying the static contact fatigue. The material properties are shown in Table 4.1.

Table 4.1 Physical and Mechanical properties of PMMA plate.

| | |
|---|---|
| Tensile strength (MPa) | 80 |
| Thermal Conductivity (W/m°C) | 0.19 |
| Thermal Expansion (1/°C) | $70 \times 10^{-6}$ |
| Yield (MPa) | 70 |
| Young's Modules (GPa) | 3.3 |
| Poisson's ratio | 0.37 |
| Impact strength (kJ $m^{-2}$) | 12 |
| Notched impact strength (kJ $m^{-2}$) | 2 |
| Density (g $cm^{-3}$) | 1.18 |

Spheres with diameter of 12.7 mm chosen as counterfaces for these experiments were made of five different materials including silicon nitride, steel, aluminium, bronze and PMMA. The properties of these balls are shown in Table 4.2.

Table 4.2 Material properties of PMMA plate and the ball using for the experiments.

| **Materials** | **Young's Modulus (GPa)** | **Poisson's ratio** | **Tensile strength (MPa)** |
|---|---|---|---|
| Silicon nitride ball | 315.0 | 0.27 | 524 |
| Steel ball | 207.0 | 0.30 | > 2145 |
| Aluminium ball | 70.6 | 0.34 | 93 |
| Bronze ball | 105.0 | 0.35 | 265 |
| PMMA ball | 2.95 | 0.30 | 75 |

Root mean square surface roughness ($R_q$) of the PMMA plate and the balls was measured. The average roughness values from five measurements are shown in Table 4.3.

Table 4.3 Roughness of the PMMA plate and the balls.

| **Ball Material** | **PMMA Plate** | **Silicon Nitride** | **Steel** | **Bronze** | **Aluminium** | **PMMA Ball** |
|---|---|---|---|---|---|---|
| $R_q$ (μm) | 0.004 | 0.196 | 0.190 | 0.241 | 0.223 | 0.041 |

The lubricant used in this experiment was the base mineral oil without additives, Talpa 20. The specification of the oil is shown in Table 4.4.

Table 4.4 Physical and mechanical properties of Talpa 20.

| Talpa 20 | specific gravity at 15 ºC | Flash point (ºC) | Pour point (ºC) | Kinetic viscosity at 40 ºC (c.s.) |
|---|---|---|---|---|
| | 0.889 | 216 | -33 | 94.6 |

### *4.2.2 Materials for dynamic contact fatigue*

The coating specimens were prepared from carbon steel discs with diameter and thickness 30 mm × 4 mm. The specimens were coated by two types of materials, namely pure molybdenum and pure titanium using powder plasma spray techniques. The spray parameters are shown in Table 4.5.

Table 4.5 Plasma spray coating parameters.

| **Coating conditions** | **Mo** | | **Ti** | |
|---|---|---|---|---|
| Torch type | SG-100 | | SG-100 | |
| Coating powder | 99.5% pure Mo | | Ti | |
| Coating thickness [μm] | 200-250 | | 200-250 | |
| | Pre-heating | Spray deposit | Pre-heating | Spray deposit |
| Sprayed distance [mm] | 100 | 100 | 100 | 100 |
| Current [A] | 500 | 800 | 700 | 800 |
| Voltage [V] | 29 | 29.6 | 36 | 36.4 |
| Arc gas | Ar | Ar | Ar | Ar |
| Gas flow [psi] | 50 | 50 | 50 | 50 |
| Auxiliary gas | - | - | He | He |
| Auxiliary gas flow [psi] | - | - | 100 | 100 |
| Torch pitchy [mm/pitch] | 4 | 4 | 4 | 4 |

Young's modulus of the coating measured by bending test for molybdenum coating and titanium coating are 235 GPa and 35-40 GPa, respectively. Surface roughness of the coating discs was measured. The average root mean square surface roughness ($R_q$) of molybdenum coating and titanium coating are 6.82 μm and 6.72 μm respectively.

The driving ball and the driven balls were made of silicon nitride and bearing steel respectively. The specifications of the balls are the same as those used in static contact fatigue tests.

The International Association for the Physical Sciences of the Ocean (IAPSO) standard seawater from Ocean Scientific International Ltd. (OSIL) was used in these experiments. The seawater has conductivity ratio ($K_{15}$) = 0.99979 and salinity = 34.992.

In order to estimate an elastohydrodynamic film parameter (λ) the viscosity and the pressure-viscosity coefficient (α) must be known. From a survey of existing data the dynamic viscosity of seawater at 20 ºC is $1.08\times10^{-3}$ $Nsm^{-2}$ and the pressure coefficient of seawater is $4.6\times10^{-10}$ $m^2N^{-1}$ (see reference).

## 4.3 Specimens Preparation

### *4.3.1 Specimen preparation for static contact fatigue*

Two sides of PMMA plate were covered with a plastic foil. The plate was cut into rectangular shape with the width and length 10 mm × 25 mm. Two through holes at each end of the specimen's length were drilled. The plastic foil was torn away form the specimen before fixing the specimen in the base of the test rig. The specimen was fixed with screws. The experiment was conducted with as supplied PMMA surface finish. The photograph of the specimens is shown in Figure 4.1.

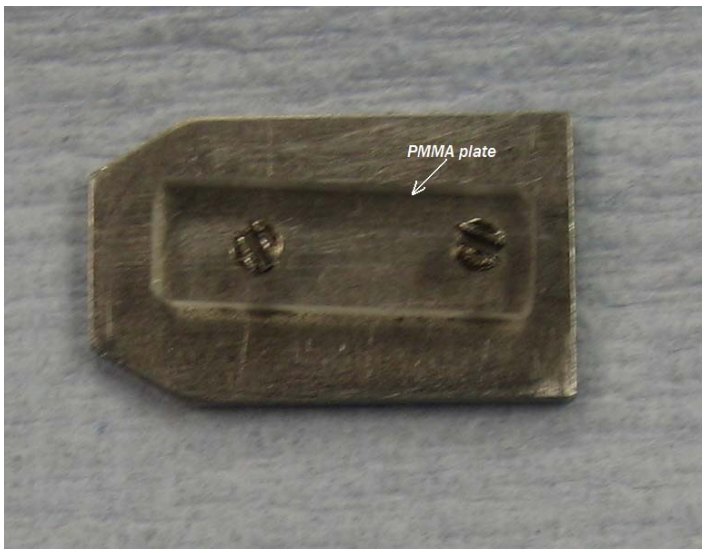


Figure 4.1 PMMA specimens and the balls.

Prior to test, the PMMA ball was cleaned with soap and was rinsed with distilled water. The steel ball, silicon nitride ball, aluminium ball and bronze ball were cleaned by a general purpose solvent in ultrasonic cleaner for 5 minute. All cleaned balls were then dried by warm air. The balls were cooled and were stored in the desiccators before the experiment was conducted.

The PMMA specimens tested in dry conditions were not cleaned after the test. However, specimens tested in oil lubricated conditions were cleaned with soap to eliminate lubricant from the surface following by rinsing with distilled water and then were dried by warm air prior to any post-test examinations. These were done to attain actual damaged surface information and to improve image quality. In addition, gold sputtering was carried out on surface of non-conductive materials including PMMA plate, PMMA ball and silicon nitride ball prior to taking them to the SEM microscope. This requirement was for increasing electrical conductivity, preventing too high brightness, and avoiding bad quality of image due to charging of specimen.

Friction between each contact pairs was measured. The specimen preparation procedures were the same as the static contact fatigue test.

### *4.3.2 Specimen preparation for dynamic contact fatigue*

The coating disc, the ball and the cup assembly were cleaned with general purpose solvent in ultrasonic cleaner for 10 minutes and were dried with warm air. All components were cooled and stored in the desiccators prior to test.

After the test, the ball and the coating disc in both dry and seawater contact conditions were cleaned prior to taking for further investigation. In dry contact conditions, the balls and the disc were cleaned by the general purpose solvent in ultrasonic cleaner for 10 minutes and were dried with warm air. In seawater conditions, the specimens were cleaned in running water followed by distilled water and then they were dried with warm air. The final cleaning step was the same as for dry conditions. Gold sputtering was unnecessary for the coated discs and the steel balls used in dynamic contact fatigue.

## 4.4 Test conditions

### *4.4.1 Static contact fatigue test*

All experiments, under both dry and oil lubricated conditions, were conducted at laboratory normal temperature 20 ± 3 °C and relative humidity (RH) 38-50%. Cyclic load applied to the contact had mean value of 80 N and amplitude equal to 40 N. The same load conditions were used for all combinations of materials in both dry and oil lubricated conditions. The frequency of cyclic loading was 10 Hz. Figure 4.2 shows corresponding nominal maximum contact stress, calculated according to Hertz's equation for point contact, for the combination of materials in contact used.

For each combination of materials two identical tests were carried out to check repetitiveness of results. A third test was conducted if the two previous tests produced significantly different results. The test was interrupted at regular predetermined time intervals, i.e.: 5, 15, 30, 60, 180 and 810 minutes.

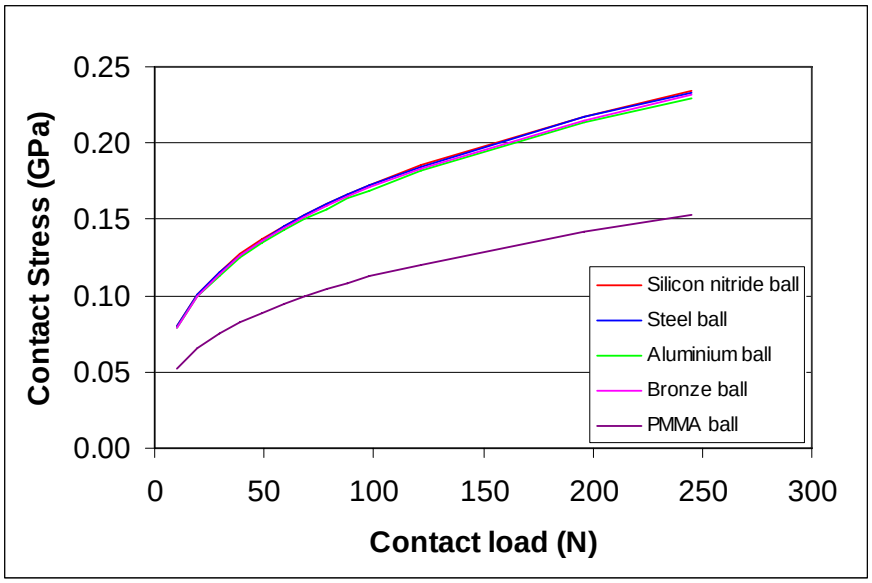


Figure 4.2 Show contact stress graph.

To evaluate the damage process and the effect of oil lubrication on static contact fatigue the following parameters were monitored:

(1) Appearance of specimen surface and wear debris.

(2) Surface profile and surface roughness.

(3) Radius of contact measurement.

### *4.4.2 Dynamic contact fatigue test*

The dynamic rolling contact fatigue experiments were conducted under dry and seawater contact conditions. The test program is shown in Table 4.6. The speed was set at 300 rpm for all the experiments. All tests were conducted in ambient environment with temperature range 20 ± 3 °C and RH 38-50%. In dry conditions, testing of molybdenum coating was conducted first with the dead weight of 0.5, 1 and 1.5 kilograms, which were corresponding to maximum contact stress of 1.32, 1.67 and 1.91 GPa respectively. The relationships between contact stress and the contact load are shown in Figure 4.3. For titanium coating, the test weight was selected at 1 kilogram, which corresponded to maximum contact stress 0.74 GPa. In seawater conditions, the tests of both molybdenum coating and titanium coating were conducted with weight of 1 kilogram. For seawater contact conditions, the magnitudes of the film parameter (λ) used in this condition for molybdenum coating and titanium coating were $3.0\times10^{-5}$ and $3.5\times10^{-5}$ respectively. Both cases indicated boundary lubrication regime. The details of calculation are shown in Appendix C.

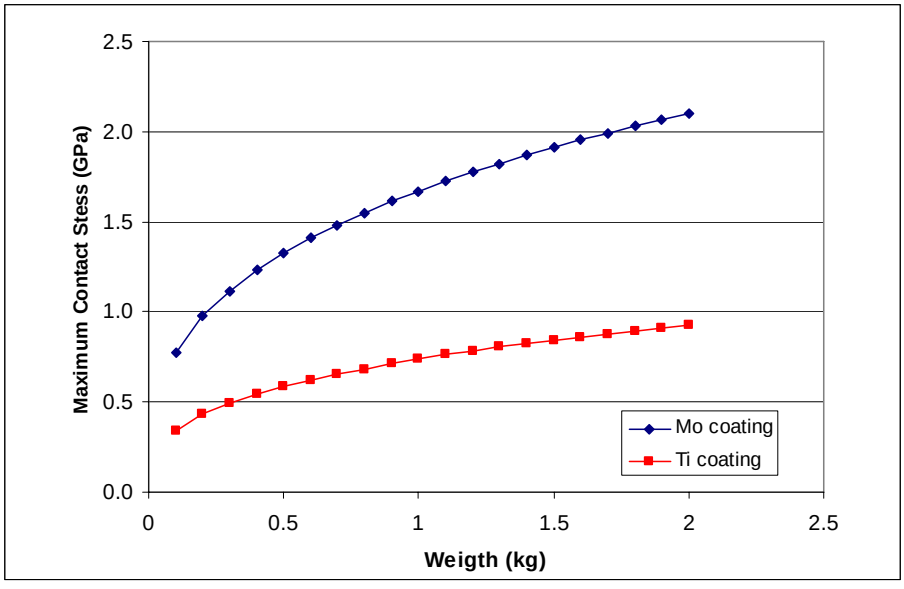


Figure 4.3 Relationships between maximum contact stress of molybdenum and titanium coatings versus weight.

To evaluate the damage process and the effect of seawater on RCF the following parameters were monitors;

(1) weight loss,

(2) contact width,

(3) surface profile and surface roughness,

(4) appearance of specimen surface and wear debris.

Table 4.6 Program of dynamic rolling contact fatigue experiments.

| **Test conditions** | **Coating materials** | **Load (Kg)** | **Test cycles** | | | | | | | | | | | | |
|---|---|---|---|---|---|---|---|---|---|---|---|---|---|---|---|
| | | | **3,118** | **6,237** | **12,474** | **18,711** | **24,948** | **37,422** | **46,777** | **56,132** | **74,843** | **149,686** | **299,373** | **399,164** | **532,903** |
| Dry conditions | Mo | 0.5 | - | - | - | - | - | Yes | - | - | Yes | Yes | Yes | - | - |
| | Mo | 1.0 | - | - | | Yes | - | Yes | Yes | Yes | Yes | - | - | - | - |
| | Mo | 1.5 | Yes | Yes | Yes | Yes | Yes | Yes | - | - | - | - | - | - | - |
| | Ti | 1.0 | - | - | - | Yes | - | Yes | Yes | Yes | Yes | - | - | - | - |
| Seawater conditions | Mo | 1.0 | - | - | - | Yes | - | Yes | Yes | Yes | Yes | Yes | Yes | Yes | Yes |
| | Ti | 1.0 | - | - | - | Yes | - | Yes | Yes | Yes | Yes | Yes | Yes | Yes | Yes |

### 4.5 Hardness Measurements

Hardness measurements for all kinds of materials in this research were conducted using Vicker's microhardness tester. Surface hardness was measured on the PMMA plate. The balls were prepared for the hardness measurements by embedding in resin and grinding and polishing. Hardness was measured along the sections.

The hardness of coatings was measured on sections. Prior to hardness measurements, the discs were sectioned, ground and polished. The results of microhardness measurements were averaged after neglecting the maximum and minimum values.

### 4.6 Surface Profile and Surface Roughness Measurements

Surface profile of the contact area of the PMMA was obtained using Talysurf equipment. For static contact fatigue, surface profiles across the contact area of PMMA plate were generated.

### 4.7 Friction Test

Friction between the PMMA plate and various ball materials was measured. The test was conducted by using the reciprocal test machine. Each test was used sliding speed 0.06 m/s at room temperature 20 ± 2 ºC, RH 32 ± 5 %. Test duration was selected for five minutes, except PMMA/PMMA combination 2 minutes. The increasing load on the contact was applied in stepwise manner from the light load to the same load range which was used in the static contact test. The friction values recorded were then averaged.

### 4.8 Microscopic Examinations of Surface and Wear Debris

The specimens were photographed before and after the test to obtain the overview information. Afterwards, the specimens were taken to further detailed microscope examinations. The stereo microscope, the optical microscope, the scanning electron microscope were employed in this examination stage.

### *4.8.1 Stereo Microscope and Optical Microscope Investigation*

#### *4.8.1.1 Static contact fatigue*

Surface within the contact area of the ball and PMMA plate was examined after the static contact fatigue test and friction measurements. In addition, cross-sections of the PMMA plate after friction measurement were investigated.

#### *4.8.1.2 Dynamic contact fatigue*

Both the driven balls and the coating disc were examined after the dynamic contact fatigue test. The examination was focused on the wear track of the disc as well as on the driven ball surface.

### *4.8.2 SEM Investigation*

Surfaces of contact pair, both static contact fatigue and dynamic contact fatigue, were examined under the scanning electron microscope (SEM). Two microscopes including ZEISS SUPRA 35VP and Joel 840A were used. The SEM gives higher resolution and higher depth of focus than optical microscope. Hence, the details of surface damage can be clearly seen. The image can be taken in a secondary electron image (SEI) or back scattered electron image (BEI), which gives different types of information.

### *4.8.3 Chemical Analysis*

Chemical analysis was carried out on tested surface using the Energy dispersive X-ray (EDX), which was connected to ZEISS SUPRA 35VP microscope and Joel 840 microscope in order to find out elements in the damaged zone. For static contact fatigue experiments, the analysis was performed especially at the slip region of PMMA plate. Elements mapping on the damaged surface of PMMA plates was carried out to find the material transferred on the surface. For dynamic contact fatigue test, the analysis was conducted on both the ball surface and the disc surface.

**References:**

http://www.maropolymeronline.com/Properties/PMMA.asp#Tensile%20Strength%20at%20Break

www.oceanteacher.org/.../index.php?module=contextview&action=contextdownload&id=gen11Srv32Nme37_44

http://www2.ocean.washington.edu/oc540/lec01-34/, 230108.
*Oceanography 540--Marine Geological Processes--Winter Quarter 2001*

# Chapter 5 EXPERIMENTAL RESULTS AND ANALYSIS

## 5.1 Introduction

This chapter is divided into two parts. The first part deals with the static contact fatigue results of PMMA. The second part deals with dynamic contact fatigue of molybdenum and titanium plasma spray coatings.

## 5.2 PMMA Static Point Contact Fatigue

### *5.2.1 Introduction*

This section involves the results of static contact fatigue of PMMA. Results include microhardness test, friction test, long-section examinations of sliding contact path, surface observations, EDX analysis, surface profile measurements and contact radius measurements under dry and oil-lubricated conditions.

### *5.2.2 Micro-hardness Measurements*

The results of micro-hardness measurement are presented in Table 5.1. The ranking of hardness values from the highest to the lowest is as follows; $Si_3N_4$ ball, steel ball, bronze ball, aluminium ball, PMMA plate and PMMA ball respectively. The hardness ratios between the ball and the PMMA plate for the case of $Si_3N_4$ ball, steel ball, bronze ball, aluminium ball, and PMMA ball are 62.4, 32.4, 4, 8.14 and 0.87, respectively. Every ball, except PMMA ball, has hardness values greater than PMMA plate.

Table 5.1 Hardness values of the balls and the plate.

| | $Si_3N_4$ ball | Steel ball | Aluminium ball | Bronze ball | PMMA ball | PMMA plate |
|---|---|---|---|---|---|---|
| HV (MPa) | 1404 | 729 | 90 | 183 | 19.5 | 22.5 |

note: All materials except PMMA hardness values was using load 1 kg. For PMMA, load was 100 g.

### *5.2.3 Friction Test*

The graphical results of friction measurements between PMMA plate and five different contact counterparts are shown in Figure 5.1. The results show that coefficient of friction in dry conditions was much higher than that in oil-lubricated conditions.

The friction coefficient value varied with normal load. Coefficient of friction value in dry conditions has a decreasing tendency with increasing normal contact load. By contrast, the coefficient of friction value under lubricated conditions has an increasing trend with increasing normal contact load.

In dry conditions, coefficient of friction for the $Si_3N_4$/PMMA pair was found to be the highest while for the PMMA/PMMA pair the friction coefficient was the lowest and that is true for the entire load range used. For example, at the contact load of 29.43 N, the ranking of materials in frictional contact with PMMA plate from the highest to lowest value of the friction coefficient is as follows: silicon nitride, bronze, steel, aluminium, and PMMA respectively, but at the contact load of 88.29 N the order is: silicon nitride, steel, aluminium, bronze and PMMA respectively.

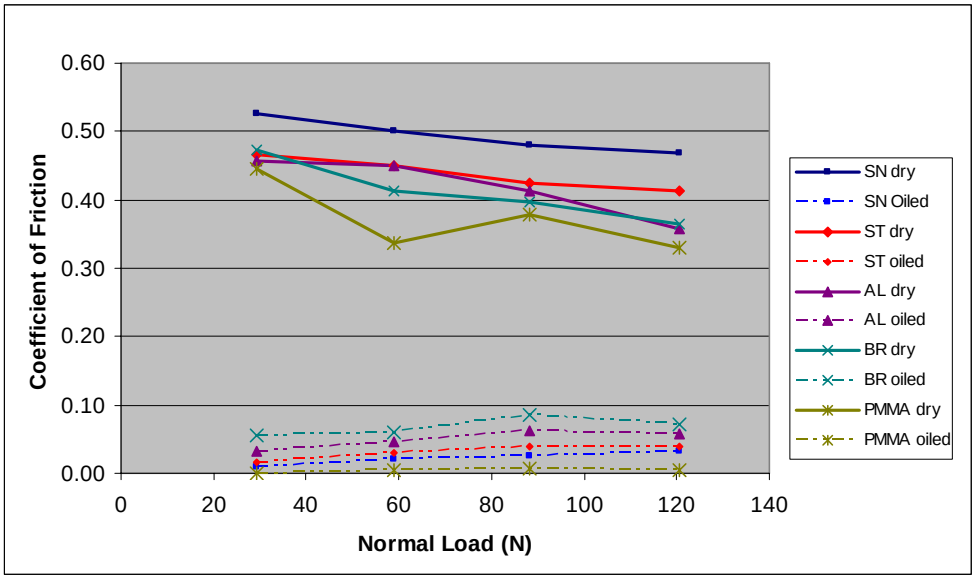


Figure 5.1 Coefficient of friction for combination of PMMA plate in contact with various ball materials in dry and oil-lubricated conditions.

In lubricated conditions, coefficient of friction between PMMA plate and the ball ranking from the highest to the lowest values is as follows: bronze, aluminium, steel, silicon nitride and PMMA respectively. This order is true for the entire load range used.

### *5.2.4 Surface and Cross-section Observations of Sliding Friction*

This section presents the results of surface and sectioned observation of PMMA plate after sliding friction test using optical microscope. In dry conditions, all specimens tested at normal load of 120.66 N were longitudinally sectioned at the middle of the contact track to examine characteristics of damage. The specimens tested in oil-lubricated conditions were not sectioned because cracks were not observed from surface observations.

#### *5.2.4.1 Dry condition*

##### 5.2.4.1.1 $Si_3N_4$/PMMA combination

Transverse cracks were found along the track surface of PMMA plate at the normal load of 29.43 N (see Figure 5.2a). Smearing of material was observed. The severity of damage increased with increasing normal load (see Figure 5.2b). Section view is shown in Figure 5.2c. Cracks orientation to the surface is mostly at the right angle.

##### 5.2.4.1.2 Steel/PMMA combination

Transverse cracks to the sliding direction appeared along the track surface at normal load of 29.43 N (see Figure 5.3a). Wear profoundly increased at normal load of 120.66 N (see Figure 5.3b). Longitudinal section shows cracks, which appear to be at slightly different angles to the surface than those resulting from testing against $Si_4N_4$ ball (see Figure 5.3c).

##### 5.2.4.1.3 Aluminium/PMMA combination

Figure 5.4a and 5.4b show wear track surfaces of PMMA plate tested against aluminium ball with normal load 29.43 and 120.66 N, respectively. Transverse cracks to the sliding direction along the track appeared at normal load 29.43 N. The density of crack was lower than that resulting from testing against $Si_3N_4$ and steel balls. Smearing of material was

observed. At 120.66 N normal load, spacing between major cracks was larger than that for specimens tested against $Si_3N_4$ and steel balls. The profile of the cracks seems to follow the contact periphery. Cross-section view shows cracks inclined to the surface (see Figure 5.4c). The depth of cracks was shallower than that resulting from testing against $Si_3N_4$ and steel balls.

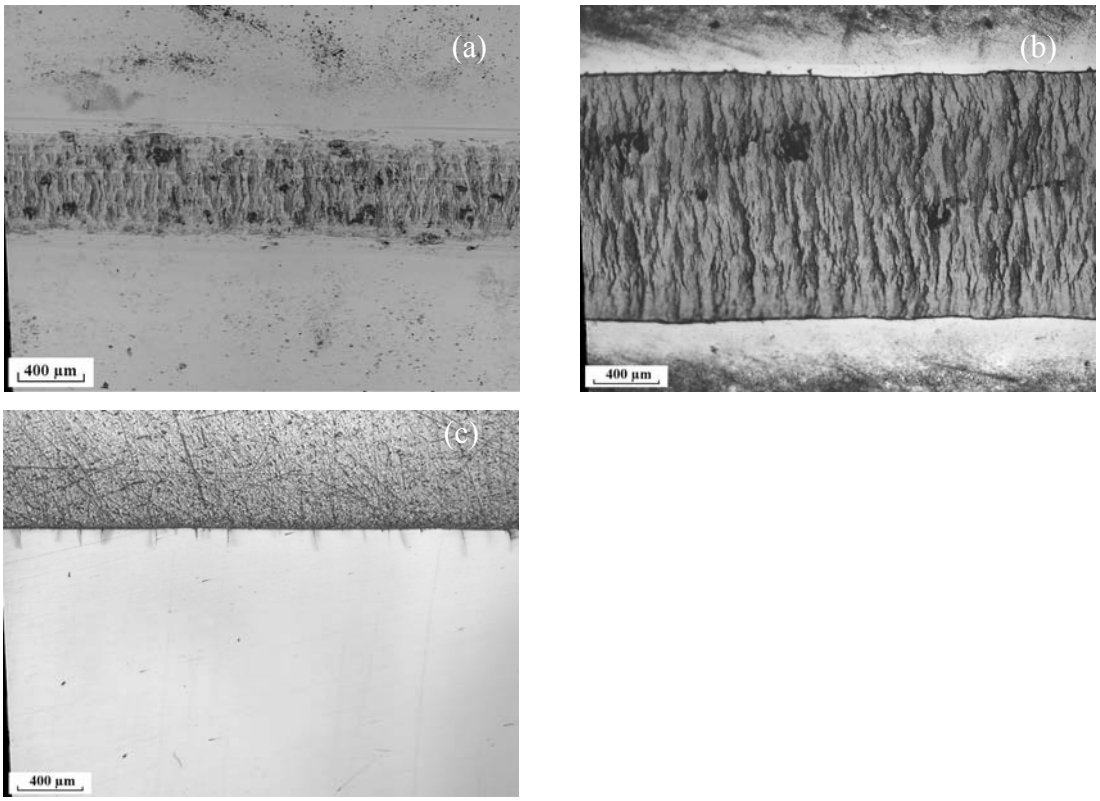


Figure 5.2 (a) and (b) surface of wear track test against $Si_3N_4$ ball; (a) normal load 29.43 N, (b) 120.66 N, (c) section view of specimen from that shown in (b).

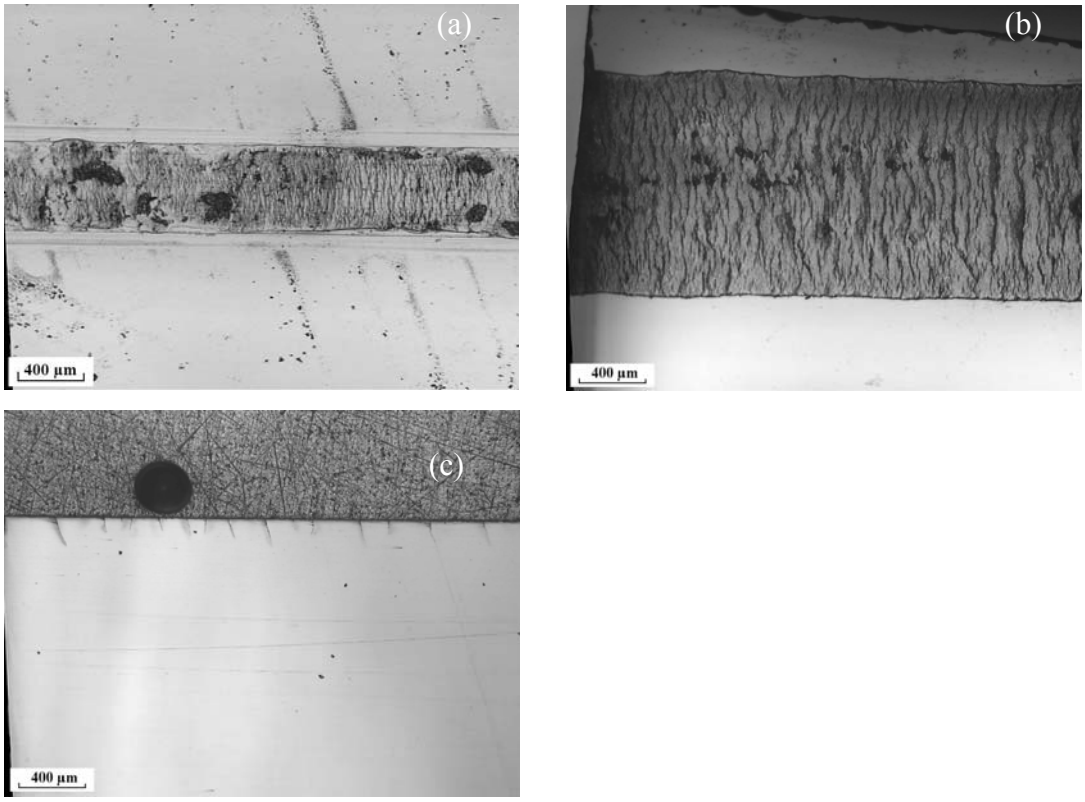


Figure 5.3 (a) and (b) surface of wear track test against steel ball; (a) normal load 29.43 N, (b) 120.66 N, (c) section view of specimen that shown in (b).

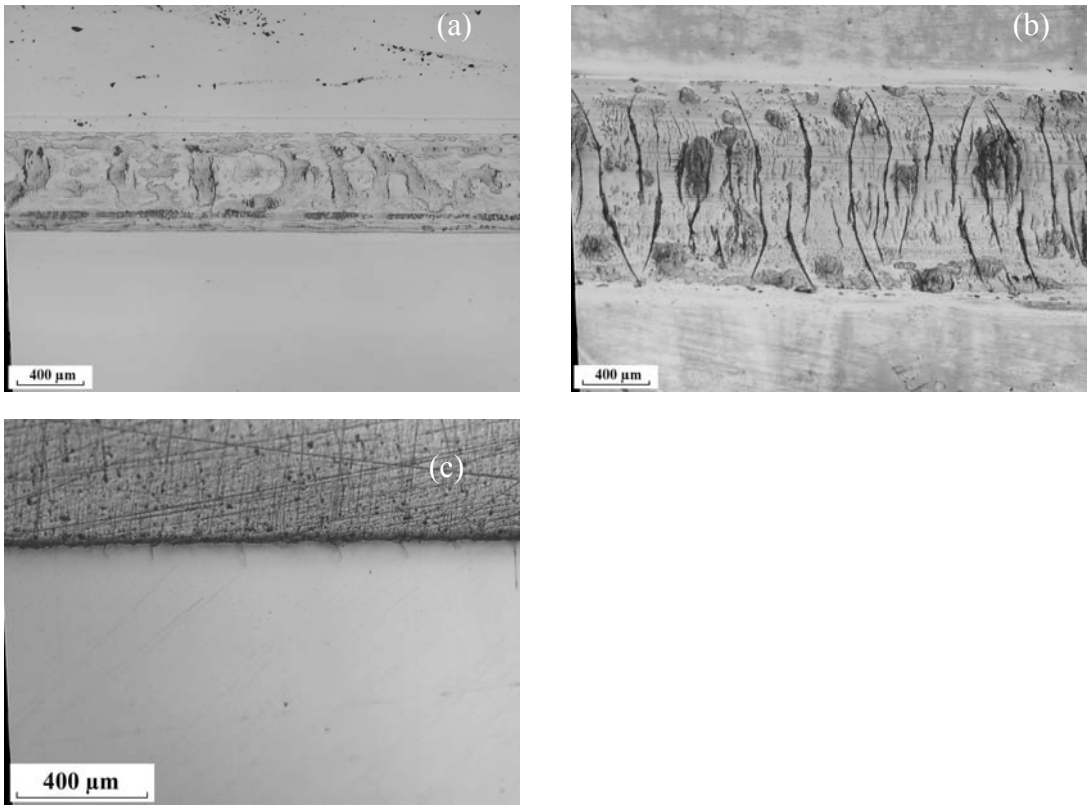


Figure 5.4 (a) and (b) surface of wear track test against aluminium ball; (a) normal load 29.43 N, (b) 120.66 N, (c) section view of specimen that shown in (b).

5.2.4.1.4 Bronze/PMMA combination

For this combination of materials, transverse cracks to the sliding direction along the track appear at normal load 29.43 N (see Figure 5.5a). However, the number of major cracks was lower than that when testing against aluminium ball. Smearing feature was observed to be more pronounced than that found in testing against aluminium ball. The number of cracks increased with increasing normal load. At 120.66 N normal load, spacing between major cracks was smaller than that of testing against aluminium ball. The profile of the cracks seems to follow the contact periphery similar to testing against aluminium. Section view showed that cracks are inclined to the surface at the largest angle among that observed for other material combinations (see Figure 5.4c). The depth of cracks was smallest among that observed for testing against $Si_3N_4$ ball, steel ball and aluminium ball.

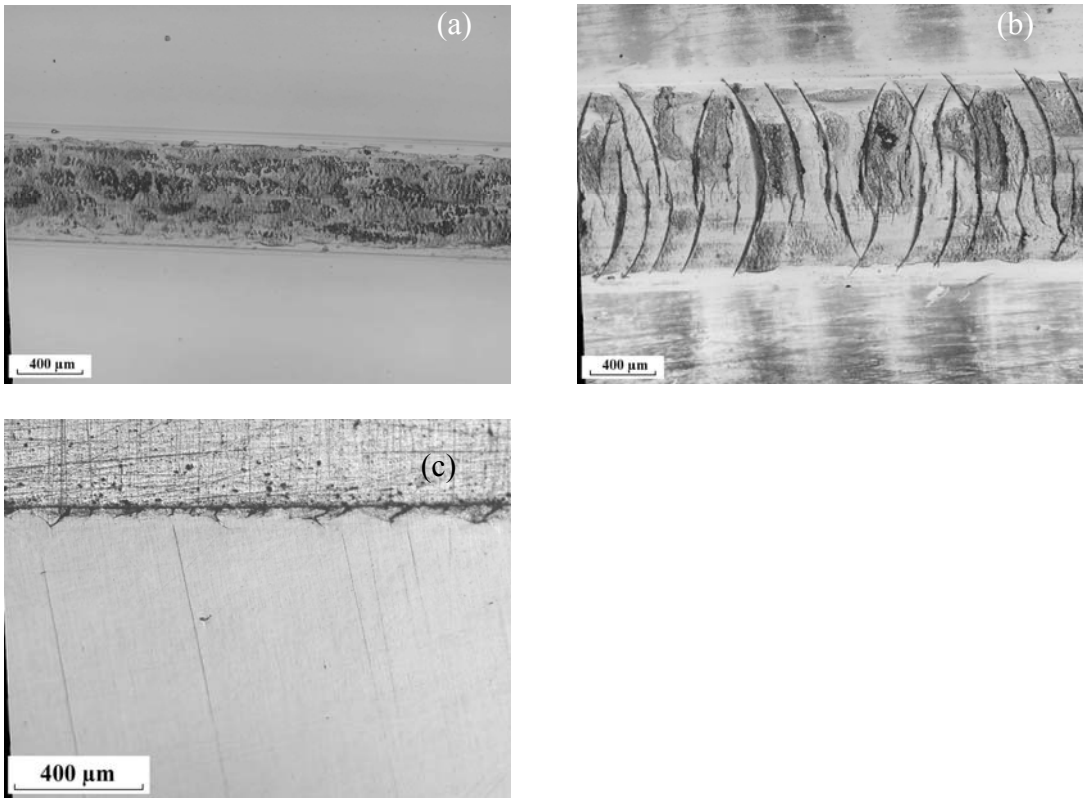


Figure 5.5 (a) and (b) surface of wear track test against bronze ball; (a) normal load 29.43 N, (b) 120.66 N, (c) section view of specimen that shown in (b).

5.2.4.1.5 PMMA/PMMA combination

Figure 5.6a and 5.6b show wear track surfaces of PMMA tested against PMMA ball with normal load 29.43 and 120.66 N, respectively. For this combination of materials, the ball was worn out very quickly. Material of the ball transferred to the PMMA plate. Melting of transferred material was observed. In general, the damage of the PMMA plate was insignificant. The section of the plate showed softening of the PMMA plate in some areas under the transferred material region (see Figure 5.6c).

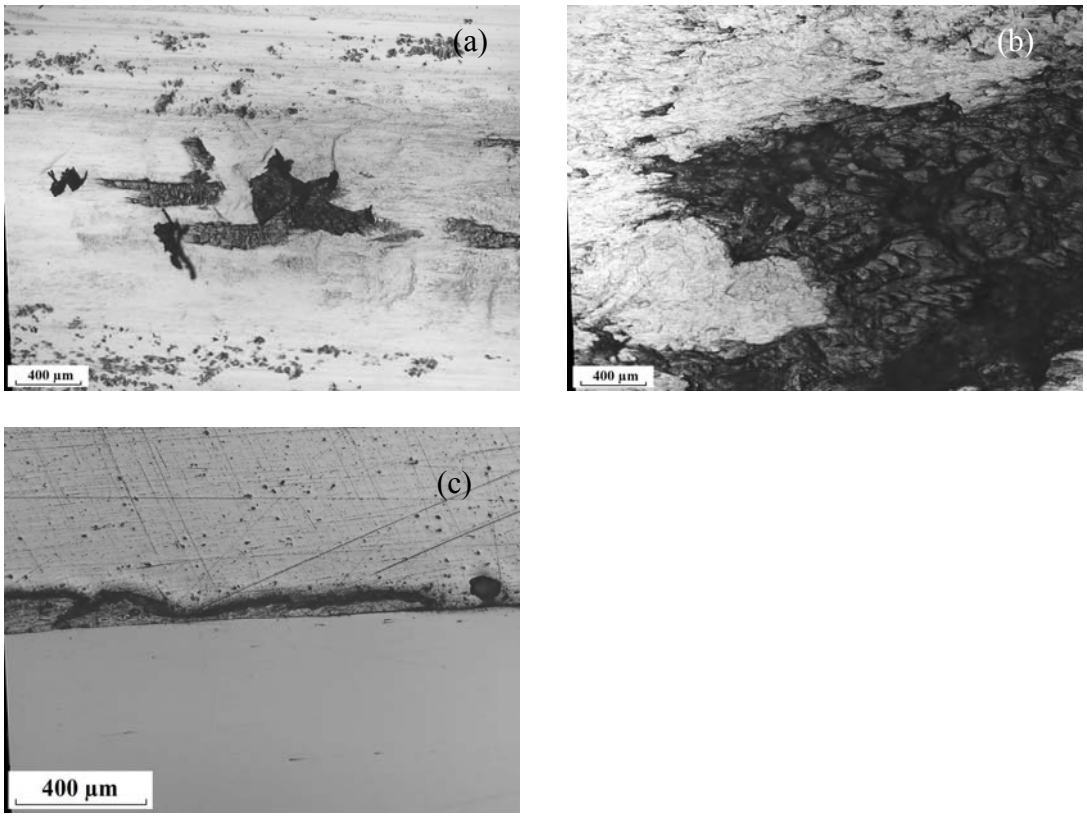


Figure 5.6 (a) and (b) surface of wear track test against PMMA ball; (a) normal load 29.43 N, (b) 120.66 N, section view of specimen that shown in (b).

*5.2.4.2 Oil-lubricated conditions*

5.2.4.2.1 $Si_3N_4$/PMMA combination

Only tiny scratches were observed with normal load 29.43 N. Increasing normal load until 88.29 N resulted in scratches increasing slightly. The scratches increased intensively when

normal load 120.66 N was used (see Figure 5.7a). However, wear of the PMMA surface was much lower than that observed during testing in dry conditions.

5.2.4.2.2 Steel/PMMA combination

The number of scratches increased comparing to that observed during testing against $Si_3N_4$ ball at normal load of 29.43 N. The number of scratches increased with increasing normal load. Grooves with dark colour, which were probably the iron compound, were found at normal load 88.29 N. The number of scratches increased markedly when the normal load reached to 120.66 N (see Figure 5.7b).

5.2.4.2.3 Aluminium/PMMA combination

Scratches on the PMMA surface were observed when tested under normal load of 29.43 N. Formation of dark colour grooves, presumably the aluminium compound, was found at this load. The scratches and the compound of aluminium significantly increased with increasing normal load (see Figure 5.7c).

5.2.4.2.4 Bronze/PMMA combination

Testing with normal load 29.43 N, a number of scratches with bronze compound appeared on the PMMA surface. The severity of surface damage increased markedly at normal load 58.86 N. At normal load 88.29 N, the number of scratches and compound deposition increased profoundly. Inspection of the ball surface confirmed existence of scratches (see Figure 5.7d). However, the number of scratches decreased at normal load of 120.66 N.

5.2.4.2.5 PMMA/PMMA combination

For this combination, very insignificant number of scratches was observed on the surface of the PMMA plate when using normal load 29.43 N. The damage of the surface insignificantly increased until normal load of 120.66 N was reached (see Figure 5.7e).

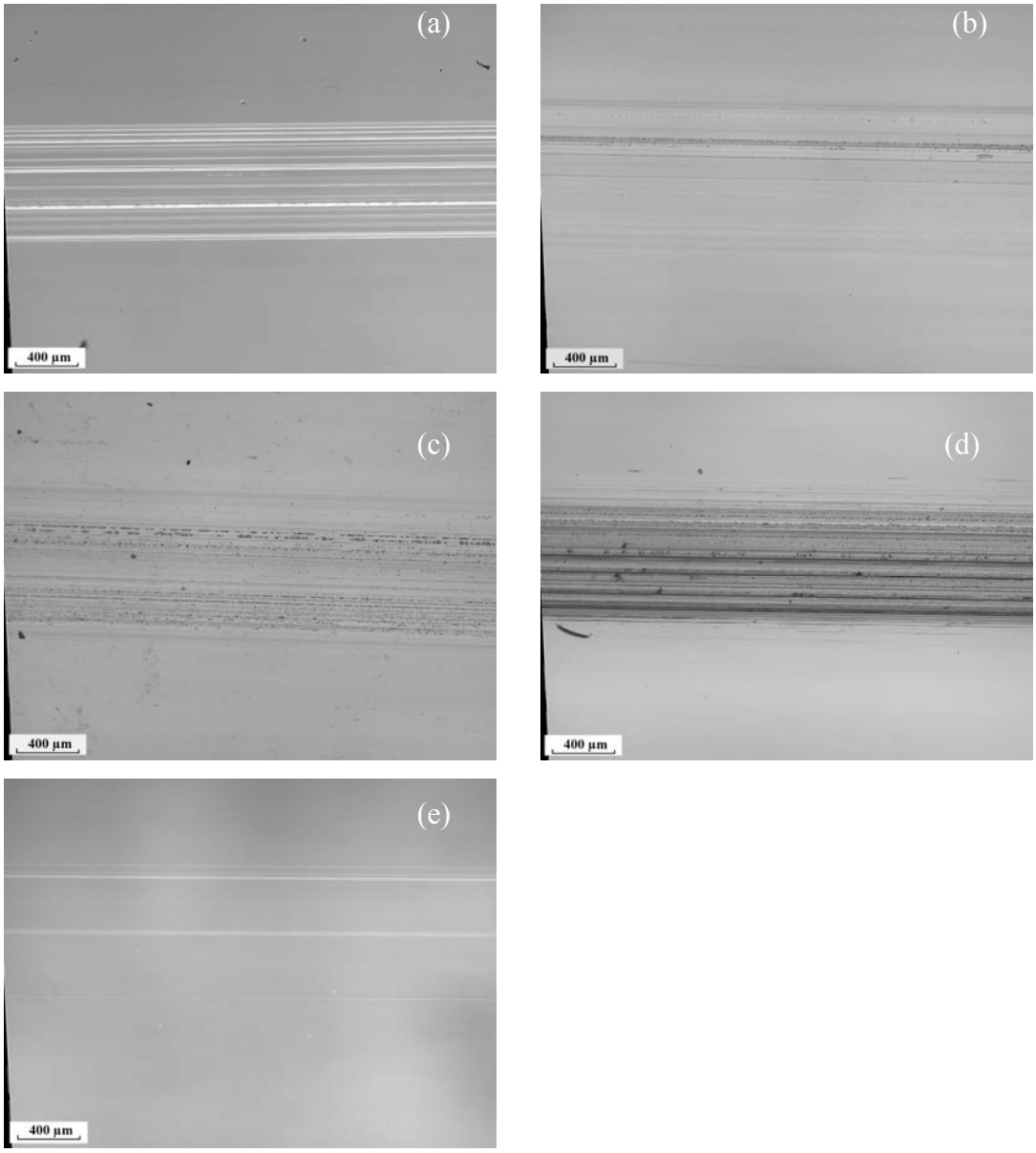


Figure 5.7 Surface of wear track test at 120.66 N produced by: (a) $Si_3N_4$ ball, (b) steel ball, (c) aluminium ball, (d) bronze ball and (e) PMMA ball.

### *5.2.5 Surface Observation from Static Contact Fatigue.*

Surface observation results were obtained from the examination using stereo microscope, optical microscope, and scanning electron microscope. Each combination of contacting materials used is discussed in turn in order to clearly identify the influence of the counterface material, the number of load cycles, and the influence of oil lubrication on surface damage of PMMA. It should be noted that optical microscope micrographs were taken in reflection mode. The transparency mode is identified where it is appropriate.

*5.2.5.1 Dry conditions*

For every combination of contacting materials, except $Si_3N_4$/PMMA, the occurrence of damage on PMMA surface was observed to happen during the first 5 minutes of testing. Figure 5.8 shows SEM micrographs depicting damage features within the contact between PMMA plate and balls made of different materials produced after 5 minutes (equivalent to 3,000 load cycles). In Figure 5.8a, damage features within the contact of PMMA and $Si_3N_4$ ball were produced after 15 minutes of testing (9,300 cycles). Figure 5.9 shows SEM micrographs illustrating damage features produced after 810 minutes (486,000 load cycles). In all cases, two regions within the contact area can be identified, namely stick region and slip region. It can be seen the severe damage occurred in the slip region for all contact material combinations.

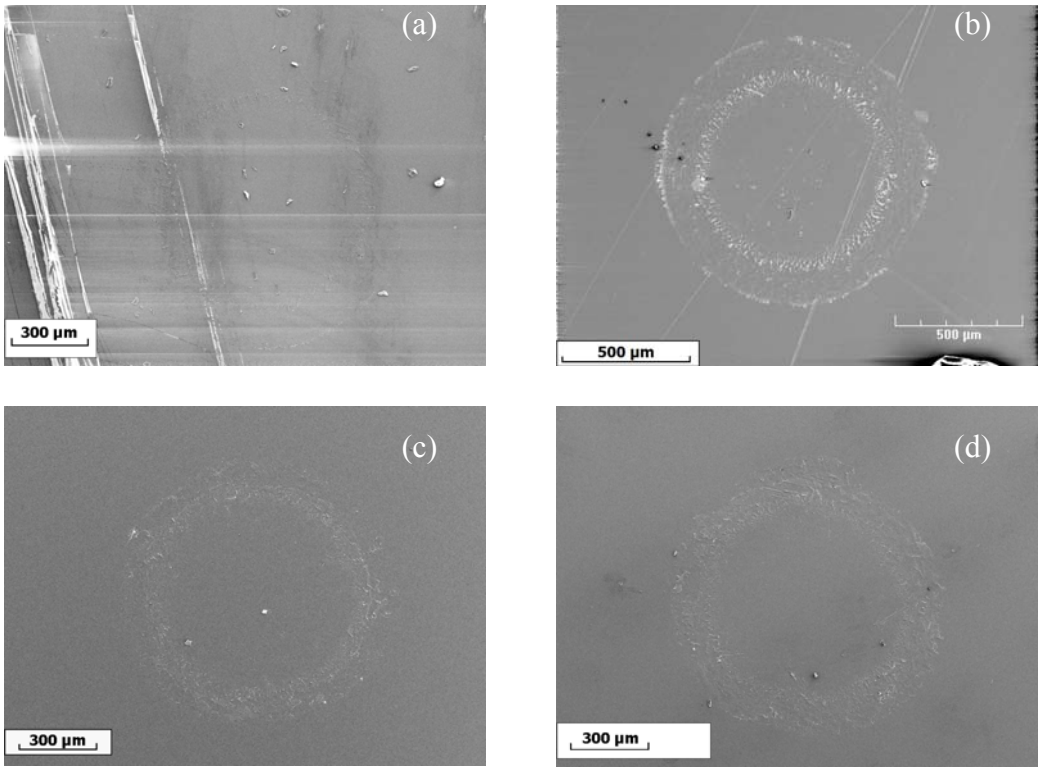


Figure 5.8 SEM micrographs of PMMA tested against different balls: (a) $Si_3N_4$ ball 15 min. (b) steel ball 5 min. (c) aluminium ball 5 min. (d) bronze ball 5 min. and (e) PMMA ball 5 min.

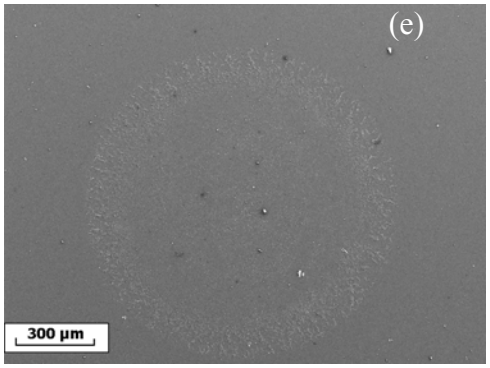


Figure 5.8 continue.

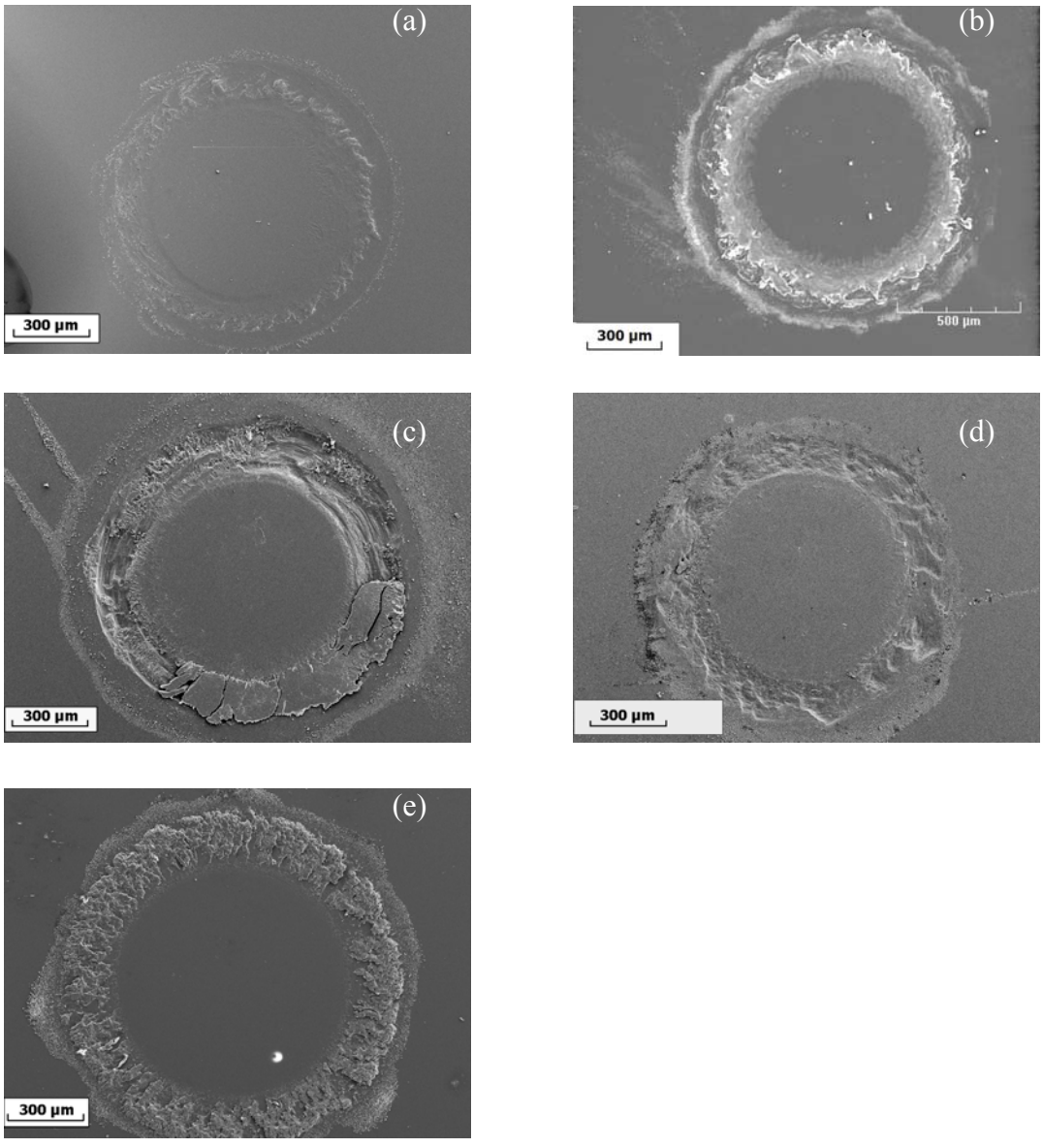


Figure 5.9 SEM micrographs of PMMA plate tested against different balls after test time of 810 min. (a) $Si_3N_4$ ball, (b) steel ball, (c) aluminium ball, (d) bronze ball, and (e) PMMA ball.

5.2.5.1.1 $Si_3N_4$/PMMA combination

Damage inflicted on PMMA plate during 5 minutes of testing was negligible. However, surface roughening at slip area can be seen at higher magnification in polarized mode (see Figure 5.10a). After 15 minutes of testing, the surface of PMMA plate was progressively roughened especially around the stick region (see Figure 5.10b, 5.10c and 5.10d). Rubbing feature is obvious on the surface in this region. Wear debris produced were deposited in the vicinity of the contact circumference. Wear debris were fine particles. After 30 minutes of testing, the surface roughness significantly increased within the slip region (see Figure 5.10e). However, between 30 minutes and 180 minutes of testing the contact area was not changed in any dramatic way. High amount of wear debris is observed at contact perimeter after testing 180 minutes (see Figure 5.10f).

Radial cracks were formed in the middle range of the slip region after 810 minutes of testing (see Figure 5.9a and 5.10g). Also, the surface roughness in the slip region increased. Wear debris generated more at the edge of contact surface.

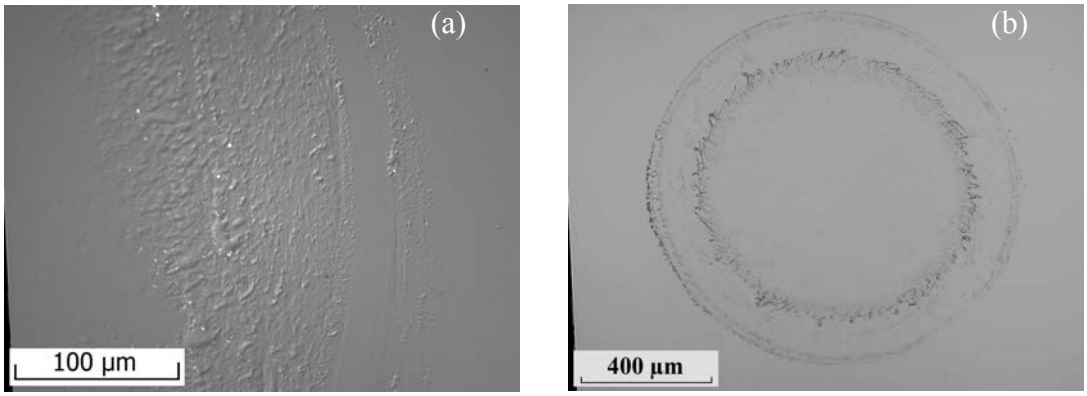


Figure 5.10 OM micrographs; (a), (b), (d), (f) and (h) and SEM micrograph; (c), (e), (g) and (i) of $Si_3N_4$/PMMA combination. PMMA plate; (a), (b), (c), (d), (e), (f) and (g). Ball; (h) and (i). (a) test time 5 min.; polarized mode, (b), (c) and (d) test time 15 min. (e) test time 30 min. (f) test time 180 min. and (g) test time 810 min. (h) test time 5 min. and (i) test time 810 min.

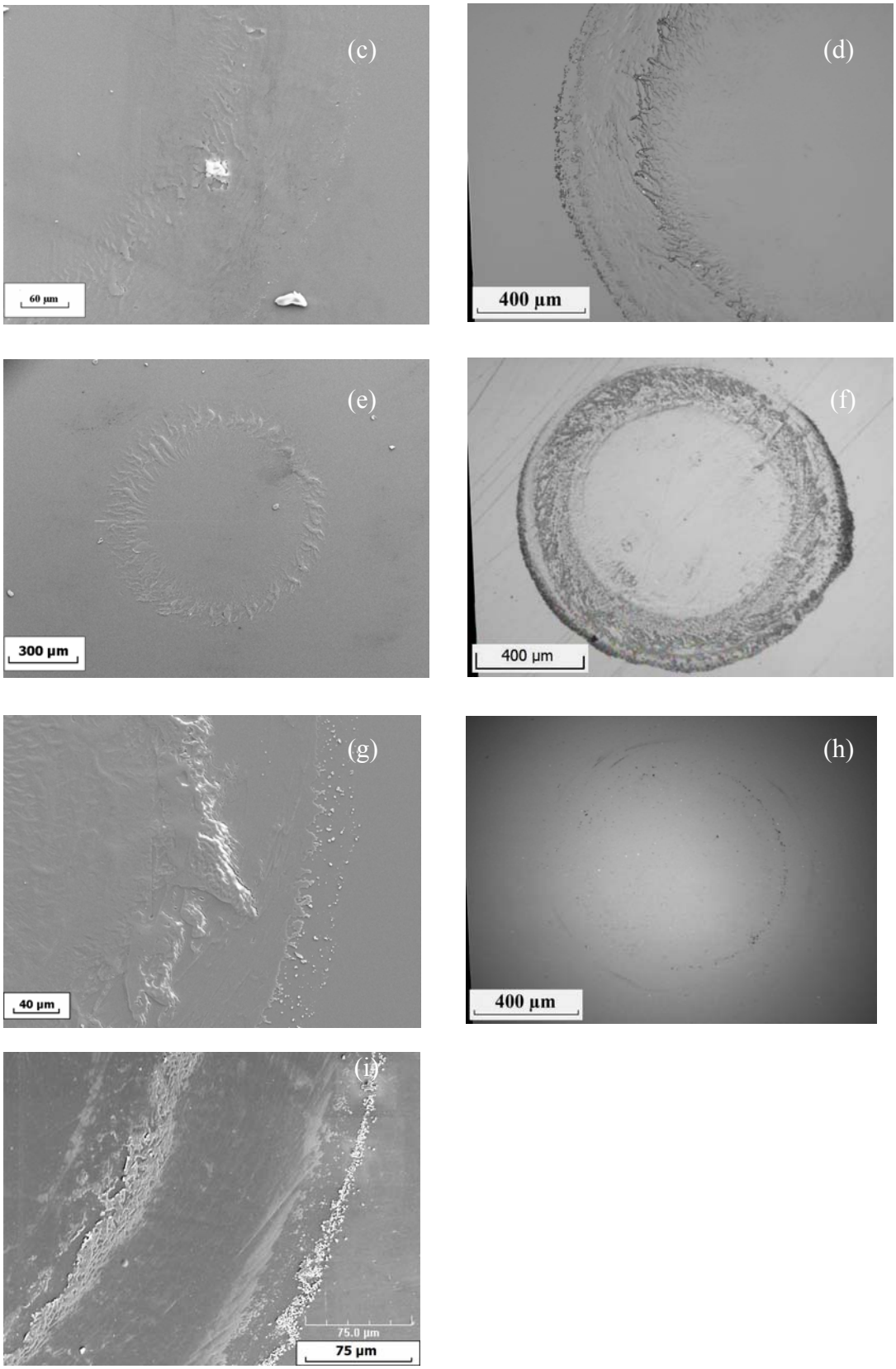


Figure 5.10 Continue.

Discrete transferred material was observed on ball surface at the boundary of the stick region and tiny amount of wear debris is attached at the edge of the contact area after testing for 5 minutes (see Figure 5.10h). Transferred material was gradually accumulated on the ball surface until testing time of 180 minutes. After 810 minutes the transferred material increased significantly (see Figure 5.10i). Progressive increasing of wear debris was observed as prolonging of testing time till the end of test. Surface damage on the ball surface was insignificant during the testing period.

5.2.5.1.2 Steel/PMMA combination

The slip region became distinctly rough after only 5 minutes of testing (see Figure 5.8b). Also a small quantity of wear debris was produced and deposited at the edge of contact. After examination under scanning electron microscope (SEM) at high magnification it was found that debris had flake-like shape (see Figure 5.11a). The general appearance of the contact region pointed to the displacement of material and piling it up at the periphery of the contact area. Signs of melting of PMMA were quite evident as near the boundary between stick and slip regions ripples can be clearly seen at high magnification (see Figure 5.11b).

After 15 minutes of testing, surface in the slip region increased its roughness and more wear debris were generated and deposited at the edge of the contact area. Surface micro-cracks appeared around the boundary of the stick region (see Figure 5.11c). The cracks were oriented at between 0º and 45º to the radial direction of the contact. The damage did not increase significantly when testing time was extended to 30 minutes.

Examinations under optical microscope clearly revealed that a ring shaped zone composed of iron was formed at the boundary of the stick region after 60 minutes of testing (see Figure 5.11d). In reflection mode this zone appeared shiny but in transparent mode it acquired a dark brownish colour (see Figure 5.11 e). This evidence can be verified by SEM micrograph in back scattered electron mode where the iron rich region will be dark because of higher absorption of electron of iron than carbon or hydrogen - main compositions of PMMA. The iron rich zone expanded outward with increasing tendency in testing time. After 180 minutes of testing lumps of detached material appeared in the slip region and abundance of wear debris accumulated at the edge of the contact area (see Figure 5.11f).

After 810 minutes of testing, ring cracks were formed along the edge of contact area (see Figures 5.9b, 5.11g and 5.11h). They appear to be initiated at the surface and grew into the bulk of PMMA plate. Propagation of cracks in the inward direction was clearly observed under optical microscope at higher magnification and transparent mode (see Figure 5.11i). Also copious quantity of wear debris was produced and deposited in the vicinity of the contact edge.

The investigation of ball shows no sign of surface wear or transferred material at the testing time during 5 minutes. After 15 min the ball surface still shows in good condition, however, transferred material observed to attach at the slip area (see Figure 5.11j). The surface conditions were not profoundly changed until 30 minutes testing time. Lump of transferred material of PMMA is attached on the ball surface after 60 minutes testing time. The surface of the ball, however, did not show an evidence of damage. Worn out of ball surface was identified especially after cleaning in 180 minutes testing time (see Figure 5.11k). The progressive damage of the ball surface in the slip region was observed after 810 minutes and all over the slip region was covered with transferred material (see Figure 5.11m and 5.11n).

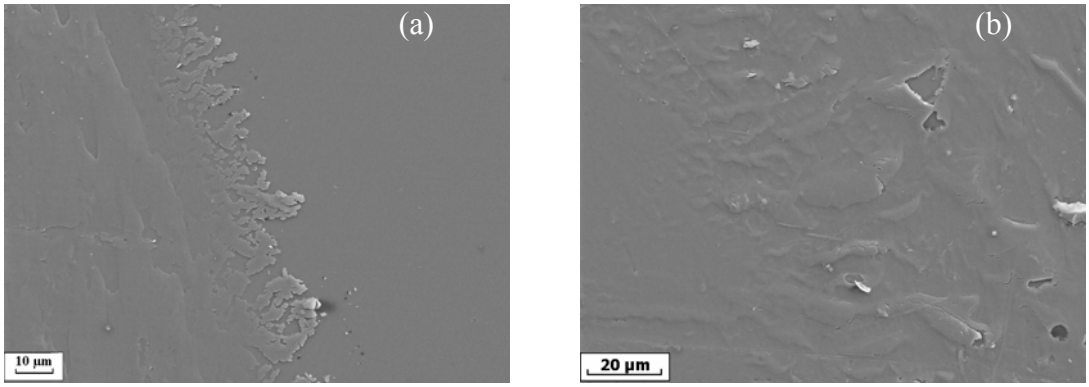


Figure 5.11 SEM micrographs; (a), (b), (c), (g), (h), (l) and (m) and OM micrographs; (d), (e), (f), (i), (j) and (k) of steel/PMMA combination. PMMA plate; (a) - (i), and Ball; (j) - (n). (a) and (b) slip area at contact perimeter and the boundary of stick area respectively, test time 5 min. (c) boundary of stick region, test time 15 min. (d) bright ring of iron rich region at the boundary of stick regiom, test time 60 min. (e) high magnification of (d) in transparent mode photograph. (f) test time 180 min, (g) test time 810 min. (h) high magnification of (g). (i) test time 810 min., transparency mode photograph. (j) test time 15 min. (k) test time 180 min. (m) test time 810 min. (n) high magnification of (m); the ball surface is worn out.

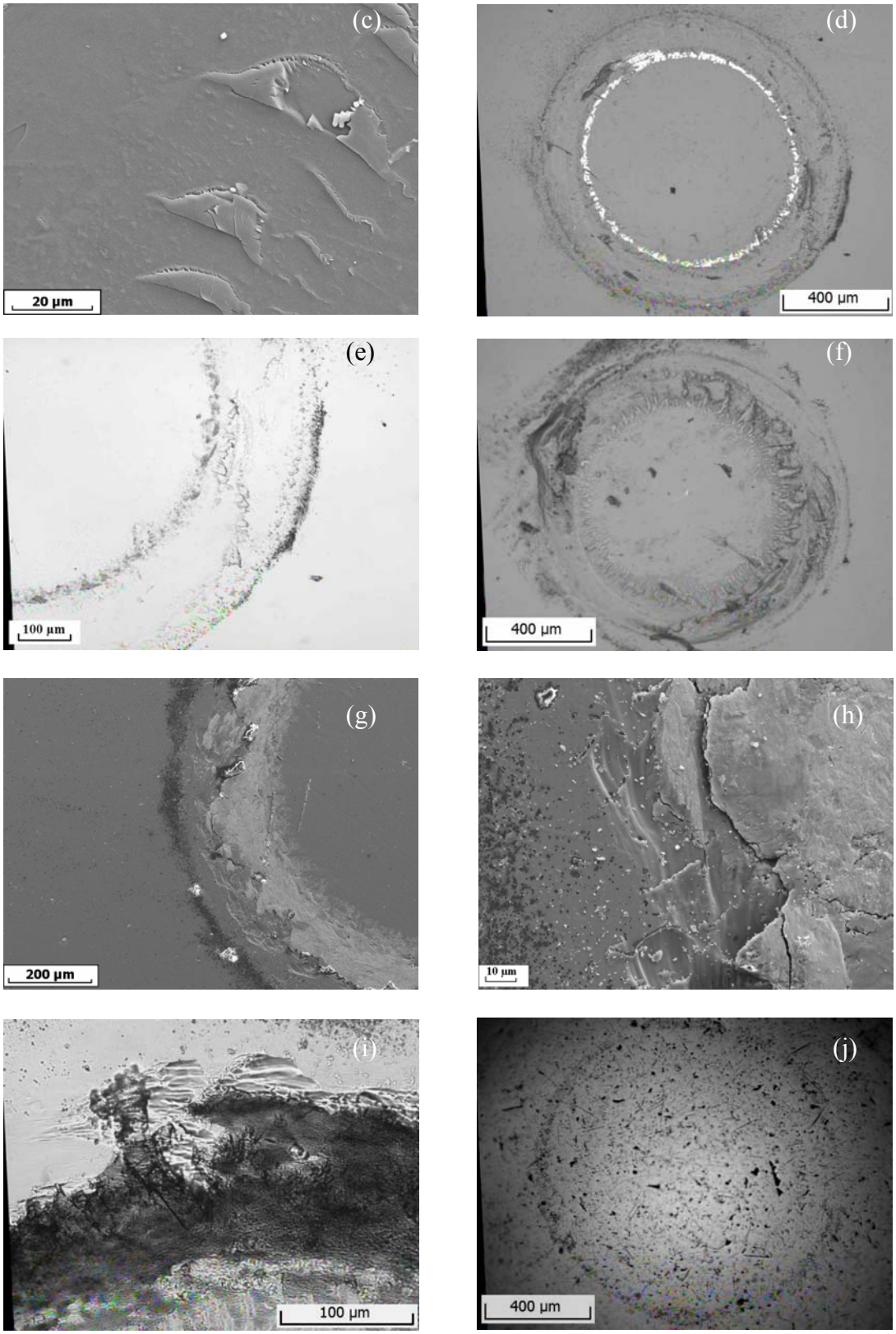


Figure 5.11 Continue.

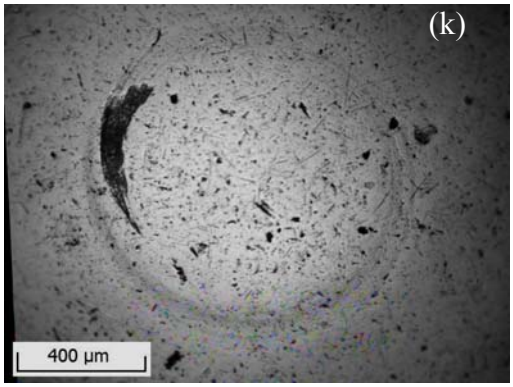


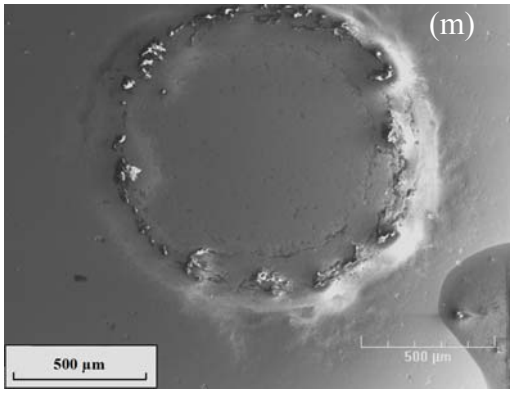


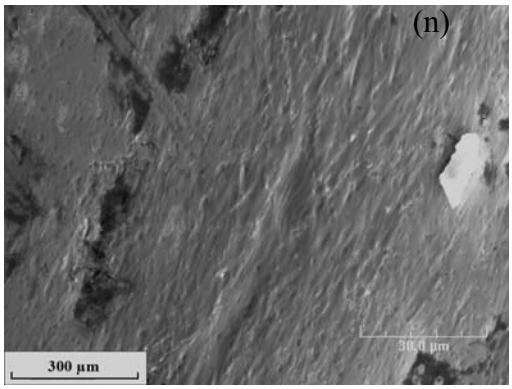


Figure 5.11 Continue.

5.2.5.1.3 Aluminium/PMMA combination

Surface roughening at the slip region was observed after 5 minutes of testing (see Figure 5.8c and 5.12a). Transfer of material in the form of a thin film took place in this region. The edge of the film was lifted up. In reflection mode, shiny fine particles could be seen in both slip and stick region under optical microscope (see Figure 6.12b). The same particles appeared to be of a dark colour in the transparent mode (see Figure 5.12c). The deposition could be aluminium particles. EDX analyses confirmed that these particles were aluminium.

As the test duration was increased to 15 minutes transfer of PMMA film continued and was mainly concentrated on the rim of the contact. However, only small amount of wear debris was produced and, as shown in Figure 5.12d, tiny white particles continued to be deposited at the boundary of the stick region. Material loss was high at the edge of slip region. Material loss increased when the test duration was extended to 30 minutes (see

Figure 5.12e). Also, in transparent mode, subsurface cracks could be seen (see Figure 5.12f). The detachment of the surface is not significantly increasing.

After 60 minutes of testing, cracks were found all over the slip region (see Figure 5.12g). Subsurface cracks could also be identified in the transparent mode (see Figure 5.12h). A typical crack was initiated near the edge of the contact area and propagated into the bulk of the material in the direction of the boundary between the stick and slip regions. Radial cracks were observed in this time. About ¾ of slip area were encountered the material loss in the form of gouging after 180 minutes. The remained area could be seen subsurface cracks (see Figure 5.12i). A lot of fine wear debris are around the contact circle.

After 810 minutes of testing, PMMA surface suffered heavy damage and sizeable pieces of material were either removed or loosely attached to the surface as evidenced by Figure 5.9c. The remaining of the contact area was covered by radial and circumferential cracks (see Figure 5.12j). Circumferential cracks were usually initiated at the edge of the contact area and propagated into the bulk of material and inward direction. At the boundary of the stick region cracks emerged onto the surface.

Transferred material deposited on the surface of the ball in the slip region since the early of 5 minutes (see Figure 5.12k). It was attached between the middle and the outermost of the slip region in the early stage. More transferred material expanded outward in the slip region as test time prolonged. Wear of ball surface at the slip area could be observed after 30 minutes (see Figure 5.12m). Sizeable of PMMA attached to the ball surface. Both transferred material and wear of the aluminium ball increased with the time (see Figure 5.6n).

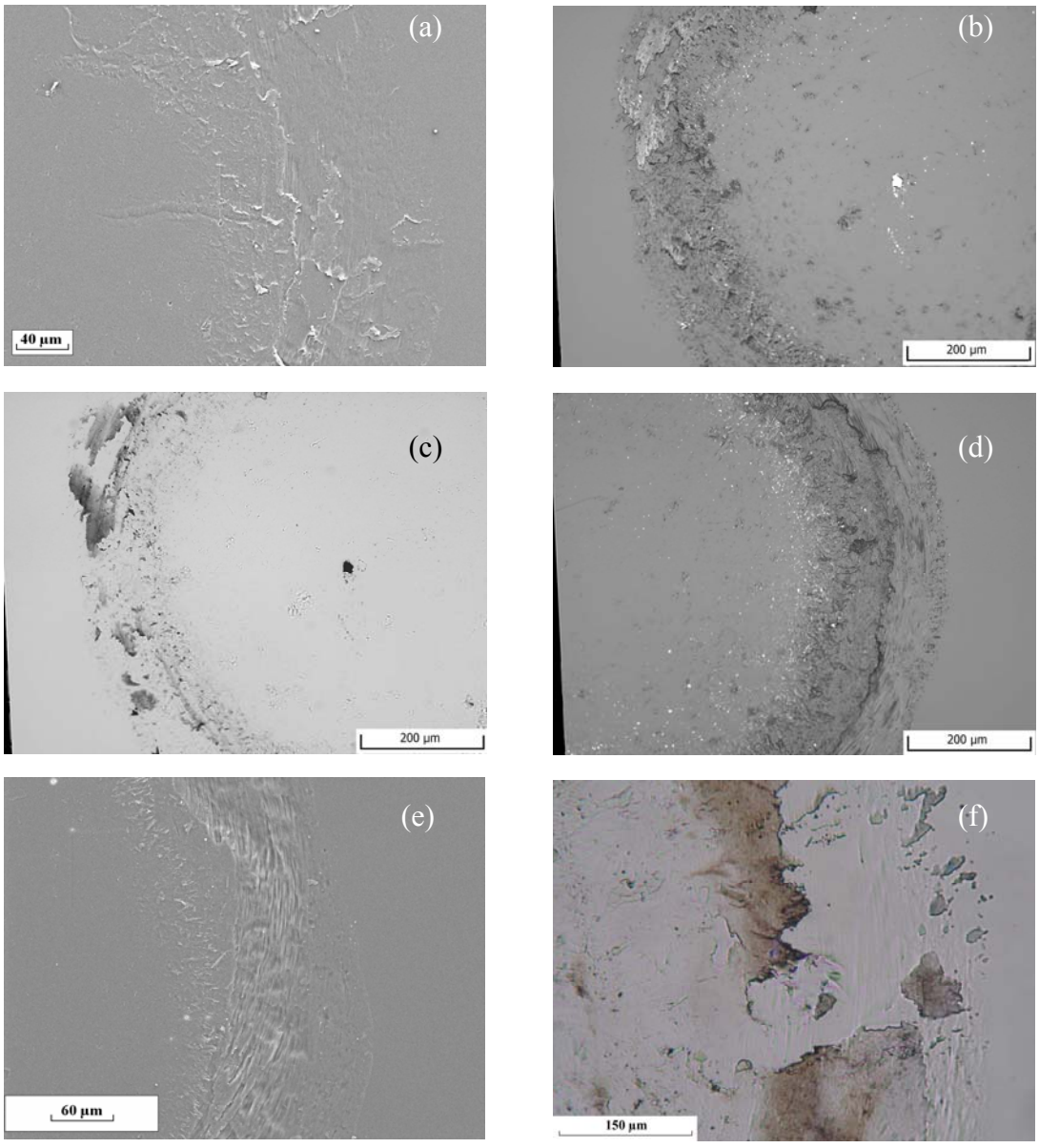


Figure 5.12 SEM micrographs; (a), (e), (i), (k) and (n) and OM micrographs; (b), (c), (d), (f), (g), (h), (j), (k) and (m) of aluminium/PMMA combination. PMMA plate; (a) – (j) and ball; (k) – (n). (a) test time 5 min. (b) test time 5 min. (c) the same position as (b), but photographed in transparency mode. (d) test time 15 min. (e) and (f) test time 30 min. (g) test time 60 min. (h) test time 60 min., transparency mode. (i) test time 180 min. (j) test time 810 min. (k) test time 5 min. (m) test time 30 min. and (n) test time 810 min.

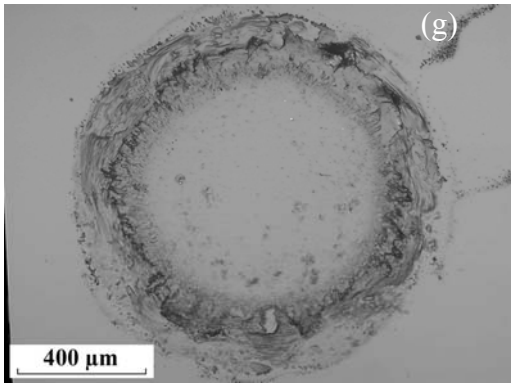


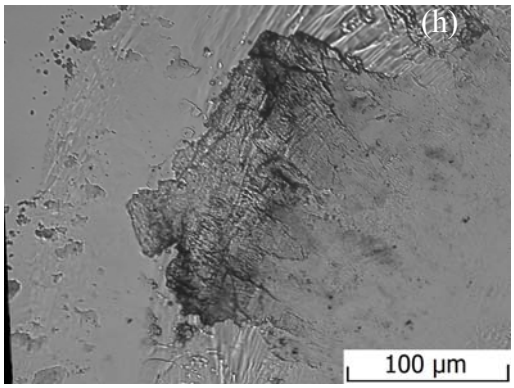


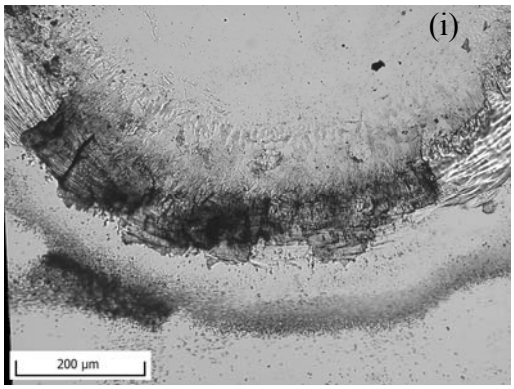


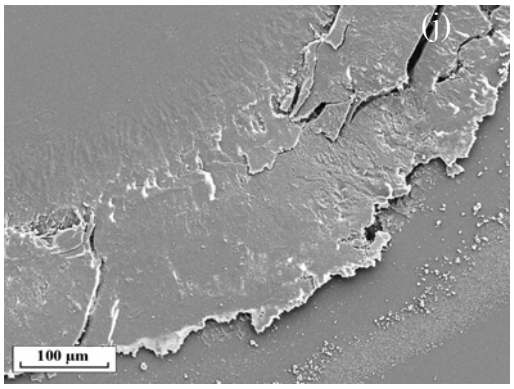


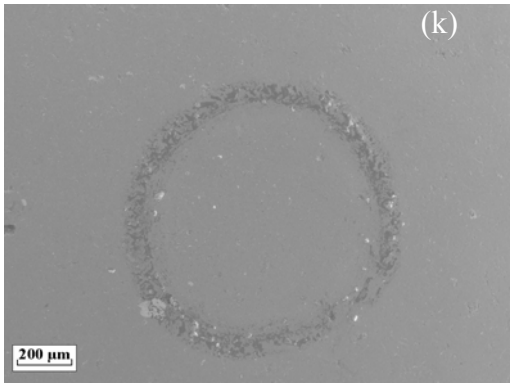


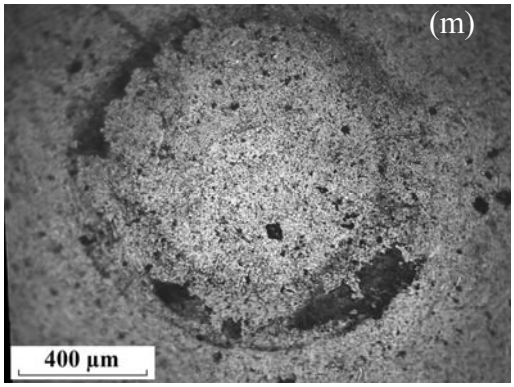


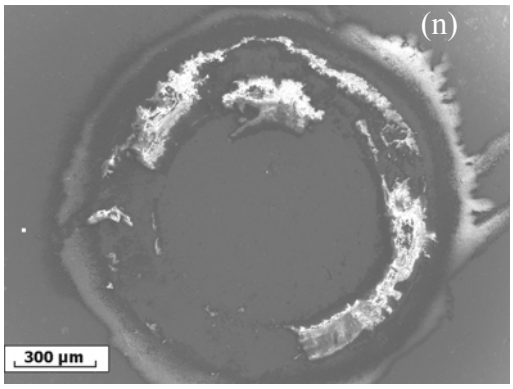


Figure 5.12 Continue.

5.2.5.1.4 Bronze/PMMA combination

In case of this combination of materials, 5 minutes of testing did not produce any noticeable wear. However, surface roughening took place in both stick and slip regions, although the slip region was slightly rougher (see Figure 5.8d and 5.13a). Transferred material in the form of thin film took place all over the slip region. The edge of the film was lifted up as found in case tested with aluminium ball. Also, some transfer of the bronze took place as bright, yellowish fine particles embedded into the PMMA surface were observed (see Figure 5.13b).

After 15 minutes of testing ripples in the slip region appeared and more bronze particles were deposited in both slip and stick regions, however, deposition was especially noticeable at the rim of the slip region (see Figure 5.13c). Wear debris were produced and accumulated mainly at the periphery of the contact. Increase of testing time to 30 minutes did not produce any new features of surface damage.

After 60 minutes, a significant detachment of PMMA particles from within the slip region took place. Fine radial cracks were observed in transparent mode (see Figure 5.13d). Surface damage intensified as testing time was increased to 180 minutes (see Figure 5.13e). The severity of the damage was high at the periphery of the contact.

Volume loss of material in the form of sizeable fragments was observed in almost entire slip region after 810 minutes of testing (see Figure 5.9d and 5.13f). Massive amount of wear debris was produced and deposited along the periphery of the contact. However, the stick region suffered relatively little damage.

The ball surface showed a trace of very thin transferred film in the slip region, but the ball itself signed insignificant wear after testing time 5 minutes (see Figure 5.13g). The deposit transferred material insignificantly increased until 30 minutes. However, high amount of the deposit was observed when testing time reached 60 minutes (see Figure 5.13h). Transferred film deposition increased especially at edge of the slip region when test prolonged to 180 minutes. After 810 of testing time, lump of PMMA deposits on the ball surface at the reciprocal slip area (see Fig 5.13i). Examination with the optical microscope revealed that surface of the ball does not have any significant damage.

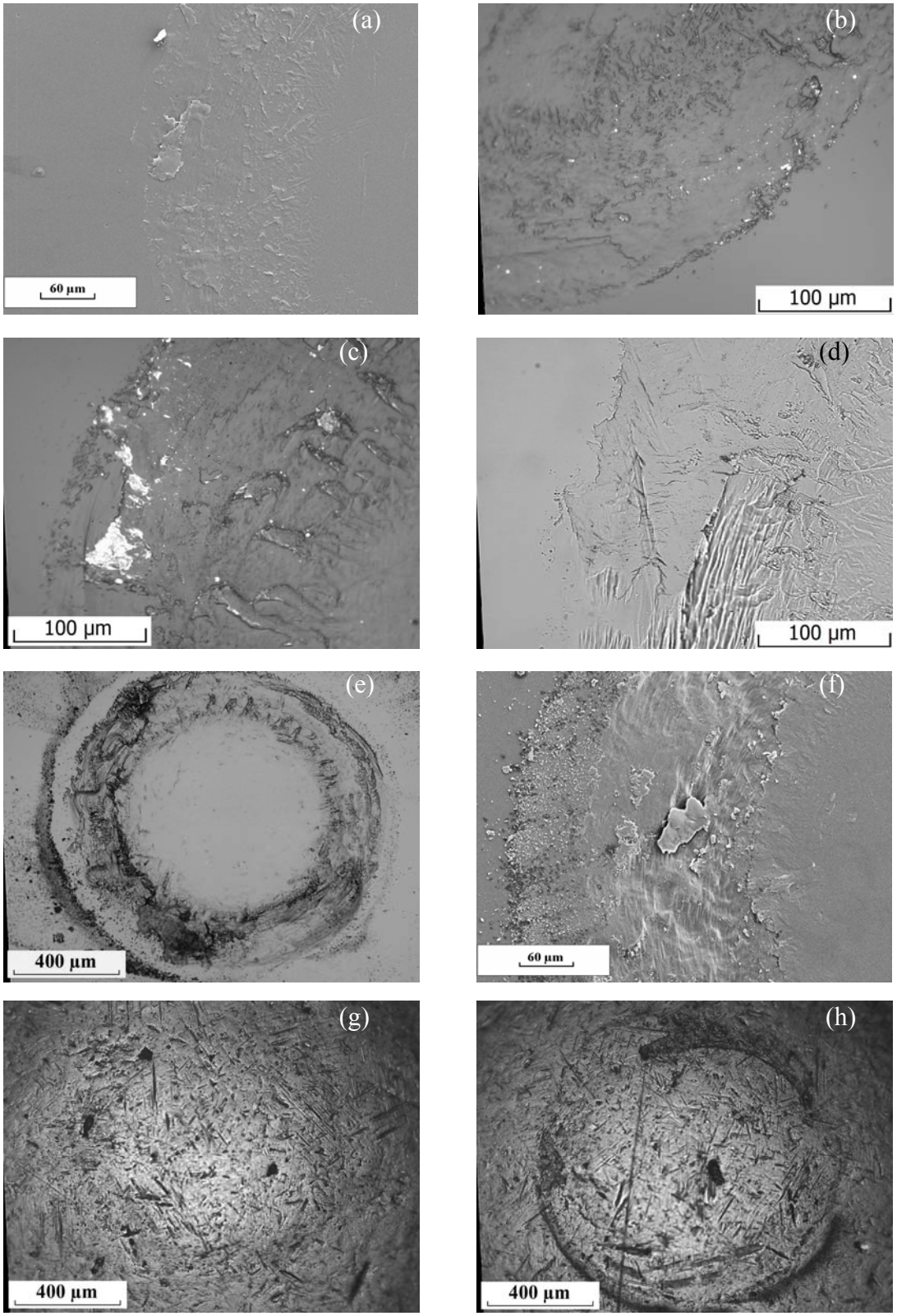


Figure 5.13 SEM micrograph; (a), (f) and (i) and OM micrographs; (b), (c), (d), (e), (g) and (h) of bronze/PMMA combination. PMMA plate; (a) – (f) and ball; (g) – (i). (a) and (b) test time 5 min. (c) test time 15 min. (d) test time 60 min., transparent mode photograph (e) test time 180 min. (f) 810 min. (g) test time 5 min. (h) test time 60 min. and (i) test time 810 min.

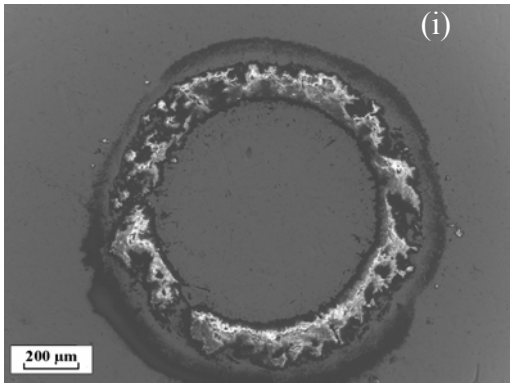


Figure 5.13 Continue.

5.2.5.1.5 PMMA/PMMA combination

When two identical materials were in contact, transfer from the ball onto the plate took place entirely in the slip region and especially intensified at the boundary of the stick and slip region within the first 5 minutes of testing (see Figures 5.8e and 5.14a). During that test interval transfer in opposite direction, that is from the plate onto the ball was not observed. Although there was no material transferred from the plate to the ball, surface roughening of the plate occurred at the slip area.

Deposition of material on the plate, resulting from transfer from the ball, increased with the increase in testing time e.g. surface feature for test time 30 minutes in Figure 5.14b. The surface of the plate became progressively rougher. Also, wear debris began accumulating at the edge of the contact.

Transfer of material from the ball to the plate continued till the testing time reached 60 minutes (see Figure 5.14c). However, the damage inflicted on the plate as quite severe comparing to the damage suffered by the ball. During 60 minutes of testing, loose particles detached from the ball were transferred onto the plate as lumps. In transparent mode some radial cracks, hidden under transferred material, could be seen (see Figure 5.14d). These cracks might be produced by expansion and contraction of the ball and the plate in circumferential direction during cyclic loading/unloading.

Severity of damage increased with testing time reaching to 180 minutes with the same damage features as early duration (see Figure 5.14e). After continuous testing for 810

hours, material from the ball transferred to the plate was covering almost entire slip region (see Figure 5.9e and 5.14f).

The ball lost its material in the slip area during 5 minutes of testing time and the amount of damage increased with testing time (see Figure 5.8g and 5.8h). Most severe wear of the ball located on the outermost region of the contact annulus. Also, the damage inflicted on the ball was far more extensive that suffered by the plate.

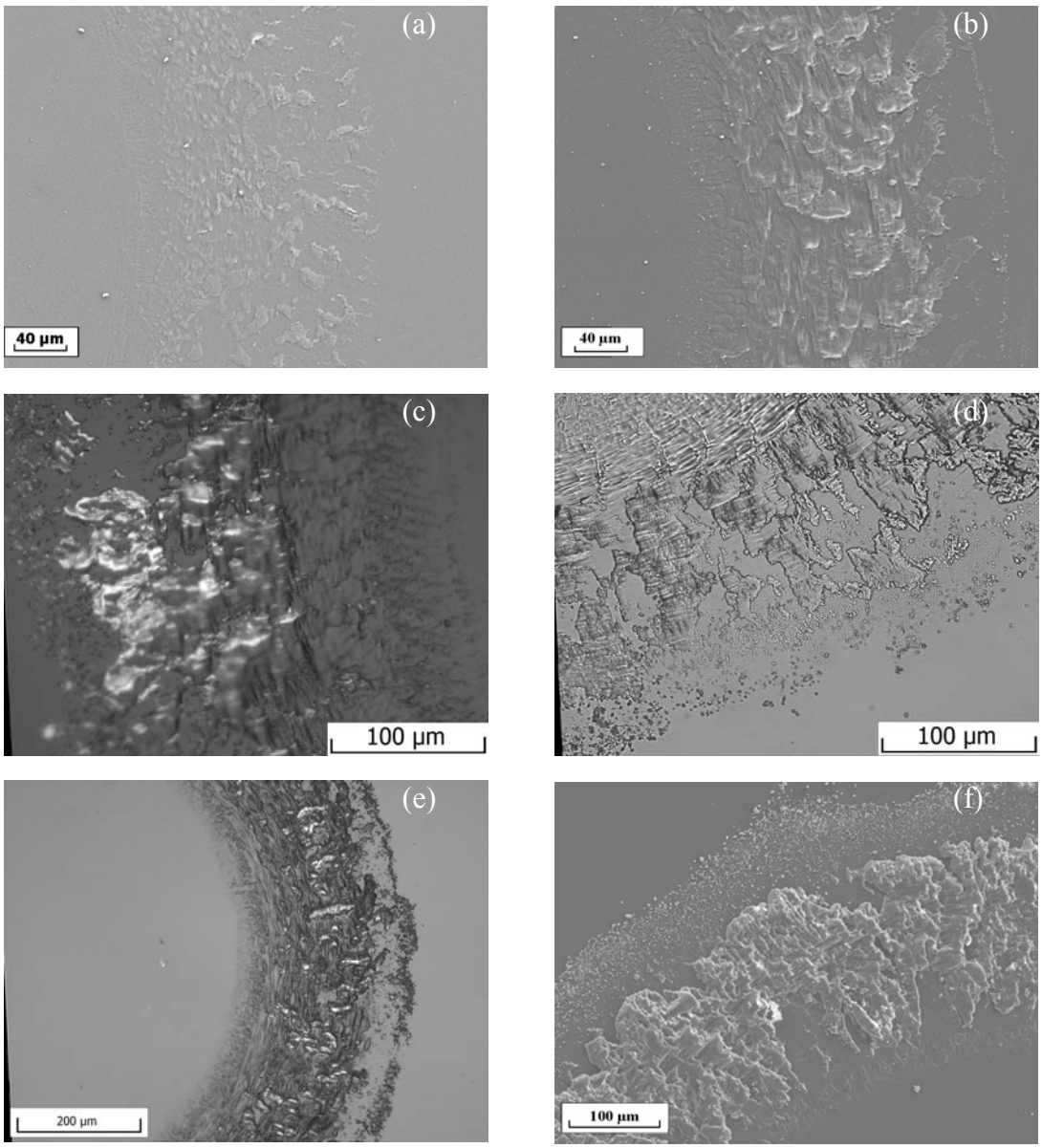


Figure 5.14 SEM micrographs; (a), (b), (f) and (h) and OM micrographs; (c), (d), (e) and (g) of PMMA/ PMMA combination. PMMA plate; (a) - (f) and ball; (g) and (h). (a) test time 5 min. (b) test time 30 min. (c) and (d) test time 60 min, but (d) in transparency mode photograph. (e) test time 180 min. (f) test time 810 min. (g) test time 5 min. and (h) test time 810 min.

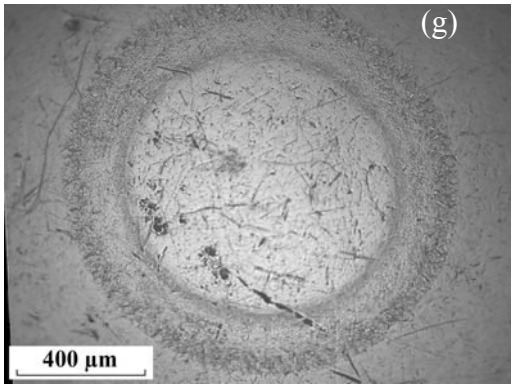


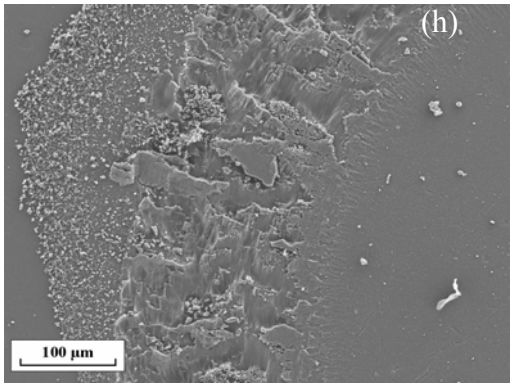


Figure 5.14 Continue.

*5.2.5.2 Oil-lubricated conditions*

In oil-lubricated conditions the occurrence of damage on PMMA surface was observed during the first 5 minutes in every combination of contacting materials. Figure 5.15 shows damage features within the contact between PMMA plate and balls made of different materials produced after 5 minutes taken by optical microscope. The severity of damage, as shown, was different. The severity order from the least to the most when contacted with different ball was as follows; PMMA, aluminium, bronze, $Si_3N_4$, and steel. SEM micrographs depicting damage features of PMMA plate produced after 810 minutes are shown in Figure 5.16. In all cases, the developing of damage is different from dry contact conditions. In these cases, the damage occurred also in the region supposed to be the stick region in dry contact conditions. However, comparing the same material combination the damage in oil-lubricated conditions was less severe than that in dry conditions.

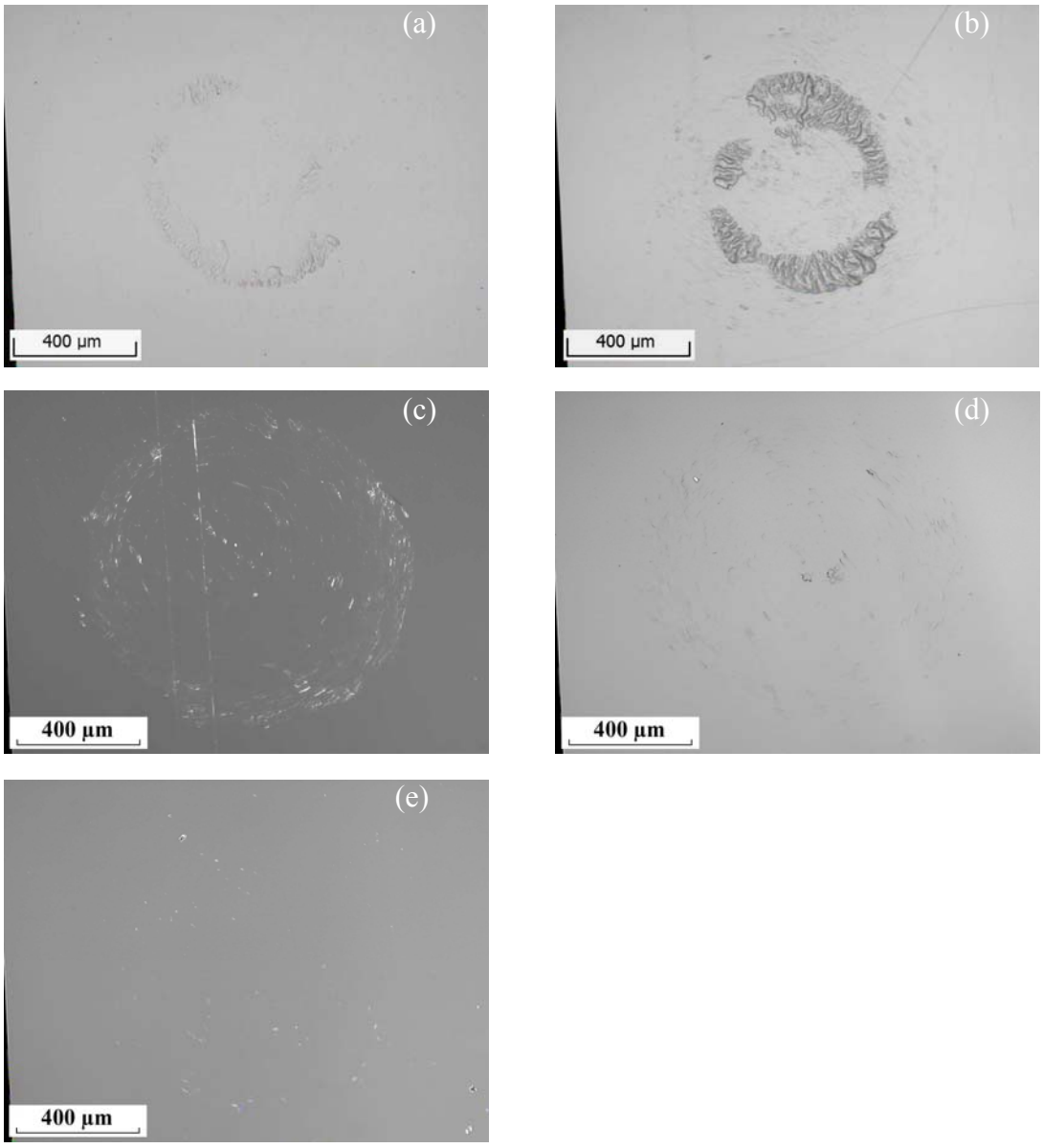


Figure 5.15 OM micrographs of PMMA plated tested against different balls in oil-lubricated conditions after 5 min. (a) Si3N4 ball (b) steel ball (c) aluminium ball, polarized light (d) bronze ball (e) PMMA ball, polarized light.

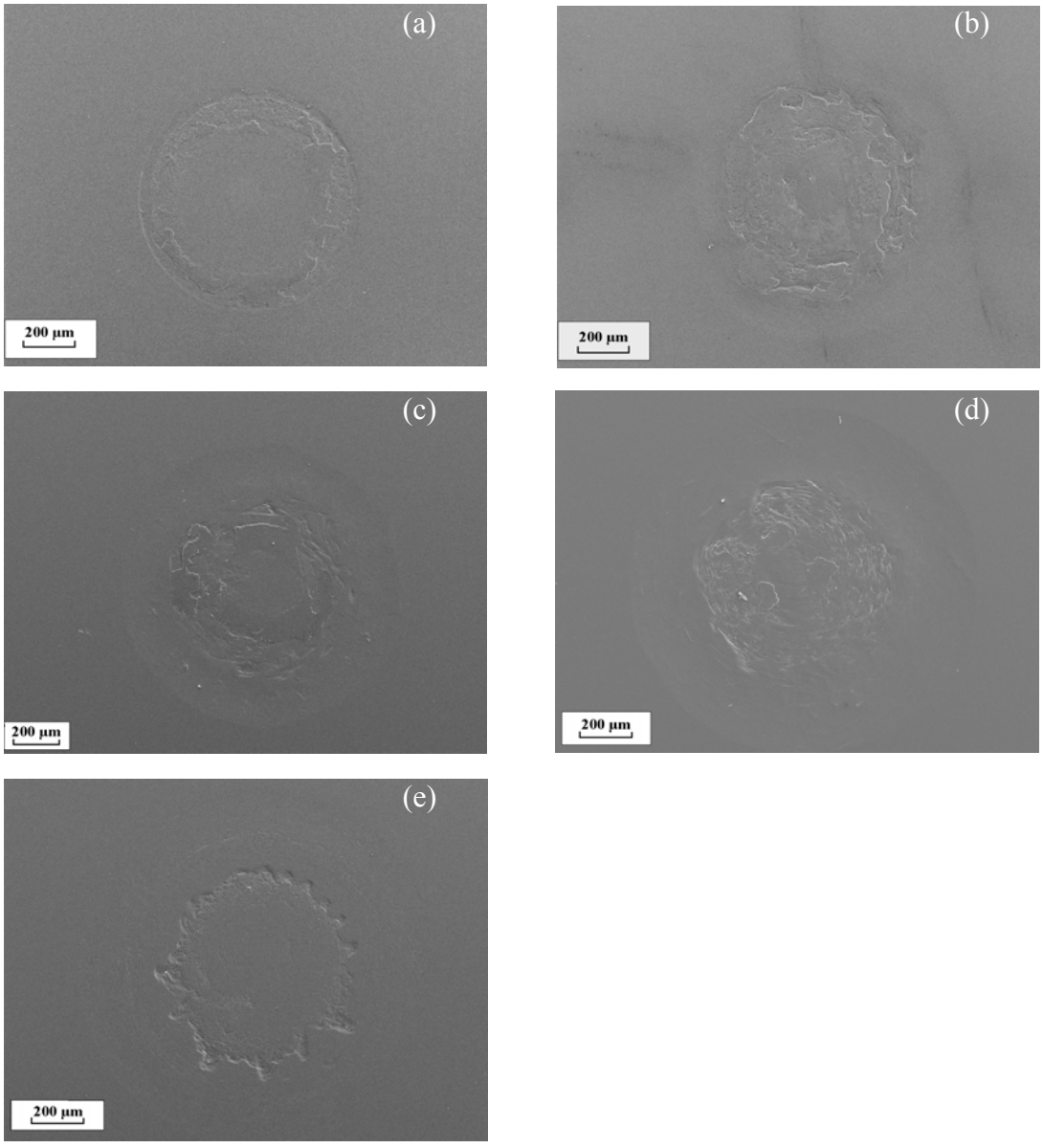


Figure 5.16 SEM micrographs of PMMA plate tested against different balls in oil lubricated conditions after test time 810 min. (a) $Si_3N_4$ ball, (b) steel ball, (c) aluminium ball, (d) bronze ball, and (e) PMMA ball.

5.2.5.2.1 $Si_3N_4$/ PMMA combination

The discrete rough region was found after 5 minutes of testing. However, the radius of this region was smaller than the contact radius calculated by Hertz's theory (see Figure 5.15a). Full annulus shape of rough surface area was obtained after 15 minutes (see Figure 5.17a). Using optical microscope in reflection mode and polarized light, three regions could be identified (see Figure 5.17b). For convenience of explanation, the regions will be named from the innermost to the outermost of contact area as the stick region, the inner slip

region, and the outer slip region. It should also be noted that this feature was found in others combination of materials.

The outer slip region was comparable in size to the slip region observed in dry contact condition. This region was relatively smooth. Surface of the outer slip region showed fine parallel lines in circular direction. Damage intensified between the inner slip region and the outer slip region and gradually increased till testing time of 60 minutes. The inner slip region expanded inwardly leading to decreasing of the stick region.

After 180 minutes of testing, more material losses at the boundary between the inner slip region and the outer slip region were observed (see Figure 5.17c). The outer slip area showed similar feature to the previous test period. Wear damage was not significantly increased after 810 minutes (see Figure 5.16a and 5.17d). Surface damaged of high severity was identified at the inner slip area.

The damage inflicted on the ball was far more negligible than that suffered by the plate throughout the duration of testing. There was small amount of transferred material on the ball surface after testing period of 180 minutes and 810 minutes (see Figure 5.17e).

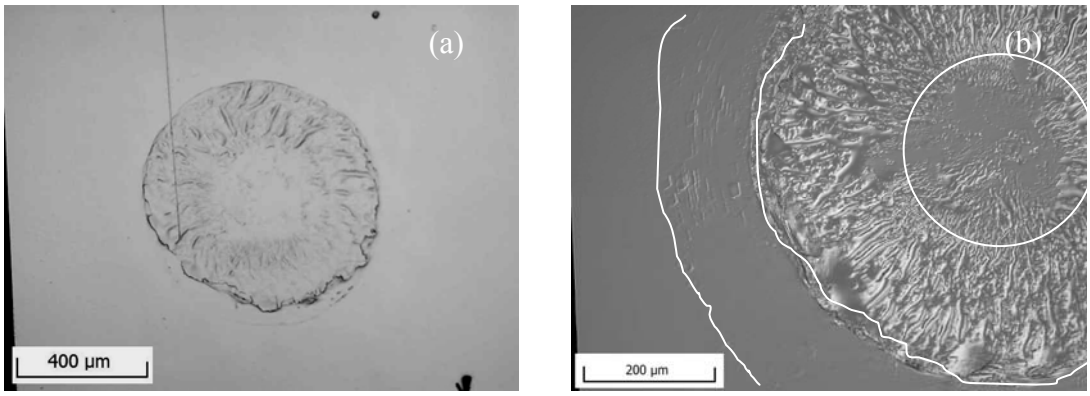


Figure 5.17 OM micrographs (a), (b), (c) and (e) and SEM micrograph (d) of $Si_3N_4$/PMMA combination in oil-lubricated conditions. PMMA plate; (a) – (d) and ball; (e). (a) and (b) test time 15 min., but (b) was taken with polarized light. (c) test time 180 min. (d) test time 810 min. and (e) test time 810 min.

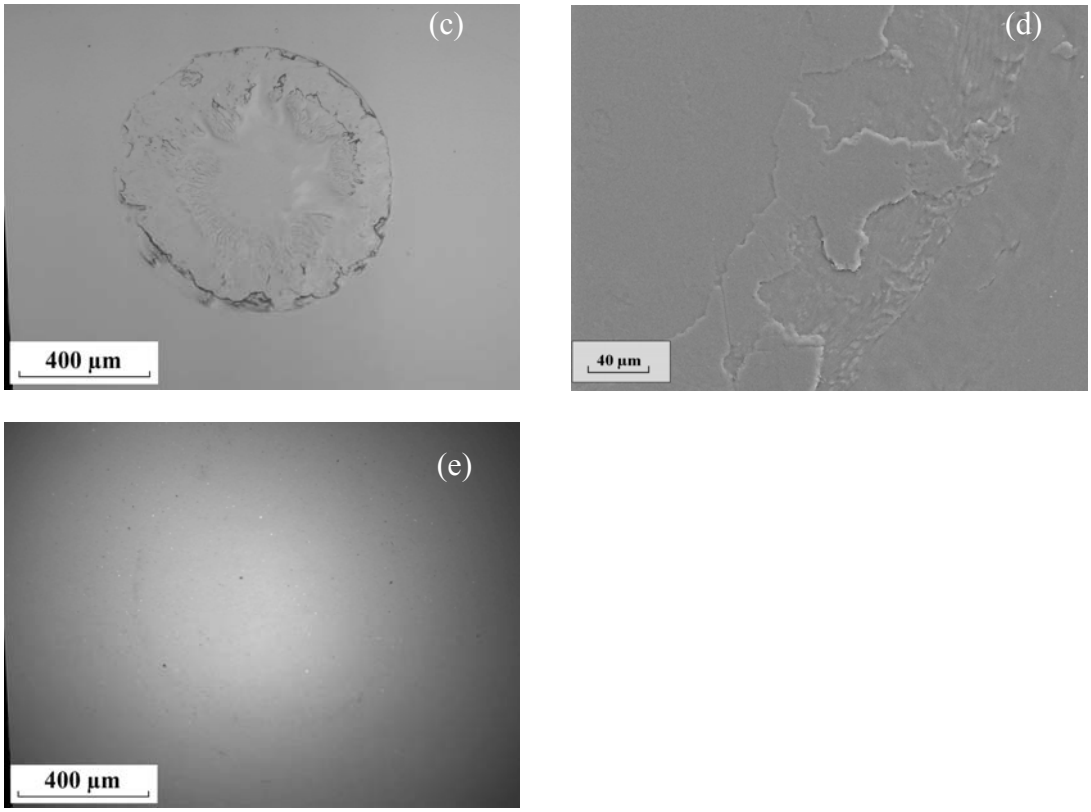


Figure 5.17 Continue.

5.2.5.2.2 Steel / PMMA combination

For steel/PMMA combination, the discrete rough region was found after 5 minutes of testing (see Figure 5.15b). The stick region was smaller than that found in dry condition. Using reflection mode and polarized light, the slip region could be clearly distinguished with the size comparable to the slip region that was formed in dry condition (see Figure 5.18a). Two zones of the slip region were defined as elaborated in the previous section. There are small amount of tiny particles embedded in the rough region. The surface in the outer slip region was smoother than that of the inner slip region. However, it was rougher than the outer slip surface produced in test against $Si_3N_4$ ball.

Surface conditions were insignificantly changed after 15 minutes of testing period. Full annulus shape of the inner slip region was formed after 30 minutes (see Figure 5.18b). The damage intensified at the boundary between the inner slip region and the outer slip region. Surface of the inner slip region was rougher than the outer slip region (see Figure 5.18c). Surface of the outer slip region showed fine parallel lines in circular direction. The damage

progressed gradually in the similar way till 180 minutes of testing (see Figure 5.18d). In this period radial cracks were observed at the inner slip region (see Figure 5.18e).

After 810 minutes of testing time, almost all the stick region was disappeared (see figure 5.16b). Brown colour on the surface of the inner slip region, which is expected to be iron rich region, was found by examining using optical microscope in transparency mode (see Figure 5.18f). Material losses occurred in both the inner and the outer slip region. The surface of outer slip region, however, was much smoother (see Figure 5.18g). Parallel texture of the inner slip region was also rougher than that of the outer slip region.

The ball surface damage could not be identified after 180 minutes. After 810 minutes of testing, wear of the ball surface could be detected (see Figure 5.18h). Surface at correspondence to the outer slip region has the feature of round parallel line and was rougher compare to the other contacted region. However, it was not significant damage.

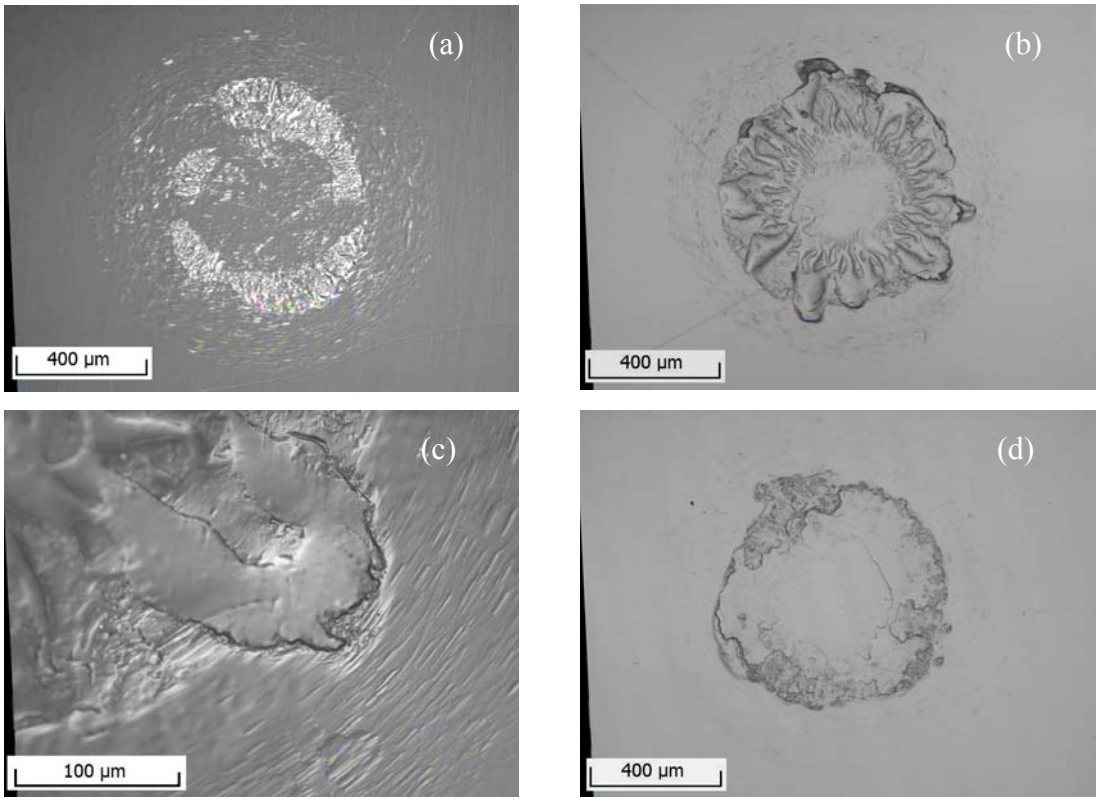


Figure 5.18 OM micrographs (a), (b), (c) and (e) and SEM micrograph (d) of steel/PMMA combination. PMMA plate (a) – (d) and ball (e); (a) test time 5 min, polarized mode. (b) and (c) test time 30 min, but (c) taken in polarized mode. (d) and (e) test time 180 min, but (e) taken in transparency mode. (f) and (g) test time 810 min, but (f) taken in transparency mode. (h) test time 810 min.

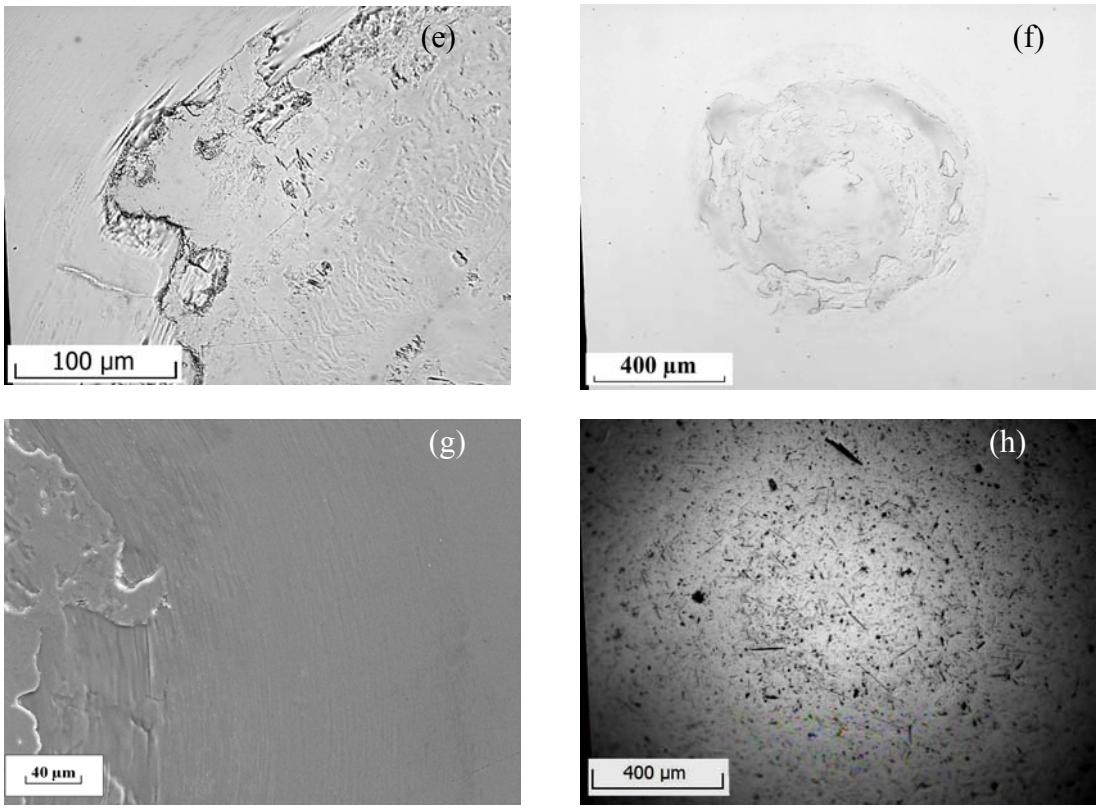


Figure 5.18 Continue.

5.2.5.2.3 Aluminium/PMMA combination

Testing under oil-lubricated conditions for this combination resulted in plate insignificantly damage after 5 minutes. In order to identify the feature of the contact area, optical photograph in polarized mode had to be taken (see Figure 5.15c). Surface in contact area was roughened without evidence of wear. At this period the slip-stick region could not be clearly identified. Small amount of fine white particles embedded on the surface in the slip region. These particles were assumed to be aluminium particles.

After 15 minutes, stick-slip region could be seen (see Figure 5.19a). However, the inner slip region and the outer slip region could not be differentiated. Very fine white particles embedded all over the slip region of the PMMA surface were intensified (see Figure 5.19b). The embedded particles in the stick region were detected at the rough area which corresponded to the impression of the aluminium ball surface. Surface wear on the plate was limited.

The outer slip region and inner slip region could be clearly identified after 30 minutes of testing (see Figure 5.19c). High amount of particles embedded in the inner slip region was found (see Figure 5.19d). The surface in the outer slip region was smoother than that in the inner slip region. The surface in this region exhibited similar features to those detected in testing against steel ball. Finer in size and lesser amount of embedded particles was observed in the outer slip region. Radial fine cracks were detected under transmission mode (see Figure 5.13e). Surface damage features were gradually developing till 180 minutes of testing including increase in of material loss, decrease of stick region and enlargement of the inner slip region (see Figure 5.19f).

After 810 minutes, more material loss was found in the inner slip region and the outer slip region (see Figure 5.16c). The outer slip region was rougher than that found after 180 minutes of testing. White particles were embedded in both slip region. The particles in the inner slip region were more intensive and coarser than in the outer slip area. SEM micrographs in the inner slip region and the outer slip region are shown in Figure 5.19(g) and 5.19(h), respectively. Both regions show similar features that is parallel ripple lines in circumferential direction. However, surface roughness in the outer region was much less than that in the inner slip region.

The ball surface experienced insignificant damage after 810 minutes of testing (see Figure 5.19i).

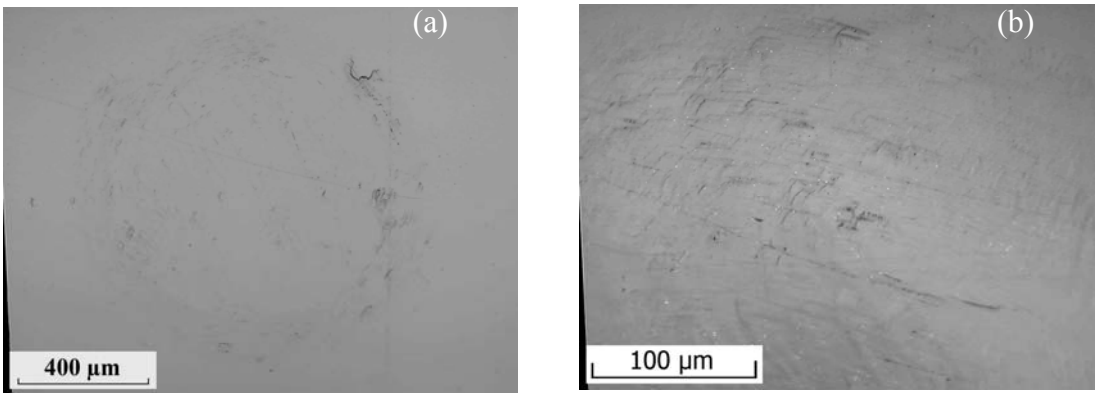


Figure 5.19 OM micrographs (a), (b), (c), (d), (e), (f) and (i) and SEM micrograph (g) and (h) of aluminium/PMMA combination. PMMA plate; (a) – (h) and ball; (i). (a) and (b) test time 15 min. (c), (d) and (e) test time 30 min., but (e) taken in transparent mode (f) test time 180 min. (g), (h) and (i) test time 810 min.

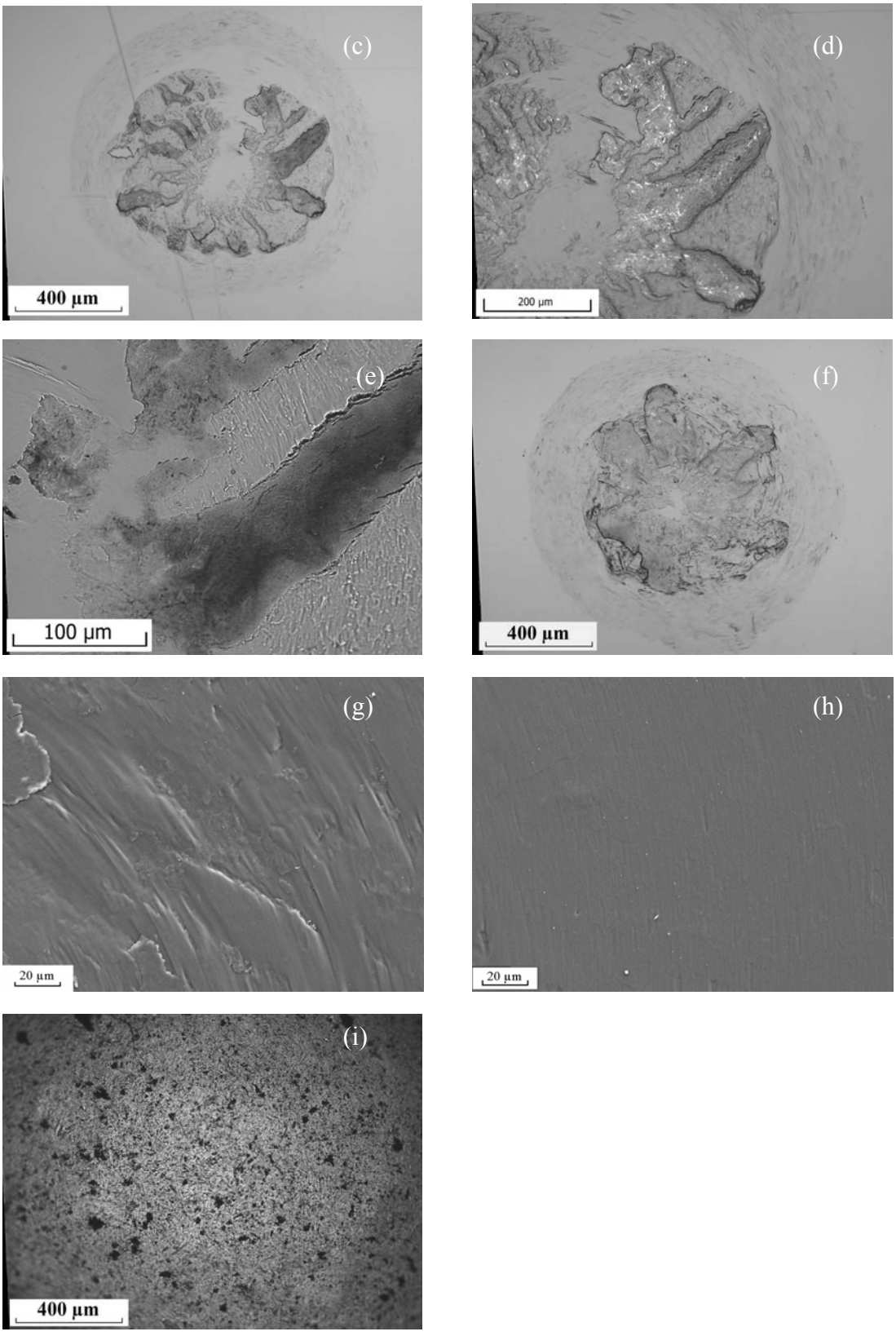


Figure 5.19 Continue.

5.2.5.2.4 Bronze/PMMA combination

For this combination of materials, surface in contact area was roughened without significant damage after the first 5 minutes (see Figure 5.15d). Using polarize mode photograph, circumferential lines oriented in parallel were observed (see Figure 5.20a). Fine yellowish shiny particles of bronze embedded in the plate surface. The stick-slip region could not be identified. These two regions could only be differentiated after 15 minutes (see Figure 5.20b). The slip region has similar texture as that previously explained for aluminium/PMMA combination. Surface in this region experienced significant damage and was embedded with bronze particles.

The inner slip region and the outer slip region could be differentiated after 30 minutes (see Figure 5.20c). The number of bronze particles embedded in the inner slip region was highest comparing to the other regions (see Figure 5.20d). The embedded particle size in the inner stick region was larger than that in outer slip area. Fine radial cracks were found in this region by using transparency mode photograph (see Figure 5.20e). Surface in the stick region was deformed resembling the asperities' shape of the bronze ball. Wear in the outer slip area was increased. The surface features in this area were similar to that produced by testing against steel and aluminium balls.

The stick region was diminished after 60 minutes of testing (see Figure 5.20f). Surface roughness of both the inner and the outer slip region increased. Material losses intensified at the boundary of the inner slip and the outer slip region. The severity of the damage progressed significantly on the entire contact area after 180 minutes. The depth of the damage and its size progressed after 810 minutes (see Figure 5.16d). Surface in the outer slip area was smoother than that in the inner slip region (see Figure 5.20g).

Wear on the ball surface could not be identified by the optical microscope until after 810 minutes of testing time.

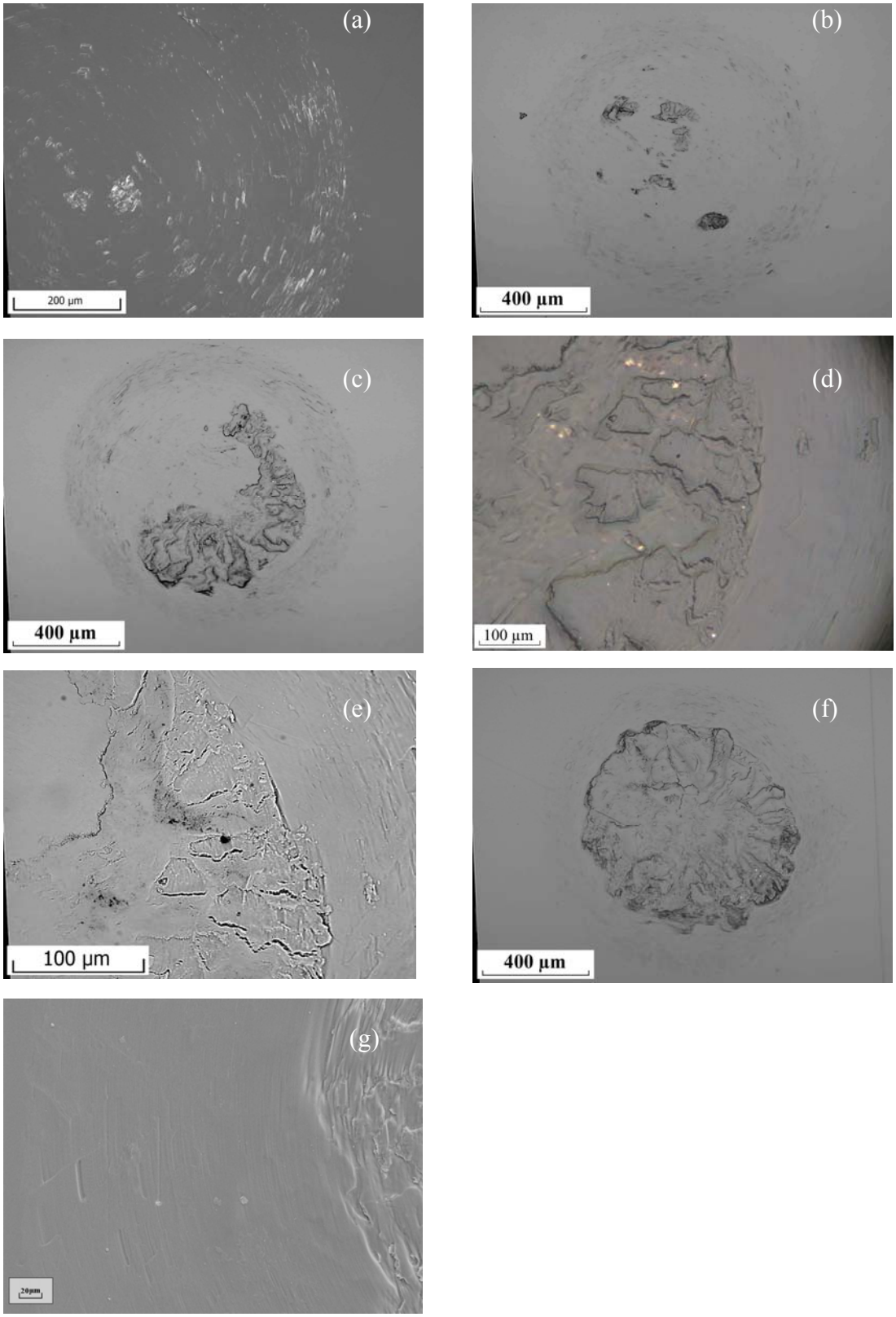


Figure 5.20 OM micrographs (a), (b), (c), (d) and (e) and SEM micrograph (f) of PMMA plate of bronze/PMMA combination (a) test time 5 min, polarize mode. (b) test time 15 min. (c), (d) and (e) test time 30 min, but (e) taken in transparency mode. (f) test time 60 min. (g) test time 810 min.

5.2.5.2.5 PMMA/PMMA combination

Surface damage in the form of surface deformation was very small in the first five minutes of testing (see Figure 5.15e). Polarized light mode had to be used in order to recognize the damage. After 15 minutes, rough surface in the inner slip region was observed (see Figure 5.21a). The contact surface did experience significant damage after 30 minutes (see Figure 5.21b). Similar surface damage features as observed for other material combinations were founded including three regions in the contact area with separate textures. Damage progressed insignificantly after 60 minutes (see Figure 5.21c). Adhesion of debris in the inner slip region was observed (see Figure 5.21d). The stick region was diminished after 180 minutes of testing time (see Figure 5.21e). Damage spread over the entire contact area. Damage intensified at the boundary between the inner slip and the outer slip region. The severity of damage did not significantly increase and the feature of damage was unchanged after 810 minutes of testing time (see Figure 5.16f and 5.21f). The worn surface in the outer slip area was rather smooth with texture similar to that explained in previous sections.

Damage of the ball surface was firstly detected after 15 minutes. The area of the damage corresponded to the damage position on PMMA plate as shown in Figure 5.21a. The corresponding damage feature was also observed on the ball surface for the other testing times (see Figure 5.21g corresponding to Figure 5.21b). Transferred material was also observed on the ball surface at the boundary of the inner slip and the outer slip area (see Figure 5.21h).

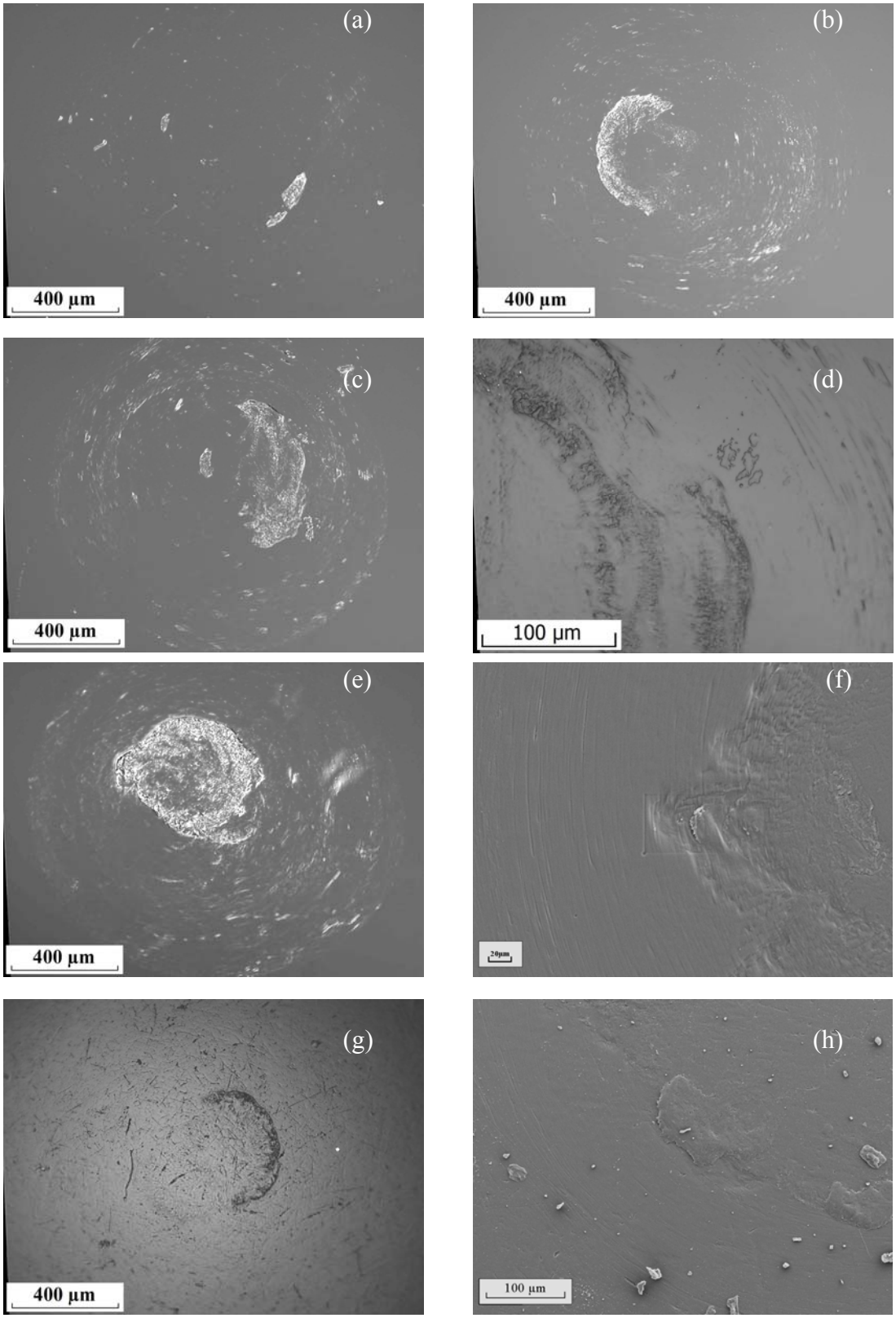


Figure 5.21 OM micrographs (a), (b), (c), (d), (e) and (g) and SEM micrographs (f) and (h) of PMMA/PMMA combination. PMMA plate; (a) – (f) and ball; (g) and (h). (a) test time 15 min, polarize mode, (b) test time 30 min, polarize mode. (c) and (d) test time 60 min, but (c) taken in polarize mode. (e) test time 180 min, polarize mode. (f) test time 810 min. (g) test time 30 min. (h) test time 810 min.

### *5.2.6 EDX Analysis of PMMA Plate Surface*

In order to confirm the adhesion between the PMMA plate and counterfaces used, energy dispersive X-ray (EDX) technique was used. Figure 5.22 shows a typical output form EDX analysis on the slip region of PMMA plate for the steel/PMMA combination. Iron and oxygen were detected in this region. This confirms that material from the steel ball was transferred onto the surface of PMMA plate. The results of element mapping are shown in Figure 5.23. The results point to a significant change of element concentration, i.e. carbon, iron and oxygen in the slip region. The element concentrations outside contact area and in the stick region were similar. This implies lack of significant adhesion in the stick region. EDX results for other contact pairs confirmed that adhesion took place but to a different extent. The Si3N4/PMMA contact proved to have the least propensity to form adhesive junctions and subsequent transfer of material.

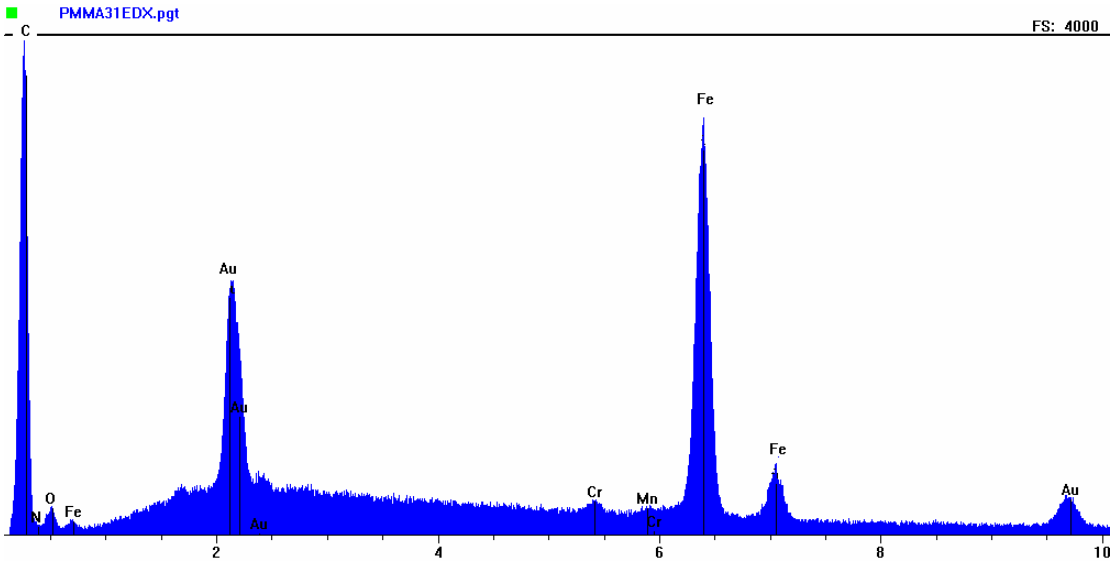


Figure 5.22 EDX analysis results show chemical compositions at the slip area of the surface of PMMA plate tested against steel ball after 810 min. Gold (Au) was from surface coating for electrical conducting purpose.

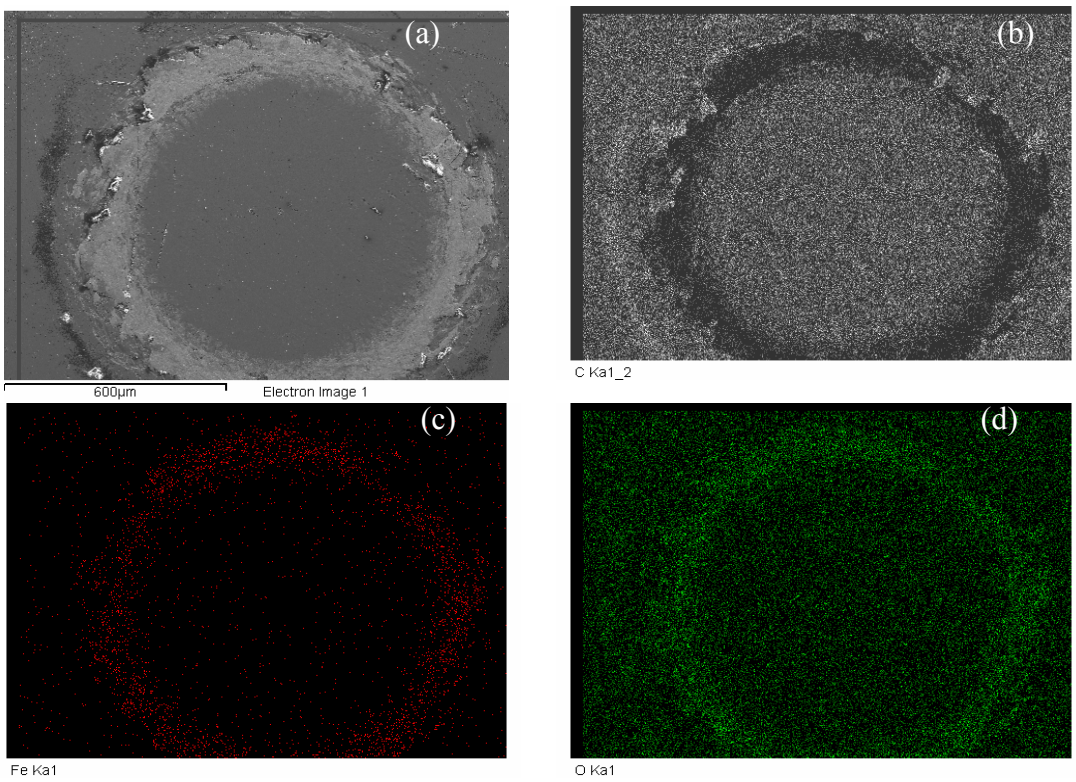


Figure 5.23 Mapping images of PMMA plate in contact area tested against steel ball for 810 min (a) electron image (b) carbon image (c) iron image and (d) oxygen image.

### *5.2.7 PMMA Plate Surface Profile Measurements*

Profile measurements were conducted across the middle of contact area. The profile was not measured in some tested samples because unable to locate the position of the damage.

#### *5.2.7.1 Dry Conditions with Time*

##### 5.2.7.1.1 $Si_3N_4$/PMMA combination

The results of profile measurements of Si3N4/PMMA combination are shown in Figure 5.24. The profile shows material loss only in the slip region. The loss gradually increased with the test time. However, the maximum depth of the profile after 810 minutes is only about 1µm. Adhesion of material was found after 5 minutes of testing time.

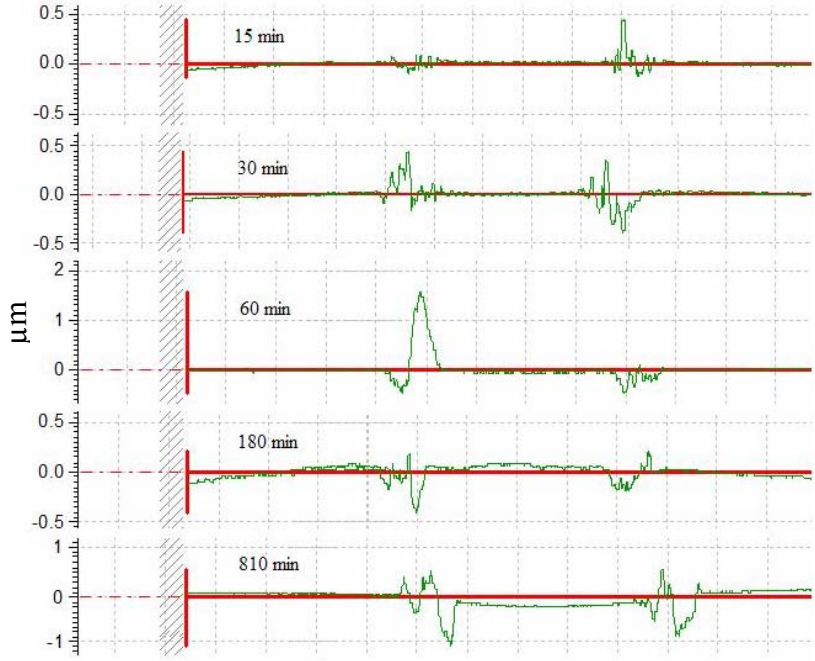


Figure 5.24 Surface profile of $Si_3N_4$/PMMA combination in dry conditions.

5.2.7.1.2 Steel/PMMA combination

The profile shows that wear and adhesion occurred within the first 5 minutes of testing time and continued until 810 minutes. Damage took place only in the slip region. The maximum depth of the profile is about 4 µm after 810 minutes.

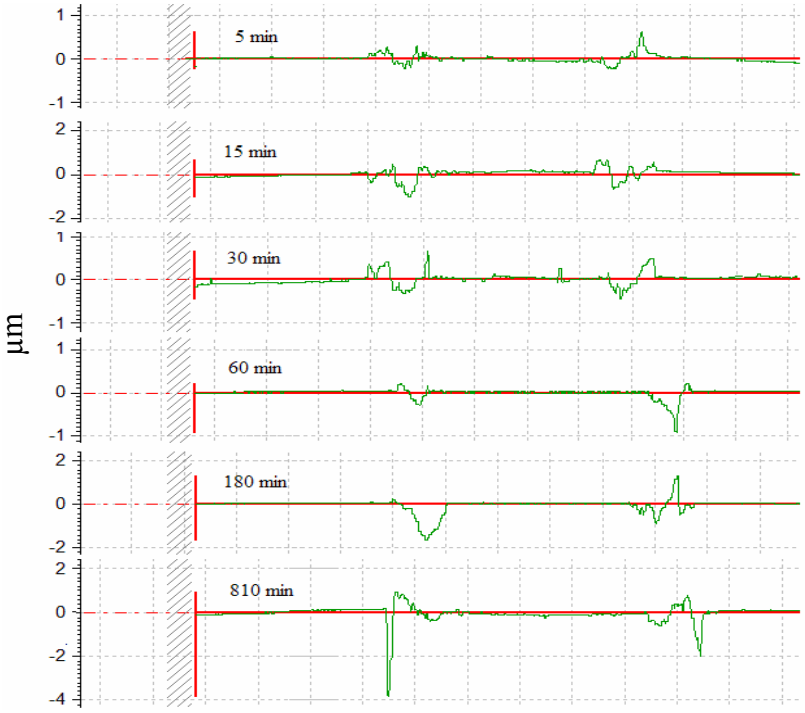


Figure 5.25 Surface profile of steel/PMMA combination in dry conditions.

5.2.7.1.3 Aluminium/PMMA combination

Figure 5.26 shows the results of surface profile measurements for aluminium/PMMA combination. Wear and adhesion in the slip region occurred within the first 5 minutes. Similar to previous contact pairs, the depth of wear scar and material volume loss increased with increasing testing time. The maximum depth of the profile is about 8 µm after 180 minutes. However, volume loss of material after 810 minutes was higher than that after 180 minutes. Damage was not obvious in the stick region.

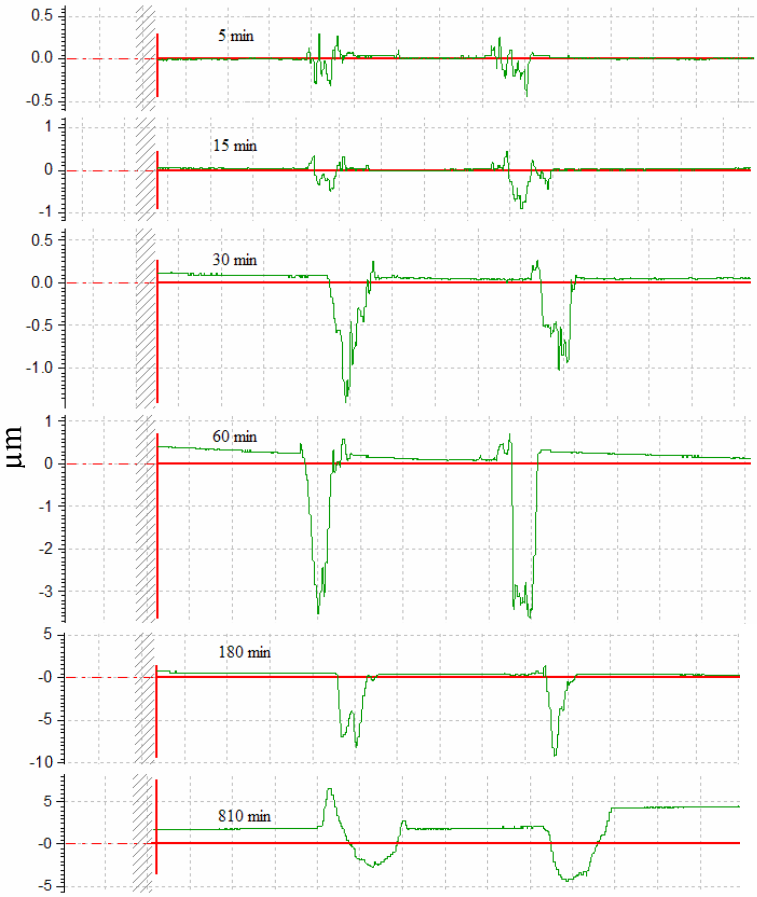


Figure 5.26 Surface profile of aluminium/PMMA in dry conditions.

5.2.7.1.4 Bronze/PMMA combination

Loss of material and adhesion were observed after the first 5 minutes of testing (see Figure 5.27). Wear damage was most severe comparing to other balls' material used. The maximum depth of the profile was 19 µm after 810 minutes. Adhesion was found along the slip region similar to other material combinations.

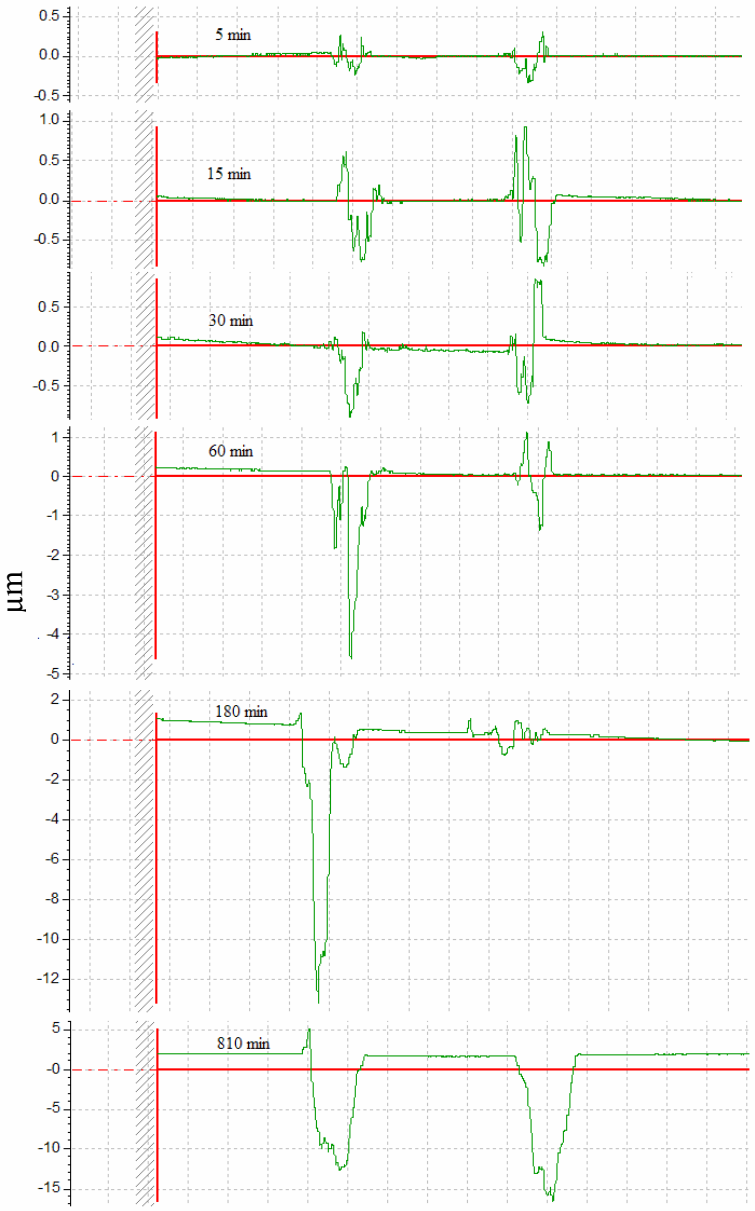


Figure 5.27 Surface profile of bronze/PMMA in dry conditions.

5.2.7.1.5 PMMA/PMMA combination

The profile shows material adhering in the slip region at the early stage of test time of 5 minutes (see Figure 5.28). The profile indicates material transferred from the ball to the plate. The height of the material accumulation increased with test time and reached 12.5 µm after 810 minutes. In the stick region insignificant wear was observed.

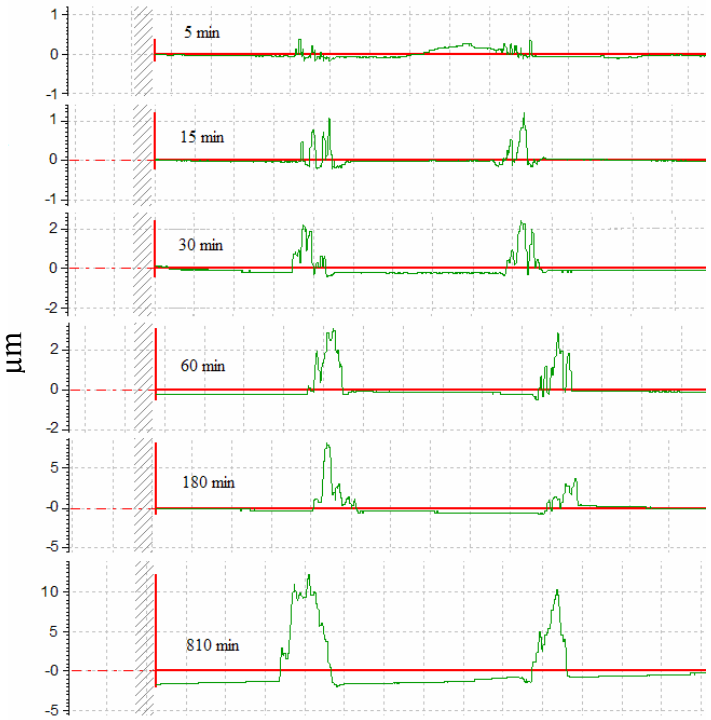


Figure 5.28 Surface profile of PMMA/PMMA in dry conditions.

5.2.7.1.6 Compare different contact pair in dry conditions

With the exception of silicon nitride ball, adhesion was clearly observed at the early test time of 5 minutes for all other contact pairs. The progression of wear was different. Bronze triggered the most severe wear and the deepest profile. After 810 minutes, the depth of wear profile of PMMA plate, from the deepest to the shallowest when in contact with different balls, can be ranked as: bronze, aluminium, steel, silicon nitride. By contrast, the ball was damaged only in the PMMA/PMMA combination.

*5.2.7.2 Oil-lubricated condition with time*

5.2.7.2.1 $Si_3N_4$/PMMA combination

Damage after the first 5 minutes test time was insignificant and hardly identifiable. After 15 minutes adhesion was observed especially at the boundary of the stick region (see Figure 5.29). The width and the depth of wear track increased with testing time. However, progression of damage severity was low. Maximum depth of the wear scar was only 1.5 µm after 810 minutes. Adhesion was found at the boundary of stick region throughout testing duration.

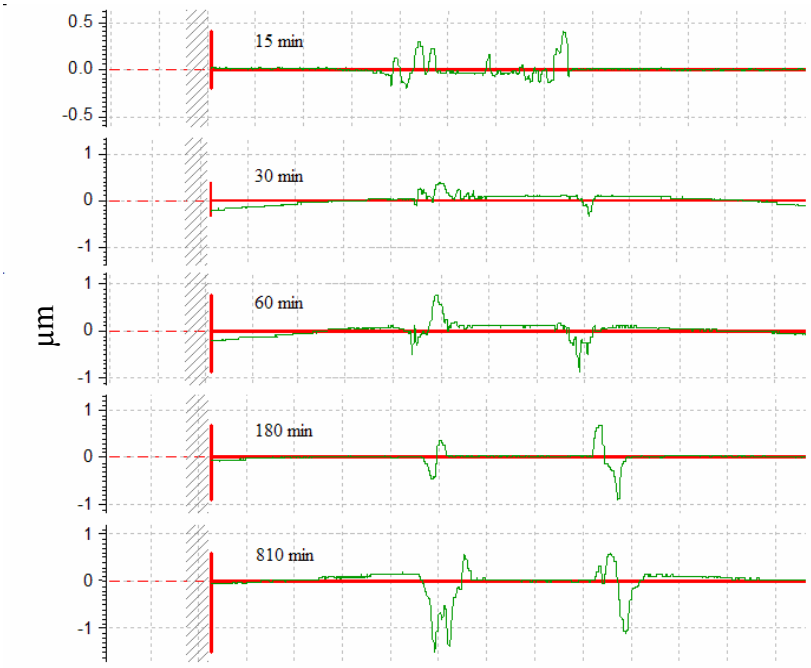


Figure 5.29 Surface profile of $Si_3N_4$/PMMA combination in oil-lubricated conditions.

5.2.7.2.2 Steel/PMMA combination

For this combination damage was detected after the first 5 minutes (see Figure 5.30). Adhesion was observed at the boundary of the stick region. The depth of wear track and material loss volume both increased with increasing test time. Maximum depth was 7 µm after 810 minutes of testing time. Material loss firstly occurred at the slip region. The damage then propagated to the stick region.

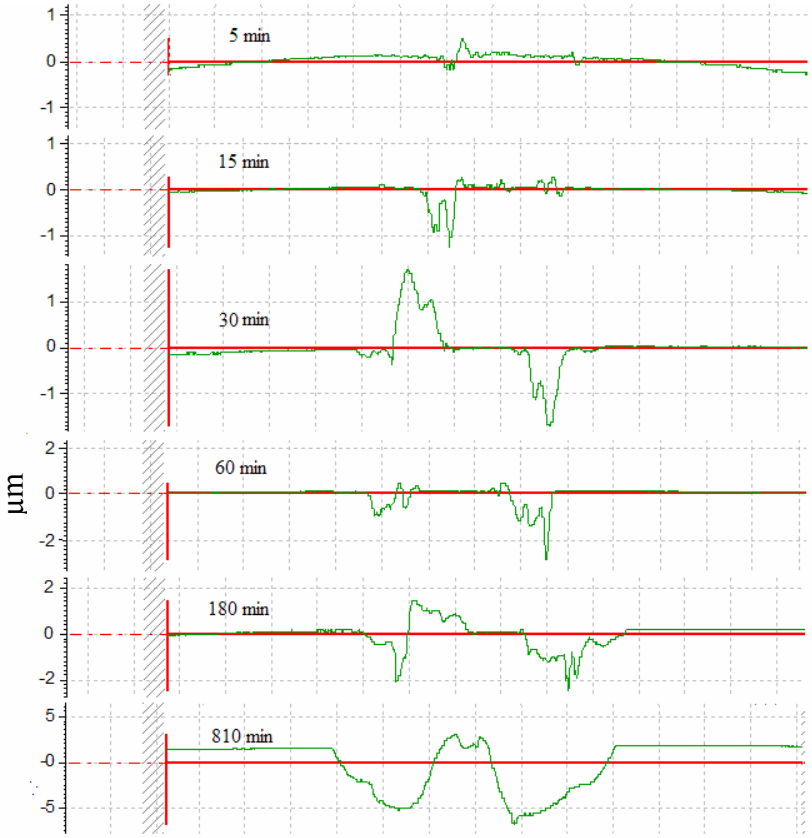


Figure 5.30 Surface profile of steel/PMMA combination in oil-lubricated conditions.

5.2.7.2.3 Aluminium/PMMA combination

Material loss in the slip region was detected after 5 minutes of the testing time (see Figure 5.31). After 30 minutes adhesion in the stick region was observed and continued to be observed until 810 minutes of testing was reached. The depth of wear track increased with increasing test time. Maximum depth of about 4 µm was reached after 180 minutes and that did not increase until 810 minutes. However, material loss volume increased during this period.

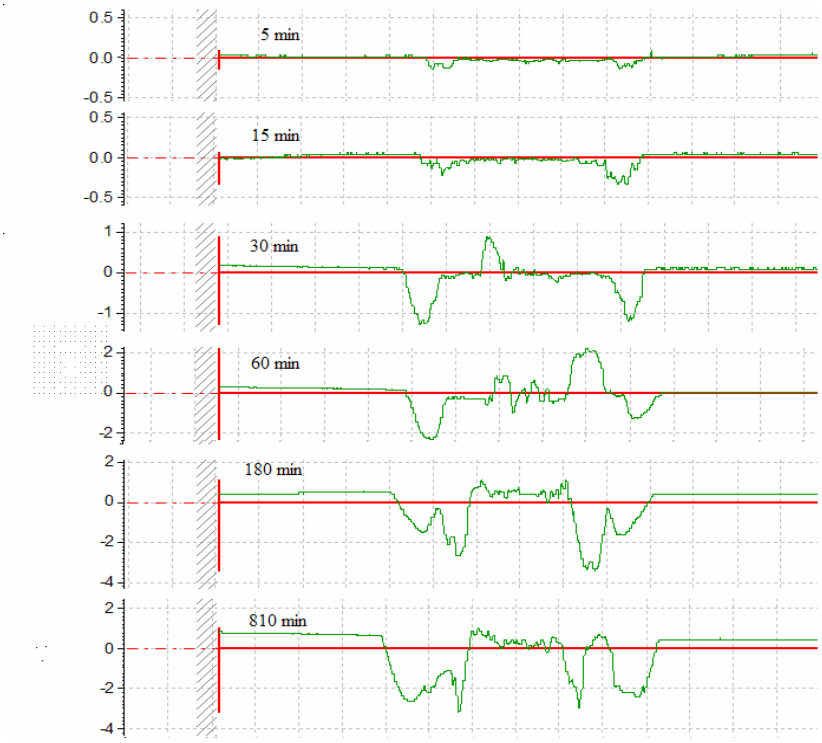


Figure 5.31 Surface profile of aluminium/PMMA combination in oil-lubricated conditions.

5.2.7.2.4 Bronze/PMMA combination

Material loss occurred after 5 minutes within the slip region and increased as the test time lengthened to cover the whole contact area (see Figure 5.32). Maximum depth of the profile was about 7.5 µm after 810 minutes. The sign of adhesion was found in the stick region especially at the boundary during the first five minutes of testing time.

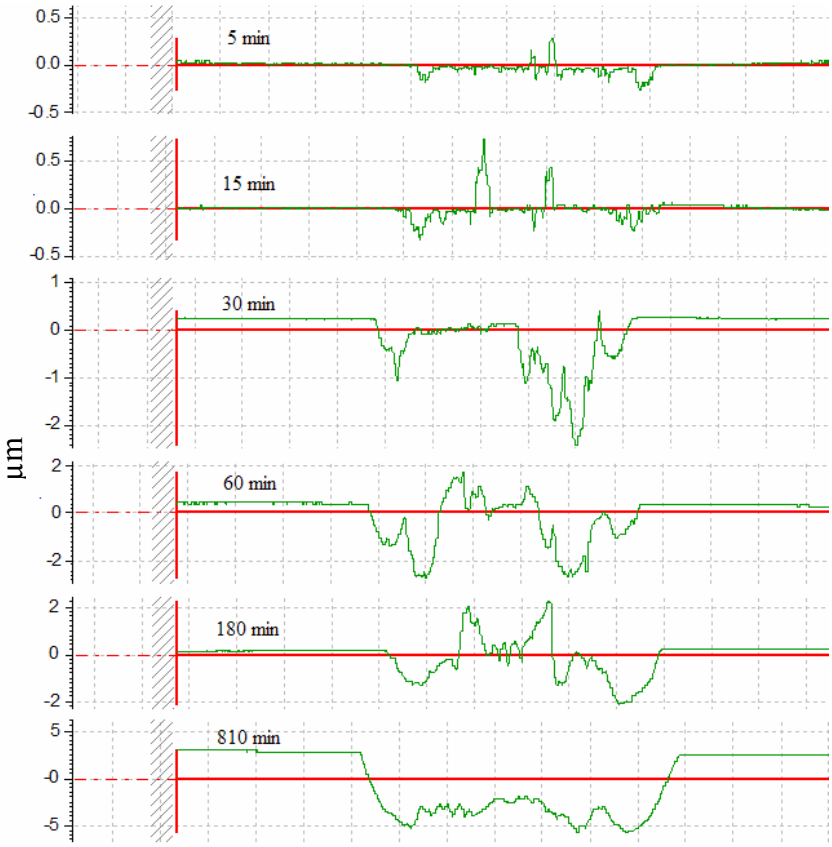


Figure 5.32 Surface profile of bronze/PMMA combination in oil-lubricated conditions.

5.2.7.2.5 PMMA/PMMA combination

Up to 15 minutes of testing the damage could be neglected as evidenced by surface observations. Wear damage started at boundary of the stick region after 30 minutes and propagated in a shallow groove (see Figure 5.33). After 180 minutes, the damage was observed throughout the contact area. The depth of profile increased slowly with test time until reaching the maximum depth approximately 2.3 µm after 810 minutes.

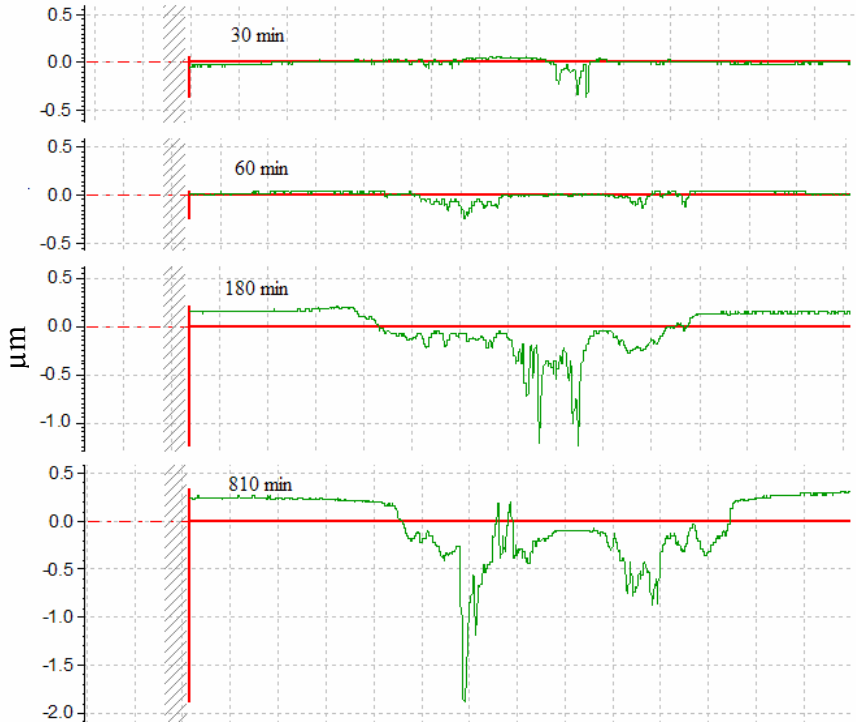


Figure 5.33 Surface profile of PMMA/PMMA combination in oil-lubricated conditions.

5.2.7.2.6 Compare different contact pair in oil-lubricated conditions

Unlike for dry contact conditions, adhesion and wear were firstly observed at different test time. Adhesion was clearly observed after 5 minutes of testing time for steel, aluminium and bronze, after 15 minutes for silicon nitride and after 30 minutes for PMMA. After 810 minutes, the maximum depth of wear track on PMMA plate ranked from the shallowest to the deepest for different ball materials is as follows: PMMA, silicon nitride, aluminium, steel and bronze, respectively. Material volume loss of PMMA/PMMA combination was small comparing to another contact pairs.

*5.2.7.3 Effect of Dry and Oil-lubricated conditions in the same contact pair*

5.2.7.3.1 $Si_3N_4$/PMMA combination

Adhesion under dry conditions was observed at the entire slip region. By contrast, adhesion under lubricated conditions was found at the boundary of the stick region while at the slip region that was not apparent. The damage after 810 minutes for both conditions was almost undistinguishable for one another. The depth of wear in dry conditions and oil-lubricated conditions was 1μm and oiled 1.5 μm, respectively.

5.2.7.3.2 Steel/PMMA combination

Material volume loss and the depth of wear track in oil-lubricated conditions were higher than in dry contact conditions after 810 minutes. The depth of wear was 4 μm in dry conditions and 7 μm in oil-lubricated conditions. However, subsurface cracks should be accounted for the severity of damage in dry conditions. In dry conditions, material adhesion was found at the slip region, while it occurred at the boundary of stick region in oil-lubricated conditions.

5.2.7.3.3 Aluminium/PMMA combination

The severity of damage in dry conditions was more intensive than that resulting from testing in oil-lubricated conditions; e.g. the depth of wear track after 810 minutes was 7 μm in dry conditions and 3 μm in oil-lubricated conditions. The damage to the stick region in dry conditions was not observed, but it occurred in oil-lubricated conditions. Adhesion was found around slip region for dry conditions, but adhesion occurred in the stick region and the boundary of the stick region in oil-lubricated conditions.

5.2.7.2.4 Bronze/PMMA combination

The damage occurred at an early stage for both contact conditions. However, the depth of wear track in dry conditions was greater; i.e. 19 μm after 810 minutes in dry conditions and 7.5 μm in oil-lubricated conditions. Wear occurred over entire contact area in oil-lubricated conditions, but damage did occur in the slip region in dry conditions.

5.2.7.3.5 PMMA/PMMA combination

In dry conditions, wear damage of PMMA plate was insignificant. High amount of material transfer from the ball to the plate took place. In oil conditions, however, material losses of PMMA plate were observed to occur in a shallow worn out surface. Only small amount of transferred materials was observed in the inner slip region.

### *5.2.8 Fatigue Life*

The contact radius was measured for all contact pairs. It was found that the contact radius was different for various ball materials used in dry conditions an oil-lubricated conditions. In dry conditions, two regions; i.e. slip and stick region in contact area could be distinguished. In oil-lubricated conditions, contact area was consisting of three regions including stick region, inner slip region and outer slip region. The following results present the relation between testing time and the size of the radius of those regions.

#### *5.2.8.1 Effect of contact combination*

5.2.8.1.1 Dry conditions

Figure 5.34 shows the results of radius measurements for different testing time and different contact combinations under dry contact conditions. In general, the size of the slip region radius for every combination of materials increased with increasing testing time. The radius of the slip region of the PMMA/PMMA combination was the largest. This was expected from the calculated Hertz's radius, which, for different ball materials, can be ranked from the largest to the smallest as follows: PMMA, aluminium, bronze, steel, and silicon nitride. This ranking agrees with the severity of damage of the plate deduced from surface observations described earlier.

The size of the stick radius of PMMA/PMMA combination was the highest at the early stage of testing time until 180 minutes. At 810 minutes the size decreased and was comparable to that typical for other combinations. The reason behind this may be that the damage of the ball significantly increased with the testing time. The size of the stick radius

for other combinations of materials was fluctuating in test time interval from five minutes and 180 minutes. At 810 minutes, the scatter decreased. The ranking from the largest to the smallest size of the stick radius was as follows: steel, PMMA, bronze, aluminium and silicon nitride, respectively.

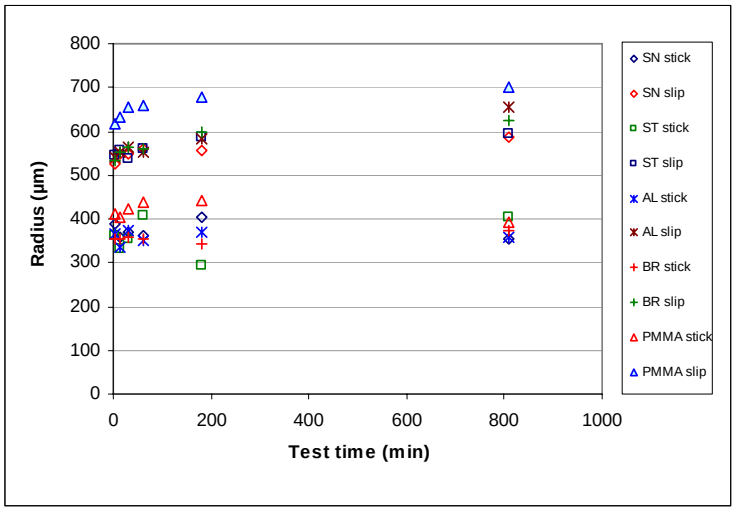


Figure 5.34 Relationships between test time and stick radius and slip radius for different contact pairs in dry conditions. The abbreviations in the graph represent the combination between the PMMA plate and the ball as follows; SN = $Si_3N_4$, ST = steel, AL = aluminium, BR = bronze and PMMA = PMMA.

5.2.8.1.2 Oil-lubricated conditions

Figure 5.35 shows the results of radius measurements as a function of testing time for different contact combinations in oil-lubricated conditions. In general, the order of the outer slip radius for all combinations of materials agreed with the calculated Hertz's radius. The size of the outer slip radius increased with increasing test time for every combination of material.

The size of the inner slip radius generally tended to increase with testing time although some points occasionally swung. The most swinging was for PMMA and the least swinging was for silicon nitride. The sizes were highly different for different material combinations at the early stage of testing time, but converged to a narrow band after 810 minutes.

The sizes of the stick radius were highly scattered for all material combinations. The size has different trend for each material combination. In case of, PMMA/PMMA combination the size of the stick radius has an increasing trend. The combination of steel/PMMA and bronze/PMMA, however, showed a decreasing trend. For $Si_3N_4$/PMMA combination, the size was alternating until 60 minutes of testing time and increased onward. The size of aluminium/PMMA combination decreased from the start until 180 minutes, but increased after that.

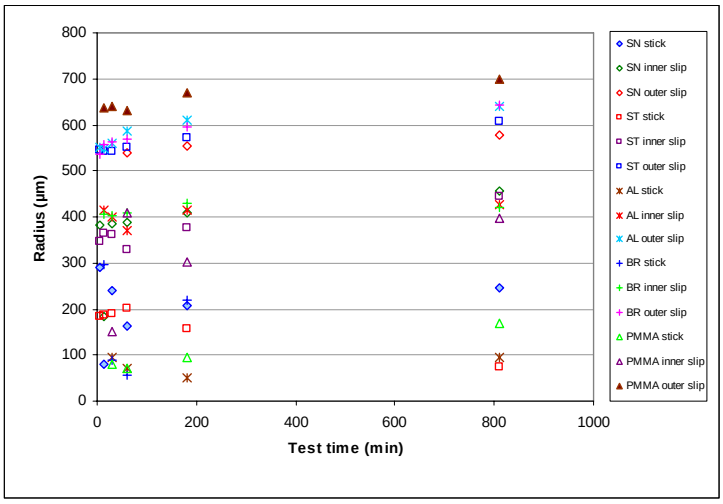


Figure 5.35 Relationships between test time and stick radius, inner slip radius and outer slip radius of different contact pairs in oil-lubricated conditions. The abbreviations in the graph represent the combination between the PMMA plate and the ball as follows; SN = $Si_3N_4$, ST = steel, AL = aluminium, BR = bronze and PMMA = PMMA.

### *5.2.8.2 Effect of oil lubrication*

This section presents the results of contact radius measurements for dry and oil-lubricated conditions and compares them.

#### 5.2.8.2.1 $Si_3N_4$/PMMA combination

For this combination, the outer slip radius could not be measured until 60 minutes (see Figure 5.34). The size of the slip radius in dry conditions was the same as that for the outer slip radius in oil-lubricated conditions during entire test time. At five minutes of testing

time the slip radius in dry conditions was slightly greater than that calculated from Hertz equation. The slip radius in dry conditions and the outer slip radius in oil-lubricated conditions increased with testing time and the slip radius of dry conditions was larger than the Hertz's radius after 15 minutes.

The stick radius in dry conditions was larger than that in oil-lubricated conditions for the entire testing period. It seems to have tendency to decrease with testing period. The stick radius in oil-lubricated conditions was fluctuating during the first 60 minutes. After that the radius tended to increase with testing time.

The inner slip radius in oil-lubricated conditions tended to increase with testing time. The size of the radius was in the range of the stick radius magnitude observed in dry conditions. Their radii for the entire range, except at 15 minutes of testing time, were larger than the stick radii in dry conditions.

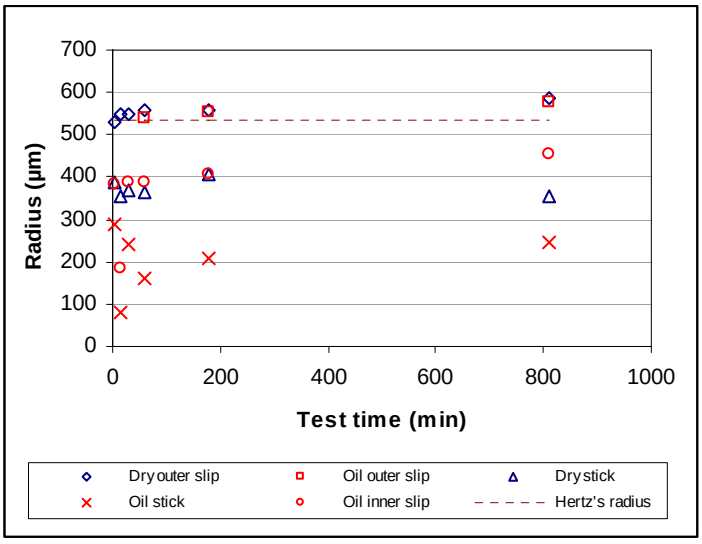


Figure 5.36 Relationships between test time and contact radius in dry and oil-lubricated conditions of Si3N4/PMMA combination.

5.2.8.2.2 Steel/PMMA combination

Figure 5.37 shows the contact radius of PMMA plate tested against steel ball. The slip radius in dry conditions and the outer slip radius in oil-lubricated conditions were insignificantly different in each point. The radiuses of both conditions at the beginning of testing time were slightly larger than that obtained from the Hertz's theory. The radius increased with increasing testing time.

The size of the stick radius in dry conditions changed alternatively. It lied between 290 and 400 µm. The stick radius in oil-lubricated conditions was smaller than that in dry conditions for the entire testing period. The radius has a tendency of reduction with increasing of testing period.

The size of the inner slip radius in oil-lubricated conditions was in the same range of the stick radius in dry conditions. The radius size tended to increase with the testing period.

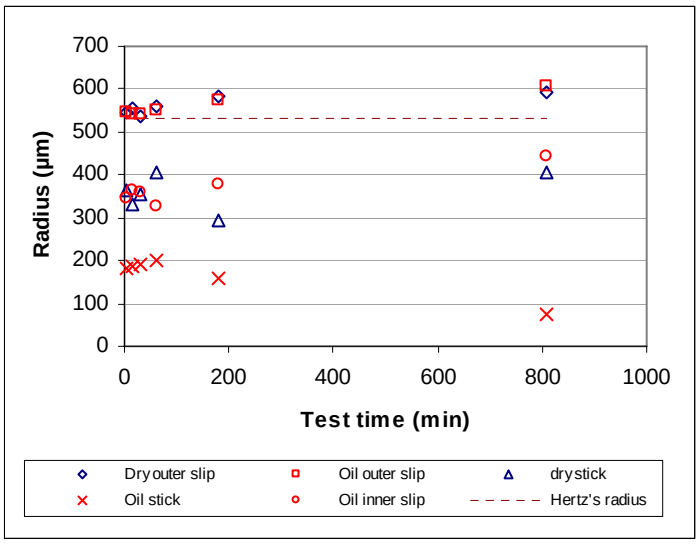


Figure 5.37 Relationships between test time and contact radius in dry and oil-lubricated conditions of steel/PMMA combination.

5.2.8.2.3 Aluminium/PMMA combination

Figure 5.38 shows the contact radius of PMMA plate tested against aluminium ball. It should be noted that the stick radius and the inner slip radius in oil-lubricated conditions could not be measured after five minutes. For this combination of materials, the size of the slip radius in dry conditions and the outer slip radius in oil-lubricated conditions were almost the same for the entire testing period. The sizes of radiuses in both conditions were slightly greater than that calculated Hertz's radius at the beginning of the testing time. The sizes increased with increasing testing period.

The stick radius of dry conditions was altering with testing time. The radius lied between 334 µm and 370 µm. The size of the stick radius in oil-lubricated conditions was smaller than that in dry conditions. The size of the radius lined between 50 µm and 96 µm. The radius decreased from 30 minutes to 180 minutes. However, it increased again after 810 minutes, but the value was not different from 30 minutes testing time.

The inner slip radius in oil-lubricated conditions was in the same range of the stick radius in dry conditions. The radius size, however, was greater than that of the stick radius in dry conditions for the same testing time. As test time prolong the inner slip radius increased.

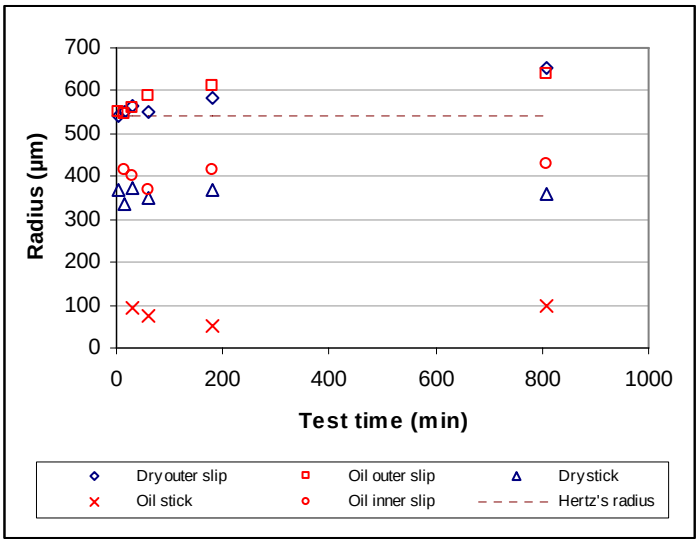


Figure 5.38 Relationships between test time and contact radius in dry and oil-lubricated conditions of aluminium/PMMA combination.

5.2.8.2.4 Bronze/PMMA combination

The results of contact radius measurement in case of test against bronze ball are shown in Figure 5.39. The inner slip radius in oil-lubricated conditions could not be measured after five minutes of testing time. The size of the slip radius in dry conditions and the outer slip radius in oil-lubricated conditions were almost similar for the entire testing period. The size of the radius in both conditions agreed with the calculated Hertz's radius at the beginning of the test. Both slip radius and outer slip radius sizes increased with increasing testing period.

The stick radius in dry conditions at the end of testing period of 810 minutes was slightly larger than at the beginning of test. The stick radius in oil-lubricated conditions tended to decrease with testing time except at 180 minutes. The radius size was highly changeable and decreased to zero after 810 minutes.

The inner slip radius in oil-lubricated conditions was in the same magnitude as the stick radius in dry conditions. However, the size was larger than the stick radius in dry conditions for the same testing time. The inner slip radius increased slightly with testing period.

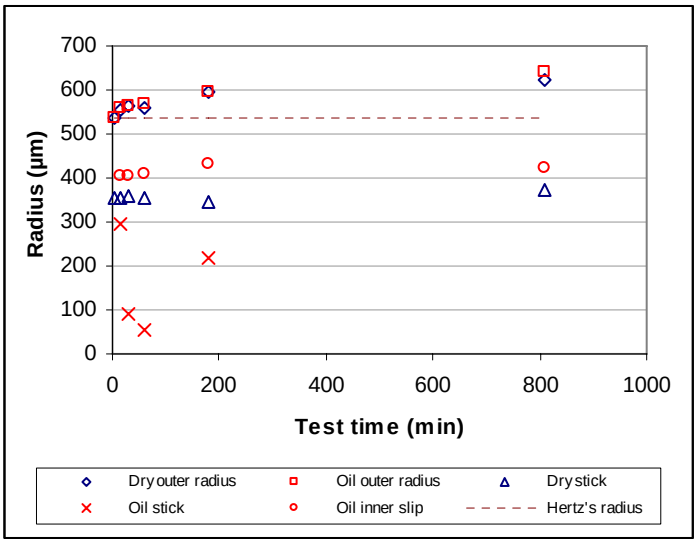


Figure 5.39 Relationships between test time and contact radius in dry and oil-lubricated conditions of bronze/PMMA combination.

5.2.8.2.5 PMMA/PMMA combination

The results of contact radius measurements for this combination are shown in Figure 5.40. The sizes of the slip radius in dry conditions and the outer slip radius in oil-lubricated conditions increased with increasing testing time. In contrast to the other combinations, contact radii of PMMA/PMMA combination in both conditions were smaller than the calculated Hertz's radius at the beginning of the testing period. The radii were just above the calculated radius after 810 minutes of testing time.

The size of the stick radius in dry conditions increased gradually with increasing testing time up to 180 minutes afterwards it decreased. The stick radius in oil-lubricated conditions tended to increase with testing time.

The size of the inner slip radius in oil-lubricated conditions was highly changeable and smaller than that the stick radius in dry conditions at the early of testing. The radius increased with the testing time and reached the stick radius value in dry conditions after 810 minutes of testing.

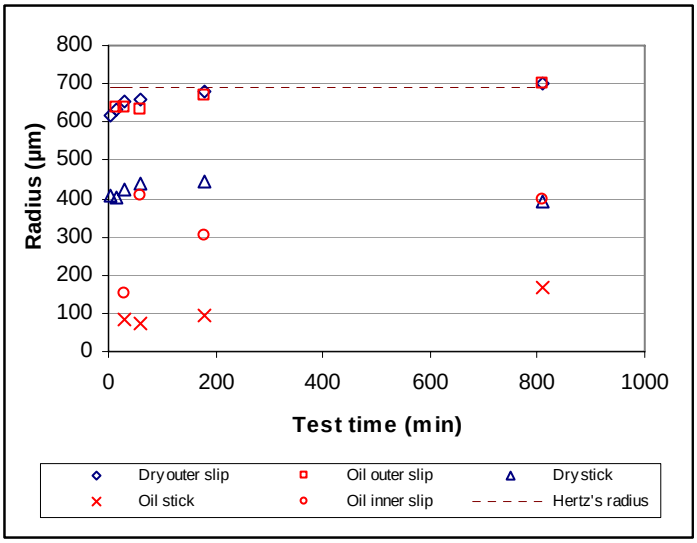


Figure 5.40 Relationships between test time and contact radius in dry and oil-lubricated conditions of PMMA/PMMA combination.

## 5.3 Dynamic Contact Fatigue of Plasma Sprayed Coatings

### *5.3.1 Introduction*

This section presents test results of dynamic contact fatigue of plasma sprayed of molybdenum coating and titanium coating. The results include micro-hardness test, surface observations, EDX analysis, weight loss measurements, wear track measurements, and fatigue life in dry conditions and seawater conditions.

### *5.3.2 Micro-hardness measurements*

All hardness measurements were done on cross sectioned specimens using a load of 100 g. The average hardness values for molybdenum and titanium coatings were 441 N/mm$^2$ and 423 N/mm$^2$, respectively. Hardness varied between 220 - 557 N/mm$^2$ for molybdenum coating and 170 - 746 N/mm$^2$ for titanium coating. These variations in hardness values probably resulted from high variations of coating microstructure. The average hardness of steel ball was 624 N/mm$^2$ with hardness range 588-661 N/mm$^2$. Substrate had average hardness value of 175 N/mm$^2$ with hardness range 153-189 N/mm$^2$.

### *5.3.3 Surface Observations of Coated Surfaces*

Surface observations were conducted after rolling contact fatigue test using a stereo microscope, an optical microscope (OM) and a scanning electron microscope (SEM). The examinations were carried out on both the disc and the ball. Example photographs of the disc and the balls after testing are shown in Figure 5.41.


Figure 5.41 Overview of titanium coating disc and balls; (a) and (b) dry conditions, after 37,422 cycles; (c) and (d) seawater conditions, after 149,686 cycles.

*5.3.3.1 Molybdenum coating*

5.3.3.1.1 Dry conditions

Figure 5.42a shows the contact track surface in dry conditions after 37,422 load cycles. Surface of the contact track was rough and adhering layer of material was observed (see Figure 5.42b and 5.42d). Surface of adhering material was smoother than the remaining contact track surface. In back scattered electron image (BEI) (see Figure 5.42c) the colour in that area was darker than other areas of the contact track. This indicates a different kind of material or compound. The edge of the adhering material area was in the form of a cliff (see more details in Fig 5.42d). In general, surface of the contact track showed no obvious deformations. The ball surface was covered by transferred material (see Figure 5.42e). The edge of the transferred material was also in the form of a cliff. The surface of uncovered area of the ball was not markedly damaged. The uncovered area of the ball surface, as seen in BEI, shows dark colour which indicates the iron (see Figure 5.42f). Comparing to the

adhering material surface of Figure 5.42c, it could be supposed that the adhering material on the surface is composed of the same elements.

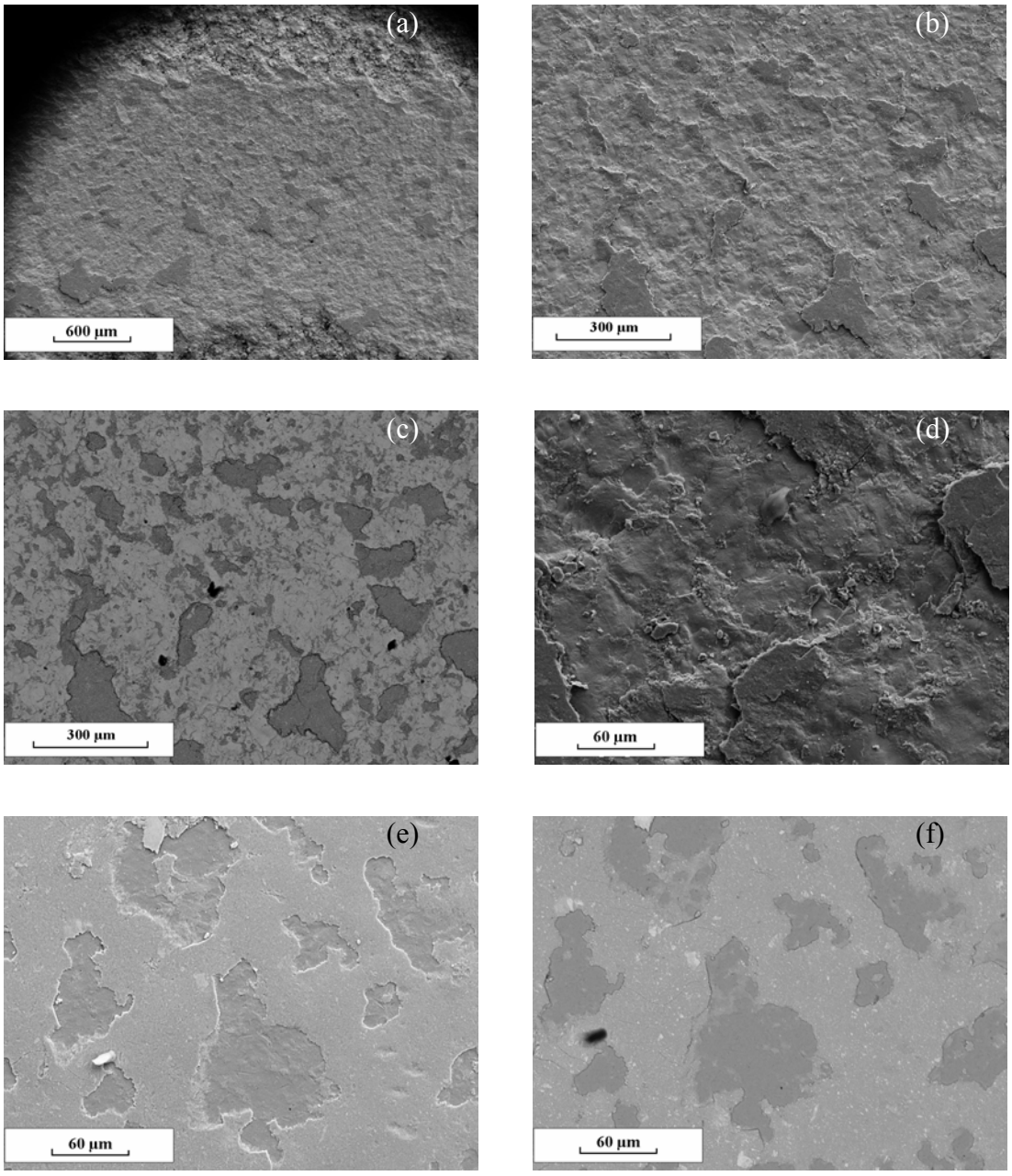


Figure 5.42 SEM micrograph of molybdenum coating in dry conditions after 37,422 load cycles; wear track (a), (b), (d) secondary electron images (SEI) (c) back scatter electron image (BEI) , ball surface (e) SEI and (f) BEI.

5.3.3.1.2 Seawater conditions

In seawater, surface of the contact track was relatively smooth after 56,132 load cycles (see Figure 5.43a) and wear did not commence (see Figure 5.43b). Some areas of the contact track were covered with a thin film of corrosion products indicated by dark areas visible in Figure 5.43b and 5.43d. The BEI also showed dark colour in the corrosion products' area (see Figure 5.43c). The dark area may be assumed to be composed of high amount of iron. Deformation of the contact track surface was observed (see Figure 5.43d).

In contrast to testing in dry conditions, the ball surface was rather smooth without transferred material (see Figure 5.43e). Some small corrosion pits were observed with low density distribution. High magnification of the ball surface revealed shallow scratches which indicated abrasion (see Figure 5.43f). Examination with optical microscope revealed shiny bright surface covered with small portion of distributed yellowish thin film of corrosion products.

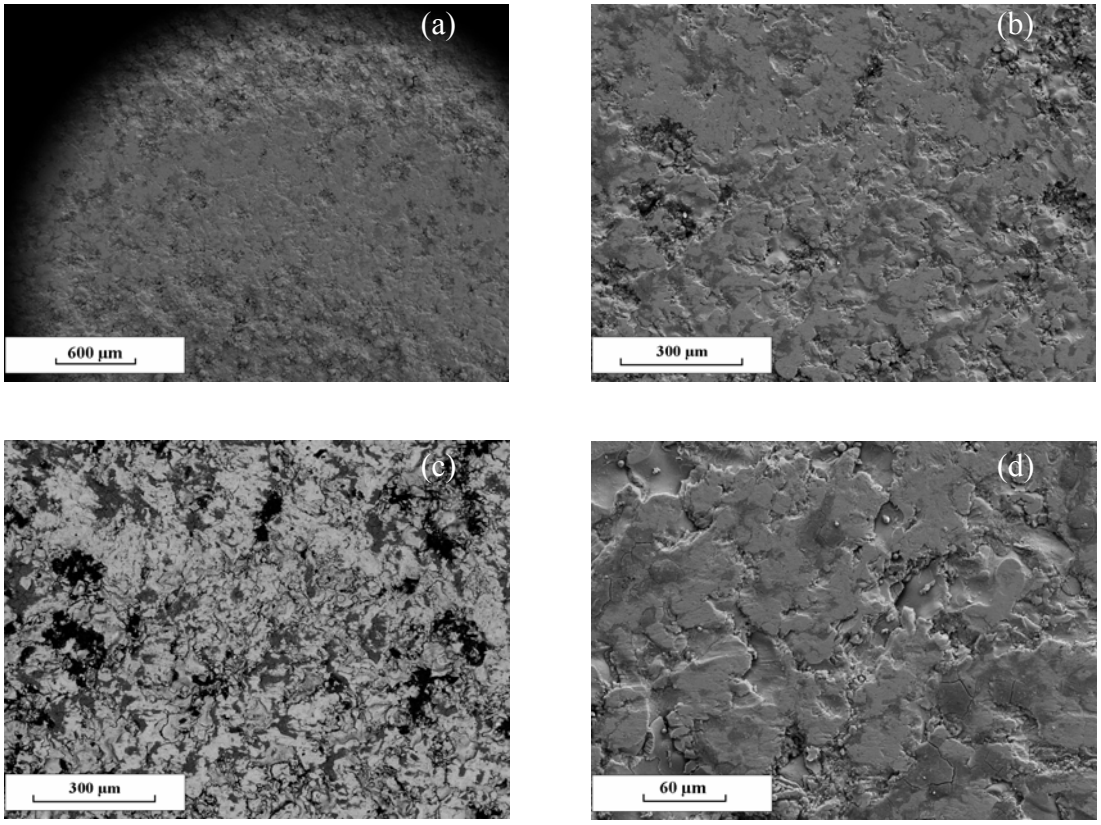


Figure 5.43 SEM micrograph of molybdenum coating in seawater conditions after 56,132 load cycles; wear track (a), (b), (d) secondary electron images (SEI) (c) back scatter electron image (BEI), ball surface (e) and (f) SEI.

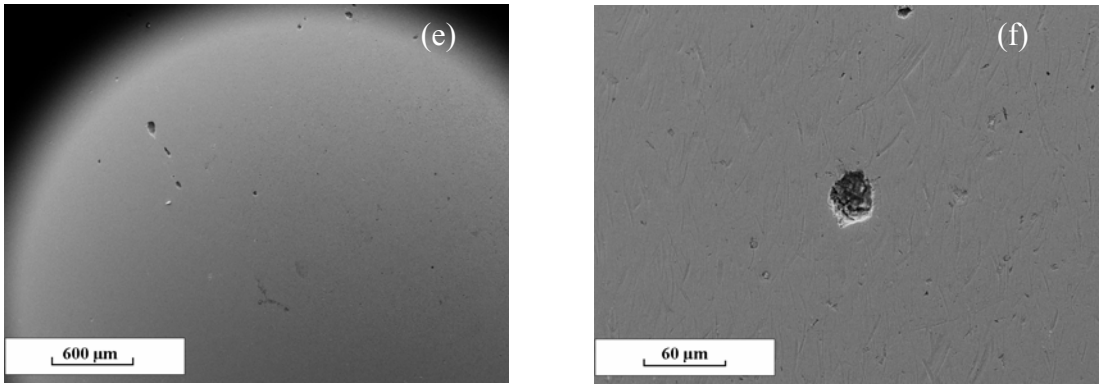


Figure 5.43 Continue.

*5.3.3.2 Titanium coating*

5.3.3.2.1 Dry conditions

Figure 5.44 shows the contact track surface of titanium coating and surface of the ball after 37,422 load cycles in dry conditions. Surface of the contact track was rough and the layer of material adhering to the surface was observed (see Figure 5.44a). Surface deformation and smearing layer in some places were observed (see Figure 5.44b and 5.44d). Shearing was detected on the track surface and the ball indicating sliding during rolling. The edge of the adhering material showed deformation (see Figure 5.44d). The BEI showed dark colour in the adhering material area (see Figure 5.44c), which also implies iron rich location.

Transferred material was all over the ball surface (see Figure 5.44e). Its thickness of was, however, uneven. The uncovered surface of the ball hardly suffered any damage. The transferred material area in BEI showed dark colour indicating different compositions from that of the steel ball (see Figure 5.44f).

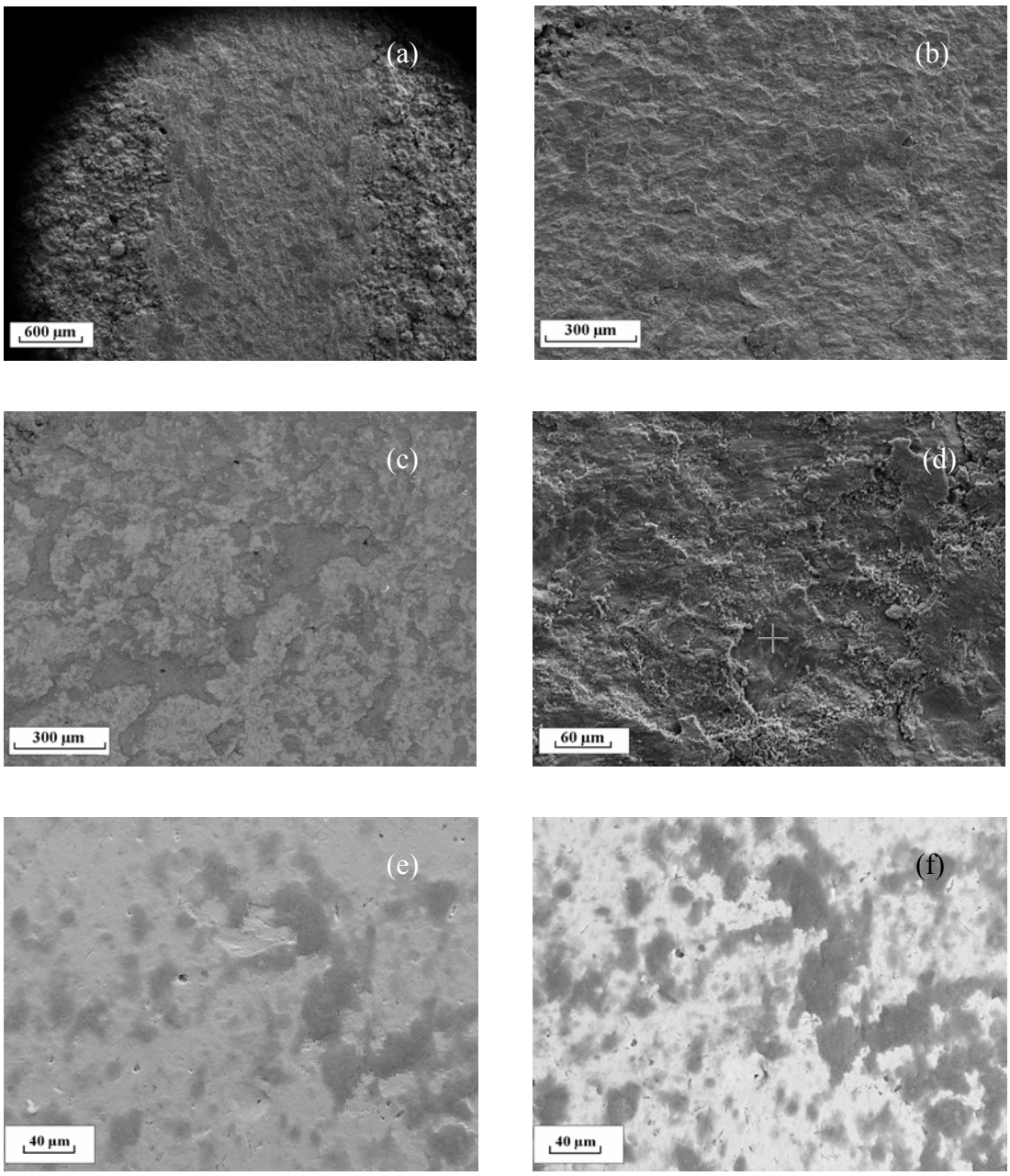


Figure 5.44 SEM micrograph of titanium coating in dry conditions after 37,422 load cycles; wear track (a), (b), (d) secondary electron (SE) images (c) back scatter electron (BE) image , ball surface (e) SE image and (f) BE image.

5.3.3.2.2 Seawater conditions

In seawater conditions, the contact track surface was smooth with visible deformation (see Figure 5.45a, 5.45b and 5.45d). Thin layer of corrosion products covering the coating surface could be identified, especially under optical microscope. The BEI showed, however, that corrosion products' film on the track surface were less than that appeared on

the molybdenum coating surface (see Figure 5.45c). Spalling occurred on the track surface after 523,902 load cycles (see details in section *5.3.5.2.2*).

In general, the ball surface was smooth and bright (see Figure 5.45e). Small corrosion pits were observed with low distribution density. At high magnification, scratches appeared all over the surface of the ball (see Figure 5.45f). Very thin film of corrosion products covered the surface in some area.

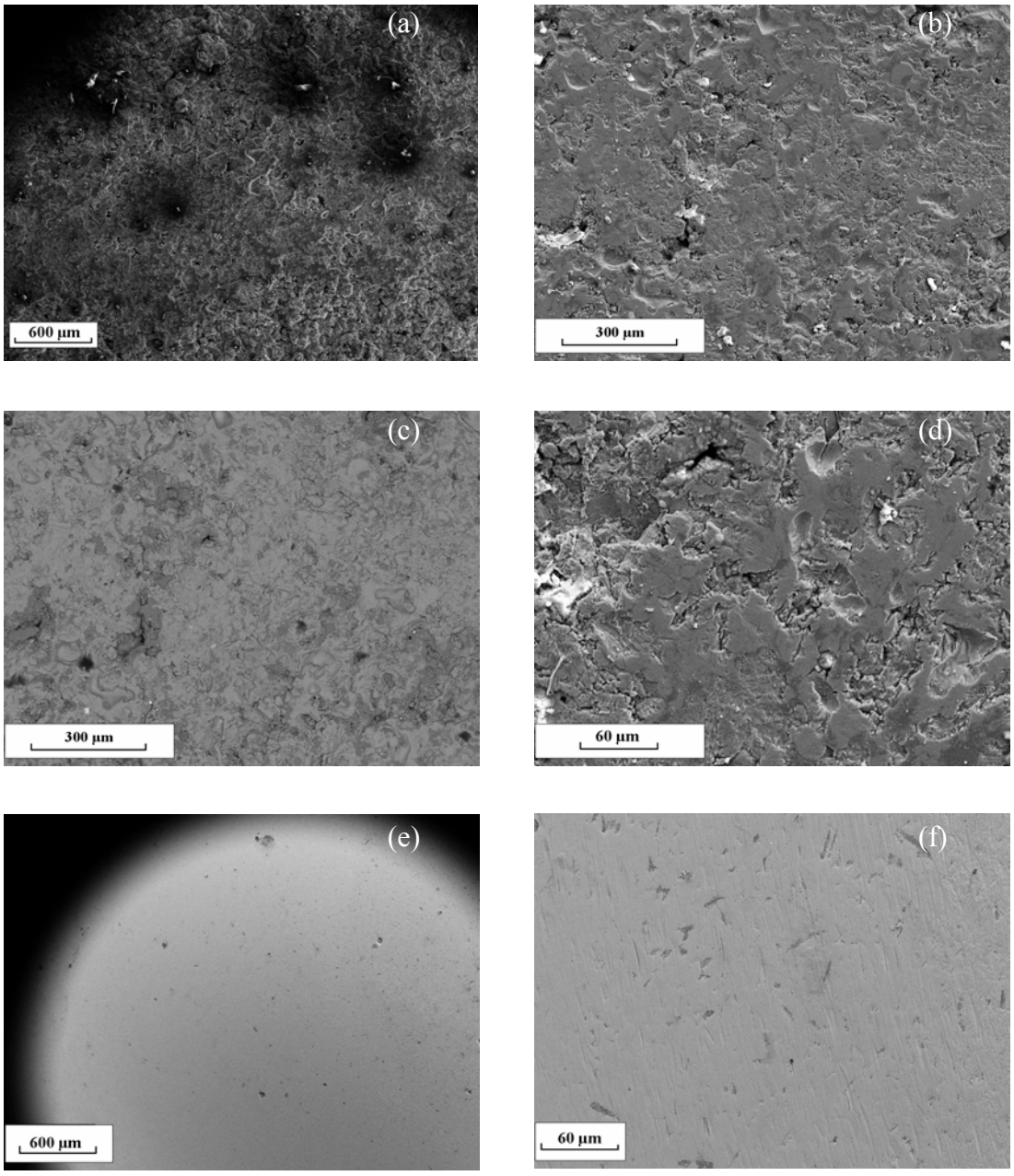


Figure 5.45 SEM micrograph of titanium coating in seawater conditions after 56,132 load cycles; wear track (a), (b), (d) secondary electron images (SEI) (c) back scatter electron image (BEI), ball surface (e) and (f) SEI.

### *5.3.4 EDX analysis*

EDX analysis was conducted on the wear track surface of the disc and the ball after the completion of test. Two areas, i.e. dark area and bright area were analysed for each sample. In case of the ball surface tested in seawater conditions which was homogeneous and bright, only one area was analysed.

#### *5.3.4.1 Molybdenum coating*

5.3.4.1.1 Dry conditions

In dry contact conditions, the dark area analysis showed that the main composition consists of molybdenum and traces of iron, silicon and oxygen (see Figure fig 5.46). Oxygen was probably in the form molybdenum oxide or iron oxide. The main composition of the bright area was molybdenum with low peak of oxygen (see Figure 5.47). The main difference in composition of the dark area from the bright area was the amount of iron and silicon. The height of the iron and silicon peaks in the dark area was greater than that in the bright area.

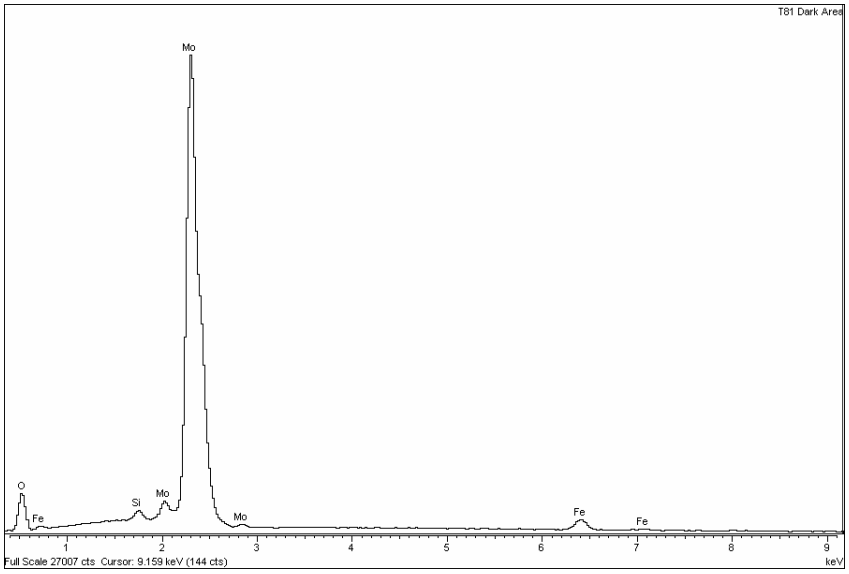


Figure 5.46 EDX analysis result on the dark area of wear track surface in dry conditions.

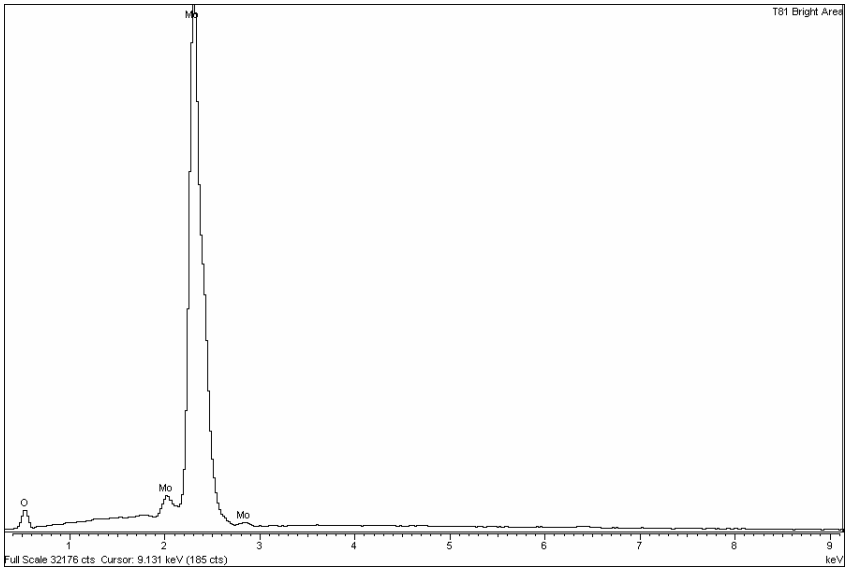


Figure 5.47 EDX analysis result on the bright area of wear track surface in dry conditions.

The ball surface in the transferred material region is composed of high amount of molybdenum with small amount of iron, silicon and oxygen while the remaining region mainly reflected the composition of the steel ball materials; i.e. iron, chromium, silicon and sulphur (see Figure 5.48 and 5.49). The composition of the dark area within the contact track surface and that of the transferred area of the ball surface were similar.

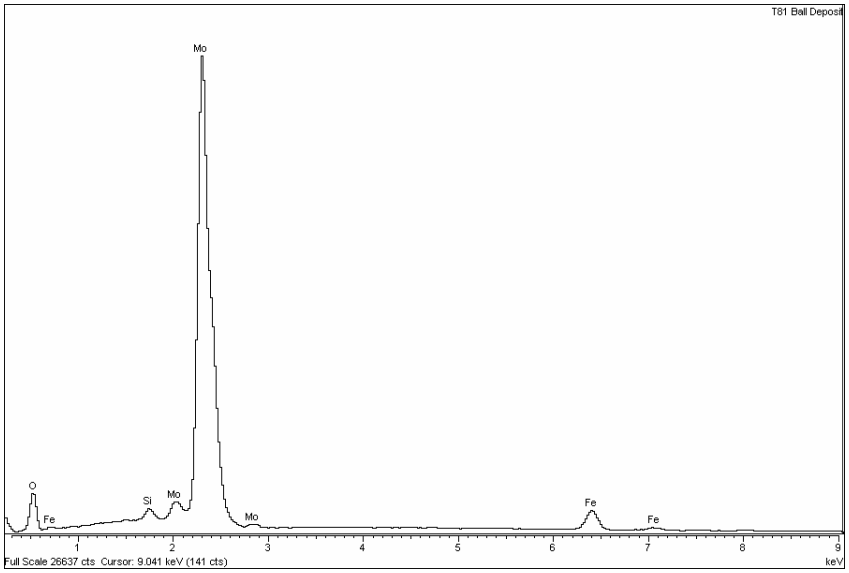


Figure 5.48 EDX analysis result on the transferred material area of the ball surface in dry conditions.

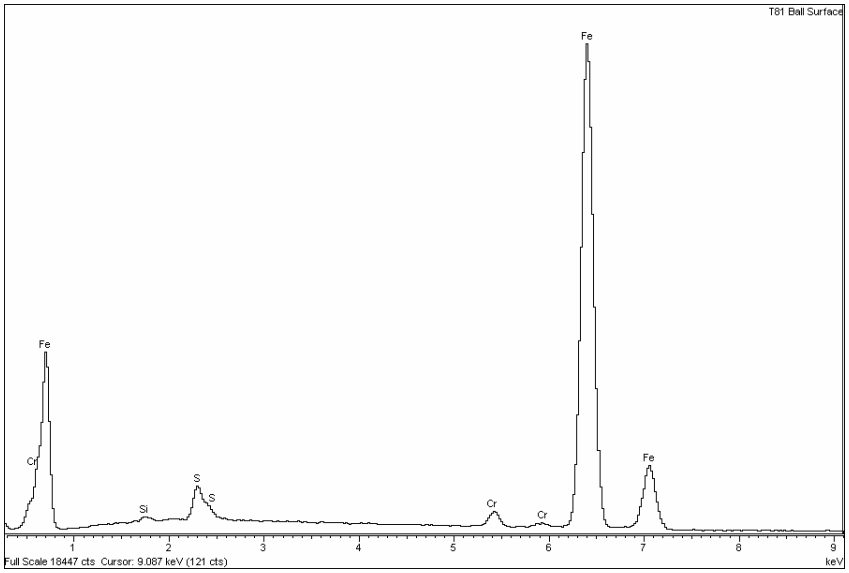


Figure 5.49 EDX analysis result on the uncovered area of the ball surface in dry conditions.

5.3.4.1.2 Seawater conditions

Figure 5.50 shows the EDX analysis results of the wear track surface created in seawater conditions. The chemical composition of the dark area consists mainly of molybdenum and traces of iron, oxygen, chromium chlorine and calcium. Molybdenum, iron and oxygen are possibly in the form of oxide or hydroxide deposited on the coating surface. Chlorine and calcium most probably came from the seawater which remained in after cleaning. Figure 5.51 shows the analysis results in the bright area. The composition of this area is almost similar to that of the dark area, but with lower peaks for iron, oxygen, chromium and oxygen and without chlorine.

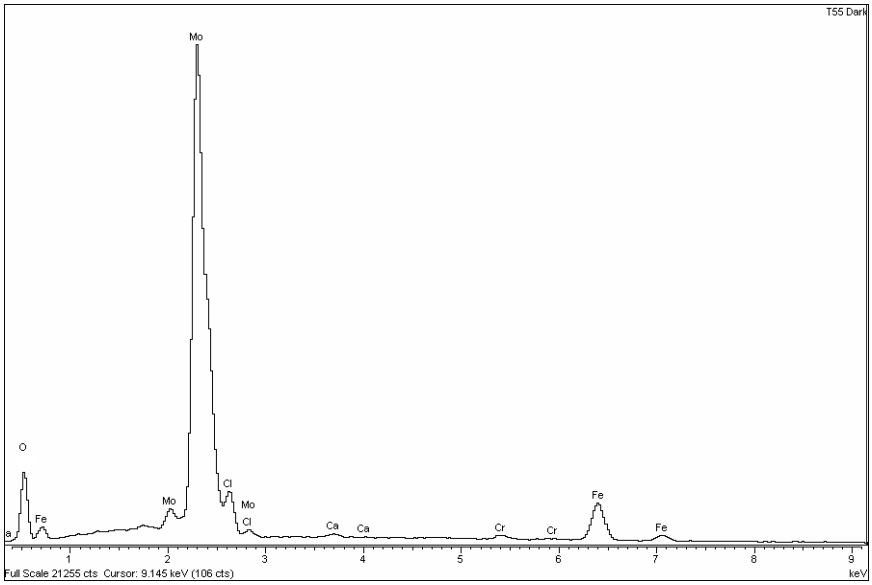


Figure 5.50 EDX analysis result on the dark area of wear track surface in seawater conditions.

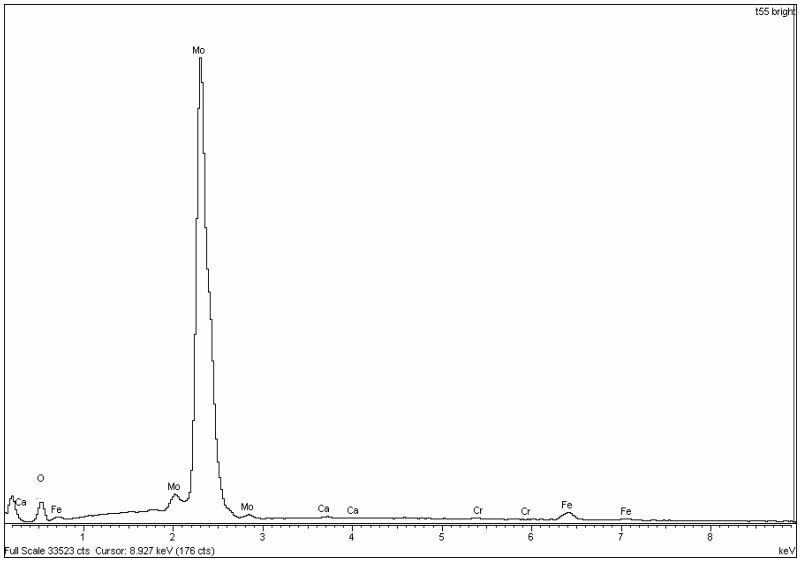


Figure 5.51 EDX analysis result on the bright area of wear track surface in seawater conditions.

The analysis results of the ball surface point to a high amount of iron with small quantities of chromium, sulphur and carbon (see Figure 5.52).

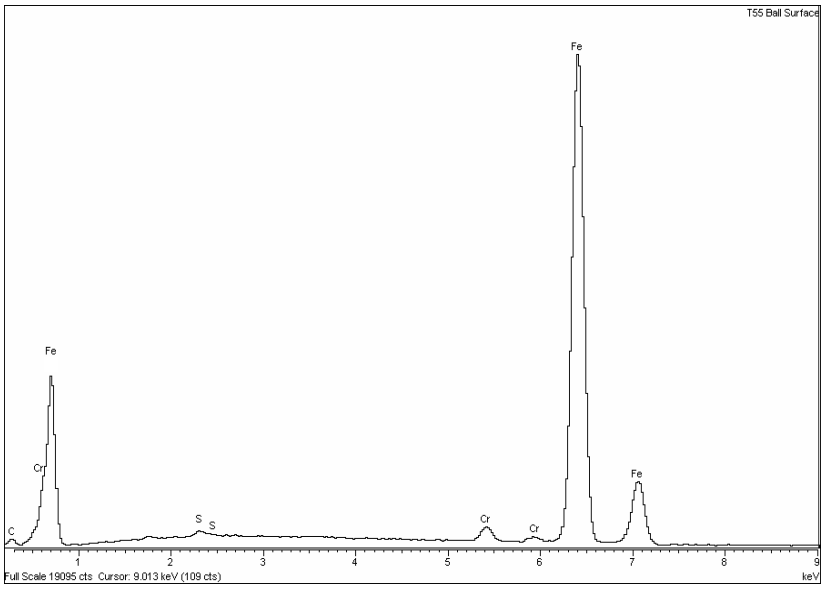


Figure 5.52 EDX analysis result of the ball surface in seawater conditions.

### *5.3.4.2 Titanium coating*

#### 5.3.4.2.1 Dry conditions

The analysis results of the dark area as well as the bright area showed that main components are titanium with traces of iron and oxygen (see Figure 5.53 and 5.54). The peaks of iron and oxygen in the dark area were, however, higher than that in the bright area. Furthermore, silicon, coming from the driving ball, was found in the dark area.

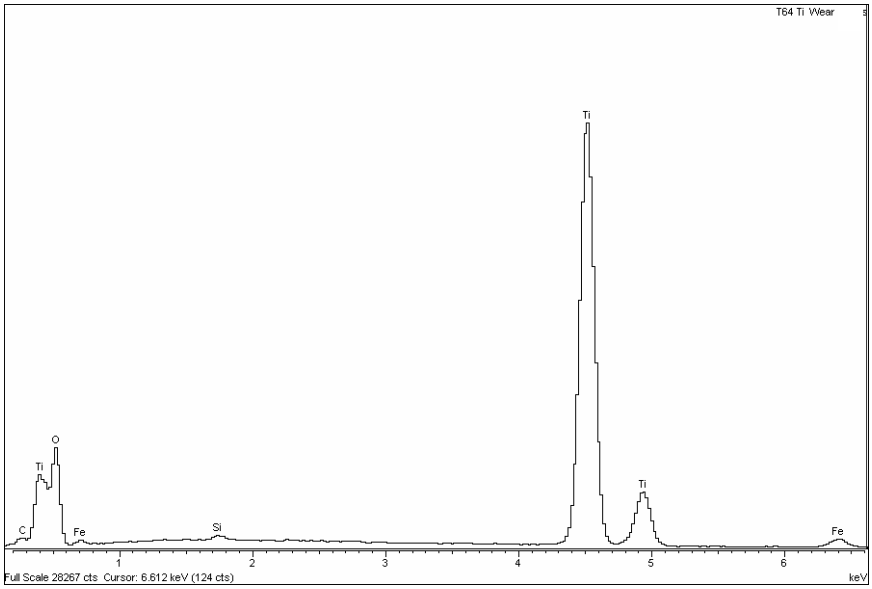


Figure 5.53 EDX analysis result on the dark area of wear track surface in dry conditions.

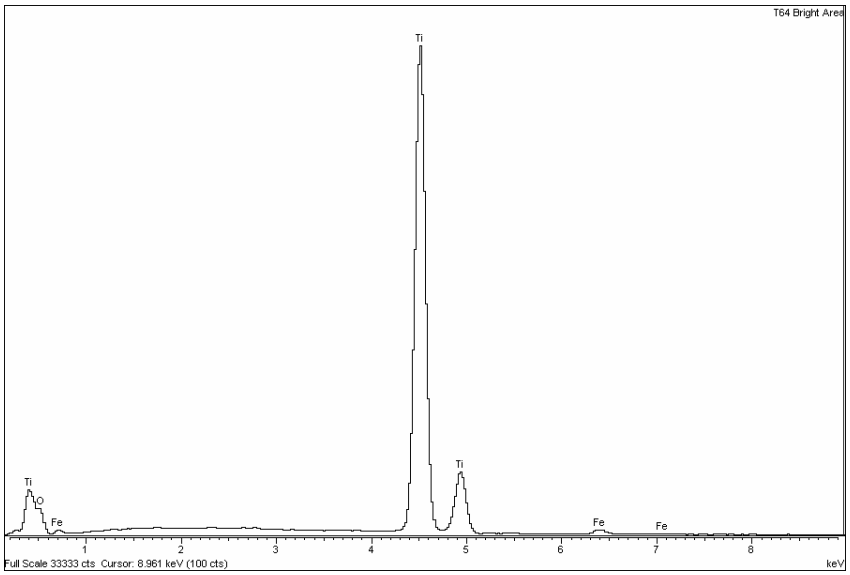


Figure 5.54 EDX analysis result on the bright area of wear track surface in dry conditions.

The analysis results of ball surface in the region of transferred materials showed that the main component is titanium and with significant amount of iron, silicon, oxygen, and trace of chromium (see Figure 5.55). The results from the non-transfer region showed mainly iron with little amount of titanium, chromium, oxygen and silicon (see Figure 5.56). All together results in dry conditions confirmed that material was mainly transferred from the coating to the ball.

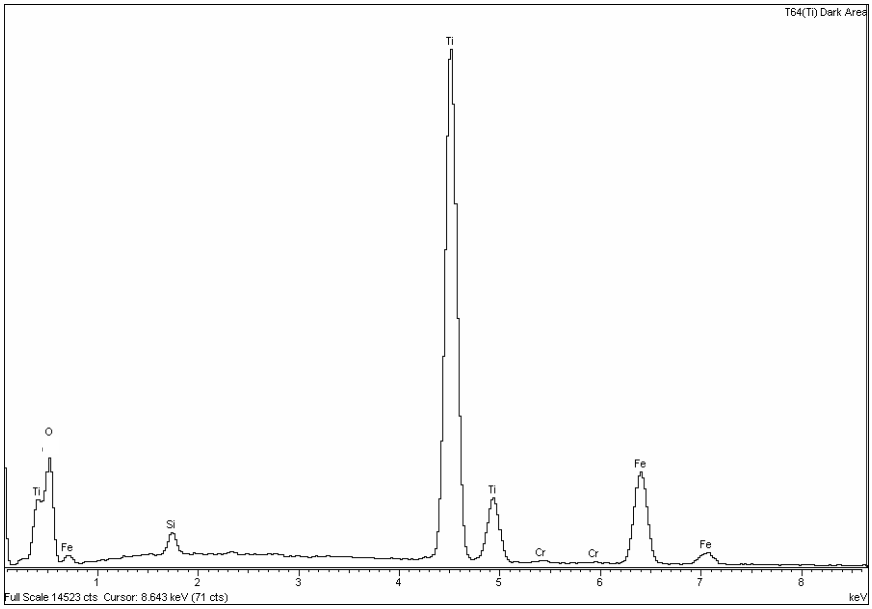


Figure 5.55 EDX analysis result on the transferred material area of the ball surface in dry conditions.

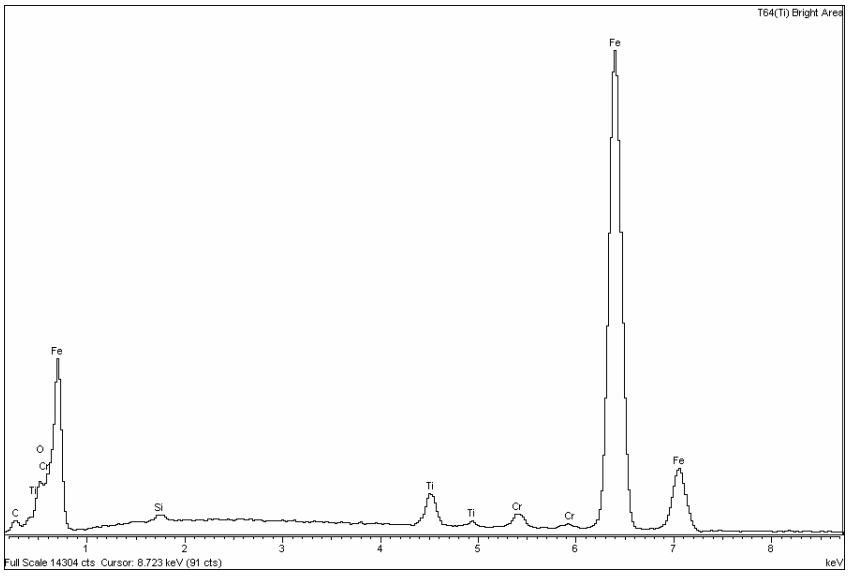


Figure 5.56 EDX analysis result on the uncovered area of the ball surface in dry conditions.

5.3.4.2.2 Seawater conditions

The analysis results of the dark area within the wear track surface are shown in Figure 5.57. Titanium was found as the main component in the dark area. Besides, high amount of iron and oxygen were observed together with quantities of chromium, silicon, calcium,

chlorine, sodium and magnesium. The bright area within the track surface contained mainly titanium with small portion of iron and oxygen (see Figure 5.58).

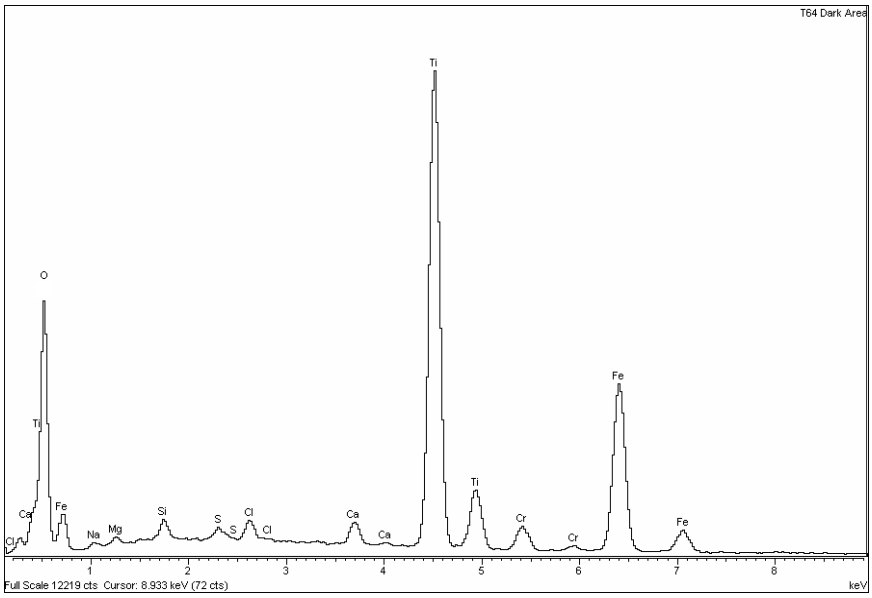


Figure 5.57 EDX analysis result on the dark area of wear track surface in seawater conditions.

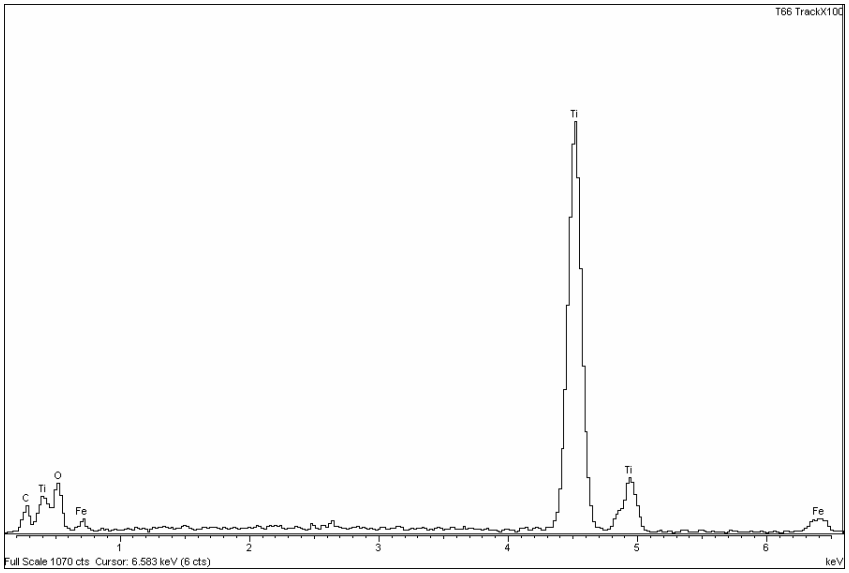


Figure 5.58 EDX analysis result on the bright area of wear track surface in seawater conditions.

The analysis results of the ball surface showed only the main components of the ball; i.e. iron, chromium, silicon and carbon (see Figure 5.59). Therefore, it implies that transfer of material from the disc to the ball hardly occurred.

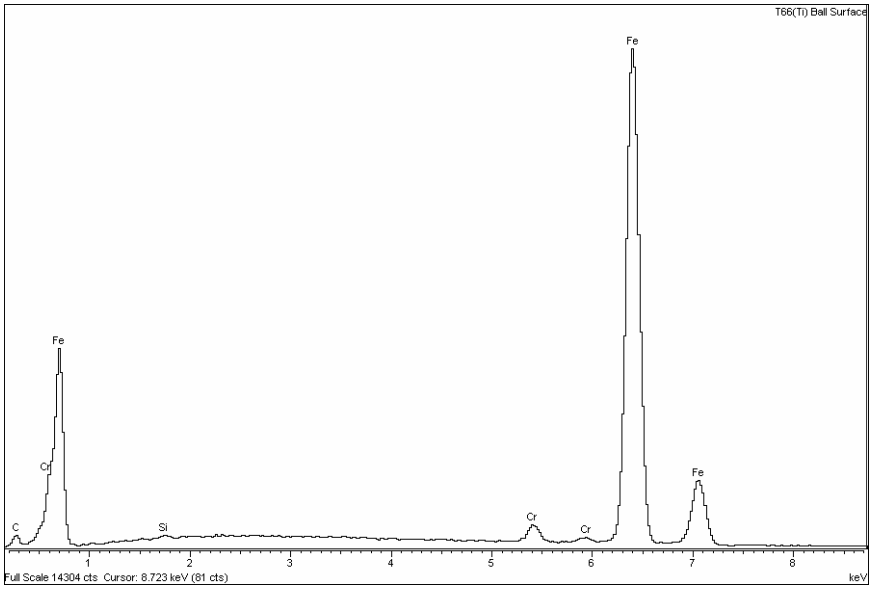


Figure 5.59 EDX analysis result of the ball surface in seawater conditions.

### *5.3.5 Section examination*

Figure 5.60 shows the structure of molybdenum coating and titanium coating microstructure. In general, the coating structure of both systems contains various defects i.e. oxides, pores, gas holes and un-melted particles. However, microstructure of molybdenum coating is more homogenous and denser than that of titanium coating.

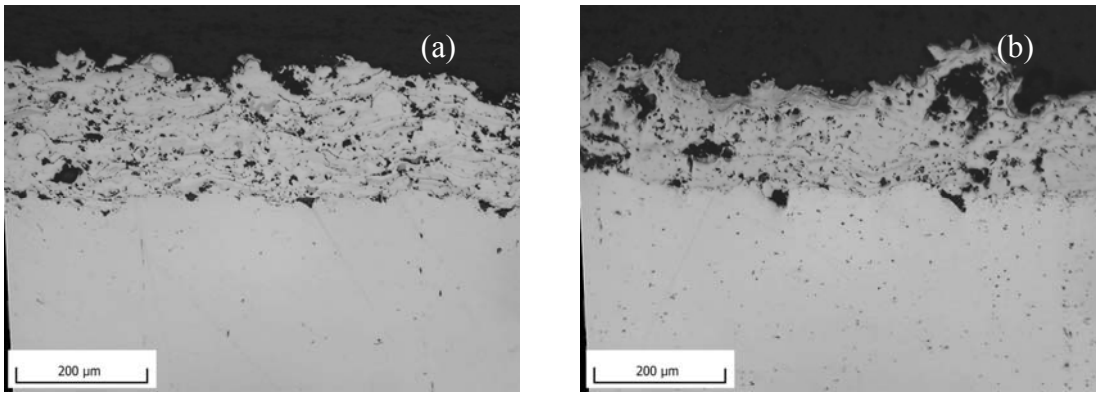


Figure 5.60 Microstructure of sectioned specimens; (a) molybdenum coating and (b) titanium coating.

All tested discs were sectioned across the wear track after surface examinations. This section presents investigation results of molybdenum coating and titanium coating cross-sections.

*5.3.5.1 Molybdenum coating*

5.3.5.1.1 Dry conditions

Cross-sections of molybdenum coating subjected to different contact stresses are shown in Figure 5.61. Under the selected rolling contact stress range, no delamination or spalling were detected in all samples. Wear rate increased with increasing contact stress. At contact stress of 1.32 GPa, the coating layer was slowly worn out (see Figure 5.61a. and 5.61b). The coating layer was still remaining after 274, 982 loading cycles. At contact stress of 1.67 GPa, wear reached to the substrate after 56,132 loading cycles and at 1.91 GPa the same happened after 24,948 loading cycles (see Figure 5.61d - 5.61f).

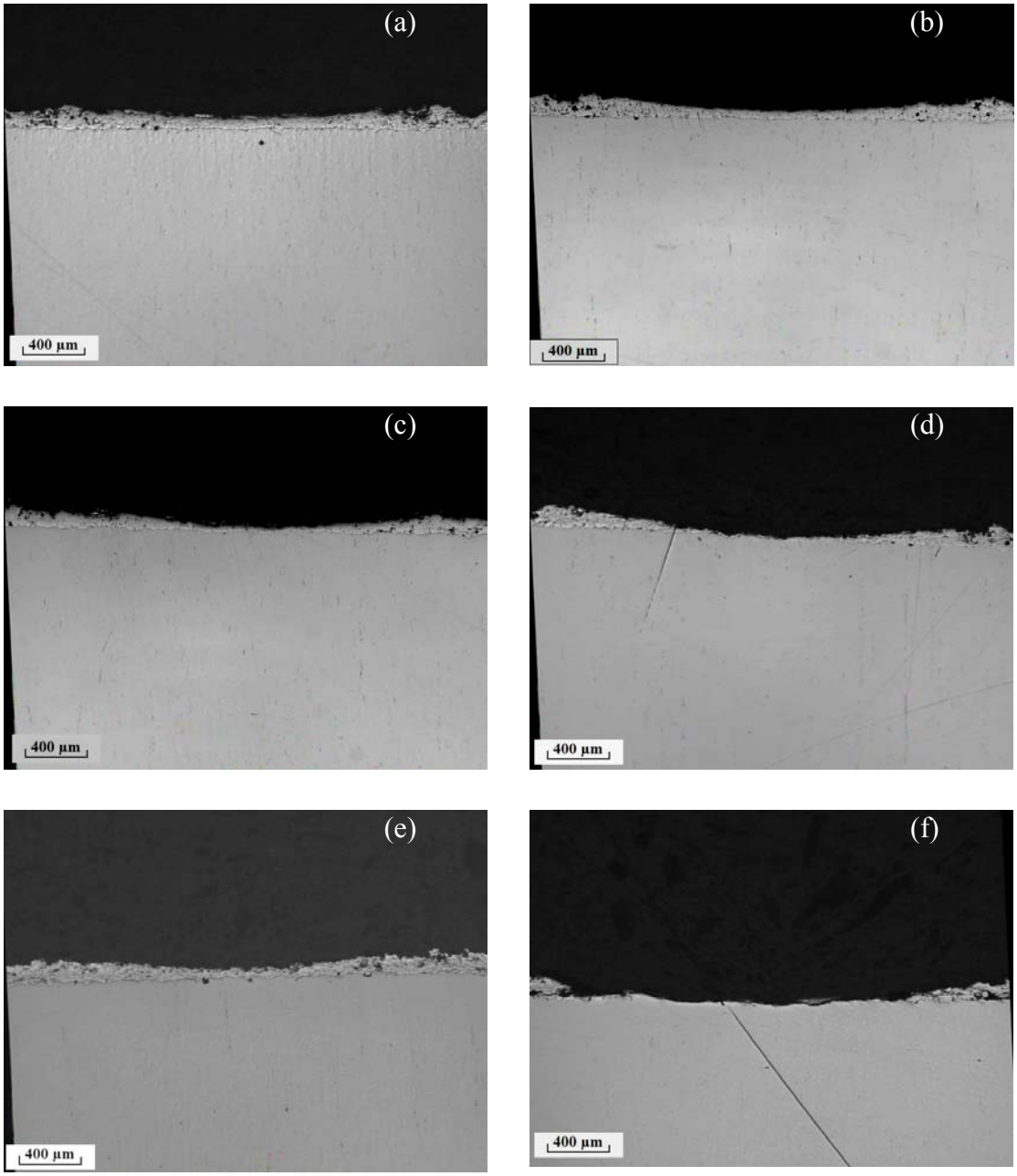


Figure 5.61 Cross-sectioned views of molybdenum coating in dry conditions tested at contact stress: 1.32 GPa (a) after 149,686 cycles and (b) after 274,982 cycles; 1.67 GPa (c) after 46,777 cycles and (d) after 56,132 cycles; (d); 1.91 GPa (e) after 12,474 cycles and (f) after 24,948 cycles.

High magnification of the track showed that the lamellar at the upper layer was broken at all contact stress levels (see Figure 5.62). However, the relationships between the depth of the broken layer and contact stress could not be found.

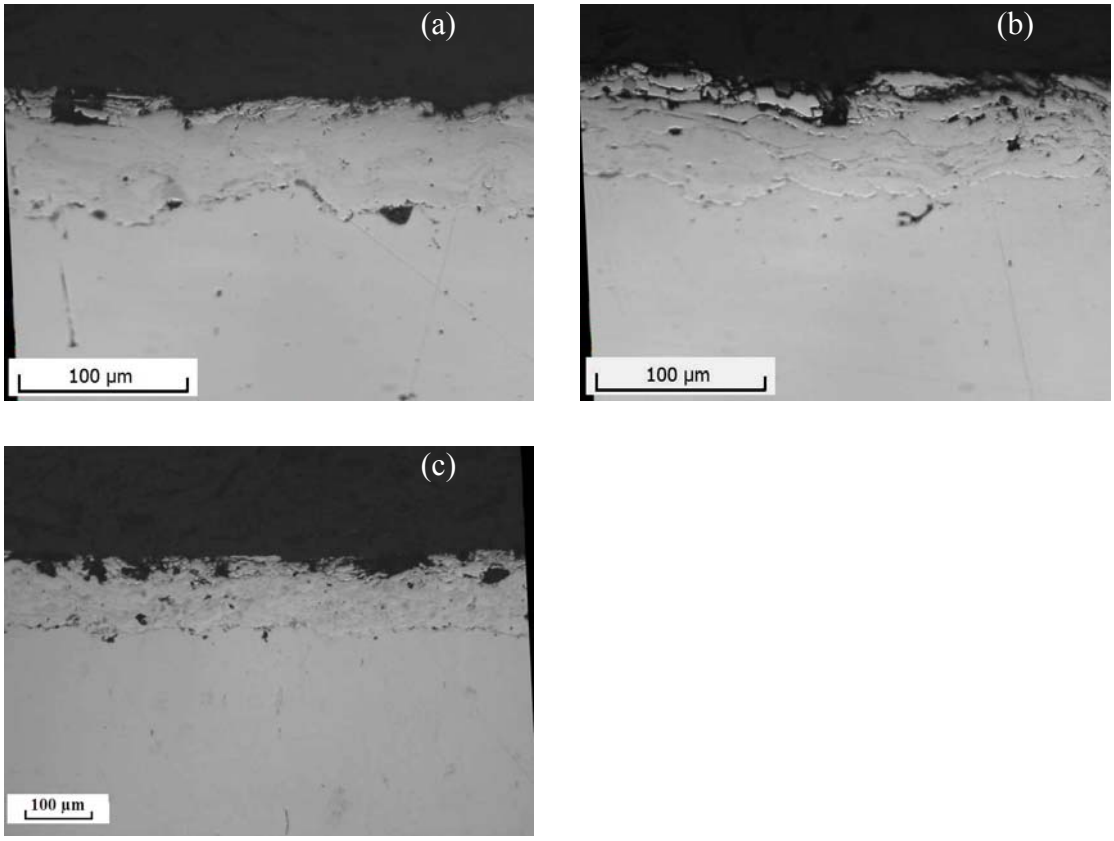


Figure 5.62 High magnifications of wear track area under dry conditions tested at different contact stresses and load cycles (a) contact stress 1.32 GPa, 274,982 cycles (b) contact stress 1.67 GPa, 46,777 cycles (c) contact stress 1.91 GPa, 6,237 cycles.

*5.3.5.1.2 Seawater conditions*

The thickness of the coatings in wear track area decreased slowly with increasing loading cycles (see Figure 5.63a – 5.63c). Comparing it to the test in dry conditions wear rate in seawater conditions was lower. The worn surfaces were smoother than that produced by testing in dry conditions. Broken upper layer of the coating was hardly seen (see Figure 5.63d).

Corrosion between the coating and substrate interface was firstly observed after 46,777 loading cycles (see Figure 5.63a). Corrosion occurred only under the contact track area. Corrosion area expanded with the number of load cycles. However, the corrosion expanded laterally rather than vertically. Under the selected rolling contact test conditions, no delamination or spalling were detected in all samples.

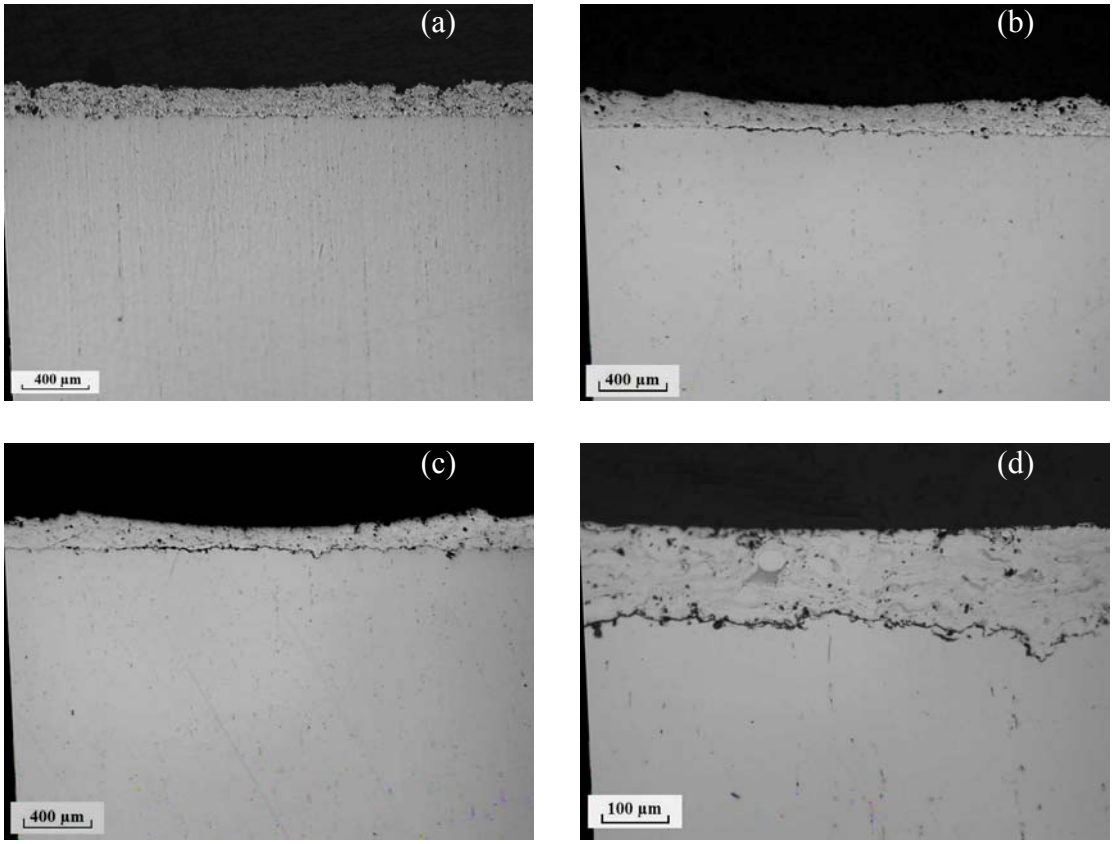


Figure 5.63 Cross-sectioned views of molybdenum coating in seawater conditions tested at contact stress 1.67 GPa; (a) after 46,777 cycles (b) after 399,164 cycles (c) after 503,902 cycles (d) higher magnification of (c).

*5.3.5.2 Titanium coating*

5.3.5.2.1 Dry conditions

Under conditions used, titanium coating was damaged by high wear rate (see Figure 5.64a and 5.64b). Delamination and spalling were not observed. Worn surface was smooth and the asperities were deformed (see Figure 5.64c). Cracking of the upper layer of coating was not detected for the entire testing program.

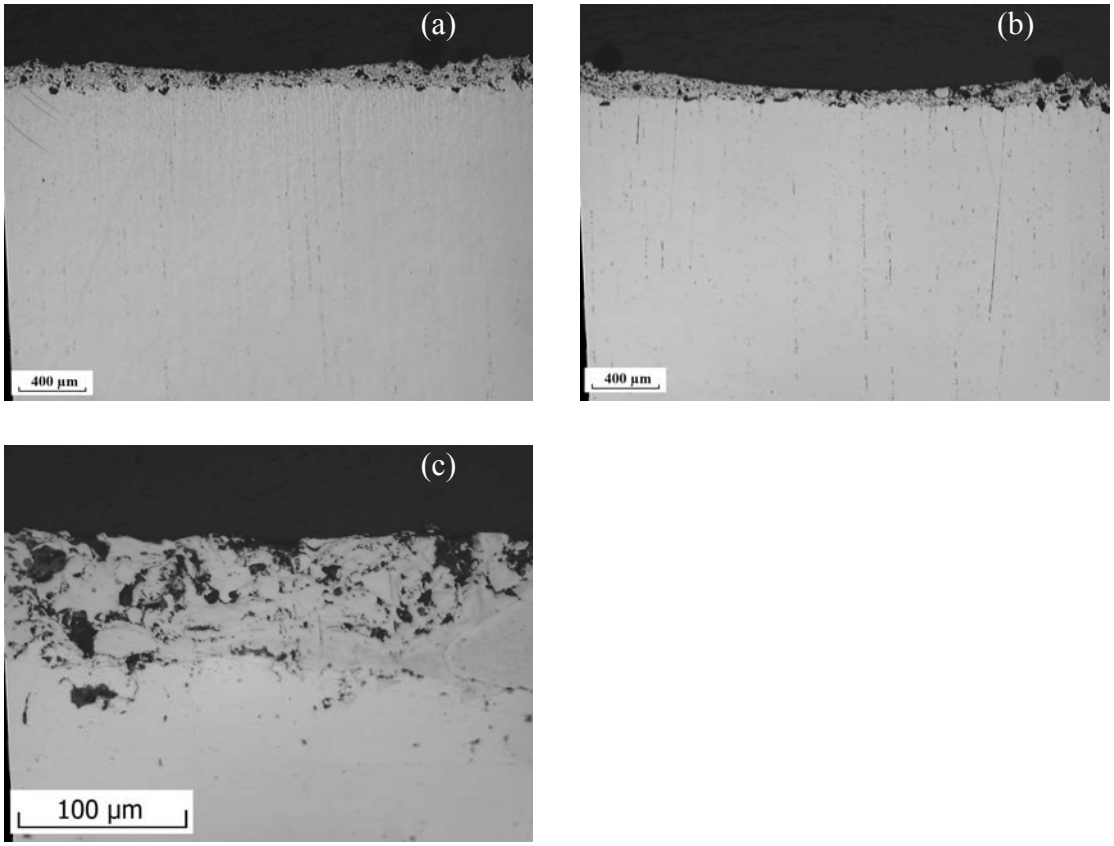


Figure 5.64 Cross-sectioned views of titanium coating in dry conditions tested at contact stress 0.74 GPa; (a) after 37,422 cycles (b) after 56,132 cycles and (c) higher magnification of (b).

*5.3.5.2.2 Seawater conditions*

Wear of coatings increased with increasing number of load cycles (see Figure 5.65a, 5.65c, 5.65f and 5.65g). Breaking of upper layer of coating was not detected. Corrosion at the interface between coating and substrate was detected after 46,777 loading cycles (see Figure 5.65b). Corrosion propagated laterally along the coating/substrate interface with increasing number of load cycles (see Figure5.65d for comparison). There was insignificant corrosion along the interface outside the rolling track. Vertical crack and spalling of the coating was observed at 424,112 cycles (see Figure 6.65f and 5.65g). Vertical crack was observed in the region where the interface was completely corroded (see Figure 5.65h).

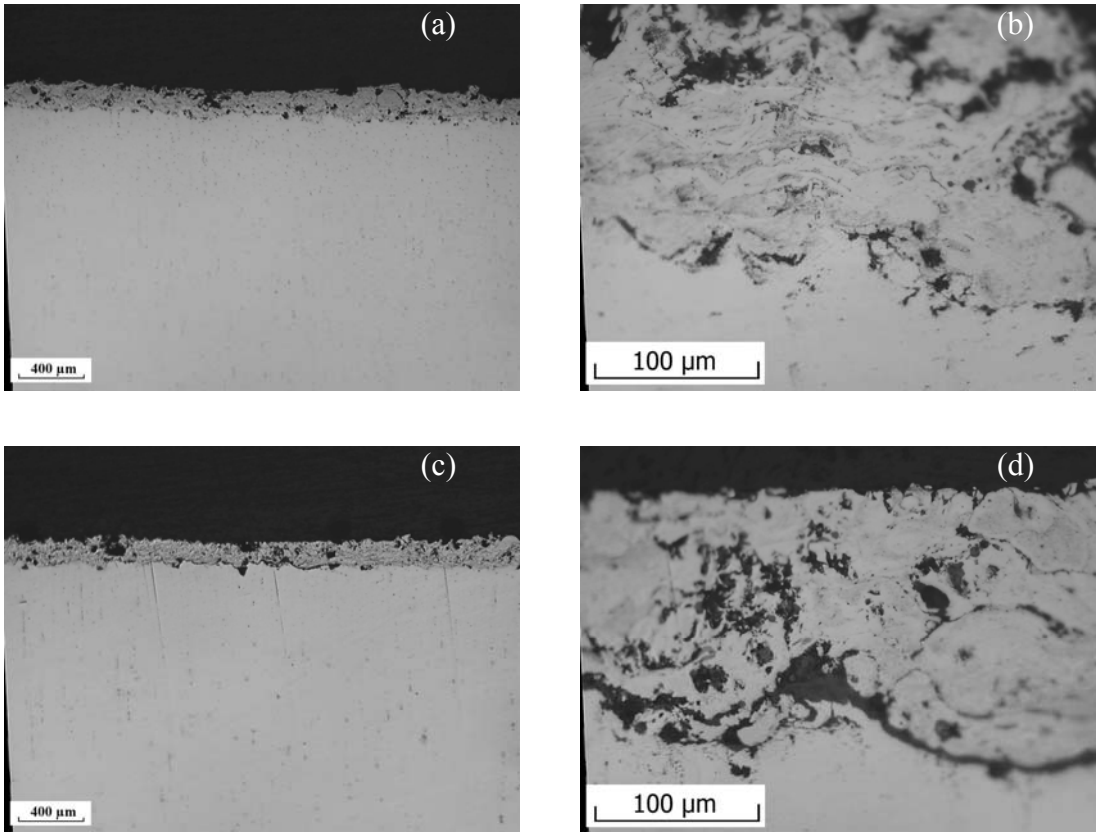


Figure 5.65 Cross-sectioned views of titanium coating in seawater conditions tasted at contact stress 0.74 GPa; (a) after 46,777 cycles (b) higher magnification of (a) at the interface (c) after 399,164 cycles (d) higher magnification of (c) at the interface (e) macro picture shows section plan of sample after testing 523,902 cycles (f) cross-sectioned picture at A position (g) cross-sectioned picture at B position and (h) higher magnification of (g) at C position.

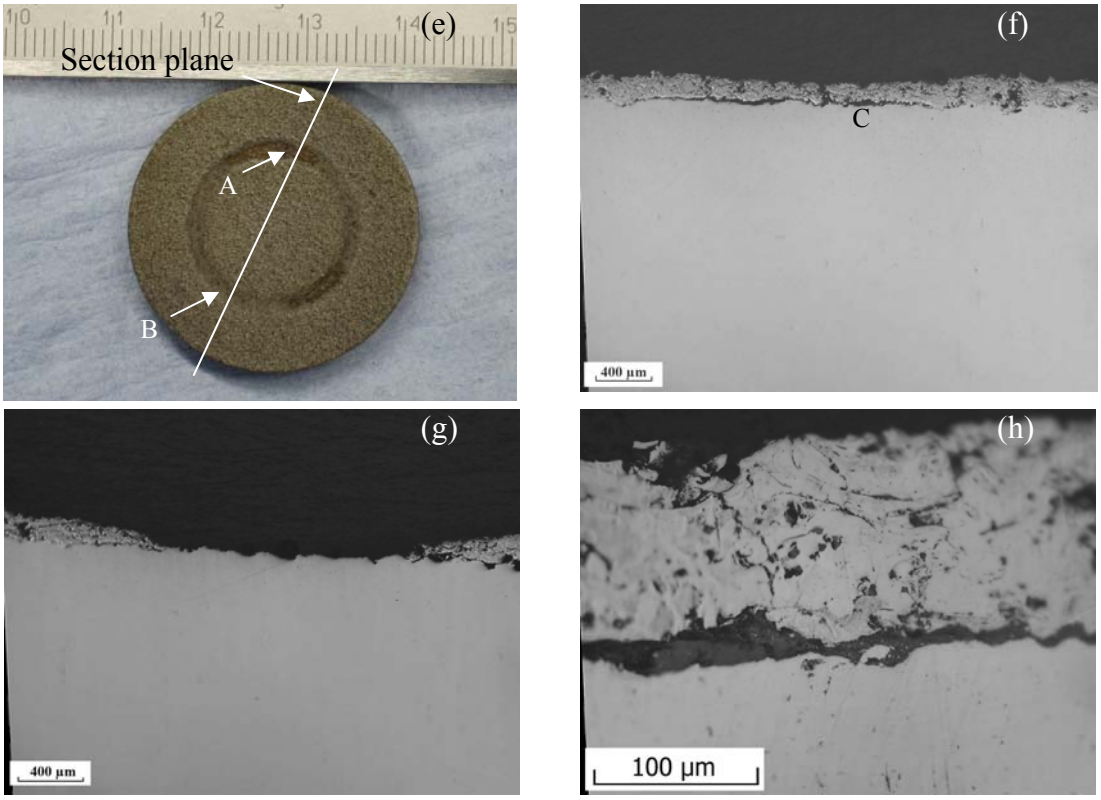


Figure 5.65 Continue.

### *5.3.6 Weight Loss Measurements*

#### *5.3.6.1 Effect of contact stress*

Weight losses of molybdenum coating tested in dry contact conditions at various contact stresses are shown in Figure 5.66. In general, high weight loss rate was obtained at high contact stress. However, weight loss rate is not a linear function of the contact stress. For contact stresses between 1.32 and 1.96 GPa, the test stopped when coating layer was completely worn out.

At contact stress of 1.32 GPa, the weight loss increased rapidly at the early stage of testing till 24,948 load cycles were attained. Then weight loss increased linearly with the number of load cycles.

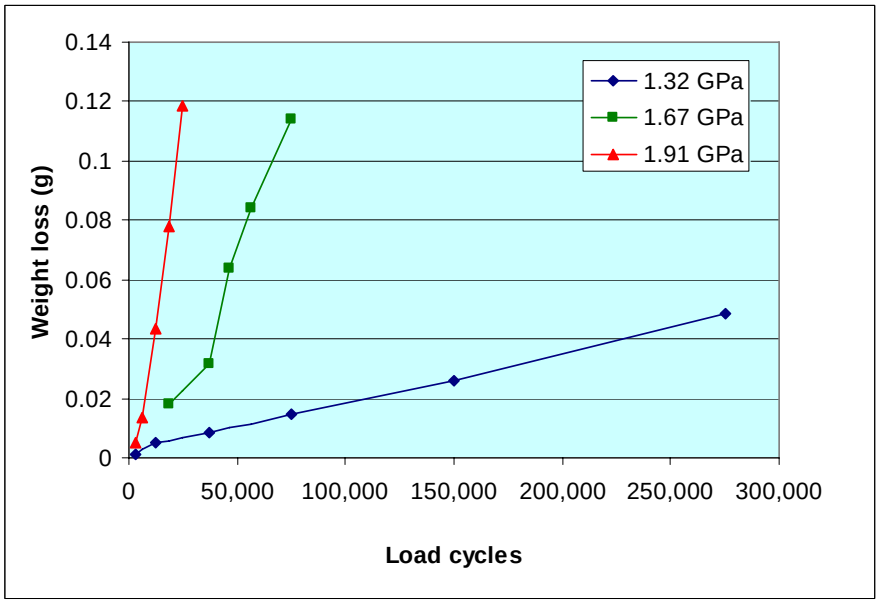


Figure 5.66 Relationships between weight loss and load cycles for contact stress of 1.32, 1.67 and 1.91 GPa.

*5.3.6.2 Effect of dry and seawater conditions*

Figure 5.67 shows weight losses of molybdenum and titanium coatings under contact stress of 1.67 GPa and 0.74 GPa respectively. In dry conditions, weight losses of both coating systems increased rapidly with the increase in testing time.

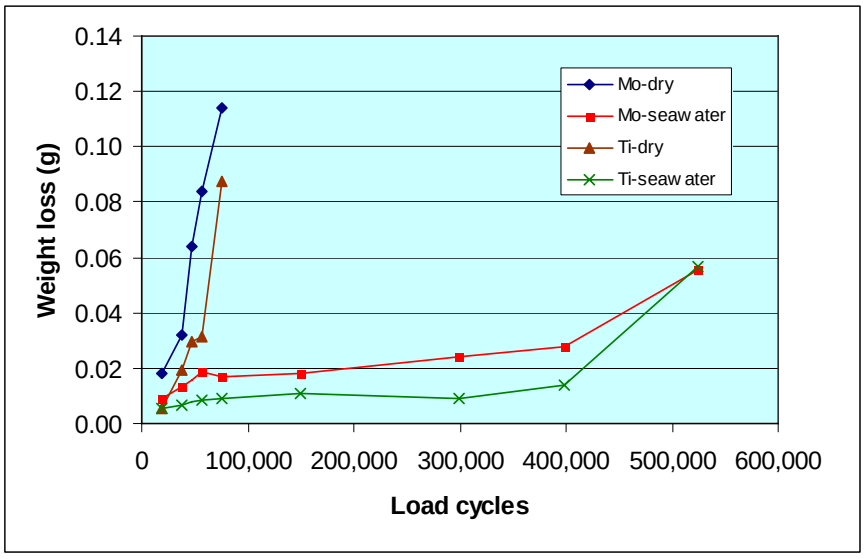


Figure 5.67 Relationships between weight loss and load cycles in dry and seawater conditions.

In seawater conditions, three stage of weight loss could be identified in both coating systems. Weight loss rate of both coating systems increased rapidly at the early stage of testing reaching a steady stage with lower wear rate. The rate was increased again after 399,164 cycles. For the same number of load cycles, the wear rate of molybdenum coating was higher than that of titanium coating at the first stage and second stage of testing, but lower at the third stage.

Comparing each material, weight loss in dry conditions is generally much faster than that pertinent to seawater conditions. At the early stage of testing weight loss was not much different for both coating systems. The difference increased as the test prolonged. When the test terminated for dry conditions at 74,843 load cycles, weight loss in dry conditions was 6.7 times higher than tested in seawater for molybdenum coating and 9.6 times for titanium coating.

In general, the molybdenum weight loss was higher than titanium for the same number of load cycles in both dry condition and seawater conditions. Weight loss of titanium coating was higher after 523,902 cycles.

### *5.3.7 Wear track measurements*

The results of width of wear track measurements are presented in Figure 5.68. Width of the wear track was measured at four different locations. The values presented in the graph are an average value. In dry conditions, width of track increased steeply with number of load cycles for both coating systems. At the same loading cycles, width of the track in molybdenum coating was greater than that in titanium coating for all numbers of load cycles.

The general observation for both coating systems tested under seawater contact conditions is that there are three stages of the track width change rate. At the first stage, the track width change rate was high until 56,132 load cycles were reached. At the second stage, track width increased much slower than at the first stage until 399,164 load cycles were attained. At the final stage, the track width increased again with a high rate. For the same number of load cycles, the width of track in molybdenum coating was smaller than that in

titanium coating at the first stage, but greater at the second stage and smaller again at the third stage.

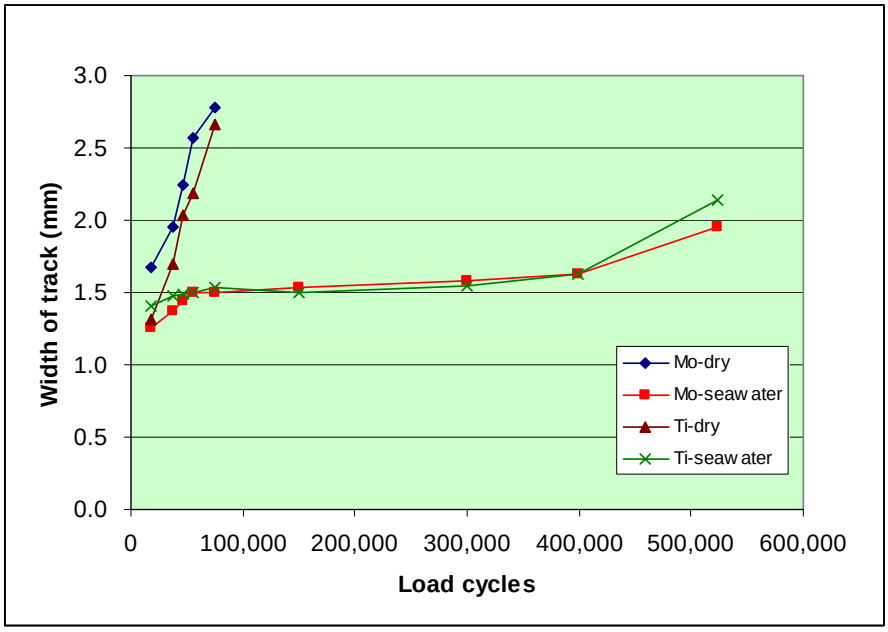


Figure 5.68 Relationships between width of the track and load cycles in dry and seawater conditions.

# Chapter 6 DISCUSSIONS

## 6.1 Introduction

The main objectives for this experimental study were to investigate the performance, the failure modes and possibly their mechanisms of different materials using two types of contact, i.e. static repeating contact and dynamic rolling contact utilising surface, sections and EDX analysis.

The results of the experiments are discussed in turn and comparison between different contact conditions is made. Both static and dynamic contact fatigue tests used ball-on-flat test configuration and alternating load. In the static contact fatigue materials were subjected by a cyclic load while in dynamic contact fatigue materials were subjected to loading-unloading cycle resulting from rolling action. Failure characteristics of both types of contact fatigue are discussed.

The chapter is organised into five sections, including this section. The main test results obtained from the static contact fatigue and the dynamic contact fatigue are discussed in turn first. Each of them is divided into two sub-sections. The static contact fatigue of PMMA is discussed and focuses on the influence of the ball's materials and the effects of oil lubrication on the surface damage of PMMA. The dynamic contact fatigue of molybdenum coating and titanium coating discussion concentrates the rolling damage behaviours in the dry conditions and seawater conditions. It should be appreciated that in this study the failure processes and probably mechanisms were only concerned with static repeating contact fatigue and dynamic rolling contact fatigue in nominally the same tribological conditions. Damage mechanisms for both fatigue configurations resulting from different contact conditions are also suggested.

## 6.2 Effect of Ball Types on Damage of PMMA

As mentioned in chapter 3, section 3.2.2, three factors generally affected the contact between materials, namely stress level, friction, and affinity to form adhesive junctions. The results obtained will be discussed in light of these factors.

Damage behaviours obtained from static contact fatigue depend on various factors, e.g. type of contacted material, loading conditions, environments which are detailed in section 1.5. The damage patterns observed by many other researchers for steels, ceramics and a number of coatings were different types of cracks and wear. In this research, damage patterns of brittle plastic, PMMA, against different ball materials i.e. $Si_3N_4$, steel, aluminium, bronze and PMMA are discussed. Results obtained for each combination of materials used are discussed in turn in order to clearly identify the influence of the counterface material and the number of load cycles on the surface damage of PMMA.

The common features within contact area for all material combinations in dry conditions consist of two distinguished regions, namely stick region and slip region. Severe damage occurred in the slip region while no or little damage was observed in the stick region.

Under selected test conditions, PMMA plate showed significantly different degrees of damage and different damage behaviours when subjected to cyclic load in dry contact with different couterface materials. In general, the common damage features of PMMA plate were in the form of adhesive wear, ring cracks and radial cracks. In this section each kind of damage is discussed separately.

### *6.2.1 Adhesive wear*

Adhesion is a phenomenon operating when materials are in an intimate, close contact and is manifested by the formation of adhesive junctions and junction growth. Boden and Tabor (1950; 1964) have demonstrated that pressing contact pairs of unreactive metals together leads to adhesion between counterfaces (*cited in* Waterhouse, 1972). When sphere is loaded on flat surface, cold welding at asperities takes place. Rupture of the welds occurs after releasing load due to the elastic recovery of counterfaces (see Figure 6.1).

Under static contact fatigue load, adhesion caused detachment of particles in similar counterface (Zhu and Zhou, 2001).

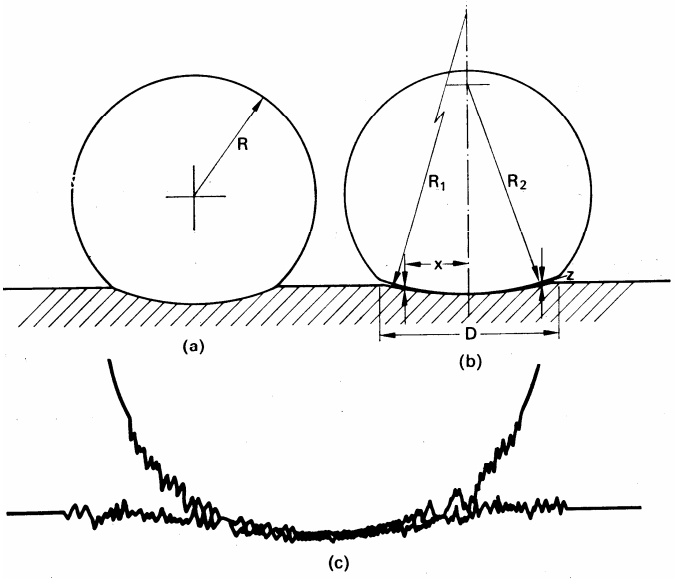


Figure 6.1 Theoretical model of adhesion; (a) under loading, (b) elastic recovery, (c) asperities and asperities bridges (Waterhouse, 1972).

In this experiment, adhesion was found in all contact combinations. However, the damage features present themselves differently to some degree. In all cases, adhesion caused transfer of material between counterfaces resulting in wear.

In case of $Si_3N_4$/PMMA combination, adhesion started with surface roughening of PMMA plate at the boundary of the stick region and material transferred on the ball surface at the corresponding position on the plate after the first five minutes (see Figure 5.10). Normally, contact between compatible materials such as between the same materials tends to weld them together without or little assisting of compression force. By contrast, it is very difficult to establish adhesion by cold weld between incompatible materials. However, adhesion in the form of mechanical interlocking between asperities of these materials can be established by increasing contact stress, which in turn increases the number of contacting asperities. According to Hertz's formula, contact pressure at the boundary between the stick region and the slip region is supposed to be the highest among the rest position of the slip region during advancing stage of load cycle (see Figure 3.4). Therefore, adhesion would be firstly expected at this position. Furthermore, the alternating of contact pressure at this position is also expected to be the highest. During the advancing stage of

load cycle mechanical interlocking process of asperities was taking place. In the receding stage, adherent layer was broken most preferential at the PMMA side because of its lower strength. This led to PMMA adhere to the $Si_3N_4$ ball surface.

Transferring expanded outward to the slip region with prolonging testing time. This might be explained in terms of microslip between conterfaces due to different Young's modules of counterfaces as explained in section 1.5. Rubbing feature in the slip region evidences the microslip. As microslip proceeded heat was generated leding to softening of the PMMA plate. As a result, mechanical interlocking could occur at lower contact pressure. Microslip between counterfaces also resulted in expelling wear debris to the edge of contact. The results of profile measurements across the contact area of PMMA plate showed that material loss of PMMA plate in the slip region increased gradually with the test time until reaching the maximum depth of only about 1μm after 810 minutes. This is because mechanical interlocking junction has normally low strength. Therefore, breaking off bulk material of PMMA was insignificant.

Negligible damage on surface of the ball was expected because the hardness value of $Si_3N_4$ ball is very much higher than that of the PMMA plate. The hardness ratio between $Si_3N_4$ and PMMA plate is 62.4.

For steel/PMMA combination, adhesion was observed after five minutes of testing (see Figure 5.8b and 5.25). Adhesive damage for this combination was more advanced comparing to $Si_3N_4$/PMMA combination even though nominal contact stress was lower. It might be suggested that the steel was more compatible to PMMA than $Si_3N_4$. Signs of melting of PMMA near the boundary between stick and slip regions imply that heat was generated and accumulated during cyclic load resulting in increasing of temperature. It was certainly exceeding softening point of PMMA as explained in Chapter 2. Iron rich ring shaped zone formed at the boundary of the stick region after 60 minutes of testing and expanded outward with testing time. This might be confirmed the results found by Higham *et al.* (1978) mentioned in section 1.5 that adherence between iron ball and the PMMA plate required incubation time. This incubation time was dependent on contact pressure. The boundary between the stick and the slip regions was exposed to the highest alternating contact pressure as mentioned above. Therefore, material loss of steel ball was taking place firstly at the boundary of the stick and the slip regions.

Lumps of detached material appeared in the slip region of the PMMA plate and attached on to the steel ball surface after 180 minutes of testing. Surface wear of the ball was really detected at this time and damage progressed into the slip region with increasing test time. This phenomenon may be explained in a similar way to that proposed by Higham *et al.* (1978) that the wear of the steel ball is caused by the $\alpha$-$Fe_2O_3$ embedded in the PMMA surface. The EDX and mapping results showed that oxygen existed in the slip region, which supports to above argument (see Figure 5.22 and 5.23). However, high amount of transferred material deposited on the steel ball surface in the slip region after 810 minutes implies that cold junction between iron and PMMA plate can occur even though $\alpha$-$Fe_2O_3$ embedded in the PMMA surface obstructed adhesion between both materials. From the experimental results, it can be inferred that interface strength between them was stronger than that of $Si_3N_4$/PMMA.

For aluminium/PMMA combination, surface roughening, wear and adhesion in the slip region of the PMMA occurred after five minutes of testing as evidenced by surface examination and profile measurements, (see Figure 5.8c, 5.12 and 5.26). Transfer of PMMA in the form of a thin film took place in this region concentrating on the rim of the contact. The lifted up edge of the film indicates adhesion between the PMMA plate and the aluminium ball. Fine aluminium particles deposited in both slip and stick region but especially at the boundary of the stick region (see Figure 5.12b and 5.12d). This evidence indicates strong adhesion between aluminium and PMMA because adhesion occurred at low contact pressure at the edge of contact region. Transferred material on the ball surface was mainly attached between the middle and the outermost of the slip area in the early stage of testing and expanded throughout the slip region as test time increased (see Figure 5.12k and 5.12m). It was different from the case of $Si_3N_4$ and steel ball which the transferring of material took place firstly at the boundary of the stick region. From this evidence, it can be said that the adhesion between PMMA and aluminium was stronger than that between PMMA and steel or $Si_3N_4$. In this combination, quite noticeable aluminium particles were attached to the PMMA surface. Also the PMMA material attached to the ball surface was in a form of sizeable pieces (see Figure 5.9c and 5.12n). From these results, it can be conjectured that the interface strength between them was occasionally stronger than that of bulk aluminium.

For bronze/PMMA combination, adhesion and material loss of the PMMA plate were observed after first five minutes of testing as evidenced by surface examination and profile measurement results (see Figure 5.13a and 5.27). Transferred material in the form of thin film took place all over in the slip region. Lifting up at the edge of the film implied strong adhesive force between these materials. Bronze was also transferred to the plate in a form of tiny particles especially intensified at the edge of contact area. Wear of bronze occurred even though hardness of bronze was much higher than that of PMMA. It may be implied that the interface strength was occasionally greater than the bulk of bronze in some areas. However, the ball surface showed insignificant wear even after test termination (see Figure 5.13h and 5.13i). A significant detachment of PMMA from within the slip region took place after 60 minutes and surface damage intensified with increasing of testing time (see Figure 5.9d, 5.13e and 5.13f). The severity of the damage was highest at the periphery of the contact and almost entire slip region suffered material loss in the form of sizeable fragments with maximum depth profile of 19 μm after 810 minutes of testing (see Figure 5.9 and 5.27). Also, large volume of transferred material attached on the ball surface (see Fig 5.13i) was observed. The results show that the damage the PMMA produced in this combination was more severe than that resulting from testing against aluminium after the same testing time. Damage of PMMA plate in this combination was similar to the damage feature of the PMMA ball in PMMA/PMMA combination. Generally, adhesion between the same materials is expected to be very strong. During maximum compression amplitude, counterfaces with propensity to adhere together formed interface layer over entire contact area. After reducing the load to a minimum, the elastic recovery produced tensile stress between counterfaces. This stress might exceed cohesive strength of either the interface or any sides of bulk materials of counterfaces leading to breaking off the material. If the interface strength were very high, the bulk material would be broken instead; in this case it was PMMA. This situation possibly led to creation of crack originating sites, which increased and propagated very fast leading to sizeable cracking of PMMA as observed in this material combination. When the interface strength was comparable to cohesive strength of bulk material, it was occasionally broken leading to slow crack propagation in bulk material where it existed. The aluminium/PMMA combination was such a case. If interface strength was weak, such as $Si_3N_4$/PMMA combination, cracking was taken place at the interface.

For PMMA/PMMA combination, adhesion in the slip region took place over entire region within the first five minutes (see Figure 5.14a). This was expected for similar material combination because the cold junctions were readily formed when surface asperities were pressed together with lower forces comparing with other combinations. Transferring was especially intensive at the boundary of the stick and the slip regions. This supports the argument that contact pressure was another factor effecting adhesion. In contrast to other contact pairs, material transferred from the ball onto the plate. The reason might be due to the lower hardness value of the ball comparing with that of the plate. In general, hardness can be correlated to tensile strength of the material. Therefore, it can be inferred that the strength of the ball is lower than that of the plate.

Damage severity of the ball increased with prolonging testing time and transferred material covered almost entire slip region after continuous testing for 810 minutes with the height of the deposit material 12.5 μm (see Figure 5.14 and 5.28). Adhesion and detachment of the material from the ball was continuously taking place during increasing testing time. This result can be conjectured that the strength of the ball material increased after de-bonding and re-bonding. However, the reason behind this could not be established in this experiment. The only damage feature on the plate surface was surface roughening in the slip area. This feature allows saying that temperature was increased up to at least softening point during cyclic stress otherwise brittle plastic would not be permanently deformed although the contact pressure in this material combination was the lowest among other combinations.

In summary, adhesion occurred within five minutes of testing for every contact pair except contacted with $Si_3N_4$ which was firstly detected after 15 minutes. The progression of adhesive wear, however, was different. Contacting with bronze produced the most severe wear to PMMA plate followed by aluminium, steel and $Si_3N_4$. After 810 minutes, the depth of wear profile of PMMA plate ranking from the deepest to the shallowest when contacted with different ball was as follows; bronze, aluminium, steel, silicon nitride. By contrast, damage of the PMMA ball inflicted by PMMA plate caused severe wear of the ball.

The results provide sufficient evidences for the ranking of the adhesive force between PMMA pate and the contact ball material. The rank of adhesive force from the weakest to the strongest is as follows; $Si_3N_4$, steel, aluminium, bronze. Although it was supposed that

the strength of adhesion between PMMA plate and PMMA ball should be high, it cannot, however, be confirmed that it was stronger than that between bronze and PMMA. This is because the damage occurred to the ball which strength was the lowest among materials used in this experiment. Therefore, it needed to prove by additional experiment, but it was not in the scope of this research.

### *6.2.2 Ring cracks*

Ring cone crack is particularly expected in static contact fatigue if only contact stress is considered. It is known that the formation of ring cone cracks is influenced by tensile stress, which maximum value is just next to the edge of contact. According to the Hertz's equation for point contact, the PMMA plate was subjected to varying contact stress. The level of contact stress can be ranked as follows; the highest was for silicon nitride, then it decreased for steel, bronze and aluminium, reaching the lowest level for PMMA ball. This ranking is illustrated in Figure 4.2.

It is apparent that the highest stress applied to the PMMA plate resulted from its contact with silicon nitride ball, hence severe damage was expected to occur in the first place but that was not the case. The calculated maximum tensile stress at contact edge in case of $Si_3N_4$ ball at maximum applied load 120 N was 17.5 MPa, which was far lower than the yield limit of PMMA plate as shown in Table 4.1. Therefore, only Hertzian stress cannot cause ring crack formation in the PMMA plate under selected load. In this study the ring crack was observed only in the steel/PMMA combination and aluminium/PMMA combination. Also, the ring crack characteristics was different from those were reported by others.

For steel/PMMA combination, ring cracks were formed along the edge of contact area after 810 minutes, (see Figures 5.9b, 5.11g and 5.11h). Cracks were initiated on the surface at the edge of the slip region and propagated into the bulk of PMMA plate. This feature was clearly observed under optical microscope at higher magnification and transparent mode (see Figure 5.11i).

As previously mentioned, the PMMA plate was subjected to contact pressure by steel ball lower than that by $Si_3N_4$ ball, hence ring crack would be expected to occur in

$Si_3N_4$/PMMA combination as well. This implies that the level of applied contact stress is not the only factor governing the ring crack formation on the PMMA plate. Clearly, the other two factors, friction, adhesion or both, must govern the extent of ring cracks in the PMMA plate.

The magnitude of friction within the contact provides indication of the shear stress at the contact interface. The results of friction measurement for PMMA in contact with various ball types show that the coefficient of friction of PMMA against $Si_3N_4$ ball was greater than that against steel ball for the entire selected load (see Figure 5.1). If friction term affected the initiation of a ring crack, contact with $Si_3N_4$ ball should also produce crack in PMMA plate. Alfredsson and Olsson (2003) have demonstrated that introducing the tangential load below the angle of friction on the static contact fatigue of case-hardened steel decreased the endurance limit of the material comparing to normal static fatigue load conditions. However, the crack was in a shape of conventional ring cone crack where the crack propagated outward, unlike in the case reported here. The analytical result proposed by Li and Berger (2003) showed that the effect of friction on the traction stress at the edge of contact was low (see Figure 3.5). Due to ring cracks originating at the edge of contact the friction term for ring crack damage was of little contribution. Furthermore, the highest value of the elastic parameter ($\xi$) for contact with $Si_3N_4$ ball, calculated according to equation (3.9), is only 0.185 which is lower than 0.4. The shear modulus used in equation (3.9) was calculated from the relationship $G = E/(2(1+\nu))$ as stated in Hosford, (2005). Together with the coefficient of friction value from the experimental results it can be said that friction has little effect on contact stress at the edge of contact.

From all the above discussions, it is concluded that no obvious correlation between the magnitude of friction/shear stress and the severity of damage can be established. In another words, the shear stress at the contact interface, as manifested by the level of friction, does not seriously affect the extent of damage inflicted on a static contact subjected to a cyclic normal load. Accordingly, the only factor that might be contributing to ring crack damage of PMMA plate in contact with the steel ball was adhesion.

Tensile stress was superimposed at the edge of contact when adhesion term existed as explained in section3.2.2.2 (see also Figure 3.3). The magnitude of tensile stress was proportional to the work of adhesion. This stress was produced during compression stage.

In releasing stage, tensile stress due to elastic recovery was also produced if adhesion between counterfaces existed. This stress would be released by creating new surface or crack. Consider the edge of contact as shown in Figure 3.3c, the stress concentration is very high. Therefore, the probability for a crack to be initiated in this area was high. However, the inward propagation of cracks can be suggested as these cracks were propagating during releasing state otherwise they would grow outward in a cone shape like other researchers have reported.

For aluminium/PMMA combination, ring cracks initiated on the surface at the edge of the slip region and propagated into the bulk of material (see Figure 5.12f - 5.12h). These cracks propagated inward direction to the boundary between the stick and slip regions after 30 minutes. The formation of ring cracks took time less than for steel/PMMA combination due to the strong adhesion between the counterfaces as mentioned in previous section. When these subsurface cracks had grown half way through the slip region, they started to emerge and reached the surface in the vicinity of the stick region's boundary (see Figure 5.12i). Unlike steel/PMMA combination the adhesive strength of the interface of aluminium/PMMA combination was substantial. Therefore, subsurface cracks propagation was faster in this combination because fragments of PMMA were usually attached to the ball surface. As a result, in the release load stage crack tip was always subjected to tensile load with magnitude higher than the case of steel/PMMA combination. This evidence can suggest that the loss of PMMA material due to the circumferential crack propagation and emerging on the surface at the stick boundary resulted in gauging of material in the slip area.

For bronze/PMMA combination, ring cracks were not clearly defined due to adhesive damage mechanism of the PMMA surface dominating in this contact pair. Also, for PMMA/PMMA combination, ring cracks were not found due to the damage inflicted on the ball surface by the plate. Damage of the ball was dominantly controlled by adhesive damage.

In summary, the experimental results suggest that under contact pressure used ring cracks cannot be produced in the absence of adhesion. Adhesion assists the initiation and propagation of cracks in PMMA plate for medium adhesive strength interface i.e. steel/PMMA combination and aluminium/PMMA combination. High adhesive strength

interface; i.e. bronze/PMMA combination and PMMA/PMMA combination, adhesive damage is dominating.

### *6.2.3 Radial crack*

Normally, radial crack in metals and ceramics, as discovered by many researchers, occurs when indentation load applied exceeds yield stress of material (e.g. Studman and Field, 1977; Swain and Hagan, 1976). Crack is initiated during releasing of load at the contact periphery and propagates outward even after the load is completely released. In case of static contact fatigue, radial crack was also observed in elastic-plastic materials such as hardened steel (Alfredsson and Olsson 2000; Abudaia *et al.*, 2005) and ceramics (Kim *et al.*, 1999). In hardened steel, radial crack initiated at the periphery of contact during releasing load due to tensile residual stress. Abudaia *et al.*, (2005) demonstrated that hoop stress turned to positive when the stress in contact area exceeded yield of material leading to radial crack. Kim *et al.*, (1999) found that radial cracks in brittle ceramics appeared inside contact area during high number of load cycles and at contact periphery after unloading. They suggested that these cracks were damaged in quasi-plastic mode and may be obscured by cone cracks after high number of load cycles. The beginning of material removal came together with the radial cracks.

In this research, radial cracks were observed in all contact pairs. These cracks, in every case, were confined within contact area (see Figure 5.10g, 5.11i, 5.12h, 5.13d and 5.14d) and they appeared at different times. The ranking from the shortest to the longest time required for crack appearance is as follows; $Si_3N_4$ after 810 minutes, aluminium, bronze and PMMA after 60 minutes and steel after 15 minutes and 810 minutes. Two type of radial cracks could be identified i.e. the first type at the boundary of the stick region and the second type at the contact periphery. In case of contact with steel, shallow radial micro-cracks occurred around the boundary of the stick region after 15 minutes and the other ones, associated with ring crack starting from the edge of contact, after 810 minutes (see Figure 5.11c and 5.11i). The first type caused little damage to the PMMA plate comparing with the second type. Similarly, contact with silicon nitride ball resulted in shallow micro-cracks between the edge of the stick region and the middle of the slip region.

The second type of radial crack was firstly observed at the outer part of contact annulus created in PMMA plate contacting with steel, aluminium, bronze and PMMA balls. This type of crack was associated with a severe damage. As mentioned above, radial crack in this study was different from what have been reported by other researchers. Also, this type of crack should have firstly occurred in contact with $Si_3N_4$ if only contact stress involved was important. Therefore, it might be that other factors are involved.

Consider frictionless Hertzian contact and circumferential stress distribution in elastic region. As shown in Figure 3.4 the stress is of compressive nature. The maximum hoop stress at the contact edge is equal to the calculated maximum tensile stress but of negative sign in elastic region. Therefore, radial crack is hardly produced by the mechanisms explained above. Again friction and adhesion should account for this crack.

The appearance of radial cracks indicated that there was tensile circumferential stress in contact area during loading/unloading cycle. It was supposed that the differences in Young's modulus and Poisson's ratio caused strain at the interface in friction contact leading to stress there.

Considering friction effect, the highest friction force is expected at the boundary of the stick region according to Li and Berger, (2003). This possibly agrees with the experiment results where radial cracks in PMMA plate were found in this region when it was in contact with $Si_3N_4$ and steel balls. The results of friction measurements also agree with this argument because the coefficients of friction between the PMMA plate and $Si_3N_4$ and steel balls were high in the high load range (see Figure 5.1). Generally, the coefficient of friction for PMMA in contact with $Si_3N_4$ ball was higher than that for steel ball. However, radial crack in this area occurred earlier when contact was with steel ball instead of $Si_3N_4$ ball. This infers that adhesion might contribute to radial crack creation.

Considering adhesion, if the surfaces adhere to one other forming strong interface, it would constrain the movement between them. As a result, high shear stress might occur during cyclic loading. This stress is superimposed onto friction force. As a result, the occurrence of the first type radial crack on PMMA plate contacting with steel ball is expected first.

It is apparent that the time required to create the second type radial crack tended to correlate with the adhesive strength between the ball and the plate. The higher adhesive strength was the shorter time to produce radial cracks was needed. This type of radial crack was likely to be associated with high material loss either accompanying ring crack in steel/PMMA combination and aluminium/PMMA combination or severe adhesive wear in bronze/PMMA combination and PMMA/PMMA combination.

In summary, radial crack in this study cannot be explained in a similar way to that proposed by previous research using tensile residual stress and quasi-plastic mode during load releasing for hardened steels and brittle ceramics, respectively. It is suggested that this crack was associated with adhesive strength between contacting bodies.

The counterpart material has an effect of on the damage behaviours of the PMMA, which is reflected in increasing the size of contact area. The increasing size of the slip radius of PMMA plate for all combinations with testing time was expected because the damage in the slip region resulting in decreasing of the contact strength while applied load was still the same (see Figure 5.34). Excluding PMMA/PMMA combination, the size of the radius of all combinations diverted with increasing testing time depending on the severity of the damage. The size of the slip radius ranked from the largest to the smallest for various balls used is as follows: aluminium, bronze, steel, and silicon nitride respectively. The ranking generally agrees with the severity of damage of the plate described in surface observation section.

The fluctuation of the size of the stick radius for the combination with steel, bronze, aluminium, and silicon nitride was at the early test time interval and might be caused by the wear process of each combination requiring different period. However, after the long testing period, the scatter decreased.

### 6.3 Effect of Lubricant on Damage of PMMA

A liquid lubricant affects the fretting process in three ways i.e. limiting the access of oxygen, carrying away debris and shifting coefficient of friction (Waterhouse, 1972). In metal, many researchers reported that the higher viscosity of the oil used resulted in the

lesser fretting damage. However, Burton and Russell (1966) reported the contrasting results of static contact fatigue in normal vibration under oil-lubricated conditions (cited in Waterhouse, 1972: p129). They found that increasing lubricant's viscosity resulted in greater damage (see Figure 6.2). However, the reasons were unclear.

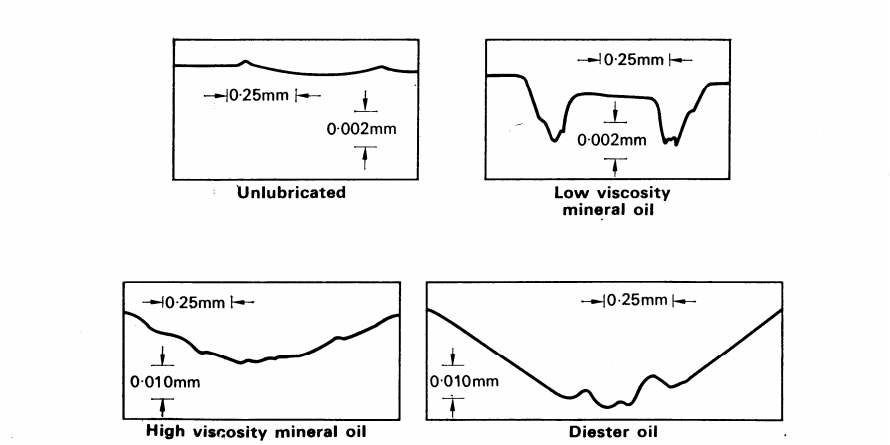


Figure 6.2 Wear scar profile from various viscosity lubricants (Waterhouse, 1972).

In this section the results of static contact fatigue in oil-lubricated conditions are discussed. Testing in oil-lubricated conditions required applying oil between the ball and the PMMA plate before loading the contact.

In contact area under oil-lubricated conditions three regions can be distinguished from the centre to the edge of the contact namely the stick region, the inner slip region and the outer slip region. In all contact combinations, the sizes of the inner slip region and the outer slip region in oil-lubricated conditions were comparable to the stick region and the slip region in dry conditions. The size of stick region in oil-lubricated conditions was smaller than that in dry condition. The results of friction measurement reveal that coefficient of friction in oil-lubricated conditions was greatly reduced comparing to dry conditions at the same normal load. It can be said that decreasing friction between contacting surfaces resulted in shifting the stick area.

The decrease of the friction coefficient due to oil film separating fully or partially contacting surfaces depends on loading conditions. The increase of coefficient of friction with increasing normal load indicated reduction of oil film thickness leading to raising the number of asperities contact between the counterparts. Higher amount of scratches and

transferred material on PMMA plate observed at high normal load support this argument (see Figure 5.7). No crack was initiated under lubricated conditions for the load range selected. This evidence can be used to conjecture that the lubricant reduced traction stress that necessarily produces cracks under dry conditions.

### *6.3.1 Adhesive wear*

In oil-lubricated conditions, lubricant penetrated between contacting surface before the beginning of the static contact fatigue test. The thickness of the lubricant film depended on contact pressure distribution. It would be the thinnest at the centre of the contact and the thickest at the contact perimeter. Due to high contact pressure at the central region of contact area, oil was expelled and direct contact of both contacting surfaces was established. This area was the stick region the same as in dry conditions. However, the stick region in this case was smaller than that created in dry conditions because decreasing of coefficient of friction led to decreasing of tangential traction. This was also suggested by Li and Berger, (2003) as mentioned in section 3.2.2.1.

The rest of the contact area, however, was still separated by a lubricant film. Probably, the lubricant regime was between boundary lubrication and mixed lubrication. The boundary lubrication regime was expected to be within the boundary of the stick region in oil-lubricated condition and its size corresponding to that of the stick radius in dry conditions at a minimum load and larger at a maximum load. This region was supposed to be the inner slip region.

During cyclic loading, there was a movement between the ball and the PMMA plate because of the differences in their elastic modulus as well as shearing at asperity contacts. After a short period of cyclic loading both surfaces in the inner slip region adhered together because oil film could not fully separate contacting surfaces. The experiment results confirmed that the inner slip region was incompletely formed at the early stage of testing for every material combination, but it was completely established after a prolonged test time (see Figure 5.15, 5.17 – 5.21). It is apparent that the time for establishing adhesion has a tendency to correlate with the adhesive strength between the counterfaces as mentioned in section 5.2.7.2.6. After the establishment of adhesion, adhesive wear process similar to that discussed earlier for dry conditions occurred in this region. The

finding of transferred materials on the contact surface either the ball or the PMMA plate in the inner slip region and lift up profiles of wear scar supports this argument (see Figure 5.29 – 5.33). Also, metal particles were found embedded in the PMMA surface in the inner slip region. Hence, severe damage was expected in this region and the depth profile measurement results confirmed this argument for all contact combinations. However, the magnitude of normal displacement for the maximum and the minimum load in this area was lower than that at the edge of contact in case of dry conditions. Therefore, the damage was much less severe. The depth profile measurements of wear scar produced in oil-lubricated conditions compared with those in dry conditions thus supporting this argument with exception of steel/PMMA combination.

### *6.3.2 Radial crack*

Under test conditions selected, radial cracks were produced in the inner slip region of PMMA plate when in contact with steel, aluminium and bronze (see Figure 5.18e, 5.19e and 5.20e). However, time to create this crack was different. For steel it was 180 minutes and for aluminium and bronze - 30 minutes. It is clear that the time needed to produce radial crack has a tendency to relate with the strength of adhesion similar to that found in dry conditions. Therefore, it is allowed to say that adhesion contributed to creation of radial cracks in oil-lubricated conditions. The coefficient of friction in oil-lubricated conditions for all materials combinations was much lower than that in dry conditions. It can be, therefore, suggested that friction had much less influence on creation radial cracks.

As explained in section dealing with dry conditions, radial cracks were associated with high material loss of the PMMA plate. Therefore, they might also cause severe damage in oil-lubricated conditions. The experimental results showed that in oil-lubricated conditions damage of the PMMA plate in contact with different balls can be ranked from the most severe to the least severe as follows; bronze, aluminium, steel, $Si_3N_4$ and PMMA. Although contact with aluminium and bronze produced radial cracks after the same period, the adhesive strength of the interface between bronze and PMMA was greater than that between aluminium and PMMA. In addition, the higher the coefficient of friction for contact between PMMA and bronze comparing to the contact between PMMA and aluminium might accelerate wear of PMMA when in contacting with bronze. However, despite the differences in the coefficient of friction it was small and, therefore, it may be

said that friction factor has little contribution to the damage of the PMMA plate. For $Si_3N_4$/PMMA combination, PMMA plate suffered little damage in dry contact condition. Therefore, less damage of PMMA plate in oil lubricated condition was expected. The experimental results confirmed this expectation. The coefficient of friction between PMMA and $Si_3N_4$ was higher than that between PMMA and PMMA. Comparing interface strength of PMMA/PMMA to that of $Si_3N_4$/PMMA the first combination could be stronger. If wear process in oil-lubricated condition is dominated by abrasive wear process then damage on PMMA plate tested against $Si_3N_4$ ball should be more severe than that against PMMA ball. However, the results of experiment showed something opposite. Therefore, it can be inferred that damage in oil-lubricated conditions was dominated by adhesive wear process.

### *6.3.3 Abrasive wear*

Consider the outer slip region, which was supposed to operate in the mixed lubrication regime. Accordingly, it was expected that the counterfaces contacted each other only with their tip of asperities. These asperities sheared one another during cyclic loading. Due to this process damage arose from abrasion and the softer material was highly abraded. Fine metallic particles embedded in this region might be inferred that the PMMA plate wore out the metals. This may also be used to support the idea that the contact in this region was taking place only at asperities.

The results of surface examinations showed that surfaces of all contact combinations in this region were relatively smooth comparing to the inner slip region. There was no sign of adhesion or crack in this area. Although the outer slip region was smooth, the smoothness was unequal. The ranking from the roughest to the smoothest was as follows; bronze, aluminium, steel, $Si_3N_4$ and PMMA. This aspect tends to have relationship to roughness of the balls as shown in Table 4.3, except steel ball, which surface was damaged more than the other balls. The ball surface in the position corresponding to the outer slip region was rougher than unaffected area. This result might be the reason why roughness of PMMA in the outer slip region was greater than in the case of $Si_3N_4$ ball. The abrasive damage was less severe comparing with adhesive damage in the inner slip area since radial cracks were not produced in this zone.

The size of the radius of contact was reflected in the severity of damage. In general, the size of the outer slip radius for all combinations of materials increased with increasing test time and agreed well with the calculated Hertz's radius (see Figure 5.35). The size of the inner slip radius generally tended to increase with testing time although some points occasionally swung. The sizes highly fluctuated for different material combinations at the early stage of testing time, but converged to a narrow band after 810 minutes. This may be conjectured that each material combination needed different incubation period for establishing adhesion. The sizes of the stick radius were highly scattered for all material combinations. The size has different trend for each material combination. This was unclear to establish the relationship with any factors.

This discussion excludes contribution the hydrostatic pressure from the lubricant, which might affect on damage mechanism to some extent. However, it should be kept in mind that this pressure existed in the contact area.

The severity of damage pertinent to different contact combinations in dry and oil-lubricated conditions may be discussed in the following way. The slip radius in dry and the outer slip radius in oil-lubricated conditions in all materials combinations were almost the same for the entire testing duration (see Figure 5.36-5.40). The radius sizes for both conditions increased with increasing test time. This was expected because the damage in the contact area reduced their interfacial strength while the stress applied was constant. With exception the PMMA/PMMA combination, the radius sizes for both conditions were larger than the calculated Hertz's radius after short testing duration. Contact radii of PMMA/PMMA combination in both conditions were smaller than the calculated Hertz's radius at the beginning of the testing period and were just above the calculated radius after 810 minutes of testing time. This was possibly due to the mechanical properties of actual material deviated from the given material data because other combinations followed the Hertz's theory.

The inner slip radius in oil-lubricated conditions for the combination with $Si_3N_4$, steel, aluminium and bronze was of the same magnitude as the stick radius in dry conditions and increased with testing period. This phenomenon was expected as explained above in case of the outer slip radius. The more damage in the inner slip region and the outer slip region reduced the load bearing area resulting in the more deformation of the PMMA plate.

Therefore, the contacting surface in the slip region was expanded outward. As a result, the sizes of the inner slip radius have a tendency greater than the stick radii in dry conditions after prolong testing time that they were relatively constant tendency.

The smaller size of the inner slip radius in oil-lubricated conditions for PMMA/PMMA combination than that resulted from dry conditions at the early of testing was probably due to greatly reduced friction between the contacting bodies. The highly changeable size of the inner slip radius at this period may be attributed to unstable surface morphology during incubation period when adhesive junctions were created. However, after adhesion was firmly established the inner slip radius increased with the testing time similar to other contact pairs and reached the stick radius value in dry conditions after 810 minutes.

The stick radius in dry conditions for all combination of materials was larger than that in oil-lubricated conditions for the entire testing period. The reason for this was explained earlier. The stick radius in dry conditions has increasing tendency for $Si_3N_4$ and bronze, but changed alternatively for steel and aluminium. For PMMA/PMMA combination, it increased gradually with increasing testing time up to 180 minutes and decreased afterwards. The stick radius in oil-lubricated conditions has different tendency with test time; increasing for PMMA; relatively constant with only slightly fluctuation for aluminium; fluctuating during the early test period for $Si_3N_4$, but with increasing tendency at the end; decreasing tendency for steel; highly changeable and diminished at the end of test for bronze.

Under oil lubrication the damage characteristics of PMMA plate are as follows. For low adhesive strength of $Si_3N4$/PMMA combination, the severity of damage in both dry and oil-lubricated conditions was insignificantly different due to main mechanism which was adhesive wear controlling damage in this combination. The lubricant did not assist in decreasing damage of this contact pair even though friction between contacting surfaces decreased dramatically.

The damage in the steel/PMMA combination was mainly wear manifested by depth of worn out material, which in oil lubricated condition was higher than in dry conditions. However, subsurface cracks in dry condition should be accounted for the severity of damage more than worn out material.

For aluminium/PMMA combination, testing with oil lubrication significantly reduced the depth of wear scar of the PMMA. Ring cracks were facilitated by lubricant shifting the adhesive area inward to the stick boundary in dry conditions and resulting in decreasing of tensile stress during cyclic loading.

The damage of bronze/PMMA combination was similar to that of aluminium/PMMA combination. However, the adhesive strength of the interface in this combination was higher than that of aluminium/PMMA resulting in a more severe damage in this combination under both dry and oil-lubricated conditions.

For PMMA/PMMA combination, oil has greatly helped reducing adhesive wear damage of the ball, even though shallow worn out surface on the PMMA plate occurred.

## 6.4 Molybdenum and Titanium Surface Coating Failure Mechanisms in Dry Conditions

Table 6.1 shows the calculation results of contact stresses, contact radius, maximum tensile and shear stress due to Hertz's theory according to equations in section 3.2.2 for the conditions used in this experiment. The average coating thickness of molybdenum coating and titanium coating was 109 μm and 169 μm, respectively. Both coatings may be categorized as thick coatings because the maximum shear stress under the load used was located in the coating layer at the beginning of the test. It can be appreciated that using the same load of 1.0 kg, but changing from molybdenum coating to titanium coating resulted in not only increasing the contact area but also decreasing the Hertzian contact stress from 1.67 GPa to 0.74 GPa.

Yield strength of molybdenum from available data has a wide range between 275.8 and 655 MPa and the yield strength of pure commercial titanium, Grade 2, is 275 MPa. Under selected contact load, maximum tensile stress in both coating systems was lower than yield strength of the corresponding materials. However, the actual yield strengths of coatings were possibly lower than those above values because the coatings consisted of many kinds of defects.

Table 6.1 Calculation results of stresses and contact radius of Mo coating and Ti coating.

| **Coating material** | **Load (kg)** | $p_0$ **(GPa)** | $a$ **(μm)** | **max.** $\sigma_r$ **(MPa)** | $\tau_0$ **(MPa)** | **Depth of** $\tau_0$ **(μm)** |
|---|---|---|---|---|---|---|
| Mo | 0.5 | 1.32 | 109 | 159 | 411 | 52 |
| Mo | 1.0 | 1.67 | 137 | 200 | 517 | 66 |
| Mo | 1.5 | 1.91 | 157 | 229 | 592 | 75 |
| Ti | 1.0 | 0.74 | 206 | 79 | 228 | 99 |

In chapter 1, it was already discussed that various factors affect to the performance of thermal spray coatings in RCF test. Those factors included; type of coating material, surface roughness, compressive strength of coating, and shear stress between the coating/substrate, the magnitude of tangential force and the direction of the sliding, deposition process, type of counterface material, residual stress, lubricant and post heat treatment. Rolling contact behaviour of coatings was affected by Hertz's contact stress, tribological conditions (friction and wear), vibration during the test, surface treatment before coating, coating thickness, and post heat treatment process.

The following discussion is based on the results obtained. The main discussed topics will be the RCF in dry conditions and the effect of contact stress.

### *6.4.1 Molybdenum coating*

Akdogan et al. (2002) have investigated surface fatigue of Mo in rolling line contact (two discs configuration) under pure rolling and rolling/sliding (5%) conditions with applied load below the yielding stress. Surface damage in pure rolling suffered in consequence of grain detachment, micro-spall, craters formation, and micro-crack and spalling fatigue. The rolling/sliding condition reduced wear rate for Mo coating. The coating demonstrated non-significant life dependency on load and had high performance in both pure rolling and rolling/sliding contacts.

The results of this experiment carried out in ball-on-flat configuration, however, showed that weight loss was highly dependence on contact stress (see Figure 5.66). This may be influenced by different contact configuration, loading conditions, spray conditions, etc.

The relationships between the rate of weight loss and contact stress was not linear. Increasing contact stress from 1.32 GPa to 1.67 GPa (in increments of 0.35 GPa) resulted in high change of weight loss rate. However, increasing contact stress from 1.67 GPa to 1.91 GPa (in increments of 0.24 GPa) altered the wear curve slope less than for 1.32 GPa to 1.67 GPa. The characteristic of the change might be explained in terms of tensile stress as shown in Table 6.1. The difference in maximum tensile stress by increasing contact stress from 1.32 GPa to 1.67 GPa was 41 MPa, while the difference of 29 MPa resulted from increasing contact stress from 1.67 GPa to 1.91 GPa.

Early stage weight loss rate was different from the later stage. It might be inferred that the early stage was unstable because many processes involved such as asperities flattening and/or adhesion were initiated. Weight loss slope at the end of first stage was almost a linear function of the number of load cycles. As the test progressed, surface wear of coating led to conforming contact and increasing the width of wear track. As a result, contact stress was decreased. The calculation of real contact stress based on wear track size measurements is shown in Figure 6.3. Contact stress decreased abruptly from the initial magnitude after a low number of load cycles, in all cases lower than 0.5 GPa. Afterward, it was gradually decreased. The decreasing in contact stress would be expected to be manifested by decreasing in weight loss rate. However, weight loss slope was insignificantly altered or even kept constant.

The coatings were not damaged by delamination or spalling at all selected contact stresses. SEM examination showed that wear track surface was rough with little deformation of coating. Material transferred between coating and the ball surface. This feature was also observed by optical microscope. The cliff edge of transferred material on both the ball and wear track surfaces allowed to say that transferred material was relatively brittle.

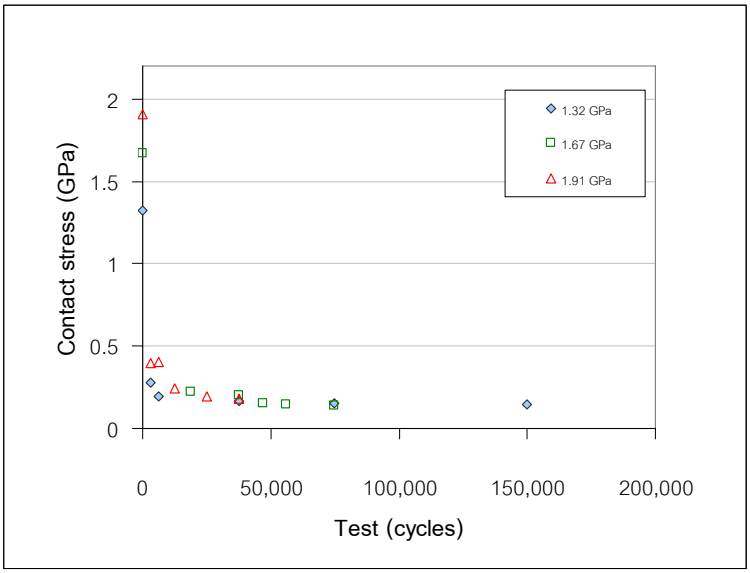


Figure 6.3 Relationships between contact pressure and load cycles.

Examination with EDX analysis revealed that the composition in the dark area of the wear track, which was the transferred material (stick material), mainly consisted of iron (see Figure 5.46). Meanwhile the main composition of transferred material on the ball surface was molybdenum (see Figure 5.48). The composition in the bright area, which is the freshly worn out surface of coating, consisted only of molybdenum (see Figure 5.47). This evidences mutual transfer of material between contacting surfaces. However, it can be suggested in this case that the cohesive strength of the steel ball was superior to that of the coating and the interface. Observation of oxygen within transferred material may imply oxidisation being involved in the wear process.

Only the upper layer of the coating was broken for all selected contact stresses as evidenced by metallographic examinations of the sections (see Figure 5.62). The lateral breaking of the coating, which occurred between the lamellas, indicated that cohesive strength between lamellas of the coating was lower than that within the lamella itself. The lamella was also broken in vertical direction. Breaking of lamella accelerated weight loss in dry conditions.

Correlation between the depths of broken layer and contact stress could not be established. It is, however, proposed that the higher contact stress acting on the material the higher probability of crack initiation sites. If the wear debris were trapped between the counterfaces, denting and scratching would occur. In the case of adhesion mechanism

being involved, high contact stress increased the number and/or the area of asperities contact. As a result, the probability of adhesion sites was also increased. The adhesion was broken at the trailing edge of the counterfaces. Therefore, higher wear rate at high contact stress would be expected.

Damage in rolling contact fatigue is thought to originate at surface cracks and subsurface cracks. Molybdenum coating in this experiment showed domination of surface crack initiation in the test conditions selected. This agrees with the results by Tobe *et al.* (1988) who have studied plasma sprayed metallic coatings on steel substrate using twin disc test configuration. They argued that cracks initiation was in mode I as a result of tensile stresses. However, this experiment showed that adhesion was the major wear mechanism. Surface cracks are supposed to accelerate wear rate.

When the counterfaces are in contact under loading, it is generally known that the harder material suffers the lesser wear damage. Hardness values of molybdenum coating were lower comparing to steel ball. The experimental results agree with that as the steel ball surface experienced mild damage only. Hardness range of the coating was large. Therefore, it is permissible to say that residual stress in the coating was high. In addition, observation of surface plastic deformation within wear track implied creation of residual stress in the coating especially on the surface. Furthermore, various kinds of imperfections, i.e. pores, oxides, un-melted particles existed in the coating causing weakening its strength. Therefore, the coating was expected to have more severe damage than the ball.

### *6.4.2 Titanium coating*

Weight loss rate of titanium coating in dry conditions was also high. The weight loss slope at the early stage of testing was lower than the later stage. Consider the first stage, asperities deformation and adhesion must be high. In the later stage, surface conformation and increasing contact area reduced contact stress resulting in lower wear rate. However, wear debris were produced during rolling contact and were accumulated with increasing test duration. It can be inferred that wear in the later stage would be a complicate mechanisms.

Surface investigation by OM and SEM, the wear track showed rough surface with adhered material (see Figure 5.44). Transferred material was also detected on the ball surface. These evidences can be suggested that adhesion between materials during rolling contact was occurred similar to the case of molybdenum coating. The morphology of transferred material, however, was different from the case of molybdenum rolling contact. It showed the smoothly edge feature which thickness of adherent gradually decreased from the middle to the edge and the cliff edge was hardly seen. The examination results allow saying that transferred layer was more plastically deformed than that of the molybdenum coating. Surface of both wear track and the ball showed smearing transferred material. This indicated sliding during rolling contact.

EDX analysis results of the transferred layer in wear track (the dark area) presented the main composition of titanium with amount of iron and oxygen (see Figure 5.53). Contrasting to the fresh worn surface (the bright area) presented fewer amounts of iron and oxygen (see Figure 5.54). The transferred material area on the ball composed of high amount of iron, oxygen and silicon other than the main composition of titanium (see Figure 5.55). According to the results, it can be inferred that adhesive process caused wear of titanium coating and the ball.

Damage of the ball surface was much lower than the coating. The reason behind this was similar explanation as molybdenum coating.

The results of metallographic investigation of cross-sectioned samples showed that the surface profile of wear track was smooth (see Figure 5.64). Surface deformation can be seen at higher magnification. Surface worn out feature was relatively similar for the whole region of the track. Crack at the upper coating layer or breaking of lamellar was not detected. From the results, it can be implied that the inter-lamellar cohesive strength in the case of titanium coating was high. Titanium coating allowed plastic deformation to occur. Only smearing on the surface could cause surface cracking.

The results of investigation demonstrated that wear process of both coating systems was mainly due to adhesive process. In molybdenum coating breaking of the upper layer of lamellar accelerated wear rate. For titanium coating, high deformability and strong cohesive strength of inter-lamellar retarded breaking at the boundary of lamellar.

Compare molybdenum coating with titanium coating weight loss of molybdenum coating was higher after the same number of load cycles. Consider contact stress, molybdenum coating was subjected to higher contact stress than that of titanium coating. In this case it could be a reason of higher weight loss rate in molybdenum coating. Furthermore, molybdenum coating exhibited more brittle behaviour than titanium coating. However, microstructure of molybdenum coating was more homogenous than that of titanium coating. Therefore, the judging which coating is better resistance to RCF in dry conditions could not be suggested in this research.

## 6.5 Molybdenum and Titanium Surface Coating Failures Mechanisms in Seawater Conditions

### *6.5.1 Molybdenum coating*

In seawater conditions, weight loss curve of molybdenum coating could be characterised into three stages (see Figure 5.67). The first stage weight loss rate was high. This stage started from the beginning of the test until 56,132 load cycles. Then the second stage which has lower wear rate, but relatively steady. This stage took the longest load cycles until 399,164 cycles. Wear rate increased again at the third stage. These characteristics will be discussed after the examination with OM, SEM and EDX.

Wear track surface tested in seawater conditions were smoother than that tested in dry conditions (see Figure 5.43). Deformation of surface was observed. Distributed thin film of corrosion products covered on the surface. Transferred material was not detected on both the ball surface and wear track surface. The experimental results allow to say that seawater prevented adhesion between counterfaces.

Although seawater might act as lubricant, the lubrication regime was boundary lubrication. Therefore, seawater in this case would not completely separate contacting surfaces or prevented asperity contact. This was evidenced by an observation of material deformation within the wear track areas. The reason why adhesion was prevented may be assumed the formation of new phases on the surface of either the coating or the ball. These phases have low surface forces which reduced the adhesive forces between the original counterfaces.

Seawater is generally aggressive medium and causes corrosion to metals. Steel is normally not serviced as bare surface in seawater because it was corroded easily. The results of SEM examination showed general corrosion and pitting corrosion on steel ball surface (see Figure 5.43e and 5.43f). Normally, steel is usually required to protect by corrosion resistant coating or by other means such as cathodic protection when applied in seawater. Molybdenum is also not a good corrosion resistance though it was alloyed in stainless steel to improve pitting corrosion resistance (Stansbury and Buchanan, 2000). Corrosion potential of low alloy steel in seawater lies between -0.625 to -0.575 V. Corrosion potential of molybdenum in seawater is not available. However, the standard half cell potential at 25 ºC for molybdenum and iron are

$Mo = Mo^{+3} + 3e$ - 200 mV

$Fe = Fe^{+2} + 2e$ - 440 mV

Also, compare molybdenum Pourbaix diagram with Pourbaix diagram of iron in water in neutral pH range reveals that the potential of immunity region of molybdenum is higher than that of iron (see Figure 6.4).

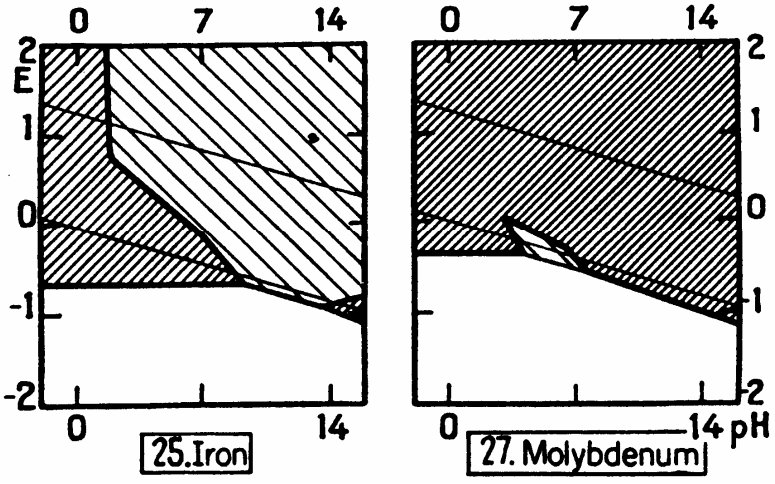


Figure 6.4 Pourbaix diagrams of iron and molybdenum. Metals immune to corrosion in the white area (Stansbury and Buchanan, 2000).

From those information, it can be conjectured that molybdenum acted as cathode comparing to steel ball. Therefore, it was protected by galvanic coupling with steel ball resulting in reduction of corrosion. This is corroborated by corrosion of steel balls and higher content of iron, oxygen and chromium in wear track in seawater conditions

compared with in dry conditions as evidenced by EDX results obtained from samples tested in seawater conditions (see Figure 5.50 and 5.51). The portion of those elements in the dark area (corrosion products film) compared with in the bright area (new worn out surface) were also higher. From the experimental results, the argument that the steel ball was damaged by combination of wear process and corrosion process would be acceptable. Corrosion product films formed on surface of the balls and the coating were probably oxide or hydroxide of metals. These films prevented adhesion between counterfaces. However, the films would be destroyed and generated again during rolling contact cycle leading to altering metal surfaces between passive and active state. Corrosion film and debris probably caused abrasive wear of coating. Shallow scratch feature and corrosion on surface of the ball together with embedding of corrosion products on wear track surface would support this argument.

The results of post-test OM, SEM and EDX investigations were allowed explaining three stage wear behaviours of molybdenum coating in seawater conditions. In the first stage, asperities flattening of the coating surface which was relatively rough and asperities breaking were taken place. In this regards, wear rate in the first stage was high. This period took time only a short period or several thousand of loading cycles. The second stage began when contact surface was more conforming and the true contact area increased. These situations resulted in decreasing real contact pressure and increasing of lubrication film thickness. Therefore, wear rate was decreased. In this stage the counterfaces were still partially in contact. Wear process would suggested to be dominated by a combination of corrosion and abrasion from either microslip or sliding in wear track from direct contact of counterfaces or third bodies abrasion. It took the longest period. As the test prolonged wear debris which were generated during rolling contact were accumulated. Third bodies wear was possibly dominated the third stage.

After high loading cycles, coating surface in the contact area was smoother than that in dry conditions. Breaking of asperities was not detected in this stage. These results could support the above arguments.

It is interesting that corrosion between the coating/substrate interfaces was observed after short period (46,777 cycles). This was supposed to be galvanic corrosion similar to that suggested earlier because substrate was low carbon steel. Corrosion at the coating/substrate

interface can occur because the solution can penetrate through the porosity of coating and created bimetallic coupling. The interface corrosion outside wear track area was negligible because corrosion products produced after the first corrosion covered metal surface prevented further reaction. As a result, corrosion reaction was greatly reduced. Corrosion under wear track, however, was more severe. It was accelerated by mechanical cyclic load due to rolling resulted in breaking and/or removal of corrosion products at the interface followed by the creation of new active metal surface that was readily corroded. Corrosion propagated laterally along coating/substrate interface. As corrosion propagated, the adhesive area between coating and substrate decreased. However, delamination or spalling was not happened after test terminate.

### *6.5.2 Titanium coating*

Weight loss curve of titanium coating in seawater conditions could be divided into three stages and its characteristics are similar to that of molybdenum coating (see Figure 5.67). The first stage weight loss rate was high till 78,430 load cycles were reached. During the second stage, wear rate was very low. Wear rate increased steeply after 399,164 cycles. In the third stage wear rate of titanium coating was higher than that of molybdenum coating.

The results of OM and SEM investigations showed that wear track surface was also smoother than that after testing in dry conditions (see Figure 5.45). Surface deformation was also detected and was similar to the case of molybdenum coating. However, cross-section examinations of the upper layer of lamellar hardly revealed cracks in this coating. Thus, it can be conjectured that lower wear rate in the first stage of titanium coating compared with molybdenum coating was due to the absence of breaking process of the upper layer of lamellas. Corrosion products covered surface of wear track. Ball surface was relatively smooth with some small pits on it. Under OM examinations brownish thin film of corrosion products was observed. Shallow scratches were detected at higher magnification. Transferred material was not detected on both surfaces. Therefore it can be accepted that adhesion was not involved in seawater conditions.

As mentioned in chapter 2, titanium is resistant to seawater. Corrosion potential of titanium in seawater is in the range -0.05 to 0.05 volts (Stansbury and Buchanan, 2000). This potential is higher than that of steel. In this regards, galvanic coupling with steel also

protected titanium coating and resulted in even less corrosion. This was supported by corrosion of steel balls and higher content of iron, oxygen and chromium in wear track in seawater conditions compared with dry conditions as evidenced by EDX results (see Figure 5.57 and 5.58). The portion of those elements in the dark area (corrosion products film) compared with that in the bright area (freshly worn out surface) was higher.

From the experimental results, the argument that the damage process of steel ball was similar to the case of molybdenum coating can be applied. Corrosion product films formed on surface of the balls and the coating were probably oxide or hydroxide of metals. These films prevented adhesion between counterfaces. However, the films would be destroyed and generated again during rolling contact cycle leading to altering metal surfaces between passive and active states. Corrosion film and debris probably caused abrasive wear of coating. Shallow scratch feature and corrosion on surface of the ball together with embedding of corrosion products on wear track surface would support this argument. In this case, titanium oxide film is usually good adherent to the titanium metal surface. Together with its intrinsic high corrosion resistant property, therefore, lower wear rate of titanium coating in the second stage resulted.

The third stage wear represents high number of load cycles. Wear rate of titanium coating was the highest in this stage. It was even higher than the third stage wear rate of molybdenum coating. Weight loss at the end of testing was also higher than that of molybdenum coating. Surface investigations found that titanium coating was damaged by spalling (see Figure 5.65e).

Metallographic examinations on cross-sectioned test samples revealed galvanic corrosion at the coating/substrate interface right under the wear track similar to that suggested earlier for molybdenum coating (see Figure 65a - 65d). It was firstly detected after 46,777 load cycles. Propagation process of corrosion observed in the case of molybdenum coating can also be relevant here. However, titanium coating contained higher amount of porosity than molybdenum coating, therefore, it was prone to corrode quicker. Furthermore, corrosion potential difference between steel and coating in case of titanium was greater than that for molybdenum, thus, faster corrosion propagation in titanium coating would be expected. The adhesive area between coating and substrate was diminished after 523,902 load cycles were reached (see Figure 5.65f and 5.65g). Coating was broken at a certain time leading to

spalling. Weight loss rate of titanium coating after high load cycles was, therefore, greater than molybdenum coating.

Comparing dry conditions with seawater conditions, weight loss in dry conditions was greater than that in seawater conditions after the same number of load cycles for both coating systems. Weight loss difference for both coating systems increased as the test duration increased. When the test duration reached 74,843 load cycles, weight loss in dry conditions was 6.7 times greater for molybdenum coating and 9.6 times greater for titanium coating comparing to weight losses recorded in seawater conditions.

In dry conditions, material transferred between coating and the ball for both coating systems. This indicates that adhesive process caused high wear rate in dry conditions. Due to adhesion between counterfaces and de-cohesion of transferred materials in the form of wear particles, wear rates of coating in both systems were higher than that under seawater conditions. Breaking of inter-lamellas especially enhanced wear rate in molybdenum coating.

In seawater conditions, wear track surfaces of both coating systems were smoother than that tested in dry conditions. Under selected testing conditions, material deformation within the wear track areas occurred for both coating systems. Adhesive process was not observed. Seawater might act partly as lubricant and prevent adhesion by creating thin film of corrosion products via corrosion process.

Two galvanic coupling, between steel ball and coating and between coating and steel substrate, existed in seawater conditions. The first case resulted in a low wear rate of coating, but high wear rate of steel ball. The second case occurred because the solution can penetrate through the porosity of coating and react with the base metal. In long term test, galvanic corrosion at the coating and substrate interface associated with mechanical cyclic load due to rolling destroyed adhesive bond between them resulting in weakening of coating/substrate interface. Spalling occurred in the case of titanium coating because corrosion was fast.

In dry conditions, insignificant wear of the balls in contact with both coating systems may due to their higher hardness comparing to coating materials. Unlike in dry conditions the ball in seawater conditions experienced more damage due to corrosion process.

**References:**

Abudaia, F. B., Evan, J. T. and B. A. Shaw (2005) "Spherical indentation fatigue cracking" *Mater. Sci. and Eng. A*, Vol. 391, pp. 181-187.

Alfredsson, B., and M. Olsson (2000) "Standing contact fatigue testing of a ductile material: surface and subsurface cracks" *Fatigue Frac Engng Mater Struct*, vol. 23, pp. 229-240.

Alfredsson, B., and M. Olsson (2003) "Incline standing contact fatigue" *Fatigue Frac Engng Mater Struct*, vol. 23, pp. 229-240.

Higham, P. A., Stott, F. H., and B. Bethune (1978) "The influence of polymer composition on the wear of metal surface during fretting of steel on polymer" *wear*, vol. 47, pp. 71-80.

Hosford W. F (2005) "Mechanical behaviour of materials" *Cambridge university press*, New York, pp.22.

http://www.futurealloys.co.uk/Downloads/MOLYBDENUM.pdf

Kim, D. K., Jung, Y.-G., Peterson, I. M. and B. R. Lawn (1999) "Cyclic fatigue of intrinsically brittle ceramics in contact with spheres" *Acta mater.,* vol. 47, no. 18, pp. 4711-4725.

Zhu, M.H. and Zhou, Z.R. (2001) "An experimental study on radial fretting behaviour" *Tribology International*, vol. 34, pp. 321–326.

Stansbury, E. E. and R. B. Buchanan (2000) "Fundamentals of electrochemical corrosion" *ASM International*, Ohio, pp. 128, 166-167.

Studman C. J. and J. E. Field (1977) "The indentation of hard metals: the role of residual stress" *J. Mater. Sci*, vol. 12, pp. 215-218.

Swain, M. V. and J. T. Hagan (1976) "Indentation plasticity and the ensuing fracture of glass" *J. Phys. D: Appl. Phys.*, Vol. 9, pp. 2201-2214.

Tobe, S., Kodama, S. and K. Sekiguchi (1988) "Rolling Fatigue behaviour of plasma coat steel" *Surface Engineering International Conference,* Tokyo, Japan, pp. 35-44.

Waterhouse, R. B. (1972) "Fretting corrosion" *Pergamon press*, pp. 32,127-128.

# Chapter 7 CONCLUSIONS AND FUTURE WORK

## 7.1 Conclusions

Experimental investigations on static contact fatigue and dynamic contact fatigue of selected materials using ball-on-flat configuration under different tribological conditions have been conducted to elucidate their possible failure modes and mechanisms.

### *7.1.1 Static contact fatigue*

Results of static contact fatigue of brittle polymer (PMMA) against balls made of five different materials, that is $Si_3N_4$, steel, aluminium, bronze and PMMA in dry and seawater conditions allow the following conclusions.

1. In dry conditions, PMMA plate exhibited severe damage in the slip region, while no or little damage was obtained in the stick region. Adhesive strength of the interface was a major factor controlling the failure modes of PMMA in combination with every material. Three failure modes i.e. adhesive wear, ring cracks and radial cracks contributed to different damage features in each material combination.
2. Adhesive wear occurred in all contact combinations, but differently progressed depending on the strength of adhesion. Contacting with bronze produced the most severe wear to PMMA plate followed by aluminium, steel and $Si_3N_4$. In contrast, damage of the PMMA ball inflicted by PMMA plate caused severe wear of the ball.
3. The ranking of adhesive bonding strength to PMMA plate from the weakest to the strongest was as follows; $Si_3N_4$, steel, aluminium, bronze.
4. Ring cracks in PMMA plate initiated at the contact periphery with assistance from adhesive force in medium adhesive strength interface i.e. steel/PMMA combination and aluminium/PMMA combination and progressed inward during releasing state in cyclic load. The time required to produce ring cracks in combination with aluminium was less than that with steel due to the stronger adhesion.

5. Two types of radial crack were produced on PMMA plate. The first type, in the form of shallow microcracks causing little damage, occurred around the boundary of the stick region in combination with $Si_3N_4$ ball and steel ball. The second type occurred at the edge of contact annulus in the combination with steel, aluminium, bronze and PMMA ball. This type of crack was associated with high material losses either assisted by ring cracks in contacting with steel and aluminium or severe adhesive wear when in contact with bronze and PMMA.
6. Time to initiate both types of ring cracks was associated with adhesive strength of the interface between contacting bodies.
7. In oil-lubricated conditions, the contact area in all contact combinations consisted of three regions from the central to the edge of the contact namely: the stick region, the inner slip region and the outer slip region. The sizes of the inner slip region and the outer slip region in oil-lubricated conditions were comparable to sizes of the stick region and the slip region in dry conditions. The size of stick region in oil-lubricated conditions was smaller than that in dry conditions.
8. Three failure modes, i.e. adhesive wear, radial cracks, and abrasive wear contributed to the damage of PMMA.
9. Adhesive wear occurred at the inner slip region in all material combinations with different starting time and damage severity. Damage mechanism was the same for both test conditions.
10. Radial cracks were produced in the inner slip region in the case of contact with steel, aluminium and bronze. The time required to produce radial cracks has a tendency to relate with the adhesive strength of the interface, except with PMMA ball.
11. Abrasive wear occurred in all contact combinations in the outer slip region. The abrasive wear caused less severe damage comparing with adhesive wear in the inner slip region. The worn surfaces in abrasive wear region, which was smoother than that in adhesive wear region, have a tendency to relate with the roughness of counterpart surface except with the steel ball because its surface was rougher after the test.
12. Damage of PMMA in all material combinations under both test conditions increased with increasing test time. Excluding PMMA/PMMA combination, the size of the contact radius of all combinations in both conditions diverted with increasing testing time depending on the severity of the damage.

13. Damage in combination with $Si_3N_4$, which has low adhesive strength in both dry and oil-lubricated conditions, was insignificantly different even though friction between contacting surfaces decreased dramatically due to adhesive wear mechanism controlled damage.
14. Wear measured as the depth of wear scar in the steel/PMMA combination in oil-lubricated conditions was greater than in dry conditions.
15. The depth of wear scar of the PMMA in combination with aluminium was significantly decreased in oil lubrication.
16. The failure modes of PMMA in combination with bronze were similar to that with aluminium, however, the higher of adhesive strength of the interface resulted in a more severe damage in this combination in both dry and oil-lubricated conditions.
17. For PMMA/PMMA combination, lubricant had a significant effect in reducing adhesive wear damage on the ball, even though shallow worn out surface on the PMMA plate occurred.

### *7.1.2 Dynamic contact fatigue*

Dynamic contact fatigue under rolling contact load of plasma sprayed molybdenum and titanium coatings in dry conditions and seawater conditions was studied. The results of investigations can be summarised as follows.

1. Under used testing conditions, delamination was not detected in dry and seawater conditions for both coating systems.
2. Under the same test conditions, weight losses in dry conditions were much higher than those in seawater conditions.
3. Titanium coating performed better than the molybdenum coating in seawater conditions. However, it was damaged by spalling at the coating/substrate interface due to galvanic corrosion associated with high number of load cycles leading to high weight losses.
4. Adhesion was a major wear process controlling the rolling contact damage of molybdenum coating and titanium coating in dry conditions. Adhesion and de-cohesion of transferred material in the form of wear particles caused higher wear rate than that in seawater conditions. Breaking the upper layer of inter-lamellas in

molybdenum coating especially enhanced the wear rate. For titanium coating, high deformability of coating and strong cohesive strength of inter-lamellas retarded inter-lamella breaking process.

5. Wear rate of molybdenum coating was a non-linear function of contact stress. Wear rate was more sensitive to contact stress at the lower load range than at the high load range.
6. Three stages of wear behaviour for molybdenum coating and titanium coating were distinguished in seawater conditions. The first stage was controlled by asperity flattening and asperity contacts breaking. The second stage was dominated by combined effect of corrosion, abrasive wear and lubrication. Third body wear was dominant in the third stage.
7. Seawater caused decreasing wear of molybdenum coating and titanium coating through a number of processes including: partial lubrication, prevention of adhesion by creating thin film of corrosion products on the ball, and creation of cathodic protection of the coatings.
8. In long duration, test galvanic coupling between coating and steel substrate associated with mechanical cyclic load in seawater conditions caused spalling of coating in long duration test especially in the case of titanium.

## 7.2 Recommendations for Future Work

### *7.2.1 The static contact fatigue*

The effect of the counterface material on static contact fatigue of PMMA was investigated experimentally and failures modes were suggested. However, in order to elucidate precise mechanisms further works are suggested.

Investigations on transferred surface film of each material combination using ESCA, FT-IR should be conducted in order to clarify the nature bonding and their bond strength.

In situ damage observation on PMMA surface using deep field optical microscope would be useful to obtain the damage processes especially the initiation and the propagation of ring cracks and radial cracks in each material combination.

The effects of lubricant viscosity on the damage of PMMA plate would be another topic for the future investigation. This investigation can clarify the effect of hydrostatic pressure. Also, it may answers the question why similar sizes of the slip radius in dry conditions and the outer slip radius in oil lubricated conditions were obtained.

### *7.2.2 Dynamic contact fatigue*

The effects of seawater have been investigated and the suggestions on its involvement in failure modes of the molybdenum and titanium coatings under dynamic rolling contact load were studied. However, further investigations are required in order to provide comprehensive characteristic of their performance in seawater conditions.

Due to the effect of galvanic corrosion between the ball and the coatings affecting wear behaviours of both coating systems inert ball material such as ceramics may be used for investigating the galvanic corrosion effect.

Wear debris cause third body wear resulting in high wear rate. It would be interesting to carry out experiments under conditions where seawater flows through the contact zone and debris are filtrated out to elucidate the effect on the third stage wear of both coating systems.

# APPENDIX A DESIGN OF STATIC CONTACT FATIGUE TEST RIG

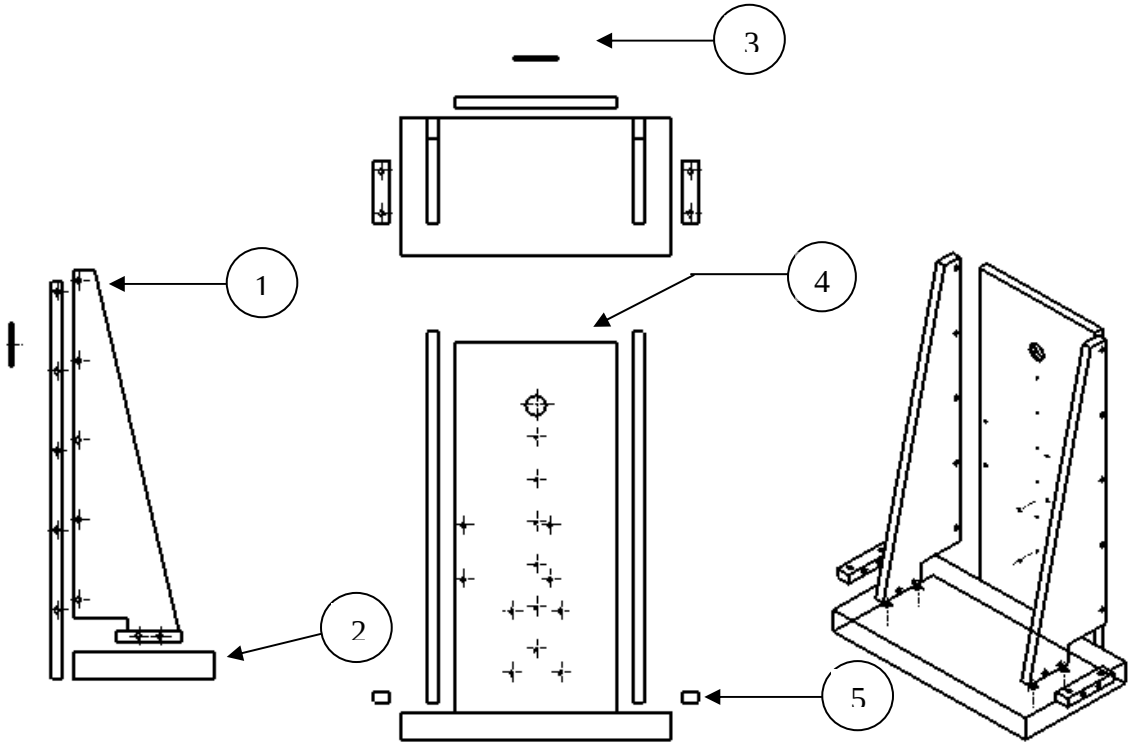


RIG HOUSING

| No. | Part Name | Quantity |
|---|---|---|
| 1 | Reinforcement | 1 |
| 2 | Basement | 1 |
| 3 | Bearing constrain | 1 |
| 4 | Support | 1 |
| 5 | Fixer | 2 |

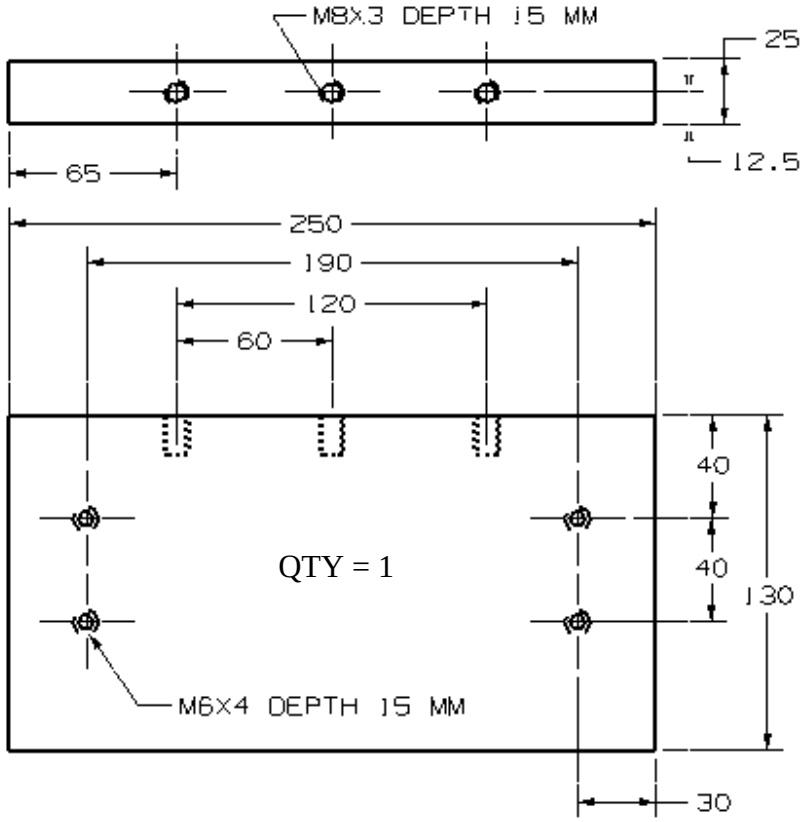


BASEMENT

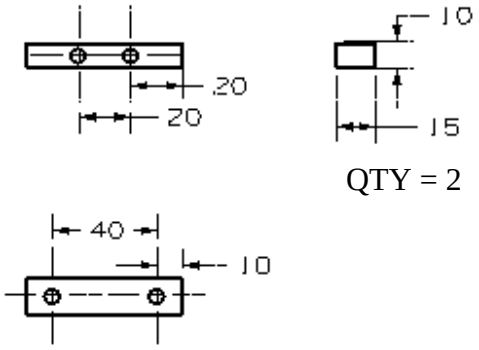


FIXER

| | |
|---|---|
| Brunel University | Do not scale |
| Unit MM | Drawn P. Vongbandit |
| Material Low carbon steel | Dwg No. 2 |
| Quantity _- | Page 2/12 |
| Title BASEMENT AND FIXER | |

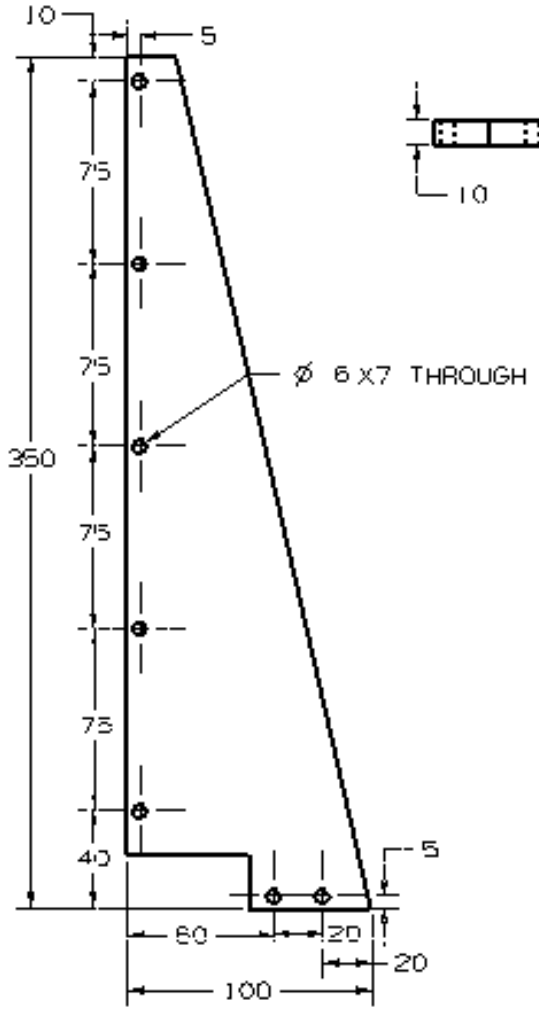


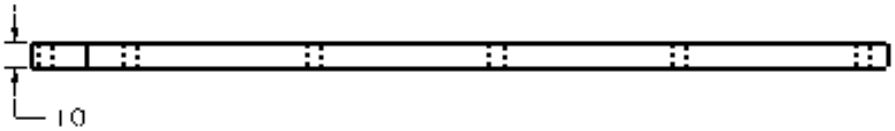


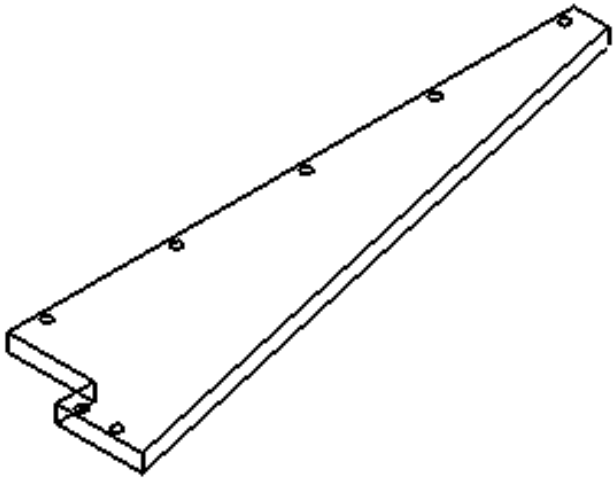

| | |
|---|---|
| Brunel University | Do not scale |
| Unit MM | Drawn P. Vongbandit |
| Material Low carbon steel | Dwg No. 3 |
| Quantity 2 | Page 3/12 |
| Title REINFORCEMENT | |

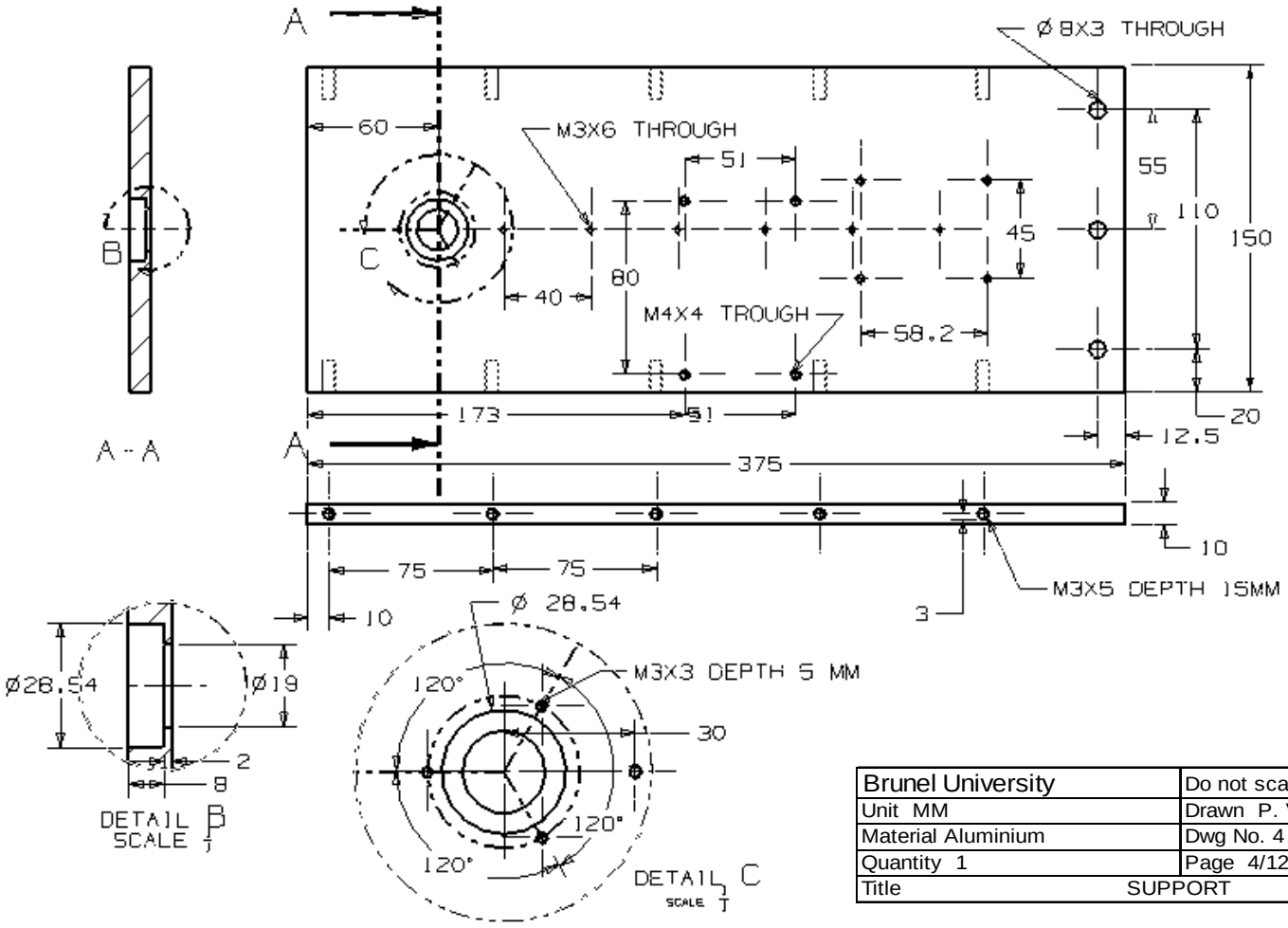


| | |
|---|---|
| Brunel University | Do not scale |
| Unit MM | Drawn P. Vongbandit |
| Material Aluminium | Dwg No. 4 |
| Quantity 1 | Page 4/12 |
| Title | SUPPORT |

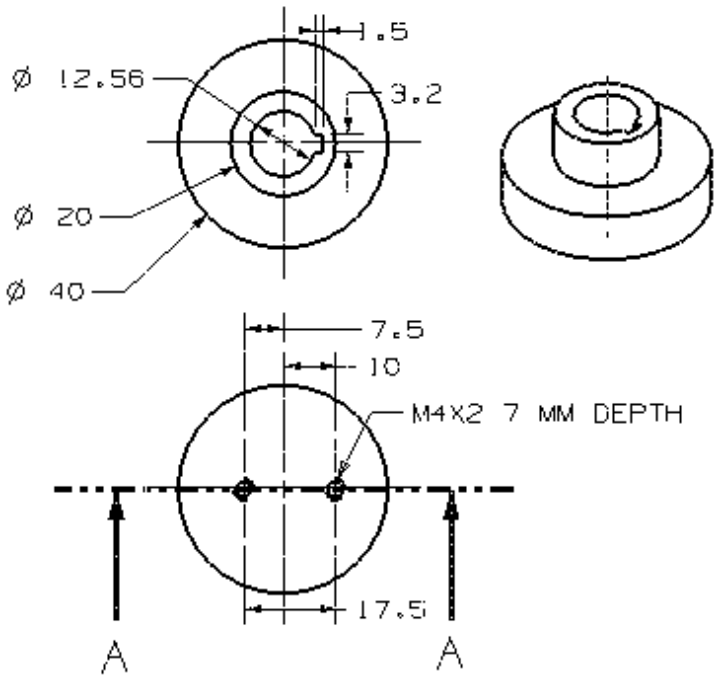


PULLEY

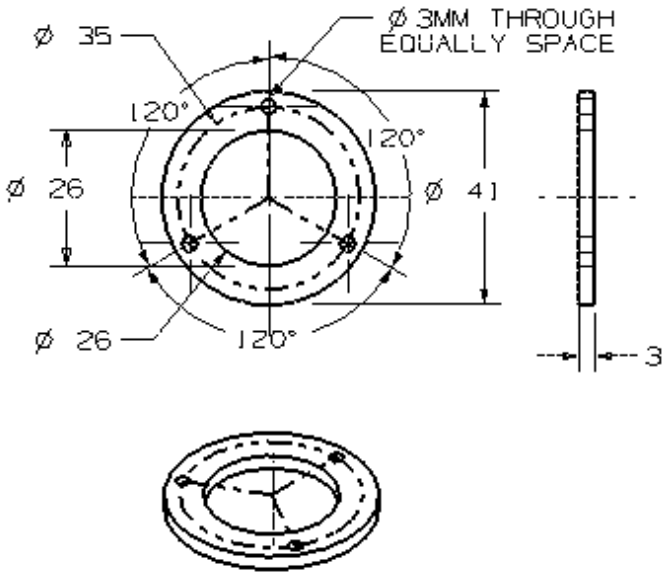


BEARING CONSTRAIN

| | |
|---|---|
| Brunel University | Do not scale |
| Unit MM | Drawn P. Vongbandit |
| Material Low carbon steel | Dwg No. 5 |
| Quantity 1 | Page 5/12 |
| Title PULLEY AND BEARING CONSTRAIN | |

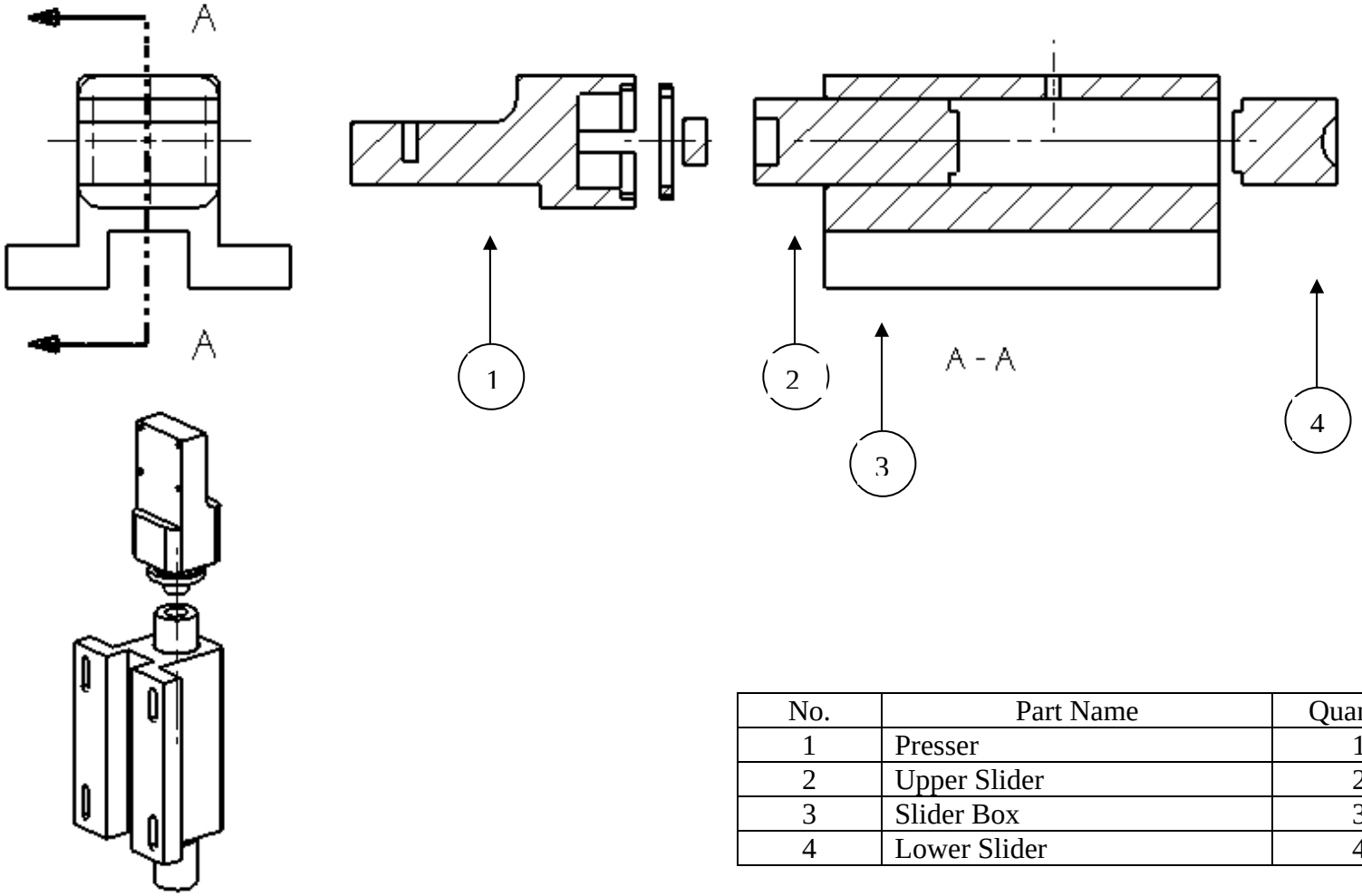


| No. | Part Name | Quantity |
|---|---|---|
| 1 | Presser | 1 |
| 2 | Upper Slider | 2 |
| 3 | Slider Box | 3 |
| 4 | Lower Slider | 4 |

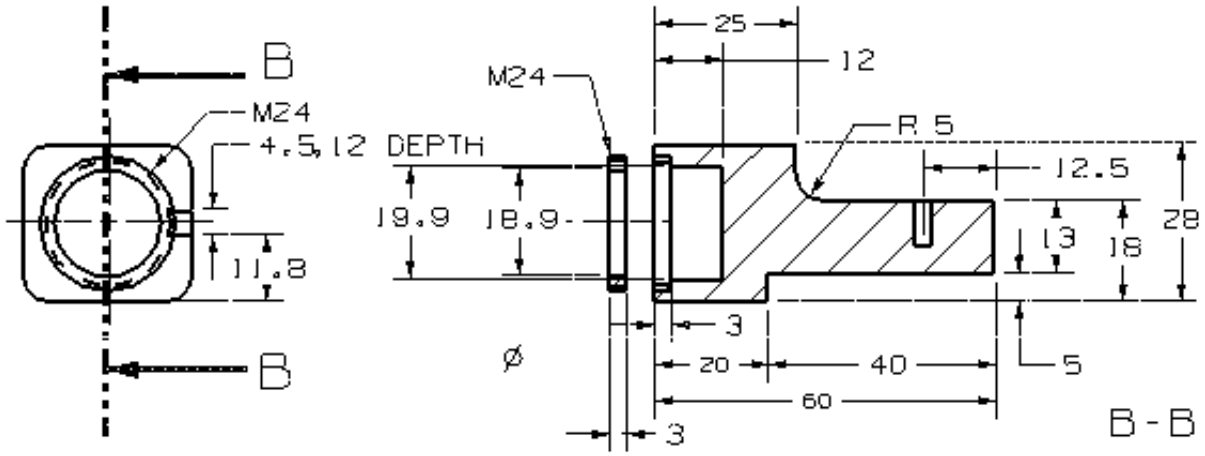


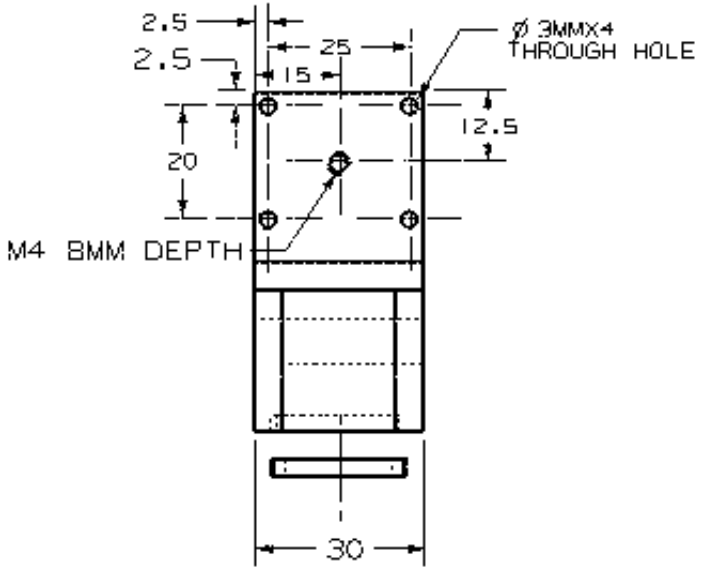


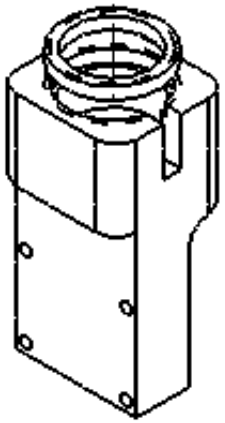

| | |
|---|---|
| Brunel University | Do not scale |
| Unit MM | Drawn P. Vongbandit |
| Material Low carbon steel | Dwg No. 7 |
| Quantity 1 | Page 7/12 |
| Title PRESSER | |

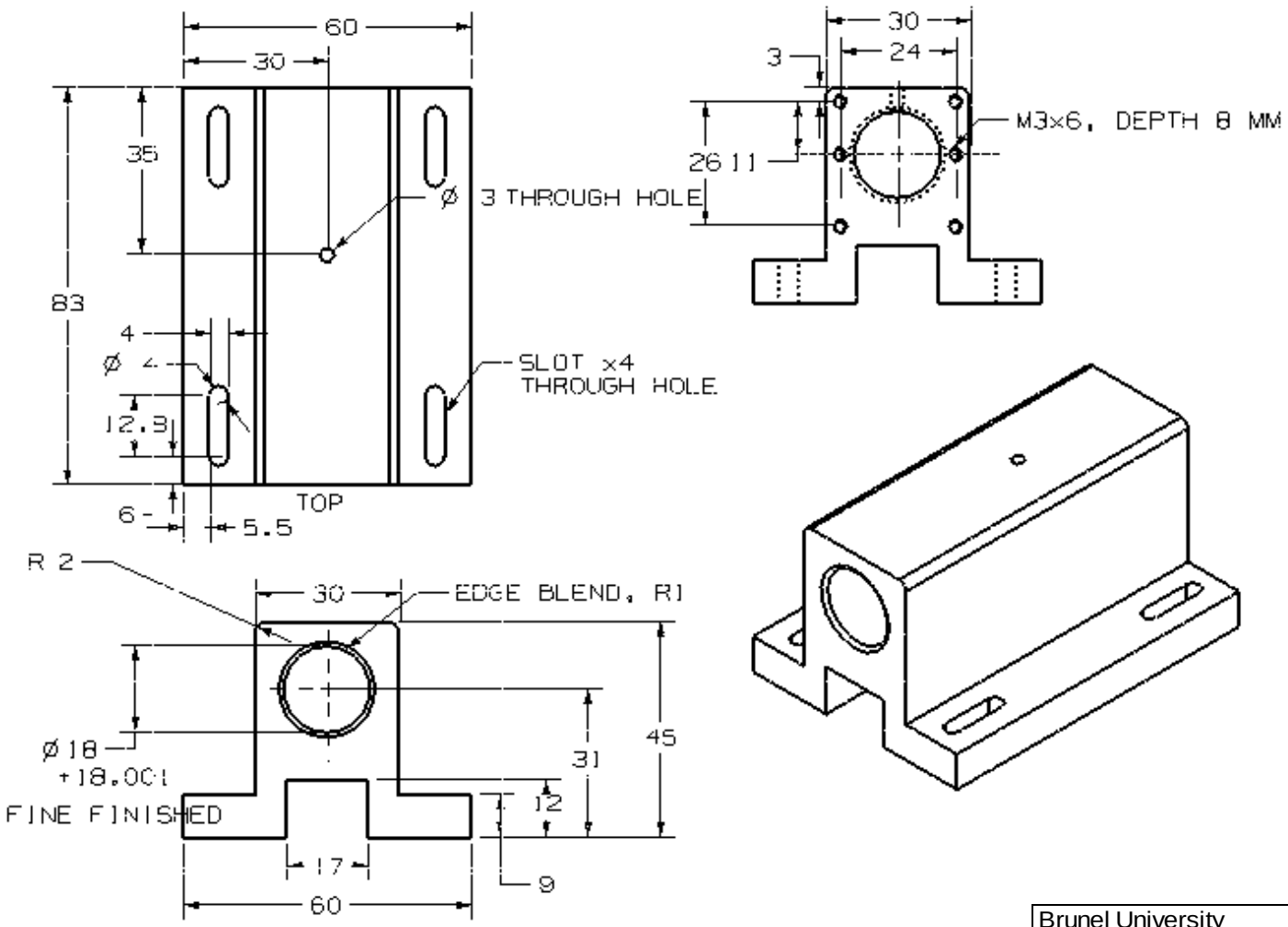


| | |
|---|---|
| Brunel University | Do not scale |
| Unit MM | Drawn P. Vongbandit |
| Material Aluminium alloy | Dwg No. 8 |
| Quantity 1 | Page 8/12 |
| Title SLIDER BOX | |

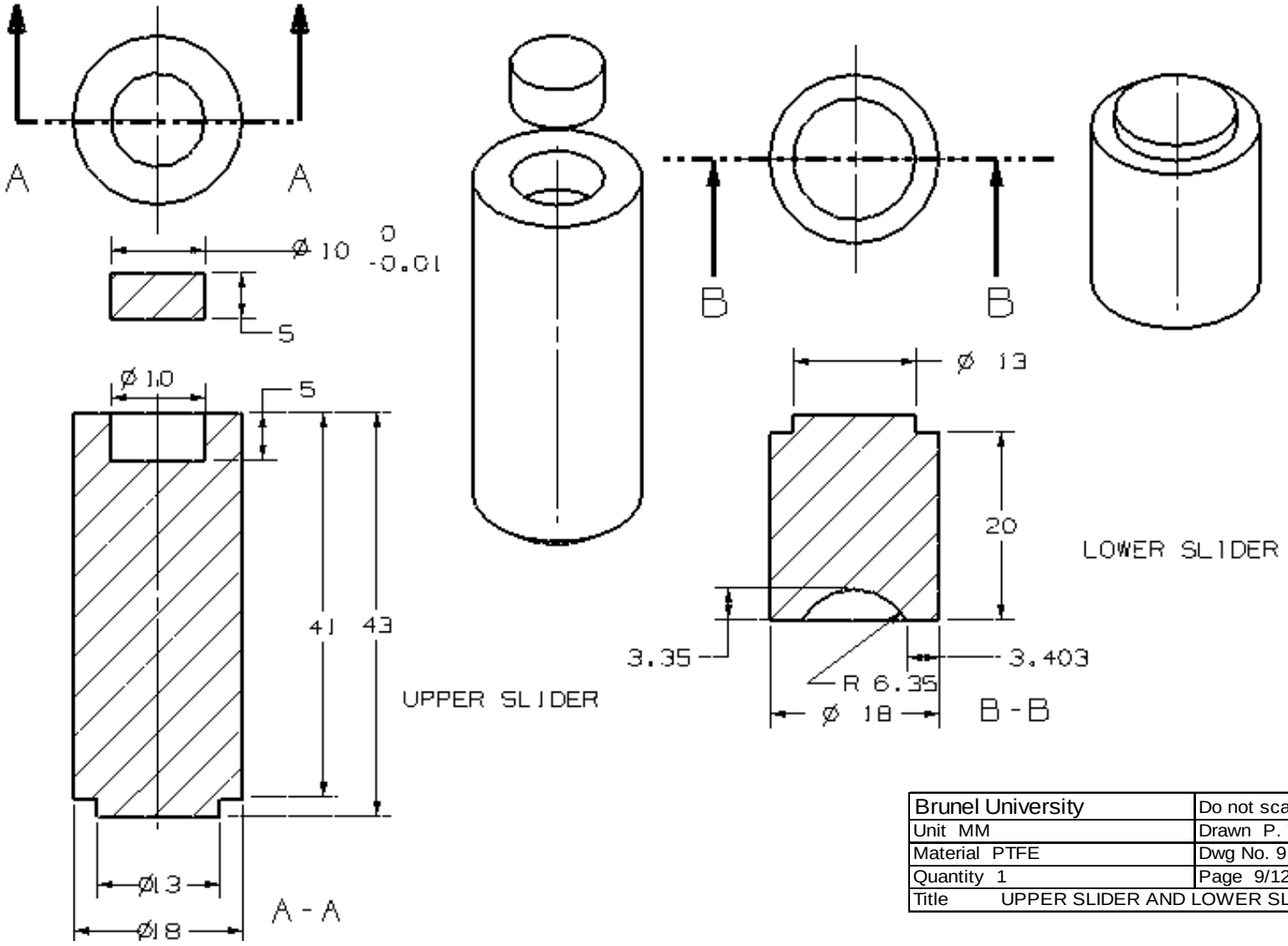


| | |
|---|---|
| Brunel University | Do not scale |
| Unit MM | Drawn P. Vongbandit |
| Material PTFE | Dwg No. 9 |
| Quantity 1 | Page 9/12 |
| Title UPPER SLIDER AND LOWER SLIDER | |

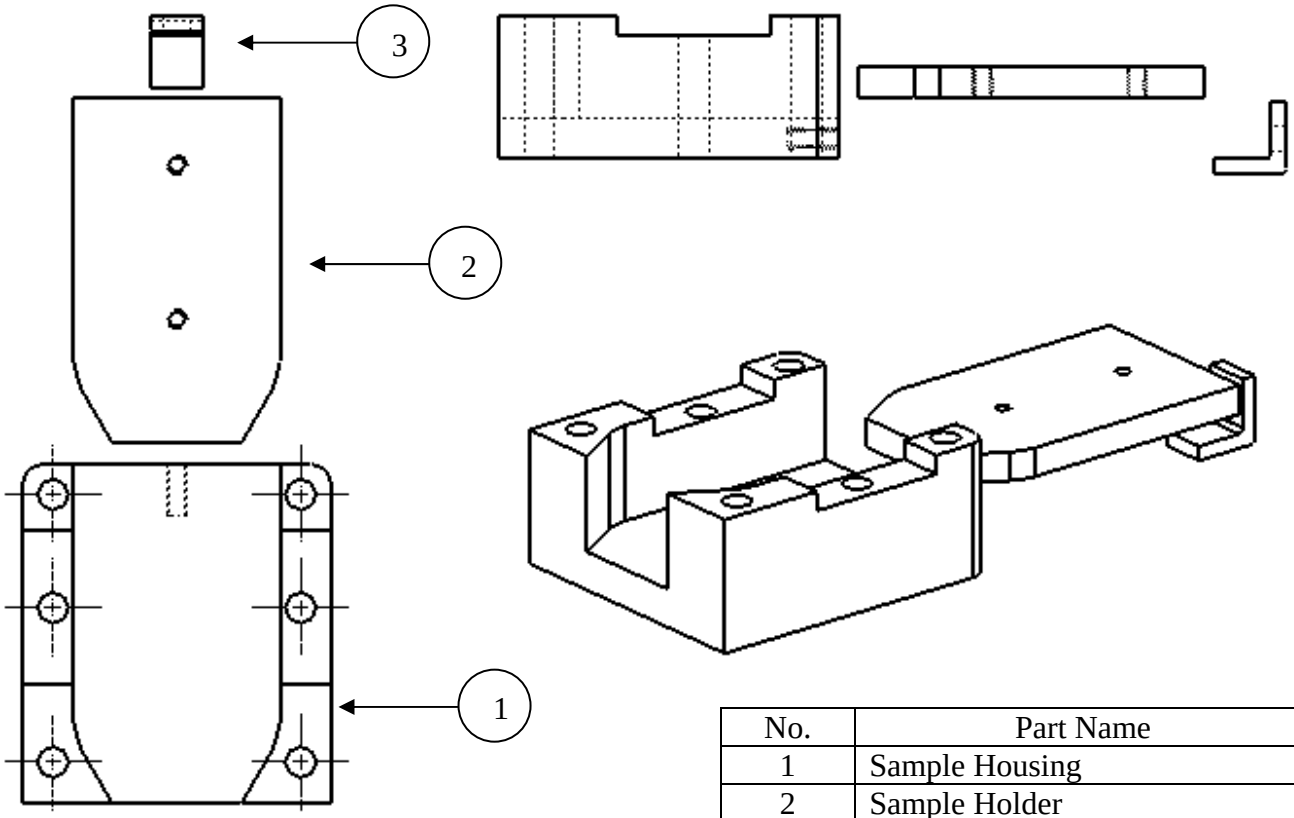


| No. | Part Name | Quantity |
|---|---|---|
| 1 | Sample Housing | 1 |
| 2 | Sample Holder | 1 |
| 3 | Sample Holder Constrain | 1 |

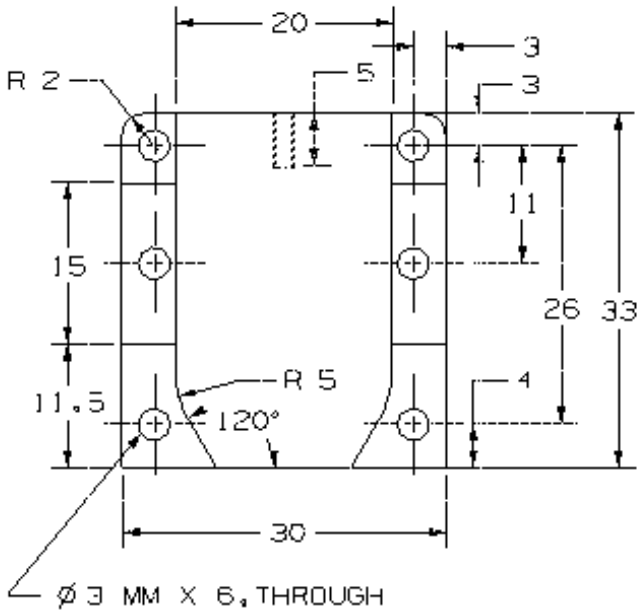


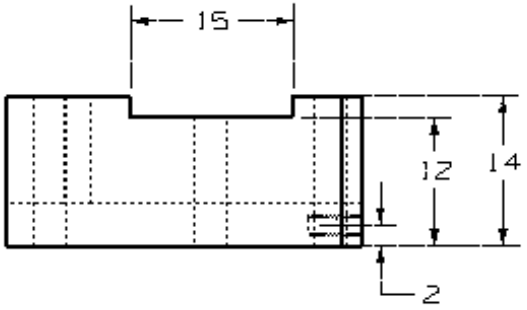


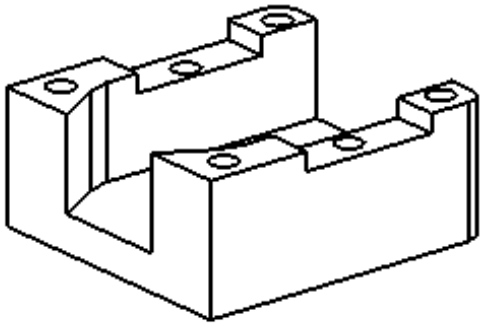

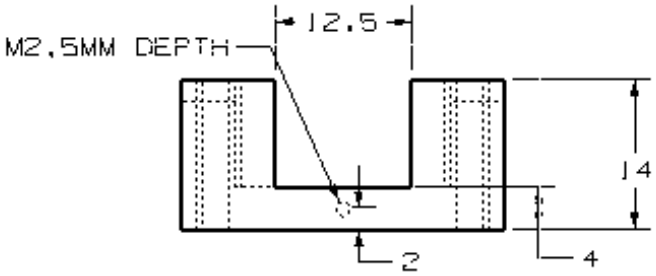


| | |
|---|---|
| Brunel University | Do not scale |
| Unit MM | Drawn P. Vongbandit |
| Material Aluminium alloy | Dwg No. 11 |
| Quantity 1 | Page 11/12 |
| Title SAMPLE HOUSING | |

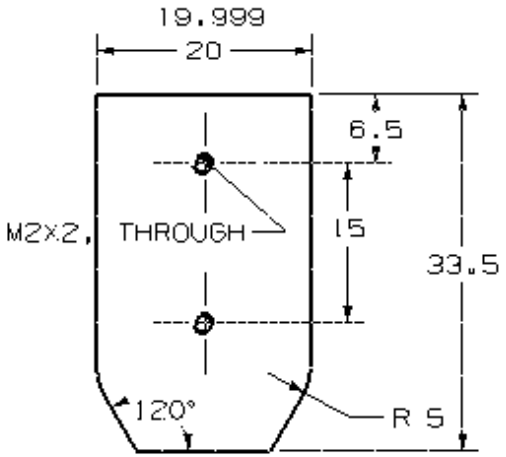


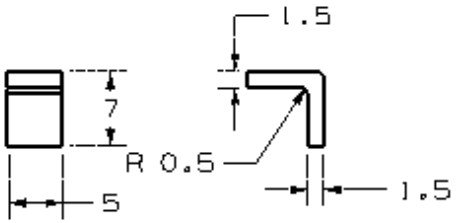


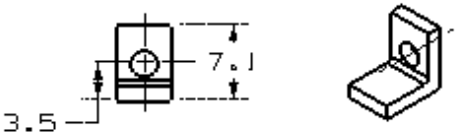


SAMPLE HOLDER CONSTRAIN

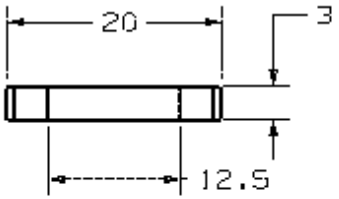


SAMPLE HOLDER

| | |
|---|---|
| Brunel University | Do not scale |
| Unit MM | Drawn P. Vongbandit |
| Material Low carbon steel | Dwg No. 12 |
| Quantity 1 | Page 12/12 |
| Title SAMPLE HOLDER AND SAMPLE HOLDER CONSTRAIN | |

## Appendix B DRAWING OF CUP ASSY FOR MODIFIED FOUR BALL MACHINE

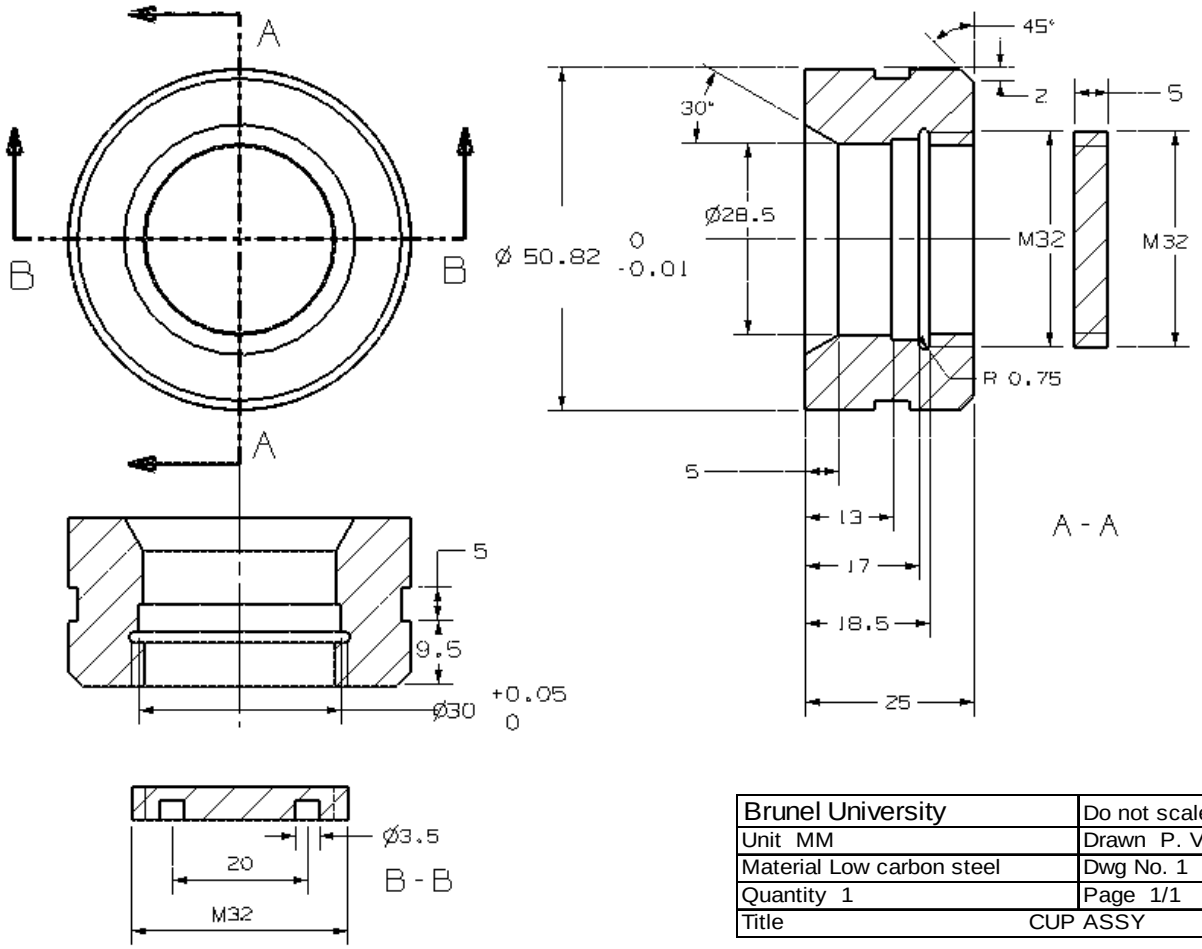


| | |
|---|---|
| Brunel University | Do not scale |
| Unit MM | Drawn P. Vongbandit |
| Material Low carbon steel | Dwg No. 1 |
| Quantity 1 | Page 1/1 |
| Title CUP ASSY | |

# Appendix C Elastohydrodynamic Lubrication

The RCF test is conducted in immerse seawater at ambient temperature and the stress range of the contact is selected in the elastic region. Therefore, elastohydrodynamic lubrication conditions are expected. Ertel and Grubin were firstly proposed the realistic model which provided the approximation of the elastohydrodynamic film thickness (cited in Stachowiak and Batcher, 2005). The succeeding work was done to complete understanding the mechanism of the elastohydodynamic lubrication (EHL). Many models have been proposed with a minor different in value. This research will used the formula for calculation the minimum film thickness, $h_{\min}$, from Hamrock and Dowson in 1981 (*cited in* Stachowiak and Batcher, 2005):

$$H_{\min} = \frac{h_{\min}}{R^*} = 3.63U^{*0.68}G^{*0.49}W^{*-0.073}(1-e^{-0.68k}) \qquad \text{(E1)}$$

where $H_{min}$ is the non-dimensional film parameter defined as $H_{\min} = \left(\frac{h_{\min}}{R^*}\right)$ (E2)

$U^*$ is the non-dimensional speed parameter defined as $U^* = \left(\frac{U\eta_0}{E_r R^*}\right)$ (E3)

$G^*$ is the non-dimensional materials parameter defined as $G^* = \alpha E_r$ (E4)

$W^*$ is the non-dimensional load parameter defined as $W^* = \left(\frac{W}{E_r R^{*2}}\right)$ (E5)

k is the non-dimensional ellipticity parameter defined as $k = \left(\frac{a}{b}\right)$ (E6)

$U$ is the entraining surface velocity [m/s] in this case the velocity is in x direction only;

$\eta_0$ is the dynamic vicoscity at atmospheric pressure of lubricant [Nsm$^{-2}$];

$E_r$ is the reduced Young's modulus [Pa];

$R^*$ is the reduced radius of curvature [m];

$\alpha$ is the pressure-viscosity coefficient [$m^2$/N];

$W$ is the contact load [N];

$a$ is the semiaxis of the contact ellipse in the transverse direction [m] and

$b$ is the semiaxis in the direction of motion [m].

where
$$E_r = \left( \frac{1}{2} \times \left( \frac{1-\nu_1^2}{E_1} + \frac{1-\nu_2^2}{E_2} \right) \right)^{-1} \tag{E7}$$

The ellipticity parameter can be calculated from

$$\tilde{k} = 1.0339 \left( \frac{R_y}{R_x} \right)^{0.636} \tag{E8}$$

The equation (E1) shows that the most dominant exponent to the least exponent is the speed parameter, material parameter and the load parameter (Hamrock *et al.* 2004). However, the variation of the material parameter in each case is limited. According to the ball on flat configuration the elliptical parameter is approach to 1 in this case.

The above equations are calculated for ideal smooth surface. However, in reality the surfaces are rough. Therefore, the ratio (λ) of elastohydrodynamic lubrication film thickness for rough surfaces is used in the follow relationship;

$$\lambda = \frac{h_{\min}}{(R_{qb}^2 + R_{qd}^2)^{1/2}} \tag{E9}$$

where $R_{qb}$ is the root mean square (RMS) surface roughness of the ball.

$R_{qd}$ is the RMS surface roughness of the plate.

The λ can effectively describe the transition of lubrication regime either boundary lubrication regime, partial lubrication regime, elastohydrodynamic lubrication regime or hydrodynamic lubrication regime (Hamrock *et al.* 2004).

Hydrodynamic lubrication $5 < \lambda < 10$

Elastohydrodynamic lubrication $3 < \lambda < 10$

Partial lubrication $1 < \lambda < 5$

Boundary lubrication $\lambda < 1$.

These values are roughly approximated.

From this research;

$E_{Mo} = 235$ GPa

$\nu_{Mo} = 0.32$

$E_{Ti} = 37.5$ GPa

$\nu_{Ti} = 0.34$

$E_{Ball} = 207$ GPa

$\nu_{Ball} = 0.3$

$R_{Ball} = 6.35\times10^{-3}$ m

$R_{Plate} = \infty$ m

$\eta_0$ of seawater $= 1.08\times10^{-3}$ $Nsm^{-2}$

$\alpha$ of seawater $= 4.6\times10^{-10}$ $m^2N^{-1}$

$U = 5.16\times10^{-2}$ $ms^{-1}$

$W = 65.4$ N

$R_{qb} = 1.9\times10^{-7}$ m

$R_{qd} = 6.82\times10^{-6}$ m for molybdenum coating and $6.72\times10^{-6}$ m for titanium coating

In this case; $R_x = R_y = R^* = 6.35\times10^{-3}$ m

Substitute the values in each corresponded equations can be calculated $\lambda$ as;

Molybdenum coating:

$$E_r = \left(\frac{1}{2}\times\left(\frac{1-0.3^2}{2.07\times10^{11}}+\frac{1-0.32^2}{2.35\times10^{11}}\right)\right)^{-1} = 2.43\times10^{11}$$

$$U^* = \left( \frac{5.16 \times 10^{-2} \times 1.08 \times 10^{-3}}{2.43 \times 10^{11} \times 6.35 \times 10^{-3}} \right) = 3.6 \times 10^{-14}$$

$$G^* = 4.6 \times 10^{-10} \times 2.43 \times 10^{11} = 112$$

$$W^* = \frac{65.4}{2.43 \times 10^{11} \times (6.35 \times 10^{-3})^2} = 6.66 \times 10^{-6}$$

$$\tilde{k} = 1.0339 \left( \frac{6.35 \times 10^{-3}}{6.35 \times 10^{-3}} \right)^{0.636} = 1.0339$$

Then

$$H_{\min} = \frac{h_{\min}}{6.35 \times 10^{-3}} = 3.63 \times (3.6 \times 10^{-14})^{0.68} \times 112^{0.49} \times (6.66 \times 10^{-6})^{-0.073} \times (1 - e^{-0.68 \times 1.0339})$$

$$h_{\min} = 2.03 \times 10^{-10}$$

$$\lambda = \frac{2.03 \times 10^{-10}}{[(1.9 \times 10^{-7})^2 + (6.82 \times 10^{-6})^2]^{1/2}} = 3 \times 10^{-5}$$

Titanium coating:

$$E_r = \left( \frac{1}{2} \times \left( \frac{1 - 0.3^2}{2.07 \times 10^{11}} + \frac{1 - 0.34^2}{3.75 \times 10^{10}} \right) \right)^{-1} = 7.15 \times 10^{10}$$

$$U^* = \left( \frac{5.16 \times 10^{-2} \times 1.08 \times 10^{-3}}{7.15 \times 10^{10} \times 6.35 \times 10^{-3}} \right) = 1.23 \times 10^{-13}$$

$$G^* = 4.6 \times 10^{-10} \times 7.15 \times 10^{10} = 32.9$$

$$W^* = \frac{65.4}{7.15\times10^{10}\times(6.35\times10^{-3})^2} = 2.27\times10^{-5}$$

$$\tilde{k} = 1.0339\left(\frac{6.35\times10^{-3}}{6.35\times10^{-3}}\right)^{0.636} = 1.0339$$

Then

$$H_{\min} = \frac{h_{\min}}{6.35\times10^{-3}} = 3.63\times(1.23\times10^{-13})^{0.68}\times32.9^{0.49}\times(2.27\times10^{-5})^{-0.073}\times(1-e^{-0.68\times1.0339})$$

$$h_{\min} = 2.34\times10^{-10}$$

$$\lambda = \frac{2.34\times10^{-10}}{[(1.9\times10^{-7})^2+(6.72\times10^{-6})^2]^{1/2}} = 3.5\times10^{-5}$$

**Reference:**

Hamrock, B. J., Schmid, S. R. and Jacobson B. (2004) "*Fundamentals of machine elements 2nd ed.*" New York: McGraw-Hill Professional.

Stachowiak G. W. and Batcher, A. W. (2005) "*Engineering tribology 3rd ed*." Elsevier Massachusetts: Butterworth-Heinemann.

# APPENDIX D PRELIMINARY AND AUXILARY EXPERIMENTS

This appendix describes the work done prior to the main work presented in this thesis.

## D1 Preliminary Experiments

### *D1.1 Static Contact Fatigue*

Prior to select test conditions of static contact fatigue, two factors were concerned including test frequency and mean stress. The following presents the result of both factors.

#### *D1.1.1 Effect of Test Frequency*

The objective in this test was to determine the appropriate frequency to for using in the main experiment in this thesis. The cyclic stress conditions applied to contact was set at mean value 60.2 N, minimum stress 0.4 N and maximum stress120 N. The frequencies selected were 5 Hz and 10 Hz. The tests were conducted in combination with $Si_3N_4$ ball for 108,000 load cycles. The damage results on the PMMA plate present in Figure D1.

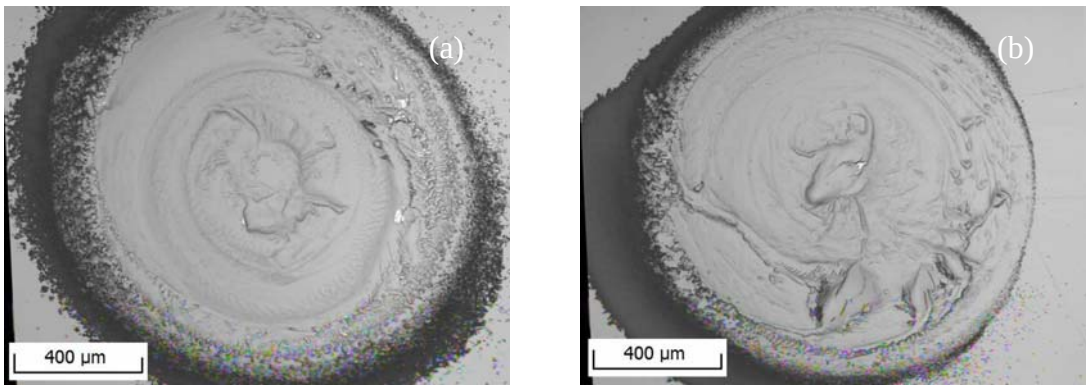


Figure D1 Damage of PMMA plate after 108,000 cycles. (a) frequency 5 Hz (b) frequency 10 Hz.

The results show that frequency 5 Hz and 10 Hz gave similar damage to the PMMA plates. In this regards, the test at 10 Hz was selected for the experiment in this thesis in order save time.

*D1.1.2 Effect of Mean Stress*

In order to study the static contact fatigue failure mechanisms of PMMA, test conditions should be assured the consistent of the test results. Mean stress is the important factor affected to the damage of fatigue of polymers as mentioned in chapter 2. The preliminary study was selected two mean stresses for comparison, i.e. 60.2 N and 80 N. The maximum stress was set the same at 120 N. The tests were conducted with frequency 10 Hz and the combinations of $Si_3N_4$/PMMA and steel/PMMA were served for this experiment. The results are shown in Figure D2.

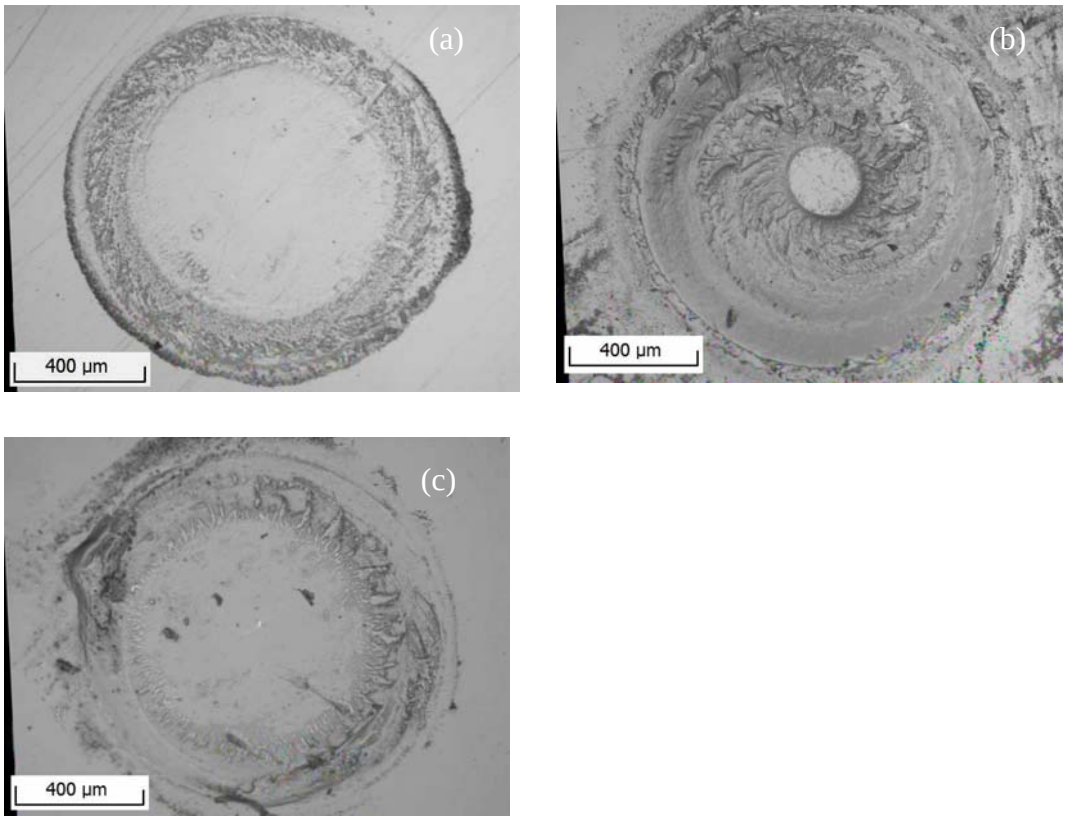


Figure D2 Damage of PMMA plate after 108,000 cycles with frequency 10 Hz;
(a) $Si_3N_4$/PMMA combination mean stress 60.2 N (b) and (c)
steel/PMMA combination (b) mean stress 60.2 N (c) mean stress 80 N.

The effect of mean stress was clearly distinguished that with constant maximum stress the mean stress 60.2 N caused more severe damage than that of the mean stress 80 N (compare between Figure D1b and D2a; Figure D2b and D2c). The low mean stress was not only results in smaller stick region but also high loading amplitude. Therefore, the contact region was less the stability because the displacement in circumferential direction could occur as seen in the damage feature leading to fast progression of damage. In this regards,

the mean stress 80 N was selected for its contact stability and better for monitoring of damage progression.

### *D1.2 Dynamic Contact Fatigue*

Corrosion resistant in seawater of molybdenum coating and titanium coating specimens were tested by immersion test. The coating discs were coated by silicone at the substrate side to prevent the reaction with seawater (see Figure D3a). The discs were immersed in seawater and corrosion was monitored visually and documented every hour. The results show that corrosion occurred firstly on molybdenum coating just after one hour while corrosion on titanium coating was detected after seven hours. Slow corrosion on titanium coating may due to slow wetting process of titanium coating the surface (see Figure D3b). The results of corrosion after soaking for 20 hours are shown in Figure D4.

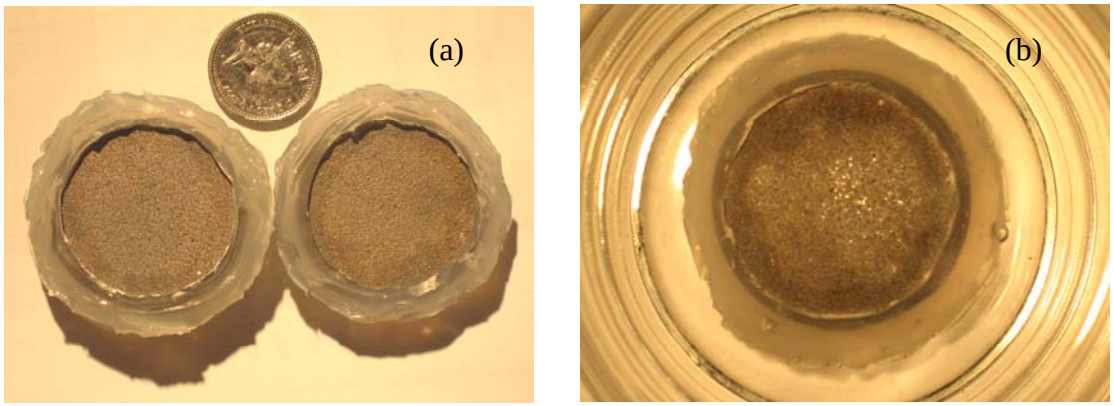


Figure D3 Coating discs of titanium coating (left) and molybdenum coating (right) before immersion test.

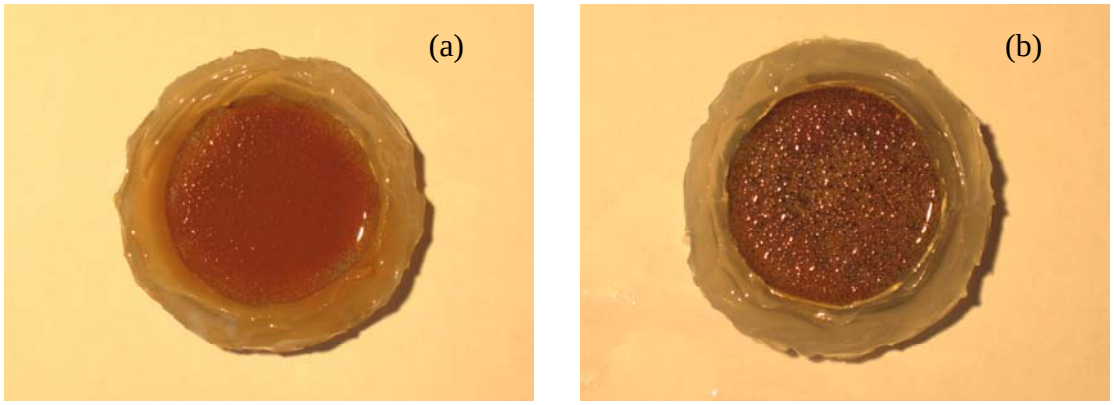


Figure D4 Corrosion after immersion test in seawater after 20 hours; (a) molybdenum coating (b) titanium coating.

Corrosion products were reddish to brownish colour. This implied that corrosion products were in the form of oxide or hydroxide of iron. Therefore, it is expected that seawater can penetrate through the coatings to react with the steel substrate.

**D2 Auxiliary Experiments**

Auxiliary experiments were the investigations of wear debris of molybdenum coating and titanium coating using SEM and EDX. The results are shown in Figure D5-D9. For molybdenum coating, the size wear debris tested with high contact stress exhibited greater than that tested with low contact stress (see Figure D5 and D6). In general, wear debris tested in dry conditions has a sharp edge compare to that obtained in seawater conditions.

In case of molybdenum coating, the composition of wear debris composed mainly with molybdenum and oxygen with trace of iron. Contrast to in dry conditions, the main compositions of wear debris tested in seawater conditions was iron and oxygen with amount of molybdenum. With the same contact stress the size of wear debris tested in seawater conditions was smaller than that tested in dry conditions (see Figure D7).

In case of titanium coating, the size of wear debris in dry conditions was much larger than that in seawater conditions (see Figure D8 and D9). The compositions of wear debris in dry conditions contained mainly titanium and oxygen with small amount of iron and silicon. It was contrary the result in seawater conditions which iron and oxygen were the main constituents with amount of titanium and silicon.

The examination with optical microscope revealed that wear debris of both coating systems in dry condition show black colour along with shiny metal particles while the debris in seawater conditions presented red to brown colour with amount of shiny metal particles. These results could be assumed that the compound of wear debris in both conditions were different.

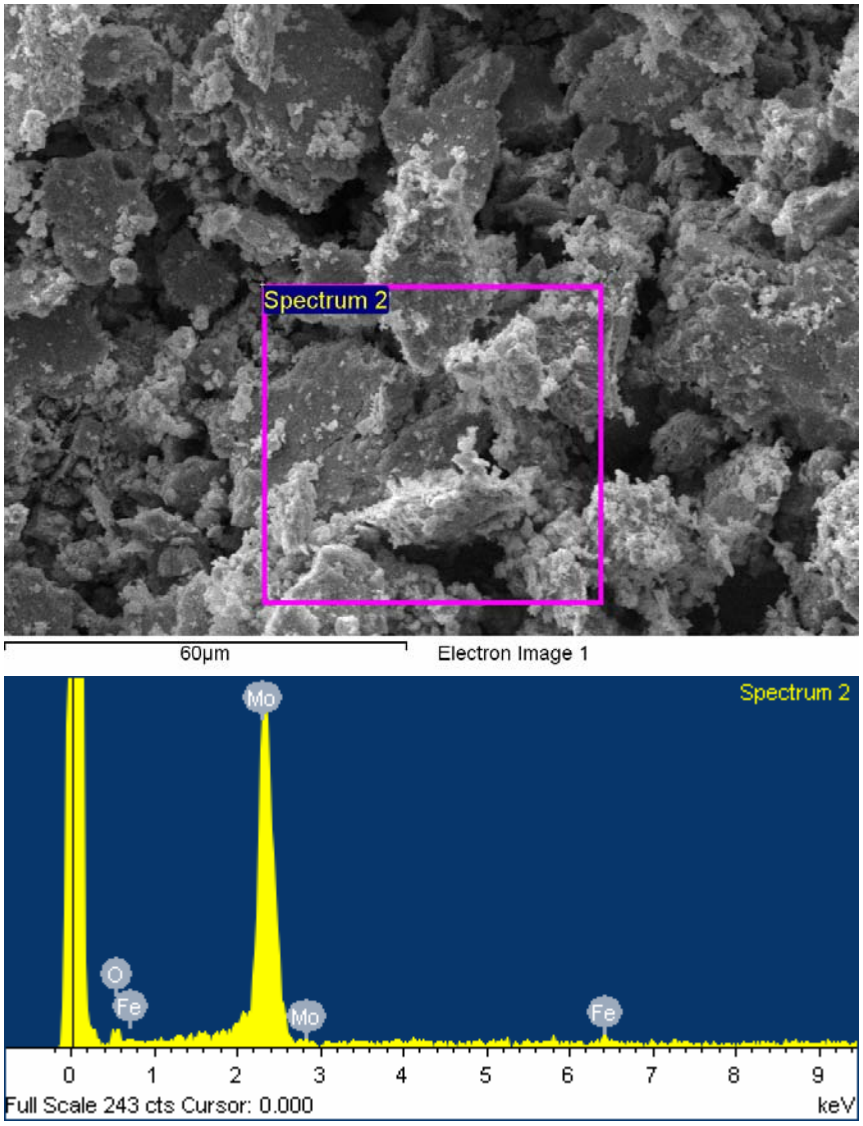


Figure D5 SEM image and EDX result of wear debris of molybdenum coating tested in dry condition at contact pressure 1.91 GPa after 12,474 cycles.

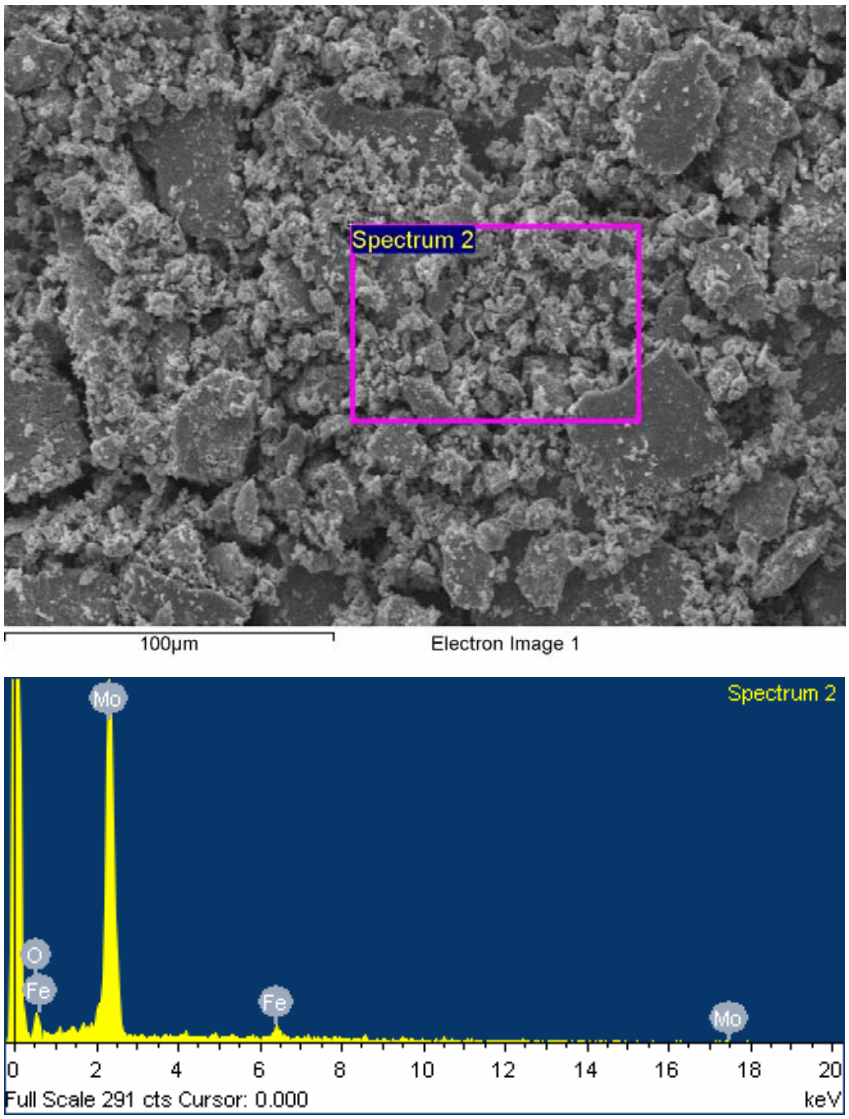


Figure D6 SEM image and EDX result of wear debris of molybdenum coating tested in dry conditions at contact pressure 1.67 GPa after 37,422 cycles.

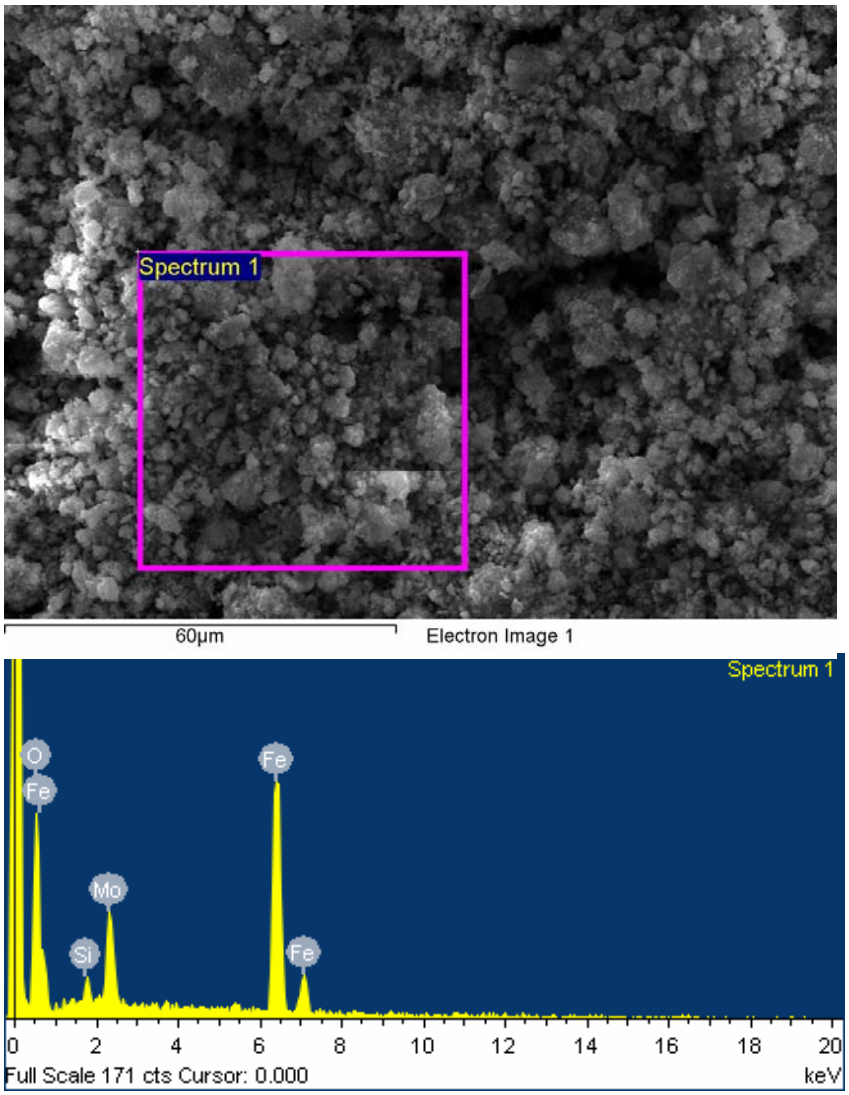


Figure D7 SEM image and EDX result of wear debris of molybdenum coating tested in seawater conditions at contact pressure 1.67 GPa after 399,164 cycles.

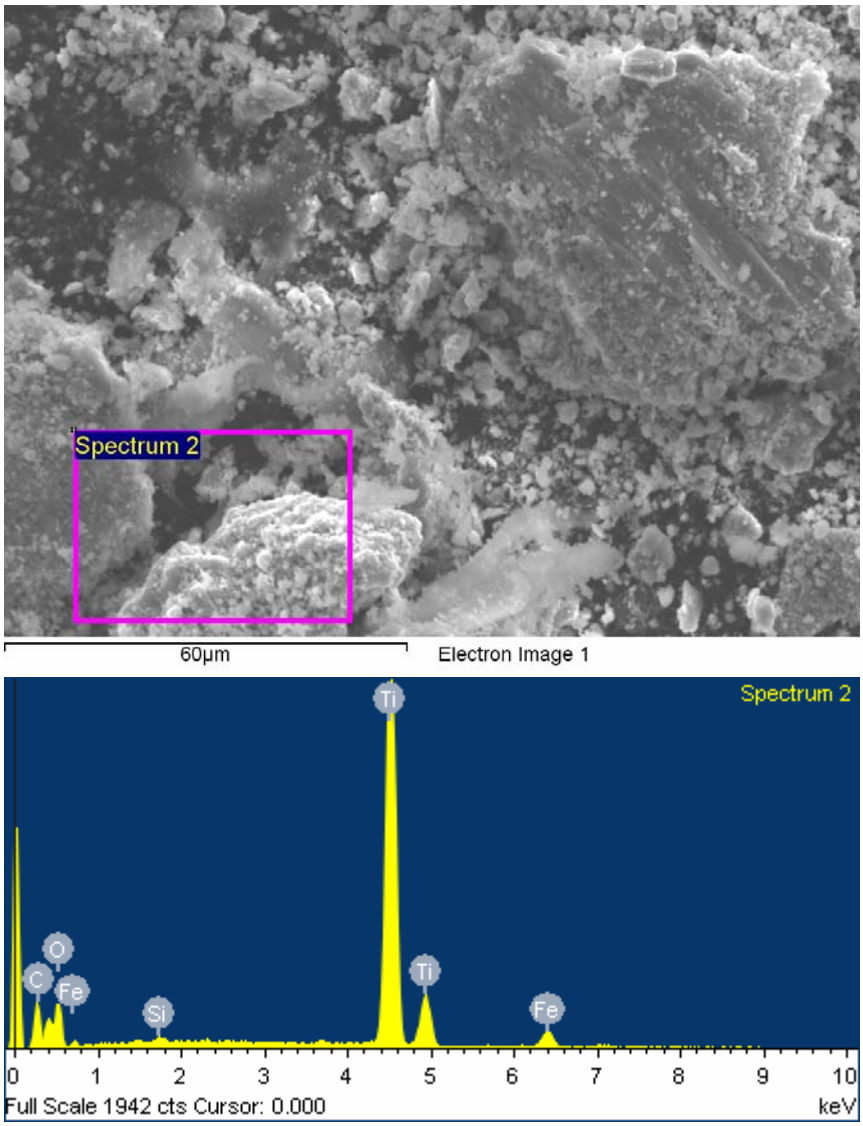


Figure D8 SEM image and EDX result of wear debris of titanium coating tested in dry conditions at contact pressure 1.67 GPa after 18,711 cycles.

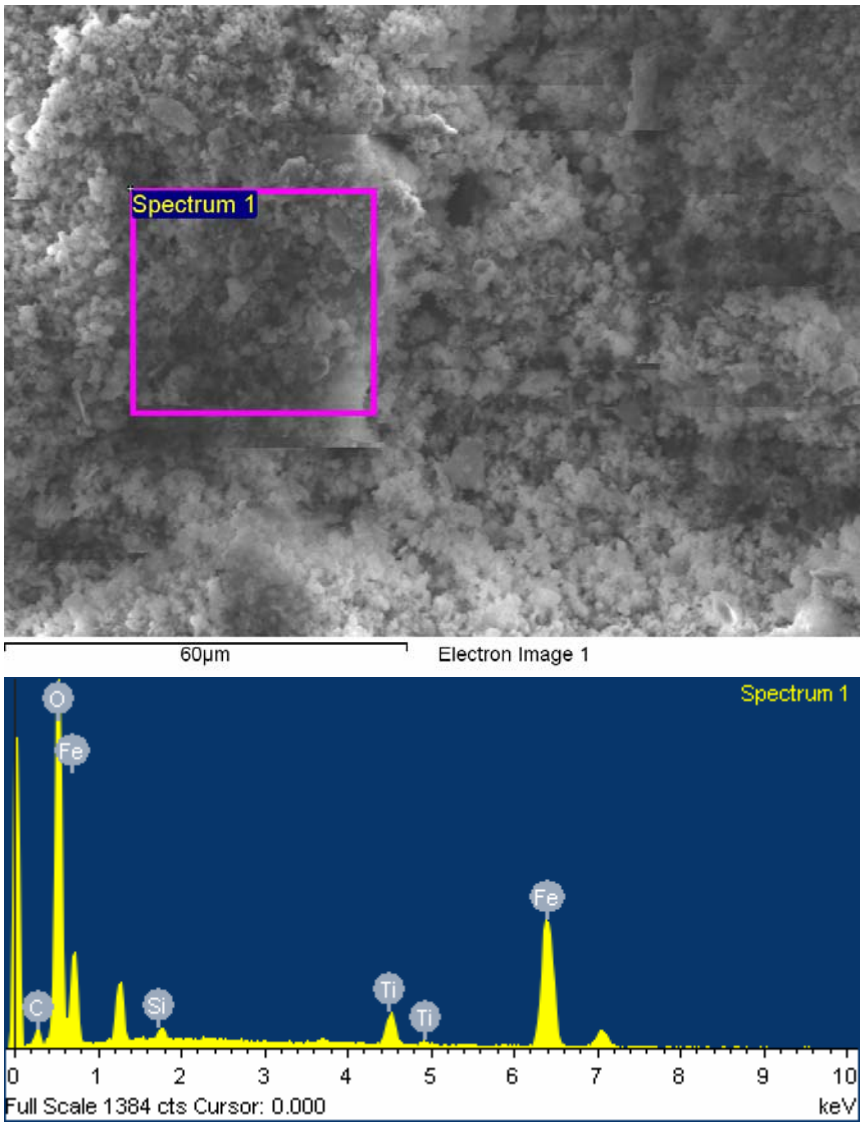


Figure D9 SEM image and EDX result of wear debris of titanium coating tested in seawater conditions at contact pressure 1.67 GPa after 74.843 cycles.